Dynamical Properties of Quasi One-Dimensional Correlated Electron Systems

Dissertation

zur Erlangung des
Doktorgrades der Naturwissenschaften
(Dr. rer. nat.)
dem Fachbereich Physik
der Philipps-Universität Marburg
vorgelegt von

Holger Benthien
aus Hamburg

Marburg an der Lahn, Februar 2005

Vom Fachbereich Physik der Philipps-Universität Marburg
als Dissertation angenommen am: 15.03.2005

Erstgutachter: Prof. Dr. F. Gebhard
Zweitgutachter: Priv.-Doz. Dr. E. Jeckelmann

Tag der mündlichen Prüfung: 21.03.2005

Zusammenfassung

Die physikalischen Eigenschaften quasi-eindimensionaler Elektronensysteme unterscheiden sich drastisch von denen verwandter Systeme in zwei oder drei Dimensionen. In Anwesenheit elektronischer Wechselwirkungen verändert sich die Natur der niedrigenergetischen Anregungen fundamental und führt zu exotischen quantenphysikalischen Phasen in niedrigen Dimensionen.

Anfang der 50er Jahre war es noch ein Rätsel, weshalb sich normale Metalle durch die Bänder freier Elektronen beschreiben lassen, obwohl die Coulomb-Wechselwirkung zwischen ihnen stark und langreichweitig ist. Erst mit der Landau-Fermi-Flüssigkeitstheorie wurde klar, daß die niederenergetischen Anregungen einfacher Metalle die gleichen Quantenzahlen, Ladung $(-e)$ und Spin $1/2$, wie die nicht-wechselwirkenden Teilchen des freien Elektronengases tragen. Diese *Quasi-Elektronen* lassen sich, bis auf eine Renormierung ihrer Masse und eine endliche Lebensdauer, durch freie Teilchen beschreiben. Darin liegt die Grundlage des Erfolgs des Fermi-Flüssigkeits-Paradigmas.

Dieser Ansatz scheitert jedoch spektakulär in eindimensionalen Metallen. Jede noch so kleine Wechselwirkung der Elektronen untereinander erzeugt einen quantenmechanischen Zustand, der mit dem freien Elektronengas nichts mehr gemein hat. Die elementaren Anregungen eines solchen Systems ähneln nicht mehr den urspünglichen Elektronen. Stattdessen scheint das Elektron in zwei neue Teilchen zu zerfallen. Eines davon, das *Antiholon*, trägt nur die Ladung $(-e)$, aber keinen Spin, welcher vom ladungsneutralen *Spinon* getragen wird. Natürlich bleibt das Elektron ganz; es handelt sich um kollektive, bosonische Anregungen des Vielteilchensystems.

Diese Spin-Ladungstrennung wirkt sich auf alle physikalischen Eigenschaften der Systeme aus, insbesondere auf frequenz- und impulsabhängige Korrelationsfunktionen. Diese dynamischen Größen tauchen immer dann auf, wenn eine zeitabhängige Störung auf das System einwirkt. Typische Beispiele sind Streuexperimente, wie die Streuung von Photonen in der winkelaufgelösten Photoemissionsspektroskopie oder inelastische Röntgenstreuung, die inelastische Streuung von Neutronen oder die Streuung von Elektronen. Dynamische Korrelationsfunktionen beschreiben aber auch die optischen Eigenschaften eines Materials oder den Tunnelstrom in eine Probe.

Experimentelle Realisierungen von eindimensionalen, korrelierten Elektronensystemen sind organische Ladungstransfersalze in deren Kristallverband einzelne organische Moleküle wie Pfannkuchen übereinander gestapelt sind. Zu diesen Verbindungen gehört TTF-TCNQ und die Familie der supraleitenden Bechgaardsalze. Diese Substanzklassen haben in den letzten Jahren großes experimentelles Interesse auf sich gezogen, da sie als prototypische eindimensionale Systeme gelten. Ebenso prominent ist das anorganische Ladungstransfersalz $SrCuO_2$, in dem einzelne Kupferoxidketten in Schichten vorliegen. Dieses Kuprat wird als idealer Mott-Isolator angesehen, dessen magnetische Eigenschaften hervorragend durch Spinketten beschrieben werden.

Wie lassen sich diese Systeme modellieren? Die theoretische Beschreibung solcher Systeme steht einem Dilemma gegenüber. Alle konstituierenden Bestandteile und die Wechselwirkungen zwischen ihnen sind bekannt. Die 10^{23} Elektronen einer makrosko-

pischen Festkörperprobe bewegen sich im Potential der Atomrümpfe des Kristallgitters und wechselwirken miteinander. Die zugehörigen quantenmechanischen Gleichungen sind bekannt. Allerdings sind sie selbst in den einfachsten Fällen nicht lösbar. Gäbe es eine Lösung, so wäre sie so kompliziert, daß sich mit ihr keine dynamischen Korrelationsfunktionen bestimmen ließen. Man ist daher darauf angewiesen, vereinfachte, effektive Modelle aufzustellen, die zwar nicht das volle Problem behandeln, aber die relevanten Energieskalen beschreiben.

Trotz der Vereinfachungen kann man dynamische Responsefunktionen selbst für diese effektiven Modelle in der Regel nicht exakt berechnen. Bis auf wenige Fälle liegen analytische Lösungen nur für extreme und unphysikalische Bereiche der Modellparameter vor oder im Grenzfall verschwindend kleiner Anregungsenergien. Dies macht einen direkten Vergleich der dynamischen Modelleigenschaften mit experimentellen Ergebnissen problematisch. Ohne zuverlässige theoretische Resultate kann über die Gültigkeit der gemachten Modellannahmen nicht entschieden werden.

Einen Ausweg aus dieser Situation bieten numerische Zugänge. Ziel der vorliegenden Arbeit ist die Weiterentwicklung und Anwendung der dynamischen Dichte-Matrix Renormierungsgruppen-Methode. Sie erlaubt die Bestimmung impuls- und frequenzabhängiger dynamischer Korrelationsfunktionen der Modelle wechselwirkender Elektronen. Die hervorragende Genauigkeit dieses Zugangs wird anhand zahlreicher Vergleiche mit exakten Ergebnissen in nichttrivialen Parameterbereichen effektiver Gittermodelle nachgewiesen. Die Anwendung der Methode auf die oben genannten Materialien und Experimente wird ausführlich dokumentiert und erlaubt den Nachweis, daß sich die Besonderheiten eindimensionaler Elektronenphysik direkt spektroskopisch beobachten lassen und mit Hilfe von erweiterten Peierls-Hubbard Modellen erklärt werden können.

Contents

1 Introduction **1**

1.1 General 1

1.2 Structure of this Thesis 2

1.3 Publications 5

I Models and Methods **7**

2 Models **9**

2.1 Hubbard Model 9

2.1.1 Spin-Rotational Invariance 10

2.1.2 η-Pairing Symmetry 11

2.1.3 Particle-Hole Symmetry 11

2.2 Extended Hubbard Models 12

2.2.1 Peierls-Hubbard Model 12

2.2.2 Extended Hubbard Model 13

2.2.3 Extended Peierls-Hubbard Model 13

3 Analytic Approaches **15**

3.1 Luttinger Liquids 15

3.1.1 Tomonaga-Luttinger Model 15

3.1.2 Physical Properties 17

3.2 Bethe-Ansatz Solution 18

3.2.1 Two-Particle Problem 19

3.2.2 Many-Particle Case 20

3.2.3 Lieb-Wu Equations 21

3.3 Thermodynamic Bethe Ansatz 22

3.3.1 Bound States 23

3.3.2 String Hypothesis 24

3.3.3 Takahashi Equations 24

3.3.4 Thermodynamic Limit of the Takahashi Equations 26

3.3.5 Spinons and Holons 28

3.4 Physical Excitations 28
  3.4.1 Spinon-Spinon Excitation 29
  3.4.2 Holon-Spinon Excitation 30
  3.4.3 Antiholon-Spinon Excitation 31
  3.4.4 $4k_\mathrm{F}$-Singlet Excitation 33
  3.4.5 k-Λ-Strings 34

4 Density-Matrix Renormalization Group 37
4.1 Exact Diagonalization 37
4.2 DMRG: Density-Matrix Renormalization 38
  4.2.1 Reduced Density Matrices 38
  4.2.2 Truncation Scheme 39
  4.2.3 Accuracy of the Truncation 41
4.3 DMRG Algorithms 41
  4.3.1 Infinite-System Algorithm 42
  4.3.2 Finite-System Algorithm 43
4.4 Technical Aspects 44
  4.4.1 Measurements 45
  4.4.2 Interacting Systems 45
  4.4.3 Wave Function Transformations 46
  4.4.4 Quantum Numbers and Symmetries 46
4.5 Conclusion 47

II Dynamical Density-Matrix Renormalization Group (DDMRG) 49

5 Introduction to DDMRG 51
5.1 DDMRG 51
  5.1.1 Dynamical Correlation Functions 51
  5.1.2 Variational Principle for Dynamical Correlation Functions 52
  5.1.3 DDMRG Algorithm 53
  5.1.4 Finite Frequency Intervals 54
  5.1.5 Matrix Elements 55
  5.1.6 Finite-Size Scaling 55
  5.1.7 Deconvolution 57
5.2 Momentum-Dependent Quantities 58
  5.2.1 Periodic Boundary Conditions 58
  5.2.2 Open Boundary Conditions 59

6 Tests 61
6.1 One-Particle Dynamics 61
  6.1.1 One-Particle Spectral Function 61
  6.1.2 Momentum Distribution 64
  6.1.3 Density of States 67

6.2 Dynamical Density Structure Factor 68
    6.2.1 Comparison with Exact Diagonalization 68
    6.2.2 Limit $q \to 0$ 70
    6.2.3 Strong-Coupling Theory 71
6.3 Dynamical Spin Structure Factor 74
6.4 Conclusion 74

III Results 77

7 Angle-Resolved Photoemission in TTF-TCNQ 79
7.1 Experimental Situation 80
    7.1.1 Structure of TTF-TCNQ 80
    7.1.2 Angular Resolved Photoemission (ARPES) of TTF-TCNQ 80
7.2 TCNQ Band 83
    7.2.1 Methods 84
    7.2.2 ARPES Spectrum at Filling $n = 0.6$ 84
    7.2.3 Comparison with Bethe-Ansatz Energies 86
    7.2.4 Exponents 88
    7.2.5 Density of States at Filling $n = 0.6$ 90
7.3 TTF Band 91
    7.3.1 ARPES Spectrum at Filling $n = 1.4$: Small Binding Energies . . . 92
    7.3.2 ARPES Spectrum at Filling $n = 1.4$: Large Binding Energies . . . 94
    7.3.3 Density of States at Filling $n = 1.4$ 95
7.4 Interpretation of TTF-TCNQ ARPES Spectra 97
7.5 Conclusion 98

8 Optical Properties of Quarter Filled Chains 101
8.1 Model and Method 101
    8.1.1 Extended Peierls-Hubbard Model 102
    8.1.2 Optical Conductivity 103
8.2 Results 104
    8.2.1 Large Dimerization 104
    8.2.2 Strong Coupling 107
    8.2.3 Weak Coupling 108
    8.2.4 From Small to Large Dimerization 111
    8.2.5 From Weak to Strong Coupling 112
    8.2.6 Nearest-Neighbor Coulomb Interaction: Excitons 114
8.3 Discussion 116
8.4 Conclusion 119

9 Dynamical Properties of $SrCuO_2$ 121
9.1 Electronic Structure of $SrCuO_2$ 121
9.2 Optical Conductivity of $SrCuO_2$ 123
9.3 Dynamical Spin Structure Factor 126
9.4 Resonant Inelastic X-Ray Scattering (RIXS) in $SrCuO_2$ 130
9.4.1 RIXS Technique 131
9.4.2 Experimental Results for $SrCuO_2$ 132
9.5 Conclusion 136

10 Quantum Phase Transition in the Extended Peierls-Hubbard Model 137
10.1 CDW and BOW Order Parameters 138
10.2 Spin and Charge Gaps 139
10.3 Electric Susceptibility 144
10.4 Conclusion 145

11 Summary and Outlook 147
11.1 Achievements 147
11.2 Outlook 148
11.2.1 Algorithmical Improvements 148
11.2.2 Physical Questions 149

Danksagung 157

List of Figures

3.1 Spin-triplet excitation spectrum ($U/t = 4.9, n_e = 0.6$) 30
3.2 Holon-spinon excitation spectrum ($U/t = 4.9, n_e = 0.6$) 31
3.3 Antiholon-spinon excitation spectrum ($U/t = 4.9, n_e = 0.6$) 32
3.4 $4k_\mathrm{F}$-singlet excitation spectrum ($U/t = 4.9, n_e = 0.6$) 33
3.5 Dispersion of a k-Λ-string of length $m = 1$ 34

4.1 Division of the superblock into the environment and the system block . 38
4.2 Finite-system DMRG algorithm 44

5.1 Deconvolved optical conductivity $\sigma_1(\omega)$ of the Hubbard model 57

6.1 $A(k, \omega)$ of the half-filled Hubbard model ($U/t = 20$) 62
6.2 Pseudo-color density plot of $A(k, \omega)$ ($U/t = 20$) 63
6.3 Comparison of the exact Bethe-Ansatz dispersion $\omega(k)$ and the dispersion $\epsilon(k)$ for $U/t = 20$ and $L = 32$ 63
6.4 Real and imaginary parts of $G(k, \omega)$ 64
6.5 Momentum distribution: open vs. periodic boundaries ($U/t = 1$) 65
6.6 Momentum distribution: open vs. periodic boundaries ($U/t = 20$) 65
6.7 Momentum distribution: open vs. periodic boundaries ($U/t = 4$) 66
6.8 Local density of states ($U/t = 4$, $L = 32$, $\eta/t = 0.2$) 67
6.9 Local density of states ($U/t = 3$, $\delta/t = 0.6$, $L = 32$, $\eta/t = 0.4$) 68
6.10 Comparison of $N(q, \omega)$ with exact diagonalizations 69
6.11 Comparison of $N(q = \pi/61, \omega)$ with $\sigma_1(\omega)/\omega$ for a 60-site system 70
6.12 Strong-coupling exciton at $q = \pi$ and $U/t = 50, 100$ 71
6.13 Finite-size scaling analysis of the resonance at $q = \pi$ 72
6.14 Comparison of strong-coupling theory and DDMRG 73
6.15 Spin structure factor $S(q, \omega)$ ($U/t = 1$, $L = 30$, $\eta/t = 0.4$) 75
6.16 Peak dispersion of $S(q, \omega)$ ($U/t = 1$, $L = 30$, $\eta/t = 0.4$) 75

7.1 Crystal structure of TTF-TCNQ 81
7.2 ARPES lineshapes in TTF-TCNQ 82
7.3 Density plot of the second derivative of the ARPES data 83
7.4 $A(k, \omega)$ of the Hubbard model for $0 < k < k_\mathrm{F}$ ($U/t = 4.9$, $n = 0.6$) . . . 85
7.5 $A(k, \omega)$ of the Hubbard model for $k_\mathrm{F} < k < \pi$ ($U/t = 4.9$, $n = 0.6$) . . . 86

7.6 Comparison of Bethe-Ansatz and DDMRG dispersion 87
7.7 Finite-size scaling analysis of $A(k \approx \pi/10 = k_{\mathrm{F}}/3, \omega)$ 89
7.8 $\rho(\omega)$ of the Hubbard model ($U/t = 4.9$, $n = 0.6$) 90
7.9 $A(k, \omega)$ of a Hubbard chain at $U/t = 4.9$ and band filling $n = 1.4$ 92
7.10 Bethe-Ansatz dispersion and DDMRG photoemission spectrum 93
7.11 Dispersive structures in the lower Hubbard band 95
7.12 $\rho(\omega)$ of the Hubbard model with $U/t = 4.9$ and $n = 1.4$ 96
7.13 $\rho^{>}_{\sigma}(\omega)$ and $\rho^{<}_{\sigma}(\omega)$ for the Hubbard model ($U/t = 4.9$ and $n = 0.6$) 97
7.14 ARPES dispersion for TTF-TCNQ derived from DDMRG 98

8.1 Optical conductivity $\sigma_1(\omega)$ in the large-dimerization limit ($\delta = 1.64$) for a strong effective coupling ($U = 3.64t \approx 20t_2$) 105
8.2 Optical conductivity $\sigma_1(\omega)$ in the large-dimerization limit ($\delta = 1.64$) for a weak effective coupling ($U = 0.546t \approx 3t_2$) 106
8.3 Reduced optical conductivity $\omega\sigma_1(\omega)$ in the strong-coupling limit ($U = 40t$) 107
8.4 Optical conductivity $\sigma_1(\omega)$ for $\delta = 2/3$, $U/t = 20/3$ 108
8.5 Optical conductivity for $\delta = 0.105$, $U = 5.263t$, and $\eta = 0.1t$ ($L = 128$ sites). 109
8.6 Extrapolation of E_c, ω_1 and $\omega_{\max}$ for $\delta = 0.105$, $U = 5.263t$, and $V = 0$. 110
8.7 Optical conductivity $\sigma_1(\omega)$ for $U = 6t$ and $\eta = 0.2t$ ($L = 32$) for various dimerizations δ 111
8.8 Evolution of $\omega\sigma_1(\omega)$ for $\delta = 1.64$ with U 112
8.9 Evolution of $\omega\sigma_1(\omega)$ for $\delta = 0.105$ with U 113
8.10 $\sigma_1(\omega)$ for $\delta = 0.105$, $U = 5.263t$, $\eta = 0.2t$ ($L = 64$), and various nearest-neighbor interactions V 114
8.11 Extrapolation of E_c, ω_1, $\omega_{\max}$ for (a) $\delta = 0.105, U = 5.263t$, $V = 2.105t$, and (b) $\delta = 0.353, U = 8.235t, V = 3.294t$ 115
8.12 Optical conductivity $\sigma_1(\omega)$ for $\delta = 0.353$, $U = 8.235t$, $\eta = 0.2t$ ($L = 64$), and various nearest-neighbor interactions V 116

9.1 The coupled chain cuprate $\mathrm{SrCuO_2}$ 122
9.2 Schematical electron density of states of $\mathrm{SrCuO_2}$ 123
9.3 Optical conductivity of $\mathrm{SrCuO_2}$ 124
9.4 Charge and spin gaps in the thermodynamic limit. 125
9.5 Exchange coupling J derived from the spinon band width 126
9.6 Lineshapes of the dynamical spin structure factor $S(q, \omega)$ 127
9.7 Density plot of $S(q, \omega)$ 128
9.8 Dispersive onsets of $S(q, \omega)$ 129
9.9 Comparison of $S(q \approx \pi, \omega)$ with the spin structure factor of the antiferromagnetic Heisenberg model 130
9.10 Cartoon of the RIXS process 131
9.11 Pseudo-color density plot of the experimental RIXS intensity 132
9.12 Dispersion of RIXS features 133

9.13 RIXS lineshapes 134
9.14 Resonance in $N(q, \omega)$ at $q \to \pi$ 135
9.15 Zeroth moment of $N(q, \omega)$ 136

10.1 CDW and BOW order parameters ($U/t = 4$, $V/t = 3$) 139
10.2 Power-law onset $|\delta - \delta_\mathrm{c}|^\beta$ of m_CDW 140
10.3 Dimerization dependence of excitation gaps Δ_1, Δ_2, and Δ_s 141
10.4 Gap $\Delta_2(\delta)$ for periodic systems, $L = 10, \ldots, 128$ 143
10.5 Extrapolation of $\delta_\mathrm{c}^\mathrm{PBC}(L \to \infty)$ and $\Delta_2(L \to \infty)$ 143
10.6 Hyperscaling of the polarizability in the extended Hubbard model 145

Chapter 1

Introduction

1.1 General

In solid-state physics, the constituents of the physical systems and all physical laws that they obey are known. Thus, the problem of theoretical condensed-matter physics is to describe the $N \sim 10^{23}$ interacting electrons (and nuclei) which macroscopic solid-state samples are composed of. In principle, the problem is solved once the Schödinger equation

$$\mathrm{i}\hbar\frac{\partial\Psi}{\partial t} = \left\{\sum_{l=1}^{N}\left(-\frac{\hbar^2}{2m}\vec{\nabla}_l^2\right)+\sum_{l<j}V\left(|\vec{r}_l-\vec{r}_j|\right)+\sum_{l=1}^{N}U\left(\vec{r}_l\right)\right\}\Psi \tag{1.1}$$

is solved for the many-electron wavefunctions

$$\Psi = \Psi\left(\vec{r}_1,\ldots,\vec{r}_N;t\right)\ , \tag{1.2}$$

where U and V describe the electron-nuclei and the electron-electron interaction, respectively.

Unfortunately, the knowledge of the microscopic equations that govern the behavior of a macroscopic number of interacting quantum particles *is of no use whatsoever* because the full equations cannot be treated exactly even for the simplest many-particle systems such as atoms or molecules. Even if it were possible to find a numerical solution of the full Schrödinger equation, the solution would be so complicated that it would be useless because the calculation of interesting correlation functions from it would pose an insurmountable task.

The consideration of energy scales in the problem offers a way out of this dilemma. The typical energy scales on the atomic level range from 1 eV to 100 eV whereas physical properties that are probed in experiments at or below room temperature may only involve a few meV. Therefore, these energy scales are well-separated and we may formulate effective theories at low energies which can look very different from the original problem on the eV-scale. The most prominent examples of quantum liquids in everyday life are simple (three-dimensional) metals. The fact that a door knob made from copper feels cool to the touch and has a shiny color can be captured in such an effective theory without a solution of the full problem (1.1). Although the conduction electrons are strongly correlated because of their mutual Coulomb repulsion, the system behaves like a free electron gas, albeit with renormalized parameters. Only a small fraction of the electrons with energies close to the Fermi surface contribute to the physical properties. The emergent particles that describe the low-energy excitations of this quantum liquid behave like the original electrons and carry the same quantum numbers – the quasi-electrons of Fermi-liquid theory. This fact manifests itself in the dynamical properties of the systems described by, in general, momentum- and frequency-dependent dynamical correlation functions. The presence of quasi-electrons is most markedly visible in the one-particle spectral function probed by angle-resolved photoemission spectroscopy. The color of our door knob is determined by a dynamical correlation function as well, namely, by the optical conductivity.

This situation changes altogether in one dimension. The excited states of interacting systems are no longer adiabatically connected to the excitations of the Fermi gas. Therefore, we cannot explain their behavior perturbatively. Except for a few lucky cases where models are amenable to an exact solution, it is very difficult to obtain results away from extreme limits of the model parameters. For instance, much is known about dynamical properties of correlated electron systems in the limit of vanishingly low energies, where the elementary excitations are no longer like the original electrons. Instead, the electron appears to decay into bosonic collective excitations – holons and spinons – which carry either spin or charge but not both. This dynamical separation of spin and charge degrees of freedom is paradigmatic in one dimension and these systems are referred to as Luttinger liquids in contrast to Fermi liquids. How can these elementary excitations be measured in an experimental setup? Can they be found spectroscopically at all? The answer to this question is very difficult because the effective low-energy (field) theories have no intrinsic energy scale by their very construction.

At finite energies only very little is known reliably about dynamical correlations in one-dimensional correlated electron systems. Only recently has it become possible to obtain reliable results in sufficiently large systems by employing numerical methods. The dynamical density-matrix renormalization group (DDMRG) is such a method. The purpose of this thesis is to present a generalization of DDMRG to momentum- and frequency-dependent dynamical correlation functions. We will use the method to determine the dynamical signatures of the emergent elementary excitations of correlated electrons in one dimension. We can answer the above questions affirmatively for a number of real systems and for different experimental probes of matter.

1.2 Structure of this Thesis

This thesis is split into three parts.

Part I The first part includes an introduction to the microscopic, Hubbard-type models which are the paradigm of correlated electron physics in one dimension. A brief discussion of many-electron Hamiltonians with short-range interactions and tight-binding kinetic energy is given. We proceed with standard analytical methods where exact results are known. We discuss the effective low-energy field theory of correlated one-dimensional metals, the Tomonaga-Luttinger model, and state some well-known results. Some correlated one-dimensional systems, such as the bare Hubbard model, are exactly solvable by the Bethe Ansatz. This permits the calculation of the dispersion of physical excitations at finite energies which we compare with numerical results in later chapters of the thesis. While we can determine eigenenergies exactly with the Bethe Ansatz, we cannot obtain any expectation values of observables with this method. However, in one dimension we have a very powerful numerical method at hand, the density-matrix renormalization group (DMRG). We introduce the basic ideas and algorithms of DMRG and comment on some more detailed aspects.

Part I comprises of introductory material only. With the exception of the presentation of results for the Bethe-Ansatz excitation spectra none of this is based on my own efforts.

Part II Part II begins with the introduction of a dynamical generalization of DMRG (DDMRG) which enables us to calculate dynamical correlation functions of model Hamiltonians. The method itself was proposed by E. Jeckelmann. I have generalized the method further to include frequency- and momentum-dependent dynamical correlation functions. I show how this can be achieved in open-chain geometries with a suitable definition of a pseudo-momentum. A full chapter is devoted to detailed tests of my method for various dynamical correlation functions relevant to experimental scattering probes. This includes the one-particle spectral function measured in angle-resolved photoemission spectroscopy (ARPES), the dynamical charge structure factor probed by electron-energy loss spectroscopy (EELS) and (resonant) inelastic X-ray scattering ((R)IXS), and the dynamic spin structure factor accessible by neutron scattering. The tests were performed by comparing with non-trivial limits of the model parameters, by comparing with exact numerical results obtained by independent methods, by the use of sum-rules, and by utilizing exact Bethe-Ansatz results. All tests yield good to excellent agreement.

The extension of DDMRG to momentum dependent quantities and the tests performed to validate the method are my own work. The program I used is based on the DMRG program of E. Jeckelmann which I have extended appropriately.

Part III Part III of this thesis contains the most important results that I have obtained during my PhD work.

In chapter 7, I give an introduction to the electronic structure of the quasi one-dimensional organic charge-transfer salt TTF-TCNQ and I show recent ARPES results. I present calculations of the one-particle spectral function of the Hubbard model both above and below half band filling. I argue that the experimental ARPES spectra can be explained in terms of essentially uncoupled TTF and TCNQ chains which display strong electronic correlations. The accuracy of the DDMRG method is impressively documented by comparison with the dispersion of Bethe-Ansatz excitations.

The Bechgaard salts, a family of organic charge-transfer salts, have attracted a lot of experimental and theoretical interest in recent years. In chapter 8, I present DDMRG results for the optical conductivity of quarter-filled dimerized Hubbard chains and discuss their relevance for the unusual optical properties of Bechgaard salts. Various limits of the parameter space are considered where I can explain the salient features of the optical spectra in simple terms. Furthermore, I discuss the transition between these limits and how the interaction parameters influence the spectra. Finally, I argue that excitonic bound states may be relevant for the optical properties of TMTTF compounds.

Some of the numerical results in chapters 7 and 8 were achieved in collaboration with E. Jeckelmann at the University of Mainz.

Among the best realization of one-dimensional electron systems is the chain-cuprate $SrCuO_2$; many experimental data for dynamical correlations are available. In chapter 9, I present results for the optical conductivity of the extended Hubbard model, compare with optical experiments, and derive appropriate interaction parameters. I proceed with this parameter set to determine the dynamic spin structure factor and show that it agrees well with recent neutron scattering data. Finally, I find qualitative and quantitative agreement between RIXS spectra and the dynamic structure factor of the extended Hubbard model. I can thus describe three different scattering probes associated with three different momentum-dependent dynamical correlation functions with one parameter set of the effective microscopic model.

In the final chapter, chapter 10, I study a quantum phase transition in the extended Peierls-Hubbard model. I present numerical data for the order parameters of the symmetry-breaking ground state from which I derive a critical exponent compatible with a two-dimensional Ising-type transition. Further studies of the gap to the excitation that becomes critical at the transition yield a second critical exponent which proves that the transition belongs to the Ising universality class. In addition, I present a hyperscaling analysis of the electric polarizability to corroborate this result.

A summary and outlook close the scientific part of my thesis.

1.3 Publications

Some parts of this thesis have been published or are being prepared for publication at the time of writing. Since other people were also involved in this process I have taken great care to point out whenever I present or rely upon their efforts. In the order of the related chapters these are:

- Chapter 7

  Spectral function of the one-dimensional Hubbard model away from half filling

  H. Benthien, F. Gebhard, and E. Jeckelmann,

  Physical Review Letters **92**, 256401 (2004).

- Chapter 8

  Optical conductivity of the one-dimensional dimerized Hubbard model at quarter filling

  H. Benthien and E. Jeckelmann,

  accepted for publication in European Physical Journal B

- Chapter 9

  Resonant inelastic x-ray scattering study of holon-antiholon continuum in $SrCuO_2$

  Y.-J. Kim, J.P. Hill, H. Benthien, F.H.L. Essler, E. Jeckelmann, H.S. Choi, T.W. Noh, N. Motoyama, K.M. Kojima, S. Uchida, D. Casa, and T. Gog,

  Physical Review Letters **92**, 137402 (2004).

- Chapter 10

  Quantum phase transition in the extended Peierls-Hubbard model in one dimension

  H. Benthien, F.H.L. Essler, F. Gebhard, and A. Grage,

  in preparation.

Part I

Models and Methods

Chapter 2

Models

Our understanding of the microscopic physics of many ($\sim 10^{23}$) quantum particles is rooted deeply in their description with simplified model Hamiltonians. In saying this, it must be noted, however, that these models are only a caricature of the real materials they are supposed to model. Nevertheless, *Hubbard*-type models [1] contain a plethora of quantum phases and a zoo of elementary and physical excitations. While this thesis only considers the limit of one dimension it is generally believed that the Hubbard model and its generalizations contain the physics of the essentially two-dimensional high-$\mathrm{T_c}$ cuprates which are thought to be doped Mott-insulators [2]. Since their discovery in 1986 [3] they have been a major driving force of research in the field of strongly correlated electron systems. In one dimension these models are believed to be a good description of a variety of different systems such as conducting polymers, organic charge-transfer salts, or carbon nanotubes. They all have in common that they are strongly anisotropic in their transport properties. Above a critical energy scale (temperature and frequency) their electronic properties can be described by effective one-dimensional models (dimensional crossover).

In this chapter, we introduce microscopic Hamiltonians for correlated electrons in one dimension. We briefly discuss the trivial limits of the model parameters and the symmetry properties of the Hamiltonians. In addition, we summarize well-known results which we will refer to later in this thesis.

2.1 Hubbard Model

The most simplistic model of interacting electrons is the Hubbard model [1]. At the same time the Hubbard model has attracted an immense amount of research effort in the past decades. For a review of its properties we refer the reader to [4, 5, 6]. The model is given by

$$\begin{aligned} \hat{H} &= \hat{T} + U\hat{D} \\ &= -t\sum_{l,\sigma}\left(\hat{c}^{+}_{l,\sigma}\hat{c}_{l+1,\sigma} + \hat{c}^{+}_{l+1,\sigma}\hat{c}_{l,\sigma}\right) + U\sum_{l}\hat{n}_{l,\uparrow}\hat{n}_{l,\downarrow}\ . \end{aligned} \tag{2.1}$$

For the remaining part, we set $\hbar = 1$ and set the lattice spacing a equal to unity, unless stated otherwise. The kinetic energy term, $\hat{T}$, describes the hopping of electrons to next-neighbor sites $l \leftrightarrow l+1$. The fermionic operators $\hat{c}^{+}_{l,\sigma}$ ($\hat{c}_{l+1,\sigma}$) create (annihilate) an electron in the Wannier orbital centered at site l with spin σ and we define $\hat{n}_{l,\sigma} = \hat{c}^{+}_{l,\sigma}\hat{c}_{l,\sigma}$. The creation and annihilation operators fulfill the fermionic anti-commutation relations

$$\left\{\hat{c}_{l,\sigma}, \hat{c}^{+}_{m,\tau}\right\}_{+} = \delta_{l,m}\delta_{\sigma,\tau} \tag{2.2}$$

while all other anti-commutators vanish. In momentum space the hopping term is diagonal and takes the form

$$\hat{T} = \sum_{l,\sigma} \varepsilon(k)\hat{c}^{+}_{k,\sigma}\hat{c}_{k,\sigma} \tag{2.3}$$

with the tight-binding energy dispersion relation

$$\varepsilon(k) = -2t\cos(k) \; . \tag{2.4}$$

The Coulomb term, $U\hat{D}$, describes the energetic penalty, $U > 0$, for two electrons with opposite spin to occupy the same site. The interaction parameter – the *Hubbard U* – mimics the Coulomb repulsion in the system by a purely local interaction. This is, of course, a crude approximation of the long-ranged $1/r$-Coulomb potential. One may argue that screening of the electron-electron interaction justifies this approach. In this work we will mostly justify this approximation *a posteriori* by comparing with experimental results. The local interaction strength U (and later a next-neighbor interaction) then becomes a fit parameter that is strongly renormalized to incorporate the effect of longer-ranged interactions. Note that the physical properties of the Hamiltonian (2.1) are completely determined by the ratio U/t. The kinetic energy t only fixes the energy scale. It is often useful to add an additional term to (2.1)

$$\begin{aligned} \hat{\hat{H}} &= \hat{H} - U\hat{N}/2 + UL/4 && (2.5) \\ &= \hat{T} + U\sum_{l}\left(\hat{n}_{l,\uparrow} - \frac{1}{2}\right)\left(\hat{n}_{l,\downarrow} - \frac{1}{2}\right) \; , && (2.6) \end{aligned}$$

which makes the charge symmetry clearly visible, see below.

The one-dimensional Hubbard Hamiltonian has an infinite number of symmetries (cf. section 3.2) with a corresponding infinite set of conserved quantities which makes it exactly integrable. These conserved quantities, however, are far from obvious. Below, we discuss Abelian and discrete symmetries that follow directly from the definition of the model. We shall switch freely between $\hat{\hat{H}}$ and $\hat{H}$ as they only differ by a constant.

2.1.1 Spin-Rotational Invariance

Rotations in the spin sector

$$\begin{aligned} \hat{\tau}_{\text{spin}} : \quad & \hat{c}_{l,\sigma} \mapsto \hat{c}_{l,-\sigma} \\ & \hat{c}^{+}_{l,\sigma} \mapsto \hat{c}^{+}_{l,-\sigma} && (2.7) \end{aligned}$$

leave the Hamiltonian invariant, $\left[\hat{H}, \hat{\tau}_{\text{spin}}\right] = 0$. The corresponding $SU(2)$-Lie algebra is generated by operators of the total spin

$$\begin{aligned} \hat{S}^{+} &= \sum_{l=1}^{L} \hat{c}_{l,\uparrow}^{+} \hat{c}_{l,\downarrow} \ , \\ \hat{S}^{-} &= \sum_{l=1}^{L} \hat{c}_{l,\downarrow}^{+} \hat{c}_{l,\uparrow} \ , \\ \hat{S}^{z} &= \frac{1}{2} \sum_{l=1}^{L} \left(\hat{n}_{l,\uparrow} - \hat{n}_{l,\downarrow} \right) \end{aligned} \tag{2.8}$$

with the linear combinations of spin operators $\hat{S}^{+} = \hat{S}^{x} + \mathrm{i}\hat{S}^{y} = (\hat{S}^{-})^{+}$.

2.1.2 η-Pairing Symmetry

The Hamiltonian commutes with the operator that maps doubly occupied sites onto empty sites and vice versa,

$$\begin{aligned} \hat{\tau}_{\text{charge}} : \quad \hat{c}_{l,\uparrow}^{+} \hat{c}_{l,\downarrow}^{+} &\mapsto \hat{c}_{l,\uparrow} \hat{c}_{l,\downarrow} \\ \hat{c}_{l,\uparrow} \hat{c}_{l,\downarrow} &\mapsto \hat{c}_{l,\uparrow}^{+} \hat{c}_{l,\downarrow}^{+} \ . \end{aligned} \tag{2.9}$$

The operators

$$\begin{aligned} \hat{C}^{+} &= \sum_{l=1}^{L} \hat{c}_{l,\uparrow}^{+} \hat{c}_{l,\downarrow}^{+} \ , \\ \hat{C}^{-} &= \sum_{l=1}^{L} \hat{c}_{l,\downarrow} \hat{c}_{l,\uparrow} \ , \\ \hat{C}^{z} &= \frac{1}{2} \sum_{l=1}^{L} \left(\hat{n}_{l,\uparrow} + \hat{n}_{l,\downarrow} - 1 \right) \end{aligned} \tag{2.10}$$

with $\hat{C}^{+} = \hat{C}^{x} + \mathrm{i}\hat{C}^{y} = (\hat{C}^{-})^{+}$, commute with both the Hamiltonian and the spin operators (2.8) and generate the associated $SU(2)$-Lie algebra. The mapping $\hat{\tau}_{\text{charge}}$ connects subspaces with different particle numbers.

Since spin-rotational and the η-pairing symmetry are not completely independent the direct product of the symmetries gives an $SO(4)$ rather than a $SU(4)$ symmetry.

2.1.3 Particle-Hole Symmetry

The particle-hole transformation

$$\begin{aligned} \hat{\tau}_{\text{PH}} : \quad \hat{c}_{l,\sigma} &\mapsto (-1)^{l} \hat{c}_{l,\sigma}^{+} \\ \hat{c}_{l,\sigma}^{+} &\mapsto (-1)^{l} \hat{c}_{l,\sigma} \end{aligned} \tag{2.11}$$

maps the Hamiltonian onto itself. If we set the chemical potential $\mu = 0$ in (2.6) this symmetry leads to half band-filling at all temperatures in the grand-canonical ensemble [4].

2.2 Extended Hubbard Models

2.2.1 Peierls-Hubbard Model

The Hubbard Hamiltonian (2.1) can be modified to include effects such as an alternating hopping amplitude or next-neighbor interactions. In the first case, we obtain the so-called Peierls-Hubbard Hamiltonian

$$\begin{aligned}\hat{H} &= -t\sum_{\sigma}\sum_{l}\left(1+(-1)^{l}\frac{\delta}{2}\right)\left(\hat{c}^{+}_{l,\sigma}\hat{c}_{l+1,\sigma}+\text{h.c.}\right) && (2.12)\\ &\quad +U\sum_{l}\left(\hat{n}_{l,\downarrow}-\frac{1}{2}\right)\left(\hat{n}_{l,\uparrow}-\frac{1}{2}\right)\ . && (2.13)\end{aligned}$$

The term $\left(1+(-1)^{l}\delta/2\right)$ causes an alternating hopping amplitude between nearest neighbors. The energy to hop from an odd to an even site is $t_1 = -t(1+\delta/2)$ and from an even to an uneven site $t_2 = -t(1-\delta/2)$. The Peierls-Hubbard model is a description of quasi one-dimensional materials that have a ground state with a broken symmetry, in which the lattice is dimerized. The transition to such a state occurs at low temperatures and is called Peierls transition [7].

When we set $U = 0$ the model describes a simple band insulator at half filling [8]. The kinetic energy term can be diagonalized by a Fourier transform and a Bogoliubov transformation. In the reduced Brillouin zone from $-\pi/2 < k \leq \pi/2$ the kinetic energy reads

$$\hat{T} = \sum_{k} E(k)\left(\hat{b}^{+}_{k,\sigma}\hat{b}_{k,\sigma}-\hat{a}^{+}_{k,\sigma}\hat{a}_{k,\sigma}\right) \tag{2.14}$$

with dispersion

$$E(k) = \sqrt{\epsilon(k)^2+\Delta(k)^2} \tag{2.15}$$

of the new quasi-particles. The operators $\hat{a}^{+}_{k,\sigma}$ ($\hat{a}_{k,\sigma}$) and $\hat{b}^{+}_{k,\sigma}$ ($\hat{b}_{k,\sigma}$) create (destroy) a particle in the lower and upper Peierls-bands, respectively. The quasi-particle operators are connected with the original bare electron operators through the canonical transformation ($\alpha_k^2+\beta_k^2=1$)

$$\begin{aligned}\hat{a}_{k,\sigma} &\equiv \alpha_k\hat{c}_{k,\sigma}+\mathrm{i}\beta_k\hat{c}_{k+\pi,\sigma}\ , && (2.16)\\ \hat{b}_{k,\sigma} &\equiv \beta_k\hat{c}_{k,\sigma}-\mathrm{i}\alpha_k\hat{c}_{k+\pi,\sigma}\ . && (2.17)\end{aligned}$$

The functions α_k and β_k are

$$\alpha_k = \sqrt{\frac{1}{2}\left(1-\frac{\epsilon(k)}{E(k)}\right)}\ , \tag{2.18}$$

$$\beta_k = \mathrm{sgn}(\Delta(k))\sqrt{\left(1+\frac{\epsilon(k)}{E(k)}\right)}\ . \tag{2.19}$$

In this definition the hybridization functions reads

$$\Delta(k) = t\delta\sin(k)\ . \tag{2.20}$$

The total band width is simply $W = 4t$ and the gap for a particle-hole excitation at half band-filling is $\Delta_{\mathrm{c}} = 2\delta t$.

2.2.2 Extended Hubbard Model

When we add a next-neighbor repulsion to the basic Hubbard Hamiltonian (2.1) we obtain the extended Hubbard model

$$\begin{aligned}\hat{H} &= -t\sum_{\sigma}\sum_{l}\left(\hat{c}^{+}_{l,\sigma}\hat{c}_{l+1,\sigma}+\mathrm{h.c.}\right) \\ &\quad +U\sum_{l}\left(\hat{n}_{l,\downarrow}-\frac{1}{2}\right)\left(\hat{n}_{l,\uparrow}-\frac{1}{2}\right)+V\sum_{l}\left(\hat{n}_{l}-1\right)\left(\hat{n}_{l+1}-1\right)\ ,\end{aligned} \tag{2.21}$$

where $\hat{n}_l = \hat{n}_{l,\uparrow} + \hat{n}_{l,\downarrow}$. This model has a rich phase diagram including charge-density wave (CDW) and bond-order wave (BOW) and Mott-insulating (MI) ground states [9]. A next-neighbor interaction $V > 2t$ leads to the possibility of forming excitonic bound states [10]. This strongly effects dynamical correlation functions that couple to the charge sector of the model. In particular, the optical conductivity and the dynamical charge structure factor are affected by the presence of excitons.

2.2.3 Extended Peierls-Hubbard Model

When we add both a dimerization term and a next-neighbor Coulomb repulsion to the original Hubbard Hamiltonian (2.1) we arrive at the extended Peierls-Hubbard model

$$\begin{aligned}\hat{H} &= -t\sum_{\sigma}\sum_{l}\left(1+(-1)^{l}\frac{\delta}{2}\right)\left(\hat{c}^{+}_{l,\sigma}\hat{c}_{l+1,\sigma}+\mathrm{h.c.}\right) \\ &\quad +U\sum_{l}\left(\hat{n}_{l,\downarrow}-\frac{1}{2}\right)\left(\hat{n}_{l,\uparrow}-\frac{1}{2}\right)+V\sum_{l}\left(\hat{n}_{l}-1\right)\left(\hat{n}_{l+1}-1\right)\ .\end{aligned} \tag{2.22}$$

The extended Peierls-Hubbard model is the minimal model for the description of well-ordered polyacetylene chains and a number of charge-transfer salts [11, 12, 13, 14].

Chapter 3

Analytic Approaches

In this chapter we give a brief introduction into analytic methods to strongly correlated one-dimensional systems. We only include topics that are relevant in later chapters and, therefore, many interesting facets have been omitted.

3.1 Luttinger Liquids

The electronic properties of one-dimensional interacting electron liquids are fundamentally different from their three-dimensional Fermi liquid analogues. In three dimensions there is a one-to-one correspondence between the excited states of the interacting and non-interacting system. This results in the pole structure of the one-particle particle spectral function which translates into the existence of *Landau quasi-particles.* These quasi-particles have the same quantum numbers as the original electrons of the free system and may therefore be called *quasi-electrons.* In one-dimension, however, this correspondence no longer holds and the elementary excitations are bosonic collective modes, *holons* and *spinons.* Their presence is most clearly signaled by power-law divergences in the one-particle spectral function that disperse with different velocities. In the following we briefly sketch the derivation of the Tomonaga-Luttinger model to make these notions more tangible and cite some well-known analytical results. For detailed reviews see [15, 16] and references therein.

3.1.1 Tomonaga-Luttinger Model

Consider a free-particle dispersion, such as the tight-binding dispersion (2.4) of the Hubbard model (2.1). In the ground state all momentum eigenstates below the two Fermi points $|k| \leq k_{\mathrm{F}}$ are occupied. In the limit of very small energy transfers ΔE the relevant excitations involve only scattering around the Fermi points. When the electron band width W is large compared to ΔE we may reduce the degrees of freedom drastically by *linearizing* the dispersion relation close to $\pm k_{\mathrm{F}}$. We may now introduce new fermionic operators for *left-moving* electrons ($\hat{l}_{k,\sigma}$) and *right-moving* electrons ($\hat{r}_{k,\sigma}$) at $k = \pm k_{\mathrm{F}}$, respectively. The electron-electron interactions are reduced to scattering terms between right- and left-moving electrons close to $\pm k_{\rm F}$ and the effective *g-ology* Hamiltonian reads [4]

$$
\begin{aligned}
\hat{H} \;=\; & \sum_{k,\sigma} v_{\rm F}^{r}(k-k_{\rm F})\hat{r}^{+}_{k,\sigma}\hat{r}_{k,\sigma} + \sum_{k,\sigma} v_{\rm F}^{l}(k+k_{\rm F})\hat{l}^{+}_{k,\sigma}\hat{l}_{k,\sigma} \\
& + \frac{1}{L}\sum_{\sigma,\sigma'}\sum_{k_1,k_2,q} g_1^{\sigma,\sigma'}\,\hat{r}^{+}_{k_1,\sigma}\hat{l}^{+}_{k_2,\sigma'}\hat{r}_{k_2+2k_{\rm F}+q,\sigma'}\hat{l}_{k_1-2k_{\rm F}-q,\sigma} \\
& + \frac{1}{L}\sum_{\sigma,\sigma'}\sum_{k_1,k_2,q} g_2^{\sigma,\sigma'}\,\hat{r}^{+}_{k_1,\sigma}\hat{l}^{+}_{k_2,\sigma'}\hat{r}_{k_2+q,\sigma'}\hat{l}_{k_1-q,\sigma} \\
& + \frac{1}{2L}\sum_{\sigma,\sigma'}\sum_{k_1,k_2,q} g_3^{\sigma,\sigma'}\left[\hat{r}^{+}_{k_1,\sigma}\hat{r}^{+}_{k_2,\sigma'}\hat{l}_{k_2-2k_{\rm F}+q,\sigma'}\hat{l}_{k_1+2k_{\rm F}-q-G,\sigma} + \text{h.c.}\right] \\
& + \frac{1}{2L}\sum_{\sigma,\sigma'}\sum_{k_1,k_2,q} g_4^{\sigma,\sigma'}\left[\hat{r}^{+}_{k_1,\sigma}\hat{r}^{+}_{k_2,\sigma'}\hat{l}_{k_2+q,\sigma'}\hat{l}_{k_1-q,\sigma} + (l \leftrightarrow r)\right]
\end{aligned}
\tag{3.1}
$$

with coupling constants $g_i^{\sigma,\sigma'}$, Fermi velocities $v_{\rm F}^{l,r} = \partial\epsilon(k)/\partial k|(k = \pm k_{\rm F})$ and the reciprocal lattice vector $G = 2\pi$. The couplings $g_i^{\sigma,\sigma'}$ are functions of the parameters of the original lattice model. The low-energy effective model (3.1) describes scattering processes associated with the four couplings:

$g_2^{\sigma,\sigma'}$, $g_4^{\sigma,\sigma'}$ Scattering of particles in the vicinity of $\pm k_{\rm F}$ with small momentum transfers.

$g_1^{\sigma,\sigma'}$ *Backscattering* of a particle. In this process a right-mover is scattered into a left-mover and vice versa. This involves large momentum transfers.

$g_3^{\sigma,\sigma'}$ In the *Umklapp* process two right-movers is scattered into two left-movers and vice versa. This process is forbidden unless $4k_{\rm F} - G \equiv 0$ which is true only at half band filling, since $k_{\rm F} = n\pi/2 = G/4$ for $n = 1$.

So far, the model (3.1) is not well-defined, since we have not specified the range of momenta for right- and left-movers. When we allow both linearized dispersion branches to extend to infinity and when we neglect both back- and umklapp scattering, i.e., $g_1^{\sigma,\sigma'}, g_3^{\sigma,\sigma'} = 0$, we obtain the *Luttinger model.* When we only allow a finite number of negative energy states by extending the linearized branches until they intersect at $k = 0$ we arrive at the *Tomonaga model.* Both models give practically identical results since the negative energy states far below the Fermi energy do not influence the physical properties of the system. Therefore, the two models are jointly referred to as the *Tomonaga-Luttinger model.*

Neglecting the umklapp- and backscattering process can be justified by renormalization group arguments. Away from half-filling the couplings $g_1^{\sigma,\sigma'}$ and $g_3^{\sigma,\sigma'}$ are irrelevant, i.e., they do not affect the low-energy spectrum of the model. This implies that Hubbard models (with finite-range hopping) are metallic away from half band-filling. At half band-filling, however, umklapp- and backscattering processes become relevant. The umklapp scattering then dynamically creates a gap in the charge excitation spectrum. This implies that the half-filled Hubbard model describes a Mott insulator at any $U > 0$.

An important observation is the fact that the Tomonaga-Luttinger Hamiltonian can be split into a commuting spin and charge part. This indicates that spin and charge propagate independently. Since the Luttinger model can be solved exactly, we can calculate the velocity of spin and charge excitations explicitely

$$v_\nu = \sqrt{\left[v_{\rm F} + \frac{g_4^\nu}{\pi}\right]^2 - \left[\frac{g_2^\nu}{\pi}\right]^2} \ , \quad \nu = \rho, \sigma \tag{3.2}$$

with $g_l^\rho = g_l^{\sigma,\sigma} + g_l^{\sigma,\sigma'}$ and $g_l^\sigma = g_l^{\sigma,\sigma} - g_l^{\sigma,\sigma'}$. The low-energy spin excitations with velocity $v_{\rm s}$ are referred to as *spinons*. Likewise, the low-energy charge modes with velocity $v_{\rm c}$ are called *holons*. Spinons and holons are bosons and the Luttinger model can be rewritten as a bilinear in these bosonic modes. The terms “holon” and “spinon” will reappear in the context of the Bethe-Ansatz solution of the Hubbard model, where these definitions can be extended to finite energies. Because the (Tomonaga-) Luttinger model is the generic low-energy fix-point of one-dimensional lattice Hamiltonians, we commonly expect *spin-charge separation* to occur. In this sense, we generally speak of *Luttinger-liquid* physics in one spatial dimension.

3.1.2 Physical Properties

In the following paragraphs we briefly recall some well known results for the Luttinger model, see [17, 18, 16, 19] and references therein. We assume that the underlying lattice model exhibits spin-rotational invariance and that the Fermi velocities of left- and right-moving electrons are equal, $|v_{\rm F}^l| = |v_{\rm F}^r| = v_{\rm F}$. Correlation functions, and other physical properties depend only on the Luttinger-liquid parameters K_ρ and K_σ which are related to the coupling constants via

$$K_\nu = \sqrt{\frac{\pi v_{\rm F} + g_4^\nu + g_2^\nu}{\pi v_{\rm F} + g_4^\nu - g_2^\nu}} \ , \quad \nu = \sigma, \rho \ . \tag{3.3}$$

The momentum distribution shows no finite jump at $k_{\rm F}$ since there are no quasi-particles. In the vicinity of $k_{\rm F}$ the momentum distribution is

$$n(k) \propto \mathrm{sign}(k - k_{\rm F})|k - k_{\rm F}|^\delta \tag{3.4}$$

and we find

$$\rho(\omega) = |\omega|^\delta \tag{3.5}$$

for the local density of states at $\omega \to 0$. In both cases, $\delta = (K_\rho + 1/K_\rho - 2)/4$. Note, that for a Fermi liquid we would have $\rho(\omega = 0) \neq 0$. In a Luttinger liquid, the one-particle spectral function has singularities

$$A(k, \omega) \sim |\omega - \epsilon(k)|^{-\alpha} \tag{3.6}$$

for energies $\epsilon(k) = v_\nu |k \pm k_F|$ given by the spinon and holon linear dispersions. The exponents α are related to the Luttinger-liquid parameter K_ρ through

$$\alpha_s = 1/2 - \delta = (4 - K_\rho - K_\rho^{-1})/4 \tag{3.7}$$

on the spinon branch ($\epsilon(k) = v_\mathrm{s}|k - k_\mathrm{F}|$) and

$$\alpha_c = (1 - \delta)/2 = (6 - K_\rho - K_\rho^{-1})/8 \tag{3.8}$$

on the holon branch ($\epsilon(k) = v_\mathrm{c}|k - k_\mathrm{F}|$). The absence of dispersing δ-peaks in $A(k, \omega)$ proves that there is no quasi-particle in the system. Instead, there are collective bosonic holon and spinon modes which alter the one-particle dynamics fundamentally.

The optical conductivity of the Luttinger model can also be calculated and reads

$$\sigma_1(\omega) = 2K_\rho v_\rho \delta(\omega) + \sigma_\mathrm{reg}(\omega) \; . \tag{3.9}$$

The weight of the metallic Drude peak is directly related to the Luttinger-liquid parameter K_ρ.

The Tomonaga-Luttinger model is critical in the sense that its static correlation functions show a power-law decay. For instance, the leading terms of the charge correlation function are

$$\begin{aligned} \langle \hat{n}(x)\hat{n}(0) \rangle &= K_\rho/(\pi x)^2 + A_1 \cos(2k_\mathrm{F} x) x^{-1-K_\rho} \ln^{-3/2}(x) \\ &\quad + A_2 \cos(4k_\mathrm{F} x) x^{-4K_\rho} + \ldots \; . \end{aligned} \tag{3.10}$$

For spin-rotionally invariant systems ($K_\sigma = 1$) the spin correlation function reads

$$\left\langle \hat{\mathbf{S}}(x) \cdot \hat{\mathbf{S}}(0) \right\rangle = 1/(\pi x)^2 + B_1 \cos(2k_\mathrm{F} x) x^{-1-K_\rho} \ln^{1/2}(x) + \ldots \tag{3.11}$$

with model-dependent constants A_i and B_i. The omitted terms include higher harmonics of $\cos(2k_\mathrm{F} x)$ but decay more rapidly.

In section 3.4 we will discuss how we can make contact between Luttinger model and the exact Bethe-Ansatz solution of the Hubbard model. This can be achieved by comparing the charge velocity v_c and the spin velocity v_s with those of *physical excitations* in the exact solution.

3.2 Bethe-Ansatz Solution

The one-dimensional Hubbard model was solved exactly in 1968 [20] by E.H. Lieb and F.Y. Wu who applied a method known as the Bethe Ansatz. They obtained a coupled set of highly non-linear equations, the so-called Lieb-Wu equations, that yields the eigenspectrum of the Hubbard Hamiltonian. This includes the excited states for any value of the band filling. This solution allows us to classify the elementary excitations we discuss in later chapters. The presentation of the subject in this and the following two sections is strongly influenced by [21], [22], [19], and especially [5]. The reader is referred to these publications (and references therein) for further details. The discussion of the topic leads to a deeper understanding of the physics of the Hubbard model and is relevant for the interpretation of numerical and experimental data in later parts of this work. Most importantly, it guides our intuition in the correlated electron problem in one dimension.

3.2.1 Two-Particle Problem

In order to illustrate the approach let us consider the general problem of two interacting particles. This problem can be solved in any Bravais lattice in any dimension [23]. The states

$$|\psi\rangle = \sum_{\sigma_1,\sigma_2} \sum_{x_1,x_2} \psi_{\sigma_1,\sigma_2}(x_1,x_2)\, \hat{c}^{+}_{x_1,\sigma_1} \hat{c}^{+}_{x_1,\sigma_2} |\text{vacuum}\rangle \tag{3.12}$$

span the 2-particle Hilbert space $\mathcal{H}_2$. We apply the Hubbard Hamiltonian (2.1) to this state and obtain the Schrödinger equation in first quantization

$$\begin{aligned}(E - U\delta_{x_1,x_2})\psi_{\sigma_1,\sigma_2}(x_1,x_2) &= -t\big[\psi_{\sigma_1,\sigma_2}(x_1+1,x_2) + \psi_{\sigma_1,\sigma_2}(x_1-1,x_2) \\ &\quad +\psi_{\sigma_1,\sigma_2}(x_1,x_2+1) + \psi_{\sigma_1,\sigma_2}(x_1,x_2-1)\big]\,.\end{aligned} \tag{3.13}$$

The Coulomb term in the Hamiltonian acts only locally when the particles are on the same site. The scattering solutions should therefore be described by plane waves in the limit $x_i \ll x_j$. Our Ansatz for the wavefunction away from the boundary $x_1 = x_2$ is

$$\begin{aligned}\psi_{\sigma_1,\sigma_2}(x_1,x_2) &= e^{\mathrm{i}(k_1x_1+k_2x_2)}\left(A_{\sigma_1,\sigma_2}\theta(x_1-x_2) + B_{\sigma_1,\sigma_2}\theta(x_2-x_1)\right) \\ &\quad -e^{\mathrm{i}(k_1x_2+k_2x_1)}\left(A_{\sigma_2,\sigma_1}\theta(x_2-x_1) + B_{\sigma_2,\sigma_1}\theta(x_1-x_2)\right)\ ,\end{aligned} \tag{3.14}$$

with quasi-momenta k_j and scattering amplitudes A_{σ_1,σ_2} and B_{σ_1,σ_2} for incoming and scattered waves, respectively. The minus sign ensures the antisymmetry of the fermionic wavefunction and its energy is simply

$$E = -2t\left(\cos(k_1) + \cos(k_2)\right)\ . \tag{3.15}$$

We now define the scattering matrix S that connects the amplitudes in different regions through

$$B_{\sigma_1,\sigma_2} = S^{\alpha_1,\alpha_2}_{\sigma_1,\sigma_2} A_{\alpha_1,\alpha_2}\ . \tag{3.16}$$

Since the wavefunction has to be unique at the boundary $x_1 = x_2$ we immediately get a condition on S

$$I - PS = S - P \tag{3.17}$$

with the spin exchange operator $P^{\alpha_1,\alpha_2}_{\sigma_1,\sigma_2} = \delta^{\alpha_2}_{\sigma_1}\delta^{\alpha_1}_{\sigma_2}$ and the identity operator in spin space $I^{\alpha_1,\alpha_2}_{\sigma_1,\sigma_2} = \delta^{\alpha_1}_{\sigma_1}\delta^{\alpha_2}_{\sigma_2}$. We can write the scattering matrix as

$$S = \frac{1}{2}(1+P) + \frac{1}{2}(1-P)s\ , \tag{3.18}$$

where $(1+P)/2$ projects onto the spin-triplet subspace and $(1-P)/2$ projects onto the spin-singlet subspace. In the spin-singlet subspace S acts only as a scalar s. Applying this to the Schrödinger equation (3.13) on the boundary $x_1 = x_2$ and solving for s gives

$$s = \frac{\mathrm{i}\,(\sin(k_1) - \sin(k_2)) + U/(2t)}{\mathrm{i}\,(\sin(k_1) - \sin(k_2)) - U/(2t)} \ . \tag{3.19}$$

Finally, using $\theta = \sin(k_1) - \sin(k_2)$ and $u = U/(4t)$, the full S-matrix of the 2-particle problem can be compactly written as

$$S(\theta) = \frac{\theta I + 2\mathrm{i}uP}{\theta + 2\mathrm{i}u} \ . \tag{3.20}$$

3.2.2 Many-Particle Case

We begin discussing the full problem by writing a general N-particle state

$$|\psi\rangle = \sum_{x_1} \cdots \sum_{x_N} \sum_{\sigma_1} \cdots \sum_{\sigma_N} \psi_{\sigma_1,\ldots,\sigma_N}(x_1,\ldots,x_N) \prod_{i=1}^{N} \hat{c}^{+}_{x_i,\sigma_i} |\text{vacuum}\rangle \tag{3.21}$$

with the vacuum as our reference state. Similar to the previous discussion we can partition the lattice into $N!$ regions $x_{Q(1)} < x_{Q(2)} < \cdots < x_{Q(N)}$ where $Q \in S_N$ is a permutation of the sequence $(1, 2, \ldots, N)$ and S_N is the permutation group of N objects. Now the wavefunction in analogy to (3.14) reads

$$\psi_{\sigma_1,\ldots,\sigma_N}(x_1,\ldots,x_N) = \exp(\mathrm{i} \sum_{j=1}^{N} k_j x_j) \sum_{Q \in S_N} \theta_Q \left[x_\alpha\right] \xi_{\sigma_1,\ldots,\sigma_N}(Q) \ , \tag{3.22}$$

where $\theta_Q \left[x_\alpha\right]$ yields unity whenever $x_{Q(1)} < x_{Q(2)} < \cdots < x_{Q(N)}$ and zero otherwise. If permutations Q' and Q differ only by the exchange $x_i \leftrightarrow x_j$ then the Schrödinger equation requires that

$$\xi(Q') = S^{ij} \xi(Q) \ . \tag{3.23}$$

If more than two particles are present there are different possibilities to go from one configuration to the other. Let, for example, $N = 3$ and denote a configuration with $x_i < x_j < x_k$ by (ijk) then we may go from (123) to (321) via

$$(123) \rightarrow (213) \rightarrow (231) \rightarrow (321)$$

or

$$(123) \rightarrow (132) \rightarrow (312) \rightarrow (321) \ .$$

If both paths are to consistently lead to the same amplitude in the final configuration, one has to have

$$S^{23} S^{13} S^{12} = S^{12} S^{13} S^{23} \ . \tag{3.24}$$

These equations – the famous *Yang-Baxter* equations [24] – lie at the heart of integrability and can be seen to be satisfied by the S–Matrix of the Hubbard model.

We now introduce periodic boundary conditions by requiring that

$$\psi_{\sigma_1,\ldots,\sigma_N}(x_1,\ldots,x_j=0,\ldots,x_N)=\psi_{\sigma_1,\ldots,\sigma_N}(x_1,\ldots,x_j=L,\ldots,x_N) \tag{3.25}$$

to quantize the momenta k_j. We define the operator Z_j acting on the spin Hilbert space of N particles by

$$Z_j=S^{j,j-1}\cdots S^{j,1}S^{j,N}\cdots S^{j,j+1} \tag{3.26}$$

such that it represents the phase shift of a particle j as is taken across all other particles. We can see that periodic boundary conditions imply that the spin wavefunctions ξ are eigenfunctions of the Z_j,

$$Z_j\xi_{\sigma_1,\ldots,\sigma_N}=e^{\mathrm{i}k_jL}\xi_{\sigma_1,\ldots,\sigma_N}\ , \tag{3.27}$$

and that their eigenvalues determine the allowed values of momenta k_j. Taking the particle around the ring may only result in a phase factor $\exp(\mathrm{i}k_jL)$. The spin Hamiltonians Z_j commute with each other owing to the Yang-Baxter equations and solving them is equivalent to the six-vertex model in classical statistical mechanics. This task was achieved by Yang [24] with the help of the Bethe Ansatz.

3.2.3 Lieb-Wu Equations

The solution of the spin problem finally yields the nested Bethe-Ansatz equations. Specifically, for N electrons, M down spins on an L site lattice with interaction $u=U/4$, the equations read

$$\begin{aligned}
\exp(\mathrm{i}k_jL) &= \prod_{l=1}^{M}\frac{\Lambda_l-\sin(k_j)-\mathrm{i}u}{\Lambda_l-\sin(k_j)+\mathrm{i}u}\ ,\quad j=1,\ldots,N\ , && (3.28)\\
\prod_{j=1}^{N}\frac{\Lambda_l-\sin(k_j)-\mathrm{i}u}{\Lambda_l-\sin(k_j)+\mathrm{i}u} &= \prod_{\substack{m=1\\ m\neq l}}^{N}\frac{\Lambda_l-\Lambda_m-2\mathrm{i}u}{\Lambda_l-\Lambda_m+2\mathrm{i}u}\ ,\quad l=1,\ldots,M\ . && (3.29)
\end{aligned}$$

Every solution of these Lieb-Wu equations is given by a set of $N+M$ spectral parameters $\{k_j,\Lambda_l\}$ and is, in general, complex. The energy and momentum of the state are

$$E=-2t\sum_{j=1}^{N}\cos(k_j)\ ,\quad P=\sum_{j=1}^{N}k_j\ . \tag{3.30}$$

Apparently, energy and momentum depend only on the spectral parameters k_j that are associated with the charge degrees of freedom. Since the Lieb-Wu equations are coupled and highly non-linear these parameters will depend sensitively on the configuration of the spectral parameters Λ_l which are associated to the spin degrees of freedom. For the ground state all k_j's and Λ_l's are real numbers. Upon taking the logarithm of (3.28) we obtain the real Bethe-Ansatz equations

$$\begin{aligned} Lk_j &= 2\pi I_j + 2\sum_{\alpha=1}^{M} \arctan\left[4\frac{\Lambda_\alpha - \sin(k_j)}{U}\right] , && (3.31) \\ \sum_{j=1}^{N} \arctan\left[4\frac{\Lambda_\alpha - \sin(k_j)}{U}\right] &= \pi J_\alpha \sum_{\beta=1}^{M} \arctan\left[2\frac{(\Lambda_\alpha - \Lambda_\beta)}{U}\right] . && (3.32) \end{aligned}$$

The "quantum numbers" I_j and J_α are all distinct and arise due to the multi-valuedness of the logarithm. The I_j are integer (half-odd integer) if M is even (odd) whereas the J_α are integer (half-odd integer) if $N - M$ is odd (even). Both sets of numbers are distributed symmetrically around zero in the ground-state and are restricted by

$$\begin{aligned} |I_j| &\leq \frac{L}{2} \mod L , && (3.33) \\ |J_\alpha| &< \frac{N - M + 1}{2} . && (3.34) \end{aligned}$$

Summing (3.31) of j and α, respectively, we can express the total momentum (3.30) as

$$P = \frac{2\pi}{L}\left(\sum_{j=1}^{N} I_j + \sum_{\alpha=1}^{M} J_\alpha\right) , \tag{3.35}$$

where both spin- and charge quantum numbers contribute. This formula indicates that charge and spin degrees of freedom contribute individually to energy and momentum. This phenomenon of spin-charge separation will be elucidated further in the next section.

How can we solve the system of $N+M$ coupled non-linear equations (3.31) and (3.32) for a given choice of quantum numbers $\{I_j, J_\alpha\}$? In general, an analytical solution is not possible but the equations are amenable to a numerical solution. The problem of solving (3.31) and (3.32) is equivalent to finding the roots of an $(N + M)$-dimensional system $f_{1,\ldots,N+M}(k_1, \ldots, k_N; \Lambda_1, \ldots, \Lambda_M) = 0$. If a good initial guess $\{k_j^0, \Lambda_\alpha^0\}$ is known we can employ a simple Newton-Raphson root-finding method [25].

In summary, we have reduced the eigenvalue problem $\hat{H}|\psi\rangle = E|\psi\rangle$ to solving the set of coupled equations (3.28). This is quite remarkable considering that the Hilbert space grows exponentially with the system size while equations (3.28) pose a problem of only polynomial complexity in N. The drawback, however, is that the Bethe-Ansatz wavefunction (3.22) is so complicated that it is impossible to evaluate matrix elements $\langle n|\hat{O}|m\rangle$ for an observable $\hat{O}$. Numerically, expectation values can be evaluated directly with exact diagonalization of the Hamiltonian for systems with 14 to 16 sites. The permutations (complexity $\sim N!$) in the Bethe-Ansatz wavefunction (3.22) render the problem intractable even for such system sizes.

3.3 Thermodynamic Bethe Ansatz

We have seen in the previous section that all excited states of the Hubbard model involving real spectral parameters can be extracted numerically from the discrete (real)

Bethe-Ansatz equations (3.31). If we want to obtain complex solutions we have to tackle the original Lieb-Wu equations (3.28). This is a daunting task and we therefore proceed along a different path. First we discuss the *string hypothesis* and present the Takahashi equations and give a short sketch of the *thermodynamic* Bethe Ansatz. The excitations of the Hubbard model can then be calculated by solving a set of Fredholm-type integral equations of second order.

3.3.1 Bound States

Consider the Lieb-Wu equations for two electrons with $N = 2$ and $M = 1$. In contrast to the previous section we now allow the spectral parameters k to be complex, namely

$$k_\pm = k \pm \mathrm{i}\xi \tag{3.36}$$

with real numbers k and $\xi > 0$. Explicitly, we have

$$\begin{aligned}
\exp(\mathrm{i}k_+L) &= \frac{\Lambda - \sin(k_+) - \mathrm{i}u}{\Lambda - \sin(k_+) + \mathrm{i}u} , & (3.37)\\
\exp(\mathrm{i}k_-L) &= \frac{\Lambda - \sin(k_-) - \mathrm{i}u}{\Lambda - \sin(k_-) + \mathrm{i}u} , & (3.38)\\
1 &= \frac{\Lambda - \sin(k_+) - \mathrm{i}u}{\Lambda - \sin(k_+) + \mathrm{i}u}\frac{\Lambda - \sin(k_-) - \mathrm{i}u}{\Lambda - \sin(k_-) + \mathrm{i}u} . & (3.39)
\end{aligned}$$

The second equation becomes exponentially large with L because we chose $\xi > 0$ which can only be true if the right hand side is close to a pole or

$$\sin(k_-) \to \Lambda + \mathrm{i}u . \tag{3.40}$$

This in turn implies that the second factor in (3.39) is exponentially small or

$$\sin(k_+) \to \Lambda - \mathrm{i}u . \tag{3.41}$$

This solution is called a k-Λ-string, since both k's are aligned symmetrically around a real Λ. Excitations involving complex spectral parameters can be shown to correspond to bound states; in our case

$$\psi(x_1, x_2|k_+, k_-, \Lambda) \propto e^{\mathrm{i}k(x_1+x_2)}e^{-\xi(x_1-x_2)} , \tag{3.42}$$

where we have taken the limit $L \to \infty$. This wavefunction describes a bound state of electrons with center of mass momentum k.

3.3.2 String Hypothesis

In the general case k-Λ-strings take the form

$$\begin{aligned} k_\alpha^1 &= \pi - \arcsin({\Lambda'}_\alpha^m + m\mathrm{i}u) \ , \\ k_\alpha^2 &= \arcsin({\Lambda'}_\alpha^m + (m-2)\mathrm{i}u) \ , \\ k_\alpha^3 &= \pi - k_\alpha^2 \ , \\ &\vdots \\ k_\alpha^{2m-2} &= \arcsin({\Lambda'}_\alpha^m + (m-2)\mathrm{i}u) \ , \\ k_\alpha^{2m-1} &= \pi - k_\alpha^{2m-1} \ , \\ k_\alpha^{2m} &= \pi - \arcsin({\Lambda'}_\alpha^m + m\mathrm{i}u) \ , \end{aligned} \tag{3.43}$$

and

$${\Lambda'}_\alpha^{m,j} = {\Lambda'}_\alpha^m + (m-2j+1)\mathrm{i}u \quad , \quad j = 1, \ldots, m \ , \tag{3.44}$$

where the index α enumerates the k-Λ-string of length m with real center $\Lambda_\alpha'^m$. Additionally, there are solutions that involve only Λ's given by the expression (3.44).

It has been established [21] that all regular solutions – i.e. solutions with finite spectral parameters – are exponentially close to a *string-solution* that comprises of

1. a single real k_j;

2. a Λ-string of length m. This includes the case of a single real Λ;

3. a k-Λ-string of length n involving $2n$ k's and n Λ's.

This is the so called *string-hypothesis* [26]. We characterize a string-solution containing $\mathcal{M}_e$ real k_j, M_n Λ-strings and M'_n k-Λ-strings by a set of *occupation numbers* $\{\mathcal{M}_e, M_n, M'_n | n \in \mathbb{N}\}$. Obviously, they satisfy the sum rules

$$M = \sum_{n=1}^{\infty} n \left(M_n + M'_n\right) \ , \tag{3.45}$$

$$N = \mathcal{M}_e + \sum_{n=1}^{\infty} 2nM'_n \ . \tag{3.46}$$

3.3.3 Takahashi Equations

When we apply the string-hypothesis to the Lieb-Wu equations (3.28) and take logarithms we get a new set of equations, the so-called *Takahashi equations* [5], similar to the real Bethe-Ansatz equations (3.31) of the previous section. They involve only the real centers of the strings. For L even we have [5]:

$$
\begin{aligned}
k_j L &= 2\pi I_j - \sum_{n=1}^{\infty}\sum_{\alpha=1}^{M_n} \theta\left(\frac{\sin(k_j) - \Lambda_\alpha^n}{nu}\right) && (3.47)\\
&\quad - \sum_{n=1}^{\infty}\sum_{\alpha=1}^{M'_n} \theta\left(\frac{\sin(k_j) - \Lambda'^n_\alpha}{nu}\right) \; ,\\
\sum_{j=1}^{N-2M'} \theta\left(\frac{\Lambda_\alpha^n - \sin(k_j)}{nu}\right) &= 2\pi J_\alpha^n + \sum_{m=1}^{\infty}\sum_{\beta=1}^{M_m} \Theta_{nm}\left(\frac{\Lambda_\alpha^n - \Lambda_\beta^m}{u}\right) \; , && (3.48)\\
2L\Re\left[\arcsin\left(\Lambda'^n_\alpha + niu\right)\right] &= 2\pi J'^n_\alpha + \sum_{j=1}^{N-2M'} \theta\left(\frac{\Lambda'^n_\alpha - \sin(k_j)}{nu}\right) && (3.49)\\
&\quad + \sum_{m=1}^{\infty}\sum_{\beta=1}^{M'_m} \Theta_{nm}\left(\frac{\Lambda'^n_\alpha - \Lambda'^m_\beta}{u}\right) \; .
\end{aligned}
$$

In these equations we have $M' = \sum_{n=1}^{\infty} nM'_n$ Λ's involved in k-Λ-strings, the definition $\theta(x) = 2\arctan(x)$, and

$$
\begin{aligned}
\Theta_{n\neq m}(x) &= \theta\left(\frac{x}{|n-m|}\right) + 2\theta\left(\frac{x}{|n-m|+2}\right) + \cdots + 2\theta\left(\frac{x}{n+m-2}\right) + \theta\left(\frac{x}{n+m}\right) \; ,\\
\Theta_{nn}(x) &= 2\theta\left(\frac{x}{2}\right) + 2\theta\left(\frac{x}{4}\right) + \cdots + 2\theta\left(\frac{x}{2n-2}\right) + \theta\left(\frac{x}{2n}\right) \; . && (3.50)
\end{aligned}
$$

Again we get integer or half-odd integer numbers I_j, J_α^n and J'^n_α from taking logarithms. The set of numbers I_j associated with real spectral parameters k_j not involved in k-Λ-strings obeys

$$
\begin{aligned}
I_j &\in \begin{cases} \mathbb{Z} & \text{if } \sum\limits_m (M_m + M'_m) \bmod 2 = 0 \\ (2\mathbb{Z}-1)/2 & \text{if } \sum\limits_m (M_m + M'_m) \bmod 2 \neq 0 \end{cases} && (3.51)\\
|I_j| &\leq \frac{L}{2} \mod L \; . && (3.52)
\end{aligned}
$$

In the ground state the I_j are distributed symmetrically around zero with no vacancies in the sequence, cf. (3.33).

The quantum numbers J_α^n associated with Λ-strings of length n obey the restrictions

$$
\begin{aligned}
J_\alpha^n &\in \begin{cases} \mathbb{Z} & \text{if } (N - M_n) \bmod 2 \neq 0 \\ (2\mathbb{Z}-1)/2 & \text{if } (N - M_n) \bmod 2 = 0 \end{cases} && (3.53)\\
|J_\alpha^n| &< \frac{1}{2}\left(N - 2M' - \sum_{m=1}^{\infty} t_{nm}M_m - 1\right) \; , && (3.54)
\end{aligned}
$$

with $t_{mn} = 2\min(m,n) - \delta_{mn}$. In the ground state only J^1_α are finite and are symmetrically distributed around zero with no vacancies, cf. (3.34).

Finally, the numbers ${J'}_\alpha$ associated with real centers of k-Λ-strings obey

$$
\begin{aligned}
{J'}^n_\alpha &\in \begin{cases} \mathbb{Z} & \text{if } (L-N-{M'}_n) \bmod 2 \neq 0 \\ (2\mathbb{Z}-1)/2 & \text{if } (L-N-{M'}_n) \bmod 2 = 0 \end{cases} & (3.55)\\
|{J'}^n_\alpha| &< \frac{1}{2}\left(L - N + 2M' - \sum_{m=1}^{\infty} t_{nm} M'_m - 1\right) . & (3.56)
\end{aligned}
$$

The ground state does not contain any k-Λ-strings so that no ${J'}^n_\alpha$ appear.

3.3.4 Thermodynamic Limit of the Takahashi Equations

We consider the Takahashi equations in the thermodynamic limit

$$L \to \infty\,,\ N \to \infty\,,\ N/L = \text{const}\,. \tag{3.57}$$

The crucial observation is that consecutive roots become dense as L becomes larger:

$$k_{j+1} - k_j,\ \Lambda^n_{\alpha+1} - \Lambda^n_\alpha,\ {\Lambda'}^n_{\alpha+1} - {\Lambda'}^n_\alpha \sim 1/L\,. \tag{3.58}$$

This enables us to express the Takahashi equations in terms of coupled integral equations. The reader is referred to [5] for a detailed derivation.

In the limit of zero temperature and zero magnetic field we obtain

$$
\begin{aligned}
\kappa(k) &= -2\cos(k) - \mu - U/2 + \int_{-Q}^{Q} \mathrm{d}q\, \cos(q) R(\sin(q)-\sin(k))\kappa(q)\,, & (3.59)\\
\rho(k) &= \frac{1}{2\pi} + \int_{-Q}^{Q} \mathrm{d}q\, \cos(q)\, R(\sin(q)-\sin(k))\, \rho(q) \quad \text{for} \quad |k| \le Q\,, & (3.60)\\
\rho^h(k) &= \frac{1}{2\pi} + \int_{-Q}^{Q} \mathrm{d}q\, \cos(q)\, R(\sin(q)-\sin(k))\, \rho^h(q) \quad \text{for} \quad |k| > Q\,, & (3.61)
\end{aligned}
$$

for the so called *dressed energy* $\kappa(k)$ and the *root density* $\rho(k)$. The integral kernel is given by the function

$$R(x) = \frac{1}{2\pi}\int_{-\infty}^{\infty} \mathrm{d}\omega\, \frac{\exp(\mathrm{i}\omega x)}{1+\exp(2u|\omega|)}\,, \tag{3.62}$$

and the pseudo-Fermi momentum $Q = Q(\mu)$ is self-consistently determined by the conditions

$$
\begin{aligned}
\kappa(\pm Q) &= 0\,, & (3.63)\\
\int_{-Q}^{Q} \mathrm{d}k\, \rho(k) &= \frac{N}{L}\,. & (3.64)
\end{aligned}
$$

Physically, the first equation means that we have set the pseudo-Fermi energy to zero and the second equation fixes the particle density to $n = N/L$.

These integral equations pose a chicken-and-egg problem: In order to solve the integral equations (3.59), (3.60) for $\rho(k)$ and $\kappa(k)$ we first need to know the integration boundary Q for a given value of the chemical potential μ. However, Q in turn depends on μ through condition (3.63) that involves the solution of equations (3.59) and (3.60). Finally, the electron density is determined by $Q = Q(\mu)$ by condition (3.64) involving the solution of (3.60).

We proceed in the following way:

1. Fix a starting μ.
2. Choose a value for Q.
3. Solve (3.59) to (3.61).
4. Check if (3.63) is fulfilled within error ε. If not start over from 2, otherwise continue.
5. Check if (3.64) yields the desired electron density within Δn_e. If not start again from 1.

Once the dressed energy $\kappa(k)$ and the root density $\rho(k)$ are known we can calculate the dressed momentum of a hole in the sea of k's through

$$p(k) = 2\pi \int_0^k \mathrm{d}q \, \left(\rho(q) + \rho^h(q)\right) \, . \tag{3.65}$$

A Λ-string of length n has dressed momenta and energies

$$\begin{aligned}
\epsilon_1(\Lambda) &= \int_{-Q}^{Q} \mathrm{d}q \, \frac{\cos(k)}{U} \frac{1}{\cosh(2\pi/U)(\Lambda - \sin(q))} \kappa(q) \, , && (3.66)\\
\epsilon_n(\Lambda) &= 0 \quad \text{for} \quad n > 1 \, , && (3.67)\\
p_1(\Lambda) &= 2\int_{-Q}^{Q} \mathrm{d}q \, \arctan\left[\exp\left(-\frac{2\pi}{U}(\Lambda - \sin(q))\right)\right] \rho(q) - \pi\frac{N}{2L} \, . && (3.68)
\end{aligned}$$

Note that Λ–strings of length larger than unity have vanishing energies when the magnetic field is set to zero. Finally, dressed momenta and energies of a k–Λ–string with length m are

$$\begin{aligned}
p'_n(\Lambda) &= -2\Re[\arcsin(\Lambda - \mathrm{i}nu)] + \int_{-Q}^{Q} \mathrm{d}k \, \arctan\left(\frac{\Lambda - \sin(q)}{nu}\right) \rho(q) && (3.69)\\
&\quad +\pi(n+1) \, , \\
\epsilon'_n(\Lambda) &= 4\Re\left[\sqrt{1 - (\Lambda - \mathrm{i}nu)^2}\right] - 2n\mu - 4nu && (3.70)\\
&\quad + \int_{-Q}^{Q} \mathrm{d}q \, \frac{nu}{(nu)^2 + (\sin(q) - \Lambda)^2} \kappa(q) \, .
\end{aligned}$$

3.3.5 Spinons and Holons

We can now give a meaningful definition of spin-charge separation which is characteristic of one-dimensional correlated electron systems. The elementary excitations of the Hubbard model correspond to independent changes in the quantum numbers I_j and J^1_α of the Takahashi equations (3.47)-(3.49).

We take a particular I_j out of the ground-state sequence (3.52) of, say, integers while we keep the sequence of J^1_α unchanged. This amounts to the excitation of a *holon* in the system. However, this will change the nature of the remaining I_j according to (3.51) which makes them half-odd integer in our example. Likewise, all the J^1_α are shifted by 1/2, see (3.53). On the other hand, we may add an I_j to the ground-state sequence which is an *antiholon* in our wording. Similar to the case of the holon excitation this will lead to a shift $I_j \to I_j \pm 1/2$, $J^1_\alpha \to J^1_\alpha \pm 1/2$ of all ground-state quantum numbers. The charge degrees of freedom have roots k distributed in the range $\pm Q$. We can interpret this as a quasi Fermi momentum k_F of particles residing in a limited phase space in analogy to the Fermi sea of electrons. Hole excitations of this quasi Fermi sea are holons and particle excitations are antiholons. In the large-U limit, the addition of a particle at half filling generates a *doublon* which can be mapped to the situation with one particle less than half filling via the particle-hole transformation (2.11) so that the doublon is a particle-hole transformed holon.

When we start from the ground-state sequence and leave the I_j unchanged we can make a hole in the sequence of J^1_α which corresponds to the excitation of a *spinon*. As in the case of the holon this results in a change of both the charge and spin quantum numbers according to (3.51) and (3.53). Unlike the holon and antiholon, the creation of a J^1_α enlarges the number of allowed roots by one, i.e, the spinons do not obey an exclusion principle. Consequently, there is no pseudo-Fermi momentum of the spin degrees of freedom and there is no *antispinon* associated with the spinon. In the large-U limit the spinons are the elementary excitations of the corresponding antiferromagnetic Heisenberg model.

Obviously, the (anti)holons and spinons contribute independently to the excitation spectrum of the one-dimensional Hubbard model. Note, however, that *physical excitations* are built from combinations of those spinons and holons. For example, a charged fermionic excitation must involve at least a spinon and an (anti)holon, because a fermion has charge and spin.

3.4 Physical Excitations

We are now in the position to construct physical excitations from the elementary excitations introduced above. It is important to note that not every combination of elementary excitations is a physical excitation. Only those combinations permitted by the selection rules (3.51) through (3.56) correspond to physical excitations of the system. Below we list examples that we will refer to throughout the following chapters. Except were otherwise stated we assume a particle number in the ground state $N_\mathrm{GS} = 2 \times \mathrm{Odd}$ and

$M = N_{\rm GS}/2$ since we only regard the case of zero magnetic field. Then only J^1_α appear, whereas $J^{n>1}_\alpha$ do not enter.

For definite results we choose an interaction strength of $U/t = 4.9$ and a band filling of $n = 0.6$ since this case will be of importance for the single-particle spectrum of TTF-TCNQ in a later chapter of this work. Other examples can be found in [5] and [19]. For the sake of brevity we only consider the case away from half-filling and remark on the half-filled case where appropriate.

3.4.1 Spinon-Spinon Excitation

The simplest charge neutral excitation involves the spin sector only. We flip a single down spin and obtain a spin-triplet excitation with spin $S = 1$. The occupation numbers of this excitation are $N = \mathcal{M}_e = N_{\rm GS}$ and $M = M_1 = (N/2 - 1)$ (even). According to conditions (3.51) the distribution of charge quantum numbers is shifted by $I_j \to I_j \pm 1/2$. This results in an extra contribution to the total momentum of $\pm n_e \pi$ resulting in two excitation branches. The allowed values in (3.53) for the quantum number J^1_α are

$$|J^1_\alpha| \leq \frac{N_{\rm GS}}{4} \ . \tag{3.71}$$

This means that the length of the sequence J^1_α in the excited state exceeds $N_{\rm GS}/2$ by two despite the fact that we only flipped one spin. In other words there are two spinons involved in the spin-triplet excitation. Energy and momentum of the two spinons with spectral parameters Λ_1 and Λ_2 with respect to the ground-state are

$$\begin{aligned} E_{\rm trip}(\Lambda_1, \Lambda_2) &= -\epsilon_1(\Lambda_1) - \epsilon_1(\Lambda_2) \ , && (3.72)\\ P_{\rm trip}(\Lambda_1, \Lambda_2) &= -p_1(\Lambda_1) - p_1(\Lambda_2) \pm \pi n_e \ , && (3.73)\\ \Lambda_1, \Lambda_2 &\in (-\infty, \infty) \ . \end{aligned}$$

A parametric plot of $E_{\rm trip}(\Lambda_1, \Lambda_2)$ versus $P_{\rm trip}(\Lambda_1, \Lambda_2)$ is shown in figure 3.1 for many pairs $\{\Lambda_1, \Lambda_2\}$. The spinon-spinon continuum has soft modes at $k = 0, \pm 2k_{\rm F}, \pm 4k_{\rm F}$ which contribute to the long-range behavior of the spin-spin correlation function, see section 3.1, equation (3.11). We therefore identify the slope $v_{\rm s}$ of the spectrum at $k = 0$ with the *spin velocity* of the spin excitations.

It is interesting to note that the spin-triplet excitation is exactly degenerate with the spin-singlet excitation involving a complex pair of Λ's (Λ-string). Recall that the spin excitations of a Heisenberg model are very similar to this excitation because the spin spectral parameter Λ comes into play when the spin part of the Hubbard eigenvalue problem is also solved by Bethe Ansatz. We will make use of the spectrum of this excitation when we discuss the dynamical spin-spin structure factor of the quasi one-dimensional chain cuprates $\rm Sr_2CuO_3$ and $\rm SrCuO_2$. These systems are half-filled but everything said here will remain valid in the Mott insulator where spin excitations remain gapless.

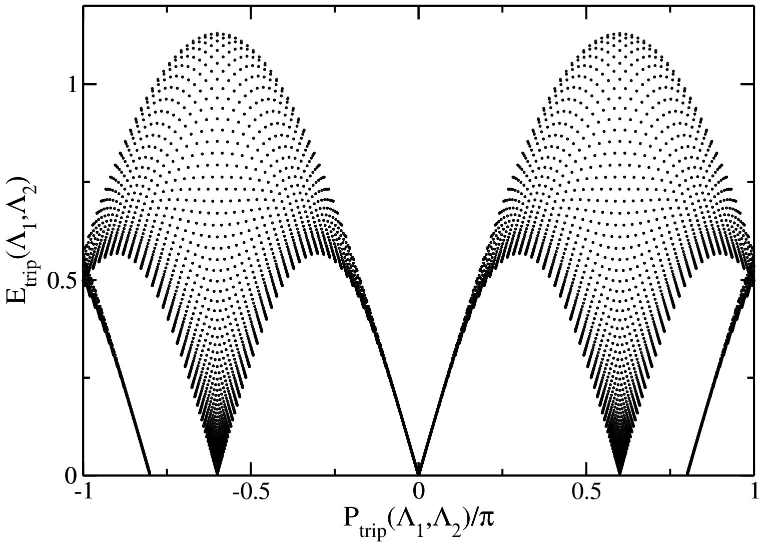

Figure 3.1: Spin-triplet excitation spectrum ($U/t = 4.9, n_e = 0.6$) with backfolding to the first Brillouin zone. Soft modes with zero energy occur at $k = 0, \pm\pi n_e, \pm 2\pi n_e \bmod(2\pi)$.

3.4.2 Holon-Spinon Excitation

When we remove an electron from the system, we make a hole in the ground-state distribution of k's and Λ's since we have removed charge $-e$ and spin 1/2. Much of our discussion will carry on to explain the angle-resolved photoemission spectra of a one-dimensional charge transfer salt in terms of holon-spinon excitations.

The excitation is described by $N = \mathcal{M}_e = N_{\text{GS}} - 1$ and $M = M_1 = N_{\text{GS}}/2 - 1$. The I_j are integers and similar to the previous case we get a contribution $\pm n_e\pi$ to the total momentum. Because there is one less root k in the sequence of real charge quantum numbers compared to the ground state, a holon contributes to the excitation spectrum. The quantum numbers J_α^1 are integers and have a range $|J_\alpha^1| < (N_{\text{GS}} - 2)/4$. There are $N_{\text{GS}}/2$ vacancies for $N_{\text{GS}}/2 - 1$ real values Λ_α and, accordingly, there is a spinon present. Altogether we get

$$\begin{aligned} E_{\text{hs}}(k,\Lambda) &= -\kappa(k) - p_1(\Lambda)\ , \\ P_{\text{hs}}(k,\Lambda) &= -p(k) - p_1(\Lambda) \pm \pi n_e\ , \\ k &\in [-Q,Q]\ , \\ \Lambda &\in (-\infty,\infty)\ . \end{aligned} \tag{3.74}$$

The excitation spectrum of this excitation is shown in figure 3.2. A parametric plot of the thermodynamic Bethe-Ansatz (TBA) solution, $E_{\text{hs}}(k,\Lambda)$ vs. $P_{\text{hs}}(k,\Lambda)$, are shown as well as the corresponding result of a finite system from equations (3.31). While there are soft spots in the (TBA) holon-spinon spectrum at momenta $k = \pm k_{\text{F}}, \pm 3k_{\text{F}}, \ldots$, there are gaps in the finite system. This is a finite size effect that vanishes in the thermodynamic limit.

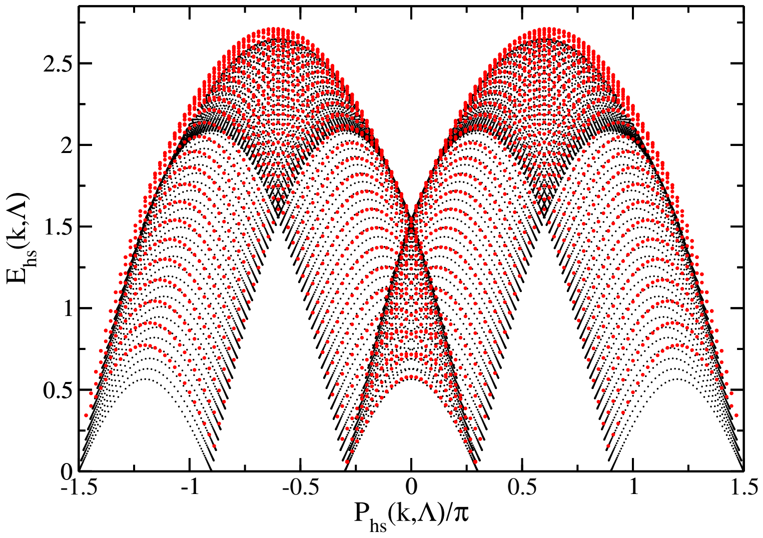

Figure 3.2: Holon-spinon excitation spectrum ($U/t = 4.9, n_e = 0.6$) in the extended zone scheme (black). Soft modes with zero energy occur at $k = \pm\pi n_e/2, \pm 3\pi n_e/2, \pm 5\pi n_e/2$. Also shown is the excitation spectrum of a finite system ($L = 90$) from the discrete Bethe-Ansatz equations (red). Notice the apparent gaps in the spectrum in the exact solution. These are *finite-size* effects that vanish in the thermodynamic limit.

Now that we can change the spin- and charge quantum numbers separately we can easily identify different excitation branches in the spectrum. If we closely inspect the holon-spinon spectrum we see that the shallow arches centered around $k = 0$ are obtained by changing J_α^1 while leaving I_j unchanged. From arch to arch I_j is changed by one yielding different spinon branches. Similarly, we can keep J_α^1 fixed and change I_j to obtain distinct holon branches. The slope of the lowest spinon branch at $k = k_\mathrm{F}$ is given by the spin-velocity v_s and the upper boundary of the continuum varies as $v_\mathrm{c}(k - k_\mathrm{F})$, where v_c is the charge-velocity.

At half-filling we can still distinguish between spinon and holon excitations in the sense above. However, all charge excitations are gapped, i.e, the system is a Mott-Hubbard insulator. The holon-spinon excitation spectrum appears shifted by half the charge gap with respect to the chemical potential. Furthermore, the overall form of the spectrum is altered. Spinon and holon branches approach their respective onset at k_F quadratically.

3.4.3 Antiholon-Spinon Excitation

Instead of removing an electron from the system we can add one. This excitation will give us a deeper understanding of the low energy ARPES spectra of a more than half-filled system consisting of linear stacks of TTF molecules in the quasi one-dimensional conductor TTF-TCNQ.

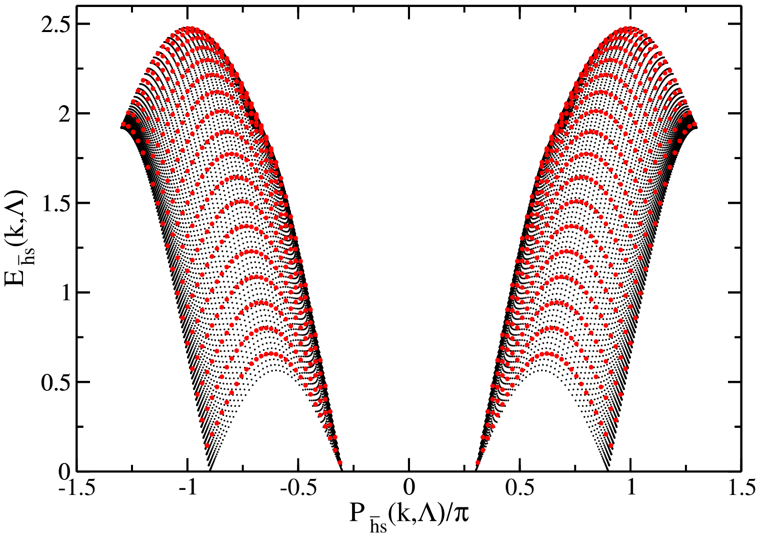

Figure 3.3: Antiholon-spinon excitation spectrum ($U/t = 4.9, n_e = 0.6$) in the extended zone scheme (black). Soft modes with zero energy occur at $k = \pm\pi n_e/2, \pm 3\pi n_e/2$. Also shown is the excitation spectrum of a finite system ($L = 90$) from the discrete Bethe-Ansatz equations (red). Notice the apparent gaps in the spectrum of the exact solution. These gaps are *finite–size* effects that vanish in the thermodynamic limit.

We choose occupation numbers $N = \mathcal{M}_e = N_{\mathrm{GS}} + 1$ and $M = M_1 = N_{\mathrm{GS}}/2$, i.e., we leave the number of down spins unchanged. Since we assumed $N_{\mathrm{GS}} = 2 \times \mathrm{Odd}$ we have both I_j and J^1_α half-odd integers. The I_j of the extra electron is added in the range $|I| \geq (N_{\mathrm{GS}} - 1)/2$ or equivalently in the range of roots $|k| > Q$. The range of spin quantum numbers is

$$|J^1_\alpha| \leq \frac{N_{\mathrm{Gs}}}{4} \tag{3.75}$$

such that we can distribute $N_{\mathrm{GS}}/2$ real roots Λ on $N_{\mathrm{GS}}/2 + 1$ vacancies. Accordingly, adding an electron also leads to the generation of a spinon which also contributes to the total momentum and energy,

$$\begin{aligned}
E_{\mathrm{hs}}(k,\Lambda) &= -\kappa(k) - p_1(\Lambda) \ , \\
P_{\mathrm{hs}}(k,\Lambda) &= -p(k) - p_1(\Lambda) \pm \pi n_e \ , \\
k &\in [-\pi, -Q) \cup (Q, \pi] \ , \\
\Lambda &\in (-\infty, \infty) \ .
\end{aligned} \tag{3.76}$$

We show the result of the TBA and for the finite system in figure 3.3. As in the case of the holon-spinon excitation, we see that finite-size gaps appear in the exact excitation spectra of the finite system despite the fact we are dealing with a metal. The phase space for the antiholon-spinon excitation vanishes as the filling approaches unity.

3.4.4 $4k_{\mathrm{F}}$-Singlet Excitation

There is a possibility of making a gapless and charge neutral excitation that does not involve the excitation of spin degrees of freedom. Let us consider occupation numbers $N = \mathcal{M}_e = N_{\mathrm{GS}}$ and $M = M_1 = N_{\mathrm{GS}}/2$ identical to the ground-state configuration. While we leave the sequence of J^1_α unchanged we make a hole in the distribution of charge quantum numbers I_j and place an I_m outside of the ground-state sequence:

$$|I_m| > \frac{N_{\mathrm{GS}}/2 - 1}{2} \; . \tag{3.77}$$

Both the hole as well as the additional “particle” can carry energy and momentum. This is why some authors have dubbed this a “particle-hole” excitation. This is somewhat misleading, however, since no particles or holes in a Fermi sea of quasi-electrons are involved. In contrast, a particle-hole pair in the sequence of the abstract charge quantum numbers I_j is created. Therefore we will follow Schulz [19] and call this excitation a $4k_{\mathrm{F}}$-singlet. The name originates from the fact that this excitation has a soft mode exactly at $k = 4k_{\mathrm{F}}$ (and $k = 0$).

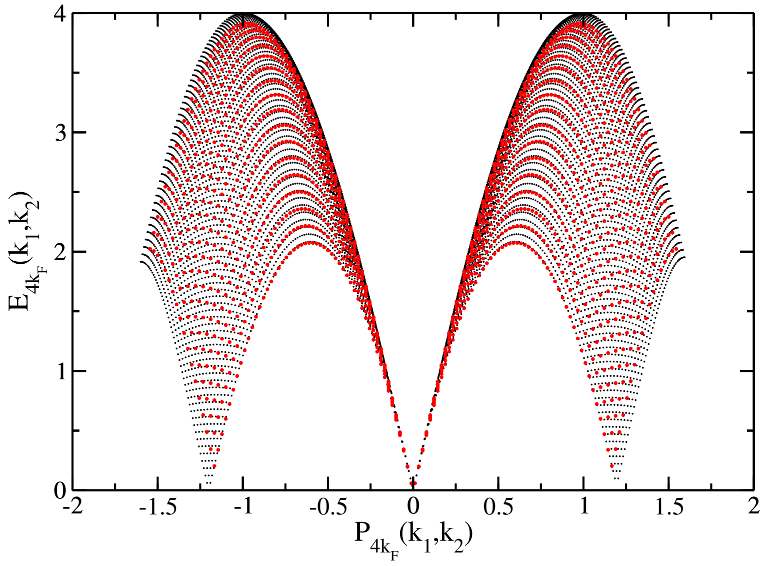

Figure 3.4: Excitation spectrum of the $4k_{\mathrm{F}}$-singlet ($U/t = 4.9, n_e = 0.6$) in the extended zone scheme (black). Soft modes with zero energy occur at $k = 0$ and $k = \pm 2n_e\pi = 4k_{\mathrm{F}}$. Red symbols denote the corresponding excited states of the finite system ($L = 90$).

In figure 3.4 we have parametrically plotted the relations

$$\begin{aligned} E_{4k_{\rm F}}(k_1,k_2) &= \kappa(k_1)-\kappa(k_2)\ , \\ P_{4k_{\rm F}}(k_1,k_2) &= p(k_1)-p(k_2)\ , && (3.78) \\ k_1 &\in [-\pi,-Q)\cup[\pi,Q)\ , && (3.79) \\ k_2 &\in [-Q,Q]\ , \end{aligned}$$

which define dressed energy and momentum of the $4k_{\rm F}$-singlet. The soft modes at $k=0,\pm 4k_{\rm F}$ dominantly contribute to the charge-charge correlation function, see equation (3.10). We can identify the slope of the low-energy modes as the charge velocity $v_{\rm c}$.

Any excitation of the Hubbard model can be combined with this gapless excitation. When half-filling is approached the phase space of the excitation shrinks to zero which can be directly seen from (3.77). This is also obvious from the fact that, at half-filling and $U>0$, there are no gapless charge-neutral excitations because the system is a Mott-insulator.

3.4.5 k-Λ-Strings

So far we have considered gapless excitations in either spin or charge sectors or both. There is, however, a hierarchy of gapful excitations even away from half filling which involve k-Λ-strings. As discussed in section 3.3.1 k-Λ-strings can be interpreted as bound states of charge degrees of freedom. F. Woynarovich was the first to show that the wavefunction of these excitations corresponds to a state with doubly occupied sites if we go to the limit $U/t\to\infty$ [27, 28, 29]. It is therefore natural to describe the dynamics of the upper Hubbard band with these excitations.

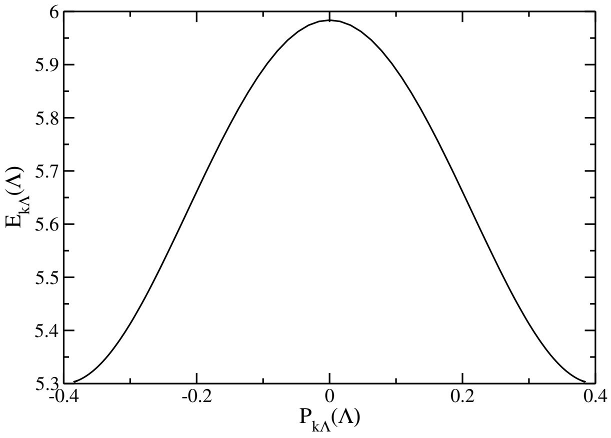

Figure 3.5: Dispersion of a k-Λ-string of length $m=1$ involving two complex conjugate k_j. The range of energies of the excitation lies well above the two-particle continuum.

We choose occupations numbers $\mathcal{M}_e = N_{\mathrm{GS}} - 2$, $M_1 = N_{\mathrm{GS}}/2 - 1$, $M_1' = 1$. There is no hole in the sequence of J_α^1's and we keep the sequence of I_j fixed such that their spacing is unity. Energy and momentum of this excitation are given by

$$\begin{aligned} E_{k\Lambda} &= \epsilon_1'(\Lambda)\ , \\ P_{k\Lambda} &= p_1'(\Lambda)\ , \\ \Lambda &\in (-\infty, \infty)\ . \end{aligned} \tag{3.80}$$

Figure 3.5 shows the dispersion of this excitation. We see that the excitation is gapped and has a maximum centered around zero momentum. There is no overlap between the dispersion of this k-Λ-string and the continuum of two-particle excitations. The lowest possible k-Λ-string excitation has an onset of

$$\epsilon_1'(\Lambda = \pm\infty) = -2\mu - U \tag{3.81}$$

which can be seen directly from (3.70).

Chapter 4

Density-Matrix Renormalization Group

This chapter is devoted to an introduction of the density-matrix renormalization group method (DMRG) that was put forward by S. White in 1992 [30]. It has since proven itself as one of the most successful methods to analyze properties of one-dimensional quantum system, equally for bosons and fermions. We begin with a discussion of exact diagonalization, the most direct approach to study quantum Hamiltonians. A suitable division of the underlying lattice into an *environment* and a *system* combines the idea of renormalization and density matrices and is the key of the success of DMRG. A review of the method and its applications can be found in [31] and [32] and the exposition of the subject in this chapter relies heavily on these sources.

4.1 Exact Diagonalization

The problem of interacting many-particle systems is straightforward to pose. We define an underlying lattice, the interaction between particles, their kinetic energy and possibly external fields and arrive at a Hamiltonian $\hat{H}$. All what is left to do is the diagonalization of the Hamiltonian to obtain the eigenspectrum and eigenstates of $\hat{H}$. This can, in general, not be achieved analytically. Numerically, the full eigenspectrum can be computed for very small systems. For instance, in case of the half-filled Hubbard model on a 8-site lattice, we would have to diagonalize a matrix with dimensions

$$D = \left(\begin{array}{c} N \\ N/2 \end{array} \right) \times \left(\begin{array}{c} N \\ N/2 \end{array} \right) = 4096 \times 4096 \; . \tag{4.1}$$

Beyond eight sites this becomes impossible even on the most powerful computers because the Hilbert space dimension grows exponentially with the system size L.

If, however, we are only interested in a few of the lowest eigenvalues and their corresponding eigenstates and the Hamiltonian is sparse we can resort to well known numerical methods such as the *Lanczos method*. There, the Hamiltonian only comes into play in matrix-vector multiplications and this only requires the non-zero entries of the Hamiltonian matrix. Nevertheless, the accessible system sizes are limited to currently 16-site half-filled Hubbard lattices. In many cases this is not sufficient to extrapolate the desired quantities to the thermodynamic limit because of finite-size effects.

4.2 DMRG: Density-Matrix Renormalization

An entirely different approach is the reduction of the number of degrees of freedom; we retain only those that are "important" in some sense. But how can this be achieved? Traditional renormalization group (RG) methods rely on an energy criterion (infrared or ultraviolet cutoff) to integrate out irrelevant degrees of freedom. It turns out that this works very poorly when applied to the problem of adding degrees of freedom to the Hamiltonian in position space. In a particular sense, the density matrix is the best object to consider for a real-space RG method, as we shall see below.

4.2.1 Reduced Density Matrices

We are only interested in the limit $T = 0$, and the system is in a pure state. Let us assume that we can divide the complete system, the *super block* into two sub-systems: the *environment block* and the *system block*. We denote the basis states of the environment block (E) with $|j\rangle$ and the basis of the system block (S) with $|i\rangle$. This is shown schematically in figure 4.1.

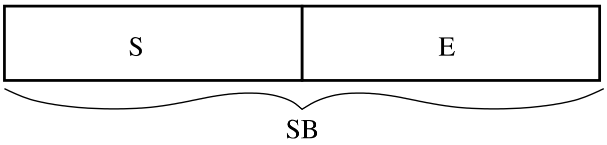

Figure 4.1: The superblock (SB) is divided into two subsystems: the system block (S) and the environment block (E). The basis states in (S) are $\{|i\rangle\}$ and those in (E) are $\{|j\rangle\}$. The superblock Hilbert space is spanned by the linear combination of direct products $|\psi\rangle = \sum_i \sum_j \psi_{ij} |i\rangle \otimes |j\rangle$.

Any state $|\psi\rangle$ of the super block (SB) can then be written as

$$|\psi\rangle = \sum_i \sum_j \psi_{ij} |i\rangle \otimes |j\rangle \ , \tag{4.2}$$

which we assume to be normalized $\langle\psi|\psi\rangle = 1$. We trace out the environment states $|j\rangle$ to obtain the *reduced* density operator

$$\hat{\rho} = \mathrm{Tr}_{\mathrm{E}} |\psi\rangle\langle\psi| = \sum_j \langle j|\psi\rangle\langle\psi|j\rangle \tag{4.3}$$

$$= \sum_{jii'} \psi_{ij} \psi^*_{i'j} |i\rangle\langle i'| = \sum_{ii'} \rho_{ii'} |i\rangle\langle i'| \ , \tag{4.4}$$

where we have defined the *reduced density matrix*

$$\rho_{ii'} = \sum_j \psi_{ij}\psi^*_{i'j} \ . \tag{4.5}$$

Of course, we could have interchanged the labeling of environment and system. We can conveniently write the reduced density matrix using the matrix representation of the wavefunction $\psi_{ij} = \langle i| \otimes \langle j|\psi\rangle$ as

$$\hat{\rho} = \psi\psi^+ \tag{4.6}$$

with $\psi = (\psi_{ij})$. Any expectation value of system block operators $\hat{A}$ can then be found as

$$\begin{aligned} \langle\psi|\hat{A}|\psi\rangle &= \mathrm{Tr}(\hat{\rho}\hat{A}) & (4.7)\\ &= \sum_\alpha w_\alpha \langle\alpha|\hat{A}|\alpha\rangle \ , & (4.8) \end{aligned}$$

with the eigenstates $|\alpha\rangle$ and eigenvalues $w_\alpha \geq 0$ of $\hat{\rho}$. Of course, $\sum_\alpha w_\alpha = 1$, since $\mathrm{Tr}\hat{\rho} = 1$, and we order the states $|\alpha\rangle$ according to their weights w_α, $|\alpha\rangle \geq |\beta\rangle$ if $w_\alpha \geq w_\beta$.

If we know the m largest eigenvalues of $\hat{\rho}$ while all other eigenvalues are small we have a good approximation of the expectation value through

$$\langle\psi|\hat{A}|\psi\rangle_{\text{approx}} = \sum_{\alpha>m} w_\alpha \langle\alpha|\hat{A}|\alpha\rangle \ . \tag{4.9}$$

The error of our approximation is bounded from above by

$$|\langle\psi|\hat{A}|\psi\rangle_{\text{approx}} - \langle\psi|\hat{A}|\psi\rangle| \leq \max_{\alpha>m}\langle\alpha|\hat{A}|\alpha\rangle \left(\sum_{\alpha>m} w_\alpha\right) \ . \tag{4.10}$$

4.2.2 Truncation Scheme

Let us make this argument more precise. Suppose we want to construct the best possible approximation $|\tilde{\psi}\rangle \approx |\psi\rangle$ of a super block state with only $m < \dim(\mathrm{S}) = \mathrm{M_S}$ system block states. The state $|\psi\rangle$ is typically the ground state or an excited state of the superblock Hilbert space which we will also refer to as our *target* state. Consider the linear combination of environment and system block states

$$|\bar{\psi}\rangle \ = \ \sum_{\alpha,j} a_{\alpha,j}|\alpha\rangle \otimes |j\rangle \ . \tag{4.11}$$

The states α are orthonormal, $\langle\alpha|\alpha'\rangle = \delta_{\alpha,\alpha'}$, and we vary both $|\alpha\rangle$ and the coefficients $a_{\alpha,j}$ to minimize

$$S \ = \ \big||\psi\rangle - |\bar{\psi}\rangle\big|^2 \ . \tag{4.12}$$

We rewrite (4.11) by defining environment states $a_\alpha|v^\alpha\rangle = \sum_j a_{\alpha,j}|j\rangle$ in the form

$$|\bar{\psi}\rangle \;=\; \sum_\alpha a_\alpha|\alpha\rangle \otimes |v^\alpha\rangle \;, \tag{4.13}$$

where the coefficients a_α are subject to the constraint that the environment states are normalized, $\langle v^\alpha|v^\alpha\rangle = 1$. The problem of minimizing S can now be reformulated in matrix notation

$$S \;=\; \left\|\psi - \bar{\psi}\right\|^2 \tag{4.14}$$

$$\;=\; \sum_{i,j}\left(\psi_{i,j} - \sum_\alpha a_\alpha \alpha_i v_j^\alpha\right)^2 \tag{4.15}$$

using the notation $\alpha_i = \langle i|\alpha\rangle$, $v_j^\alpha = \langle v^\alpha|j\rangle$ and $\|\cdot\|$ is the Frobenius norm.

The matrix representation ψ can be decomposed by a singular value decomposition

$$\psi = UDV^+ \;. \tag{4.16}$$

The dimension of ψ is dim(SB) $= N =$ dim(S) $\times$ dim(E) $\equiv \mathrm{M_S} \times \mathrm{M_E}$ which is the dimension of the superblock Hilbert space. The $(M_\mathrm{S} \times M_\mathrm{S})$ matrix U is orthogonal, $U^+U = UU^+ = \mathbb{I}$, and the $(M_\mathrm{E} \times M_\mathrm{S})$ matrix V is column-orthonormal, $V^+V = \mathbb{I}$. The $(M_\mathrm{S} \times M_\mathrm{S})$ matrix D is the diagonal matrix $D = \mathrm{diag}(\sigma_1, \ldots, \sigma_l)$ with the singular values σ_i of ψ on its diagonal. Using the product form (4.6) we see that U is the unitary transformation that diagonalizes the density matrix ($\rho = (\rho_{ii'})$)

$$U^+\rho U \;=\; U^+\psi\psi^+U \tag{4.17}$$

$$\;=\; U^+(UDV^+)(UDV^+)^+U \tag{4.18}$$

$$\;=\; U^+UDV^+VD^+U^+U \tag{4.19}$$

$$\;=\; \mathrm{diag}(\sigma_1^2, \ldots, \sigma_l^2) \tag{4.20}$$

where the diagonal elements $\sigma_\alpha^2 = w_\alpha$ are the density-matrix eigenvalues. Accordingly, we can minimize (4.15) if we choose $a_\alpha = \sqrt{w_\alpha}$ using the *largest* eigenvalues w_α of the density matrix and the α_i (v_j^α) with the corresponding entries in the columns of U (V).

We can treat a superblock in a mixed state along the same lines. Assume, for example, that the superblock is described by the mixture

$$|\psi\rangle \;=\; \sum_k W_k|\psi^k\rangle \;, \tag{4.21}$$

with states

$$|\psi^k\rangle = \sum_i \sum_j \psi_{ij}^k |i\rangle \otimes |j\rangle \;. \tag{4.22}$$

The probability that the superblock is in the state $|\psi^k\rangle$ is W_k. In case of finite temperatures the W_k correspond to the Boltzmann weights of low-lying excited states but can otherwise be chosen equal. The expression (4.15) translates into

$$S = \sum_k W_k \sum_{i,j} \left(\psi^k_{i,j} - \sum_\alpha a^k_\alpha \alpha_i v^{k,\alpha}_j \right)^2 . \tag{4.23}$$

Since we are interested in a single, optimal set of states $|\alpha\rangle$ to approximate the target state $|\psi\rangle$ we do not change the α_i for different k. The density matrix is

$$\rho_{ii'} = \sum_k W_k \sum_j \psi^k_{ij} (\psi_{ij})^+_{ji'} \tag{4.24}$$

and, as before, the optimal choice of states are the density-matrix eigenstates with the largest eigenvalues. Note, that equations (4.15) and (4.23) are *variational principles* for the wave function.

This is the prescription we sought for: We can neglect those density matrix eigenstates $|\alpha\rangle$ of the system block that have an eigenvalue w_α below some cutoff. In practice, the criterion is that one keeps a certain number m of density matrix eigenstates.

4.2.3 Accuracy of the Truncation

Clearly, the success of the method depends upon the eigenvalue spectrum of $\hat{\rho}$. If the sequence $\{w_i\} = w_1 \geq w_2 \geq w_3 \geq \dots$ does not decay quickly enough our renormalization will truncate relevant parts of the Hilbert space and the approximation (4.11) is bad even for large values of m.

A good measure of the error in the truncation is the *discarded weight* of eigenvalues

$$1 - P_m = 1 - \sum_{\alpha=1}^{m} w_\alpha . \tag{4.25}$$

If $1 - P_m = 0$ there is no truncation error and results are exact (within the numerical roundoff error).

Quite generally, in *gapped* one-dimensional quantum systems the eigenvalue spectrum decays exponentially. This observation has been confirmed, for instance, in the one-dimensional quantum Ising model in a transverse field [33] and numerically in many cases. The situation becomes less favorable in systems that have gapless modes, such as the Hubbard model, where the spin excitations are gapless, or critical systems. From numerical calculations it is known that the decay of the density matrix spectrum is less than exponential [31] and longer chains require a growing number of retained eigenstates that diverges with the system length L.

4.3 DMRG Algorithms

Thus far, we presented a truncation scheme that allows us to retain only those states of the system block Hilbert space that we need for a good approximation (4.11) of the desired target state. We can now formulate an algorithm [30] that enlarges the system size in real-space while keeping the maximal dimension of the superblock Hilbert space constant. In the following we assume, without loss of generality, that we are interested only in the ground state. For simplicity, we also assume that the Hamiltonian is reflection-symmetric and we have an even number of sites. The formulation of the algorithms closely follows [31].

4.3.1 Infinite-System Algorithm

The infinite-system algorithm proceeds as follows.

1) Form a superblock consisting of L sites which is small enough to be diagonalized exactly.

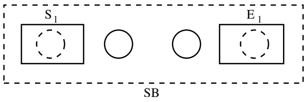

2) Find the ground state $|\psi_0\rangle$ (or more generally the target state(s)) and the ground state energy E_0 (or the eigenvalue of the excited state(s)) of the superblock Hamiltonian H_L^{SB}.

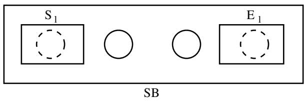

3) Using (4.5) form the reduced density matrix $\rho_{ii'}$ of the new system block S_{l+1}. We denote the new environment block by $\mathrm{E}_{l'+1}$, where $l = l' = L/2 - 1$.

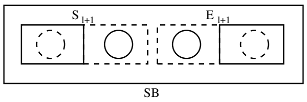

4) Diagonalize $\rho_{ii'}$ with a dense matrix diagonalization routine and obtain the first m eigenvalues $w_1, \dots, w_m$ and their corresponding eigenvectors $u_1, \dots, u_m$. Form the transformation-matrix of the truncation $O_L = (u_1, \dots, u_m)$.

5) Construct the Hamiltonian H_{l+1}^{S} and other operators A_{l+1} in the new system block and transform them to the (truncated) reduced density matrix eigenbasis via $\bar{H}_{l+1}^{\mathrm{S}} = O_L^+ H_{l+1}^{\mathrm{S}} O_L$ and $\bar{A}_{l+1} = O_L^+ A_{l+1} O_L$.

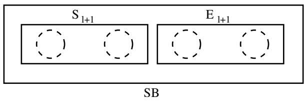

6) Form an enlarged superblock H^{SB}_{L+2} of size $L+2$ using $\bar{H}^{\mathrm{S}}_{l+1}$, two single sites, and the environment Hamiltonian $\bar{H}^{\mathrm{E}}_{l+1}$ which we obtain by reflecting $\bar{H}^{\mathrm{S}}_{l+1}$.

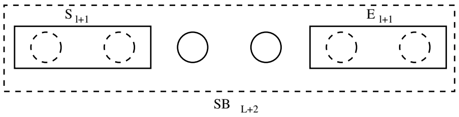

7) Start again at step 2) by replacing $L+2 \rightarrow L$.

The infinite-system algorithm provides an environment in which the system is embedded. However, the environment is not exact but approximate. This introduces a new kind of error, the environment error. The truncation of the Hilbert space is performed in step 5). When the new superblock is built from the renormalized system and environment Hamiltonians the dimension of the new superblock Hilbert space is

$$\dim(\mathrm{SB}) \quad = \quad m^2 M^2_{\mathrm{site}} \, . \tag{4.26}$$

Here, M_{site} is the dimension of the additional sites which, for instance, in the Hubbard model is $M_{\mathrm{site}} = 4$. Even though the system grows by two sites in every step of the algorithm, the dimension dim(SB) stays constant. Note that the most time consuming part in the algorithm is step 2) where the ground state and other target states of the superblock Hamiltonian are calculated.

4.3.2 Finite-System Algorithm

The accuracy of the infinite-system algorithm can be greatly improved. Once the infinite-system algorithm has achieved a desired system length L of the superblock we stop and choose the environment differently. If we have stored all the renormalized environment block Hamiltonians $\bar{H}^{\mathrm{E}}_{l}$ of the previous steps $l = 1, \ldots, L/2-2$ and the operators that connect the blocks, we can continue the renormalization scheme while keeping $L = l + l' + 2$ fixed. This is achieved by using the appropriate Hamiltonian $\bar{H}^{\mathrm{E}}_{l}$ at each step. The zipping procedure described below is shown in figure 4.2.

When we include this build-up step, the finite-size algorithm proceeds in the following way.

0) Use the infinite size algorithm to build up a superblock of size L while storing all $\bar{H}^{\mathrm{E}}_{l}$ and the operators that connect both blocks or any observables we wish to measure.

1) Perform steps 3) to 5) of the infinite-system algorithm to obtain $\bar{H}^{\mathrm{S}}_{l+1}$ as well as $\bar{A}_{l+1}$ and store them. Right and left blocks now have different sizes $l = l' - 1$.

2) Form a superblock of size L using $\bar{H}^{\mathrm{S}}_{l+1}$, two single sites and $\bar{H}^{\mathrm{E}}_{l'-1}$ stored in 0). The environment block has size $l' = L - l - 2$.

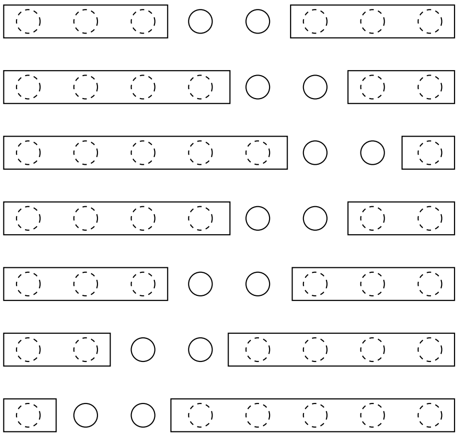

Figure 4.2: Left-right and right-left parts of the finite-system algorithm. The renormalization path reminds of a zipper.

3) Repeat steps 1) to 2) until the environment size reaches $l' = 1$. This is the left-right zipping phase of that enlarges the system block.

4) Reverse the roles of $\bar{H}^{\mathrm{E}}_{l'=1}$ and $\bar{H}^{\mathrm{S}}_{l=L-3}$ and zip backwards to build up the right block. Store $\bar{H}^{\mathrm{E}}_{l'+1}$ at each step.

5) Form a superblock of size L from $\bar{H}^{\mathrm{S}}_{l-1}$, two single sites, and $\bar{H}^{\mathrm{E}}_{l'+1}$.

6) Repeat 4) to 5) until the system block has length $l = 1$. This is the right-left phase.

7) Repeat starting at 1) and zip back and forth until convergence is reached.

At every step the superblock has the same dimension

$$\dim(\mathrm{SB}) \quad = \quad m^2 M^2_{\mathrm{site}} \,, \tag{4.27}$$

as in the infinite-system algorithm. Everytime the algorithm changes direction we update all stored blocks $\bar{H}^{\mathrm{S,E}}_{l}$ and begin to add two single sites with their M^2_{site} degrees of freedom at each step. In this way, the blocks are iteratively improved. In almost all applications, the finite-system algorithm is used because the infinite-system algorithm alone may result in poor, or worse, even wrong results.

In the following sections we briefly remark on details of the implementation of interacting systems and the use of symmetries to optimize performance.

4.4 Technical Aspects

In this section we briefly comment on some technical aspects of the implementation. This concerns optimizations through quantum numbers and wave function transformations.

We begin by commenting on the quantum mechanical expectation values and details for interacting systems.

4.4.1 Measurements

So far, we have not mentioned how to measure quantum mechanical observables. Any local observable $\hat{O}_l$ acting only on the site l can be directly evaluated once the superblock wavefunction $|\psi\rangle$ is known via

$$\begin{aligned}\langle\psi|\hat{O}|\psi\rangle &= \sum_{i,i',j,j'} \langle\psi|i\rangle\otimes|j\rangle\langle j|\otimes\langle i|\hat{O}_l|i'\rangle\otimes|j'\rangle\langle i'|\otimes\langle j'|\psi\rangle && (4.28)\\ &= \sum_{i,i',j} \psi^*_{ij}\,[O_l]_{ii'}\,\psi_{i'j}\ . && (4.29)\end{aligned}$$

Here, we have inserted the resolution of unity $\mathbb{I}=\sum_{ij}|i\rangle\otimes|j\rangle$ twice. Common examples are the local density $\hat{n}_{l,\sigma}$ or the z-component of the spin $\hat{S}^z_l$. Of course, we have to keep track of the matrices $[O_l]_{ii'}$ during the DMRG procedure.

Frequently, the operator is a product of two local operators $\hat{O}_{lm}=\hat{A}_l\hat{B}_m$. If l and m are on system and environment block, respectively, then, upon inserting the identity operator, we have

$$\langle\psi|\hat{O}_{lm}|\psi\rangle = \sum_{i,i',j,j'} \psi^*_{ij}\,[A_l]_{ii'}\,[B_m]_{jj'}\,\psi_{i'j'}\ , \tag{4.30}$$

and it suffices to keep $[A_l]_{ii'}$ and $[B_m]_{jj'}$ during the calculation. Assuming that $\hat{A}_l$ and $\hat{B}_m$ both act on the system block then we cannot simply use

$$\langle\psi|\hat{O}_{lm}|\psi\rangle \approx \sum_{i,i',i'',j'} \psi^*_{ij}\,[A_l]_{ii'}\,[B_m]_{i'i''}\,\psi_{i''j}\ . \tag{4.31}$$

While equation (4.30) evaluates the correlator exactly within the approximate superblock state $|\psi\rangle$ equation (4.31) does not. We have only inserted an approximate resolution of unity.

Instead, we should keep track of the composite matrices $[A_lB_m]_{ii'}$ throughout the calculation and then evaluate

$$\langle\psi|\hat{O}_{lm}|\psi\rangle = \sum_{i,i',j} \psi^*_{ij}\,[A_lB_m]_{ii'}\,\psi_{i'j}\ , \tag{4.32}$$

as we have done before in (4.29). Static correlation functions of this type frequently are density-density correlations, $\langle\psi|\hat{n}_l\hat{n}_m|\psi\rangle$, or spin-spin correlations, $\langle\psi|\hat{S}^z_l\hat{S}^z_m|\psi\rangle$.

4.4.2 Interacting Systems

In interacting systems there are operators that connect two subsystems. Examples are the kinetic energy in the Hubbard model

$$\hat{T} = -t\sum_{l,\sigma}\left(\hat{c}^+_{l,\sigma}\hat{c}_{l+1,\sigma}+\hat{c}^+_{l+1,\sigma}\hat{c}_{l,\sigma}\right) \tag{4.33}$$

or next-neighbor spin interactions

$$\sum_l \hat{\vec{\mathrm{S}}}_l \cdot \hat{\vec{\mathrm{S}}}_{l+1} = \hat{S}^z_l \hat{S}^z_{l+1} + \frac{1}{2}\left(\hat{S}^+_l \hat{S}^-_l + \hat{S}^-_l \hat{S}^+_l\right) \tag{4.34}$$

in the Heisenberg model. Joining two blocks is the most general situation and includes adding a single site to the system block. Let us denote the two blocks as B_1 and B_2 with Hamiltonians $\hat{H}_{B_1}$ and $\hat{H}_{B_2}$, respectively. The *rightmost* site of B_1 is l and the *leftmost* site of B_2 is $l' = l + 1$. For simplicity we consider a specific example, namely $\sum_l \hat{\vec{\mathrm{S}}}_l \cdot \hat{\vec{\mathrm{S}}}_{l+1}$, of an operator acting *between* two blocks. The basis set of the joined system $B_1 B_2$ is denoted with $\{|i\rangle \otimes |j\rangle\}$. The Hamiltonian of the joined system $\hat{H}_{B_1,B_2}$ in matrix notation is

$$\begin{aligned}
\left[H_{B_1,B_2}\right]_{ij;i'j'} &= \left[H_{B_1}\right]_{ii'} \delta_{jj'} + \left[H_{B_2}\right]_{jj'} \delta_{ii'} + \left[S^z_l\right]_{ii'} \left[S^z_{l+1}\right]_{jj'} \\
&+ \frac{1}{2}\left[S^+_l\right]_{ii'} \left[S^-_{l+1}\right]_{jj'} + \frac{1}{2}\left[S^-_l\right]_{ii'} \left[S^+_{l+1}\right]_{jj'} \; .
\end{aligned} \tag{4.35}$$

Using the identity operator $\mathbb{I}_{B_i}$ in the Hilbert space of B_i this can be written more concisely as

$$\begin{aligned}
\hat{H}_{B_1,B_2} &= \hat{H}_{B_1} \otimes \mathbb{I}_{B_2} + \mathbb{I}_{B_1} \otimes \hat{H}_{B_2} + \hat{S}^z_l \otimes \hat{S}^z_{l+1} \\
&+ \frac{1}{2}\hat{S}^+_l \otimes \hat{S}^-_{l+1} + \frac{1}{2}\hat{S}^-_l \otimes \hat{S}^+_{l+1} \; .
\end{aligned} \tag{4.36}$$

The blocks in the DMRG algorithm have to contain both the internal Hamiltonians and the operators connecting the blocks and have to be updated.

4.4.3 Wave Function Transformations

The most time intensive step in the algorithm is the sparse diagonalization of the superblock Hamiltonian. Typically, a Davidson algorithm is employed in this step. If the Davidson routine converges to a state other than the target state the derived density matrix is wrong and the complete sweep may be ruined. Usually, the starting vector of the routine is, without further input, a random state vector. Any better guess than a random vector will significantly reduce the number of Davidson iterations and stabilizes the convergence.

An excellent guess for the finite-size system algorithm at step i is the wave function of the previous step $(i - 1)$. Unfortunately, this state is in a different basis than the current state due to the different setup. The appropriate transformation that takes the initial guess to the current basis is described in detail in [31] and requires the storage of the transformation matrices at previous steps. With this wave function transformation a factor of 20-50 in speed can be achieved.

4.4.4 Quantum Numbers and Symmetries

The matrices which are stored and diagonalized in the DMRG algorithm are very large and require large amounts of memory. Implementing conserved quantum numbers is therefore imperative to optimize performance.

$U(1)$ Symmetries

The simplest case are the additive quantum numbers N and S_z. If the particle number operator or the operator of the total z-component of the spin commute with the Hamiltonian

$$[\hat{N}, \hat{H}] = 0 \ , \qquad [\hat{S}_z, \hat{H}] = 0 \ , \tag{4.37}$$

the matrix representations of both $\hat{\rho}$ and $\hat{H}$ are block-diagonal in the quantum numbers N and S_z. Since, in practice, we are interested in the lowest-lying state(s) of a specific sector (N, S_z) of the Hilbert space we can reduce the computational effort significantly through (4.37).

$SU(2)$ Symmetries

The spin and η-pairing $SU(2)$ symmetries introduced in sections 2.1.1 and 2.1.2 can also be implemented and lead to impressive gains in performance [34]. This is especially useful because one can directly target a state with a particular total spin S. An implementation of these symmetries is very involved and requires the calculation of Clebsch-Gordan coefficients and the use of the Wigner-Eckhart theorem.

Discrete Symmetries

Aside from the continuous abelian and non-abelian symmetries above, there are a number of discrete symmetries present in interacting lattice models. We can have *reflection* symmetry and, in more than one dimension, *rotational* symmetries. In the absence of full spin-rotational or η-pairing symmetry their respective subgroups, global *spin-flip* symmetry or *particle-hole* symmetry, may be present. All these symmetries commute with each other.

4.5 Conclusion

In this chapter we have presented the basic DMRG algorithm and the truncation scheme which it is based on. We have commented on the implementation and the optimizations for interacting systems as well as measurements of observables and the use of quantum numbers.

For the sake of brevity, however, we have left out many relevant topics. We refer to publications [31, 30, 32] and references therein. There, the reader can find valuable insight into why DMRG performs so well for one-dimensional quantum systems with open boundary conditions, but not in higher dimensions, for periodic boundary conditions, or for critical systems. Much of this insight has only evolved very recently through input from the field of quantum information theory employing concepts such as *matrix-product states* [35], *quantum entanglement* [36, 37], and *quantum information entropy* [38].

Part II

Dynamical Density-Matrix Renormalization Group (DDMRG)

Chapter 5

Introduction to DDMRG

Most scattering experiments probe dynamical correlation functions. This innocuous sentence bears a great deal of difficulty for theory because the calculation of dynamical correlation functions in strongly correlated electron systems is a *very* difficult task. Analytical results can be achieved only in trivial limits of the parameter space when either the details of the lattice (field theory) or significant parts of the Hilbert space (strong coupling) are neglected. In this chapter we introduce a very recent numerical method, the *dynamical density-matrix renormalization group* introduced by E. Jeckelmann [39, 40] which overcomes these limitations. First, we describe the DDMRG method. Next, we discuss how it can be extended to *momentum-dependent* quantities in periodic and in open-chain geometries. Finally, we test the method in both trivial and non-trivial cases for a set of representative correlation functions which are relevant for scattering experiments. Aside from verifying our numerical approach this chapter already contains numerical results relevant for Part III of this work.

5.1 DDMRG

In this section we introduce the dynamical density-matrix renormalization group method. We follow [39, 40] in the presentation and in notational details.

5.1.1 Dynamical Correlation Functions

The (zero-temperature) dynamic response of a quantum system to a time-dependent perturbation is given by a correlation functions of the form ($\omega \geq 0$)

$$G_{\hat{A}}\left(\omega + \mathrm{i}\eta\right) = -\frac{1}{\pi}\left\langle \psi_0 \left| \hat{A}^{+} \frac{1}{E_0 + \omega + \mathrm{i}\eta - \hat{H}} \hat{A} \right| \psi_0 \right\rangle \ . \tag{5.1}$$

Generally, we are interested in the positive-definite imaginary part of the correlation function

$$I_{\hat{A}}\left(\omega + \mathrm{i}\eta\right) = \Im\left[G_{\hat{A}}\left(\omega + \mathrm{i}\eta\right)\right] = \frac{1}{\pi}\left\langle \psi_0 \left| \hat{A}^{+} \frac{\eta}{(E_0 + \omega - \hat{H})^2 + \eta^2} \hat{A} \right| \psi_0 \right\rangle \geq 0 \ . \tag{5.2}$$

In the limit of vanishing η we have the spectral representation

$$
\begin{aligned}
I_{\hat{A}}(\omega) &= \lim_{\eta\to 0} I_{\hat{A}}(\omega + \mathrm{i}\eta) &(5.3)\\
&= \sum_n \left|\left\langle \psi_n \left| \hat{A} \right| \psi_0 \right\rangle\right|^2 \delta(\omega + E_0 - E_n) \ . &(5.4)
\end{aligned}
$$

The effect of the finite broadening η is a convolution of the spectrum in the thermodynamic limit $I_{\hat{A}}(\omega)$ with a Lorentzian distribution of width η,

$$
\begin{aligned}
I_{\hat{A}}(\omega + \mathrm{i}\eta) &= \int_{-\infty}^{\infty} \mathrm{d}\omega' I_{\hat{A}}(\omega) \frac{1}{\pi} \frac{\eta}{(\omega - \omega')^2 + \eta^2} &(5.5)\\
&= C_\eta \left[I_{\hat{A}}(\omega) \right] \ . &(5.6)
\end{aligned}
$$

The spectrum $I_{\hat{A}}(\omega)$ fulfills sum rules which are useful to check calculations in practical applications. For instance, the first three moments of the spectrum obey

$$
\begin{aligned}
\int_{-\infty}^{\infty} \mathrm{d}\omega I_{\hat{A}}(\omega) &= \left\langle \psi_0 \left| \hat{A}^+ \hat{A} \right| \psi_0 \right\rangle \ , &(5.7)\\
\int_{-\infty}^{\infty} \mathrm{d}\omega I_{\hat{A}}(\omega)\,\omega &= \left\langle \psi_0 \left| \hat{A}^+ \left[\hat{H}, \hat{A} \right]_- \right| \psi_0 \right\rangle \ , &(5.8)\\
\int_{-\infty}^{\infty} \mathrm{d}\omega' I_{\hat{A}}(\omega)\,\omega^2 &= \left\langle \psi_0 \left| \left[\hat{A}^+, \hat{H} \right]_- \left[\hat{H}, \hat{A} \right]_- \right| \psi_0 \right\rangle \ , &(5.9)
\end{aligned}
$$

where $\left[\hat{C}, \hat{D}\right]_- = \hat{C}\hat{D} - \hat{D}\hat{C}$. The first sum rule holds also for the broadened spectrum with $\eta > 0$, whereas the other sum rules are exact only in the limit $\eta \to 0$.

5.1.2 Variational Principle for Dynamical Correlation Functions

The dynamical correlation function (5.1) can be calculated directly once the *correction vector* [41, 42]

$$
\left|\psi_{\hat{A}}(\omega + \mathrm{i}\eta)\right\rangle = \frac{1}{E_0 + \omega + \mathrm{i}\eta - \hat{H}} \hat{A} \left|\psi_0\right\rangle \tag{5.10}
$$

is known because, obviously,

$$
G_{\hat{A}}(\omega + \mathrm{i}\eta) = -\frac{1}{\pi} \left\langle A | \psi_{\hat{A}}(\omega + \mathrm{i}\eta) \right\rangle \ , \tag{5.11}
$$

with $|A\rangle = \hat{A}\left|\psi_0\right\rangle$. The correction vector can be split up into imaginary and real part,

$$
\left|\psi_{\hat{A}}(\omega + \mathrm{i}\eta)\right\rangle = \left|X_{\hat{A}}(\omega + \mathrm{i}\eta)\right\rangle + \mathrm{i}\left|Y_{\hat{A}}(\omega + \mathrm{i}\eta)\right\rangle \ , \tag{5.12}
$$

which are related to each other through

$$
\left|X_{\hat{A}}(\omega + \mathrm{i}\eta)\right\rangle = \frac{\hat{H} - E_0 - \omega}{\eta} \left|Y_{\hat{A}}(\omega + \mathrm{i}\eta)\right\rangle \ . \tag{5.13}
$$

Then, the problem of calculating $G_{\hat{A}}(\omega + \mathrm{i}\eta)$ can be cast into an inhomogeneous linear equation

$$\left[(E_0 + \omega - \hat{H})^2 + \eta^2\right] |\psi\rangle = -\eta\, |A\rangle \ , \tag{5.14}$$

whose unique solution for $\eta > 0$ is the imaginary part $\left|Y_{\hat{A}}(\omega + \mathrm{i}\eta)\right\rangle$ of the correction vector. Real and imaginary parts of $G_{\hat{A}}(\omega + \mathrm{i}\eta)$ are thus given through

$$\Re\big[G_{\hat{A}}(\omega + \mathrm{i}\eta)\big] = -\frac{1}{\pi} \left\langle A|X_{\hat{A}}(\omega + \mathrm{i}\eta)\right\rangle \ , \tag{5.15}$$

$$\Im\big[G_{\hat{A}}(\omega + \mathrm{i}\eta)\big] = -\frac{1}{\pi} \left\langle A|Y_{\hat{A}}(\omega + \mathrm{i}\eta)\right\rangle \ . \tag{5.16}$$

The linear equation (5.14) can be solved directly with standard iterative techniques. Such an algorithm yields an approximate solution

$$|\psi\rangle = \left|Y_{\hat{A}}(\omega + \mathrm{i}\eta)\right\rangle + \epsilon\, |\phi\rangle \ , \tag{5.17}$$

with normalized $\langle\phi|\phi\rangle = 1$ where $\epsilon \ll 1$ quantifies the numerical error. According to (5.16), the error in the spectrum $I_{\hat{A}}(\omega + \mathrm{i}\eta)$ is proportional to the error ϵ. If we can find a *variational* procedure to determine $I_{\hat{A}}(\omega + \mathrm{i}\eta)$ the error is much smaller, namely, of the order of ϵ^2. This can be achieved by recasting the linear problem (5.14) into a minimization problem [39]. To see this, consider the functional

$$W_{\hat{A},\eta}(\omega, |\psi\rangle) = \left\langle\psi\left|(E_0 + \omega - \hat{H})^2 + \eta^2\right|\psi\right\rangle + \eta\,\langle A|\psi\rangle + \eta\,\langle\psi|A\rangle \tag{5.18}$$

which depends on both the state $|\psi\rangle$ and on the frequency ω for a given operator $\hat{A}$ and finite $\eta > 0$. For any fixed frequency ω, this functional has a well-defined and non-degenerate solution $|\psi_{\min}\rangle$ which solves the linear equation (5.14). The minimum of $W_{\hat{A},\eta}(\omega, |\psi\rangle)$ at $|\psi_{\min}\rangle$ can be directly related to the desired spectrum through

$$W_{\hat{A},\eta}(\omega, |\psi_{\min}\rangle) = -\pi\eta I_{\hat{A}}(\omega + \mathrm{i}\eta) \ . \tag{5.19}$$

Thus, the error on $I_{\hat{A}}(\omega + \mathrm{i}\eta)$ is now proportional to ϵ^2 because we have employed a *variational* method.

5.1.3 DDMRG Algorithm

We can now formulate a *dynamical* DMRG algorithm [39] for the spectrum $I_{\hat{A}}(\omega + \mathrm{i}\eta)$. The algorithm combines both the finite-system DMRG algorithm described in section 4.3.2 and the variational principle (5.19).

1) Find the ground-state vector $|\psi_0\rangle$ and the ground-state energy E_0 in the superblock subspace.

2) Calculate the state $|A\rangle$ by applying the operator $\hat{A}$ to the ground state.

3) Minimize the functional $W_{\hat{A},\eta}(\omega, |\psi\rangle)$ with an iterative minimization method, i.e., a conjugate-gradient method. This yields the imaginary part $\big|Y_{\hat{A}}(\omega + \mathrm{i}\eta)\big\rangle$ of the correction vector and the spectrum $I_{\hat{A}}(\omega + \mathrm{i}\eta)$.

4) Calculate the real part of the correction vector $\big|X_{\hat{A}}(\omega + \mathrm{i}\eta)\big\rangle$ via equation (5.13). Obtain the real part of the dynamical correlation function through (5.15).

5) Include the four states $|\psi_0\rangle$, $|A\rangle$, $\big|Y_{\hat{A}}(\omega + \mathrm{i}\eta)\big\rangle$, $\big|X_{\hat{A}}(\omega + \mathrm{i}\eta)\big\rangle$ as targets in the reduced density-matrix to build a new superblock.

6) Continue with step 1) until both the ground-state energy and the functional $W_{\hat{A},\eta}(\omega, |\psi\rangle)$ have converged to their respective minima.

5.1.4 Finite Frequency Intervals

Since DMRG is a method that works in a subspace of the total Hilbert space, it can be considered as a variational procedure. Therefore, the algorithm described above simultaneously minimizes the energy functional $E(|\psi\rangle) = \langle\psi|\hat{H}|\psi\rangle/\langle\psi|\psi\rangle$ and the functional $W_{\hat{A},\eta}(\omega, |\psi\rangle)$. This minimization has to be repeated for *every* frequency ω we are interested in. The optimized basis we determine in step 1) of the algorithm is optimized for a *particular* frequency since we include the ω-dependent states $\big|Y_{\hat{A}}(\omega + \mathrm{i}\eta)\big\rangle$ and $\big|X_{\hat{A}}(\omega + \mathrm{i}\eta)\big\rangle$ as targets. The effective DMRG Hamiltonian represents only a particular energy scale close to ω. However, if we target two frequencies ω_1 and ω_2 that are close to each other we may calculate intermediate frequencies $\omega_1 < \omega < \omega_2$ without including the corresponding $\big|Y_{\hat{A}}(\omega + \mathrm{i}\eta)\big\rangle$ and $\big|X_{\hat{A}}(\omega + \mathrm{i}\eta)\big\rangle$ as target states in step 6). With this method the computational time to obtain the full spectrum over a finite frequency interval can be significantly reduced.

Alternatively, we can use the derivatives of the real and imaginary parts of the dynamical correlation function to speed up calculations on finite frequency intervals. It is easy to check that we have first derivatives

$$\begin{aligned}
\frac{\mathrm{d}}{\mathrm{d}\omega}\Re\big[G_{\hat{A}}(\omega + \mathrm{i}\eta)\big] &= \frac{1}{\pi}\Big[\big\langle X_{\hat{A}}(\omega + \mathrm{i}\eta)|X_{\hat{A}}(\omega + \mathrm{i}\eta)\big\rangle \\
&\quad - \big\langle Y_{\hat{A}}(\omega + \mathrm{i}\eta)|Y_{\hat{A}}(\omega + \mathrm{i}\eta)\big\rangle\Big] , \qquad (5.20) \\
\frac{\mathrm{d}}{\mathrm{d}\omega}\Im\big[G_{\hat{A}}(\omega + \mathrm{i}\eta)\big] &= \frac{2}{\pi}\big\langle X_{\hat{A}}(\omega + \mathrm{i}\eta)|Y_{\hat{A}}(\omega + \mathrm{i}\eta)\big\rangle . \qquad (5.21)
\end{aligned}$$

The calculation of these derivatives can be included after step 4) of the DDMRG algorithm. Once the derivatives are known, we can use them to interpolate between frequencies ω_1, ω_2 that we have included as targets in step 6).

As soon as we have determined the complete spectrum $I_{\hat{A}}(\omega + \mathrm{i}\eta)$, we can use the sum rules (5.7)-(5.9) for the spectral moments as a consistency check.

5.1.5 Matrix Elements

From the spectral representation of the dynamical correlation function (5.4)

$$I_{\hat{A}}(\omega) = \sum_n \left|\left\langle \psi_n \left| \hat{A} \right| \psi_0 \right\rangle\right|^2 \delta(\omega + E_0 - E_n) \tag{5.22}$$

we see that only those eigenstates $|\psi_n\rangle$ contribute to the spectrum with matrix elements $\left|\left\langle \psi_n \left| \hat{A} \right| \psi_0 \right\rangle\right| \neq 0$. We can determine the non-zero spectral weights $\left|\left\langle \psi_n \left| \hat{A} \right| \psi_0 \right\rangle\right|^2$ and the corresponding excitation energies $E_n - E_0$ by directly minimizing $W_{\hat{A},\eta}(\omega, |\psi\rangle)$ with respect to ω *and* $|\psi\rangle$. In the limit of vanishing $\eta \to 0$ this minimization yields

$$\omega_{\mathrm{min}} \to E_n , \tag{5.23}$$

$$|\psi_n\rangle \to |\psi_{\mathrm{min}}\rangle , \tag{5.24}$$

$$-W_{\hat{A},\eta}(\omega_{\mathrm{min}}, |\psi_{\mathrm{min}}\rangle) \to \left|\left\langle \psi_n \left| \hat{A} \right| \psi_0 \right\rangle\right|^2 . \tag{5.25}$$

Frequently, we are only interested in the excitation energy E_n of the first excited state $|\psi_n\rangle$ that yields a non-vanishing contribution to the spectrum. We can thus determine the onset

$$\omega_{\mathrm{onset}} = E_n - E_0 \tag{5.26}$$

of $I_{\hat{A}}(\omega + \mathrm{i}\eta)$ very precisely. In a finite system the excitation energies are not distributed densely. We assume that the smallest energy separation between states with non-vanishing spectral weight is $\Delta E > 0$. If we choose the broadening $\eta < \Delta E/2$ we can resolve the single excitation peaks. Upon reducing η we can obtain a very good estimate of ω_{onset} for a given system length L.

5.1.6 Finite-Size Scaling

The dynamical DMRG procedure outlined above requires a finite broadening η. Otherwise, the linear equation (5.14) becomes an ill-defined problem. The resulting spectra have the general form

$$I_{L,\eta}(\omega) = \frac{1}{\pi} \sum_n A_n(L) \frac{\eta}{[\omega_n(L) - \omega]^2 + \eta^2} , \tag{5.27}$$

where we have included the system size L in the notation and $A_n(L)$, $\omega_n(L)$ are the size dependent spectral weights and frequencies, respectively. If we let $\eta \to 0$ for a finite lattice size L the spectrum $I_{L,\eta}(\omega)$ will consist of single δ-peaks with weights $A_n(L)$ because there are only a finite number of eigenstates in a finite system. Accordingly, we have to perform the thermodynamic limit such that we first let $L \to \infty$ before we take the limit $\eta \to 0$. Explicitely,

$$I(\omega) = \lim_{\eta \to 0} \lim_{L \to \infty} I_{L,\eta}(\omega) , \tag{5.28}$$

where we have dropped the dependence on the operator $\hat{A}$ for simplicity. The spectrum $I(\omega)$ may contain discrete and continuous parts in the thermodynamic limit. In principle, we have to perform a finite-size-scaling analysis for every point ω of the spectrum according to (5.28). Of course this is computationally prohibitive.

In practice, this does not pose a severe problem if we perform both limits simultaneously with an appropriately chosen, size-dependent broadening $\eta = \eta(L)$. Consider the number of excited states $M_\epsilon(\omega, L)$ in a small interval $(\omega-\epsilon, \omega+\epsilon)$ that contribute spectral weight. If for any given $\epsilon > 0$ the number of excited states $M_\epsilon(\omega, L)$ remains finite in the limit $L \to \infty$, then the spectrum is discrete at ω. In this case, we may take the $\eta \to 0$ limit first in equation (5.28). On the other hand, if we have $\lim_{L\to\infty} M_\epsilon(\omega, L) = \infty$ for any $\epsilon > 0$ then the spectrum is dense at ω and the order of the limits in (5.28) cannot be inter-changed. We can, however, choose a broadening $\eta(L)$ that does not violate (5.28) and such that $\lim_{L\to\infty} \eta(L) = 0$. Let us assume that the maximal distance between consecutive states in the spectrum is $\Delta\omega(L) = \max_n[\omega_{n+1}(L) - \omega_n(L)]$. If we choose $\eta(L) \gg \Delta\omega(L)$ sufficiently large for all L then we can let $\eta(L)$ approach zero as the system length approaches infinity, compatible with (5.28).

Numerically, we find in all cases that

$$\eta(L) = C/L \tag{5.29}$$

with a constant $C = \mathcal{O}(W)$ is sufficient. This type of scaling is especially useful since we can extract the exponents that govern power-law divergences in both dense and non-dense parts of the spectrum. We discuss two common examples. For a more detailed discussion see [39].

(i) Consider a spectrum of the form

$$I(\omega) = W_0 \delta(\omega - \omega_0) + f(\omega) \tag{5.30}$$

in the thermodynamic limit with a continuous function $f(\omega)$ and $W_0 > 0$. The finite-system spectrum $I(\omega + \mathrm{i}\eta(L))$ has a maximum $I_{\max}(\eta(L))$ in the vicinity of ω_0. For $\eta(L)$ sufficiently small one expects a divergence

$$I_{\max}(\eta(L)) \sim \eta(L)^{-1} , \qquad \eta(L) \to 0 . \tag{5.31}$$

This relation will prove useful to identify excitonic bound states in the optical conductivity and in the dynamic charge structure factor.

(ii) Another typical situation is a power-law divergence at a band edge

$$I(\omega) = W_0 \theta(\omega - \omega_0) |\omega - \omega_0|^{-\alpha} , \tag{5.32}$$

with the step function $\theta(x \geq 0) = 1$ and an exponent $\alpha > 0$. The spectral maximum for this situation diverges as

$$I_{\max}(\eta(L)) \sim \eta(L)^{-\alpha} , \qquad \eta(L) \to 0 . \tag{5.33}$$

We will make use of this relation to determine power-law exponents at the onsets of the one-particle spectral function.

5.1.7 Deconvolution

An entirely different strategy to reach the thermodynamic limit is the *deconvolution* of the Lorentz-broadened spectra $I(\omega + \mathrm{i}\eta) = C_\eta\,[I(\omega)]$. We will only discuss the most trivial example, a direct linear deconvolution, and refer the reader to [43, 44] for more sophisticated, non-linear approaches.

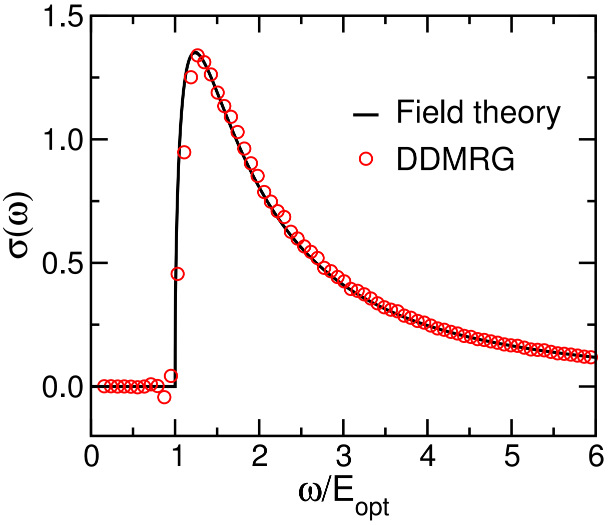

Figure 5.1: Deconvolved optical conductivity, $\sigma_1(\omega)$, of the Hubbard model compared to analytical field theory result [39] at $U/t = 3$ in units of the Mott-gap E_{opt}. The resolution $\eta/t = 0.1$ is significantly smaller than the width of the square-root onset, hence the good deconvolution [45].

The DDMRG method determines $I(\omega + \mathrm{i}\eta)$ for a finite number N of frequencies ω_j which we assume equidistant $\omega_{j+1} - \omega_j = \Delta\omega$ for simplicity. The discretized version of (5.5) sampled at N frequencies ω_i is

$$I_\eta(\omega_i) \;=\; \sum_{j=1}^{N} L_\eta(\omega_i - \omega_j) I(\omega_j)\;, \tag{5.34}$$

$$L_\eta(\omega_i - \omega_j) \;=\; \frac{1}{\pi}\frac{\eta}{(\omega_i - \omega_j)^2 + \eta^2}\Delta\omega \tag{5.35}$$

where the exact spectrum in the thermodynamic limit appears on the right hand side of the equation. Switching to matrix notation, we have the inverse problem

$$\vec{I} = \mathbf{L}^{-1}\vec{I}_\eta \tag{5.36}$$

which yields the deconvolved spectrum. In general, this problem is ill-defined because the exact spectrum may contain structures with spectral width less than the resolution η. If this is the case, a direct inversion will yield artifacts in the deconvolution, and worse, may result in the non-negativity of the deconvolved data in violation of (5.2). For spectra that contain only structures with spectral width larger than η the deconvolution (5.36) works surprisingly well. In these cases the spectrum in the thermodynamic limit can be very well approximated without finite-size-scaling in quite small systems ($L \approx 32$) and low resolution ($\eta \approx 0.4t$).

To make our point more tangible, figure 5.1 shows a deconvolution of the optical conductivity $\sigma_1(\omega)$ (cf. chapter 8) in the Hubbard model together with the analytical prediction from field theory [39]. The infinite-system spectrum features a broad square-root onset which can be easily deconvolved.

5.2 Momentum-Dependent Quantities

The DMRG method is usually implemented in real space where it performs excellently for lattice Hamiltonians with predominantly short-ranged interactions (see [46, 47] for realizations of momentum space DMRG). When the lattice is defined such that periodic boundary conditions are fulfilled the relevant operators can be readily expanded in plane waves to obtain frequency- and momentum-dependent correlation functions. If, however, the chain has open boundary conditions momentum is no longer a good quantum number. We suggest that a suitable definition of a pseudo-momentum allows for the expansion of operators in open chains as well.

5.2.1 Periodic Boundary Conditions

In translationally invariant systems the momentum is a conserved quantity. We may therefore expand any position dependent operator $\hat{A}_l$ in terms of plane waves

$$\hat{A}_k = \frac{1}{\sqrt{L}} \sum_l e^{\mathrm{i}kl} \hat{A}_l = \hat{A}_k^c + \mathrm{i}\hat{A}_k^s \, , \tag{5.37}$$

$$k = Z\frac{2\pi}{L} \, , \qquad Z = -\frac{L}{2}+1, \ldots, -\frac{L}{2} \, . \tag{5.38}$$

The set of plane waves $\exp(\mathrm{i}kl)/\sqrt{L}$ are the free-particle solutions on an L-site ring. A momentum and frequency dependent dynamical correlation function can thus be calculated directly with DDMRG when we generalize the variational approach such as to include momentum dependent operators $\hat{A}_k$ via

$$G_{\hat{A}_k}(\omega + \mathrm{i}\eta) = -\frac{1}{\pi} \left\langle \psi_0 \left| \hat{A}_k^+ \frac{1}{E_0 + \omega + \mathrm{i}\eta - \hat{H}} \hat{A}_k \right| \psi_0 \right\rangle \, . \tag{5.39}$$

The spectrum $I_{\hat{A}_k}(k, \omega + \mathrm{i}\eta)$ is then defined as before

$$I_{\hat{A}_k}(k, \omega + \mathrm{i}\eta) = \Im\left[G_{\hat{A}_k}(\omega + \mathrm{i}\eta)\right] = \frac{1}{\pi} \left\langle \psi_0 \left| \hat{A}_k^+ \frac{\eta}{(E_0 + \omega - \hat{H})^2 + \eta^2} \hat{A}_k \right| \psi_0 \right\rangle \, . \tag{5.40}$$

The DDMRG algorithm remains otherwise unchanged, except that we repeat the algorithm for all L momenta k.

In order to avoid the use of complex numbers and to simplify the calculation we write

$$G_{\hat{A}_k}\left(\omega+\mathrm{i}\eta\right) = -\frac{1}{\pi}\left\langle \psi_0 \left| \left(\hat{A}_k^{c+} - \mathrm{i}\hat{A}_k^{s+}\right) \frac{1}{E_0+\omega+i\eta-\hat{H}} \left(\hat{A}_k^{c} + \mathrm{i}\hat{A}_k^{s}\right) \right| \psi_0 \right\rangle . \tag{5.41}$$

For real Hamiltonians and real local operators $\hat{A}_l$ the imaginary part of the correlation function reduces to

$$\begin{aligned} I_{\hat{A}_k}\left(k,\omega+\mathrm{i}\eta\right) &= -\frac{1}{\pi}\Im\left\langle \psi_0 \left| \hat{A}_k^{c+} \frac{1}{E_0+\omega+i\eta-\hat{H}} \hat{A}_k^{c} \right| \psi_0 \right\rangle \\ &\quad -\frac{1}{\pi}\Im\left\langle \psi_0 \left| \hat{A}_k^{s+} \frac{1}{E_0+\omega+i\eta-\hat{H}} \hat{A}_k^{s} \right| \psi_0 \right\rangle \qquad (5.42) \\ &= I_c(k,\omega) + I_s(k,\omega) \, . \qquad (5.43) \end{aligned}$$

For a non-degenerate ground state the momentum is $k = 0, \pi$ and the spectrum simplifies further to

$$I_{\hat{A}_k}\left(k,\omega+\mathrm{i}\eta\right) = \begin{cases} 2I_c(k,\omega) & : \quad 0 < |k| < \pi \\ I_c(k,\omega) & : \quad k = 0 \\ I_s(k,\omega) & : \quad k = \pi \end{cases} \tag{5.44}$$

The spectra $I_{c,s}(k,\omega)$ can be directly included in the DDMRG algorithm and no changes other than the expansion (5.38) of local operators are required.

5.2.2 Open Boundary Conditions

In a chain with open boundaries the above approach cannot be used since plane waves are no longer the eigenstates of the free-particle problem. Instead, we suggest to use the eigenstates of a free particle in a box of length L. The *particle-in-a-box* solutions are

$$\begin{aligned} \psi_q &= \sqrt{\frac{2}{L+1}}\sin(ql) \, , \qquad (5.45) \\ q &= Z\frac{\pi}{L+1} \, , \qquad Z = 1, \ldots, L \, . \qquad (5.46) \end{aligned}$$

The numbers q enumerate the solutions ψ_q according to their eigenenergies, analogously to the plane-wave quantum numbers k for the free-particle on a ring. We therefore interpret q as a *pseudo-momentum* in systems with open boundaries. Accordingly, we expand position dependent operators $\hat{A}_l$ using

$$\hat{\hat{A}}_q = \sqrt{\frac{2}{L+1}}\sum_l \sin(ql)\hat{A}_l \, , \tag{5.47}$$

and, analogously, define the dynamical correlation function as

$$\tilde{G}_{\hat{\hat{A}}_k}\left(\omega+\mathrm{i}\eta\right) = -\frac{1}{\pi}\left\langle \psi_0 \left| \hat{\hat{A}}_k^{+} \frac{1}{E_0+\omega+\mathrm{i}\eta-\hat{H}} \hat{\hat{A}}_k \right| \psi_0 \right\rangle . \tag{5.48}$$

As we let the size of the system approach infinity, we expect that the dynamical correlation functions (5.39) and (5.48) should become equivalent

$$\lim_{L\to\infty} \tilde{G}_{\hat{\tilde{A}}_q}(\omega + \mathrm{i}\eta) = \lim_{L\to\infty} G_{\hat{A}_k}(\omega + \mathrm{i}\eta) \ . \tag{5.49}$$

In the following chapter we will provide ample evidence that this procedure gives accurate results even for moderately sized systems, i.e., $L = 32$.

A few remarks are in order. A different approach was put forward in [48] where open boundaries are treated by applying filter functions to the local operators $\hat{A}_l$ and then expanding with plane waves (5.37). We have tested this method using Parzen filters as suggested in [48] as well as other filter functions. None yield satisfactory results when compared to the expansion (5.47). Apparently, the application of filter functions is not well suited for the calculation of momentum-dependent quantities in open chains.

A priori, one expects that the expansion (5.47) with *particle-in-a-box* eigenfunctions should work well away from the long-wavelength limit ($\lambda \ll L$) or equivalently in the limit of large momenta ($q \gg 2\pi/(L+1)$) since then physical properties should be less affected by the presence of the boundaries. It turns out, however, that the approach (5.47) works well in the *entire* Brillouin zone. This is documented in the following chapters.

Chapter 6

Tests

This chapter presents tests of the DDMRG method for momentum and frequency dependent dynamical correlation functions. The first section is devoted to one-particle dynamics, namely the one-particle spectral function, the local density of states and the momentum distribution. In the second section, we show tests for the dynamical charge structure factor. Finally, in the third section, we present tests for the dynamical spin structure factor. These correlation functions describe very different experimental scattering probes, such as (angle-resolved) photoemission spectroscopy ((AR)PES), tunneling spectroscopy, electron-electron loss spectroscopy (EELS), (resonant) inelastic X-ray scattering ((R)IXS), and neutron scattering, among others.

6.1 One-Particle Dynamics

In this section we present tests for the one-particle spectral function in moderately sized systems. We pay special attention to sum rules to validate our results. In particular, we calculate the momentum distribution of small Hubbard rings and compare with results independently obtained through momentum space DMRG (k-DMRG) [49]. In addition, we calculate the local density of states in periodic and open systems to further test our method.

6.1.1 One-Particle Spectral Function

The photoemission spectral function $A(k,\omega)$ is defined through the imaginary part of the one-particle Green function

$$\begin{aligned} A(k,\omega) &= \lim_{\eta\to 0}\frac{1}{\pi}\Im\langle\psi_0|\hat{c}^{+}_{k,\sigma}\frac{1}{\hat{H}+\omega-E_0-\mathrm{i}\eta}\hat{c}_{k,\sigma}|\psi_0\rangle & (6.1)\\ &= \sum_n \left|\langle\psi_n\left|\hat{c}_{k,\sigma}\right|\psi_0\rangle\right|^2\delta\left(\omega+E_0-E_n\right) & (6.2)\end{aligned}$$

where $|\psi_0\rangle$ and E_0 are the ground-state wavefunction and energy, $|\psi_n\rangle$ are excited states and the operators $\hat{c}^{+}_{k,\sigma}$ ($\hat{c}_{k,\sigma}$) create (annihilate) a particle with spin σ and momentum k.

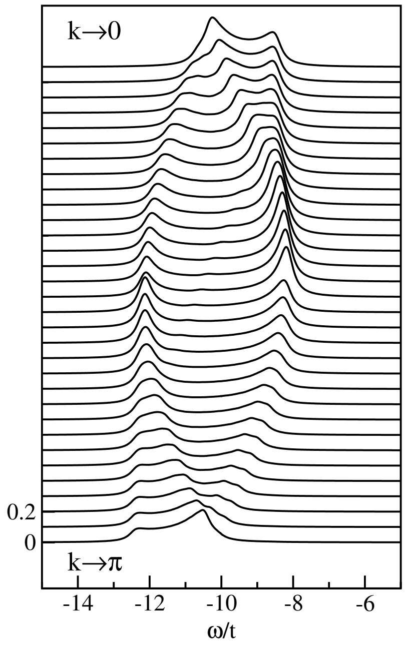

Figure 6.1: Line-shapes of the one-particle spectral function of the half-filled Hubbard model with on-site interaction $U/t = 20$. We can distinctly observe the dispersive branches attributed to separate spin and charge degrees of freedom.

In our calculations we use a finite broadening $\eta > 0$ and, accordingly, the resulting spectra are convolved with a Lorentz-distribution as discussed in section 5.1. Figure 6.1 shows the results of a DDMRG calculation of $A(k, \omega)$ in a 32-site open Hubbard chain at half filling and an on-site repulsion of $U/t = 20$. The Fermi momentum is $k_{\mathrm{F}} = \pi/2$ in the half-filled band and we we use the particle-hole symmetric form (2.6) of the Hubbard Hamiltonian. The broadening $\eta/t = 0.2$ is chosen such as to conceal the finite-size effects (cf. section 5.1.6).

We can clearly distinguish two separately dispersing peaks at lower binding-energies in the momentum interval $k \in (0, \pi/2)$ that merge at $k_{\mathrm{F}} = \pi/2$. Similarly, we have two dispersive peaks at high binding-energies in the interval $k \in (\pi/2, \pi)$ that separate as they approach the zone boundary. In addition, we see a dispersive branch commonly referred to as "shadow band" in the literature. The dispersive structures can be visualized more clearly in a pseudo-color density plot shown in figure 6.2.

How well does the dispersion of these excitation branches fit the exact result from the Bethe-Ansatz? To this end we have extracted the position of the peaks in the DDMRG spectrum and calculated the exact dispersion of holon and spinon branches with the discrete Bethe-Ansatz equations (3.31) and (3.32). The comparison is shown in figure 6.3. Since the Bethe-Ansatz equations describe a system with periodic boundaries we can directly quantify the effect of open boundary conditions.

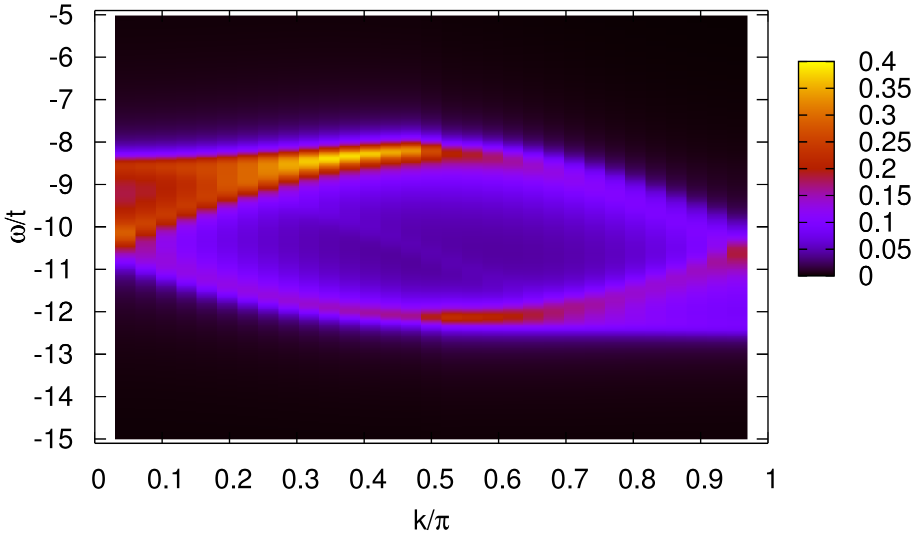

Figure 6.2: Density plot of the one-particle spectral function of the half-filled Hubbard model with on-site interaction $U/t = 20$. Despite the small system size of $L = 32$ and a broadening $\eta/t = 0.2$, spin-charge separation is clearly visible.

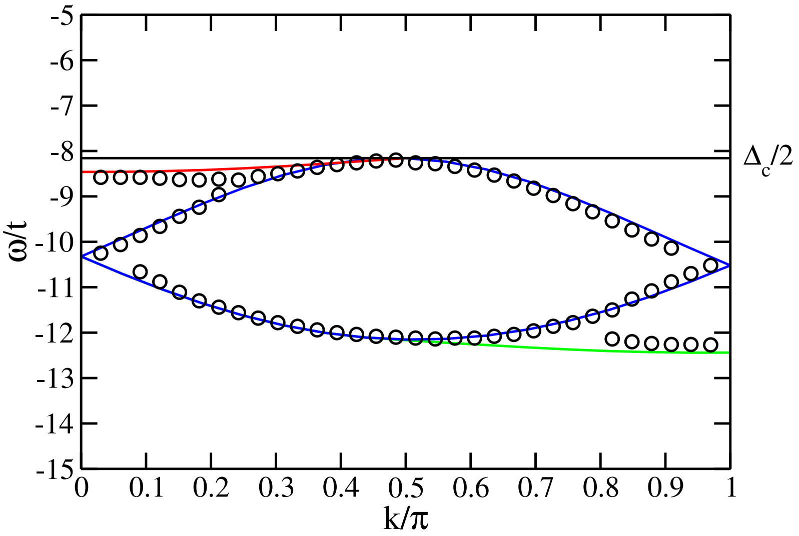

Figure 6.3: Comparison of the exact Bethe-Ansatz dispersion $\omega(k)$ (full lines) and the DDMRG dispersion $\epsilon(k)$ (open symbols) in $A(k,\omega)$ for $U/t = 20$ and $L = 32$. The agreement is excellent despite the small system size and the open boundaries used in the DDMRG calculation. Deviations are at most of the order η in the entire Brillouin zone. The red line is the spinon dispersion, the blue lines correspond to holon branches and the green line is the lower onset of the spinon-holon excitation continuum.

The overall agreement of the peak positions is excellent and the error is at worst of the order of η. This is a very notable result considering the small system size $L = 32$. We can clearly identify the nature of the excitations as spinon (red line) and holon excitation branches (blue lines) and the lower onset of the holon-spinon excitation continuum (green line). The spinon dispersion is quite flat as expected in the limit of large on-site repulsion U since the spinon band width is proportional to the exchange coupling $J = 4t^2/U$. Furthermore, the upper onset of the peaks of $A(k, \omega)$ in figure 6.3 is fully compatible with the value of the charge gap $\Delta_c/2 = 8.157t$ indicated as black line.

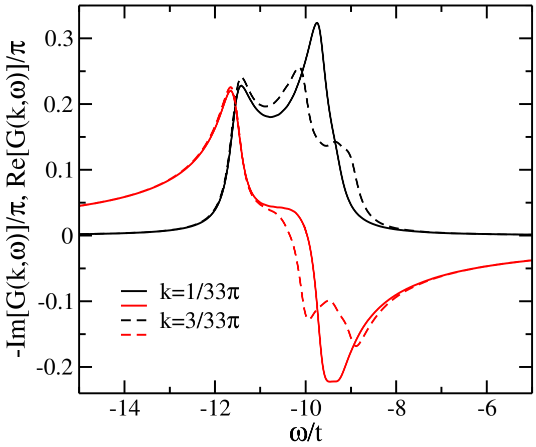

Figure 6.4: Real and imaginary parts of $G(k, \omega)$ for $U/t = 20$, $L = 32$ and $\eta/t = 0.2$.

We can also calculate the real part of dynamical correlation functions. The real part, however, contains no new information about the system, since real- and imaginary parts are related through a Kramers-Kronig transformation. An example is shown in figure 6.4 where we have plotted real and imaginary parts of $G(k, \omega)$ for two momenta close to $q = 0$. In the remaining part of this work we only present results for the imaginary parts of dynamical correlation functions since these can be directly interpreted physically.

In summary, the results for $A(k, \omega)$ fully confirm our use of pseudo-momenta (5.46) and the expansion (5.48). Since there are no analytical expressions for the complete line-shape of $A(k, \omega)$ of the Hubbard model we cannot present a direct comparison. We can, however, make use of well known sum-rules. This is discussed in the following two subsections.

6.1.2 Momentum Distribution

A direct comparison with an independent method is possible by considering the frequency integrated spectral function, namely, the momentum distribution.

$$n(k) = 2\int_{-\infty}^{\infty} A(k,\omega)\mathrm{d}\omega \; . \tag{6.3}$$

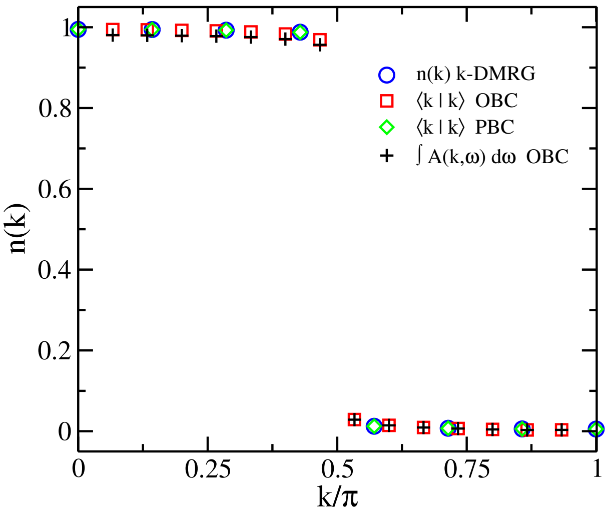

Figure 6.5: Momentum distribution $n(k)$ of the Hubbard model with $U/t = 1$, $L = 14$, $n = 1$. The broadening $\eta/t = 0.2$ was used for $A(k, \omega)$. Both periodic and open boundaries were used in the calculation and yield only small differences. (k-DMRG data courtesy of Ö. Legeza)

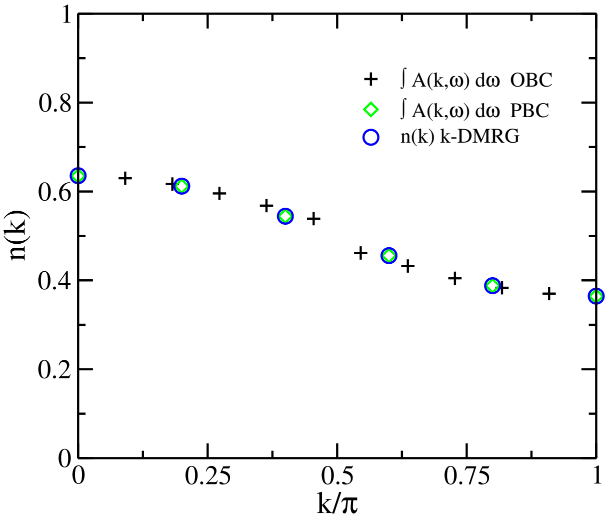

Figure 6.6: Momentum distribution $n(k)$ of the Hubbard model with $U/t = 20$, $L = 10$, $n = 1$. The broadening $\eta/t = 0.2$ was used for $A(k, \omega)$. Both periodic and open boundaries were used in the calculation and yield only small differences. (k-DMRG data courtesy of Ö. Legeza)

The factor of 2 stems from the fact that we have included only one spin species in the definition of the Green function. This relation is very useful since we can calculate $n(k)$ independently with standard DMRG by targeting the state $\hat{c}_{k,\sigma}|\psi_0\rangle = |k\rangle$ and then calculating the norm

$$n(k) = 2\,\langle k|k\rangle \ . \tag{6.4}$$

Apart from DMRG in position space $n(k)$ can be easily calculated using a momentum space DMRG (k-DMRG) method [46, 47]. We thus have two independent ways to check the sum rule (6.3).

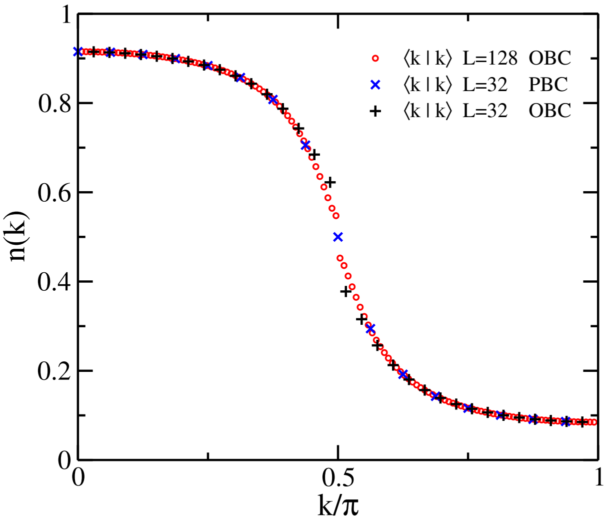

Figure 6.7: Momentum distribution $n(k)$ of the Hubbard model with $U/t = 4$, $L = 32, 128$, $n = 1$. The error in $n(k)$ around $k = \pi/2$ vanishes roughly like $1/L$ for the open chain.

Figures 6.5 and 6.6 show comparisons of the momentum distribution $n(k)$ calculated with equations (6.3) and (6.4) in the Hubbard model for interactions $U/t = 1$ and $U/t = 20$, respectively. The overall agreement is excellent despite the small system sizes ($L = 10, 14$). The integrated spectral weight calculated in an open chain is only slightly smaller than the exact result since the integration does not have infinite boundaries but is truncated at a finite value. At $U/t = 20$ the error for open boundaries is more pronounced than in the case $U/t = 1$. The differences are most notable close to $k = k_{\mathrm{F}} = \pi/2$ but remain small. This confirms that the pseudo-momentum (5.47) is the appropriate definition for open boundaries.

An example for intermediate couplings, $U/t = 4$, is shown in figure 6.7. For open boundary conditions, we can easily treat systems as large as $L = 128$, whereas for periodic boundaries we are limited to $L = 32$. Again, the deviations are largest around $k_{\mathrm{F}} = \pi/2$. However, we find that the error in the momentum distribution close to k_{F} vanishes roughly as $1/L$ when we consider larger system sizes.

In summary, we have checked the sum-rule (6.3) for the one-particle spectral function $A(k,\omega)$ for various non-trivial cases and we find good agreement both for open and periodic boundary conditions. In addition, we have shown that the error in the momentum distribution $n(k)$ in open systems vanishes with growing system size.

6.1.3 Density of States

A different numerical test of the method is the evaluation of the local density of states directly via DDMRG or by momentum integration of the spectral function

$$\rho(\omega \leq 0) = \frac{1}{L}\sum_q A(q,\omega) = \frac{1}{L}\sum_n \sum_{i=1}^{L} |\langle \psi_n\, |\hat{c}_{i,\sigma}|\, \psi_0\rangle|^2\, \delta\left(\omega + E_0 - E_n\right) \qquad (6.5)$$

This sum-rule gives a quantitative measure of the error that the open boundary introduces to the spectrum.

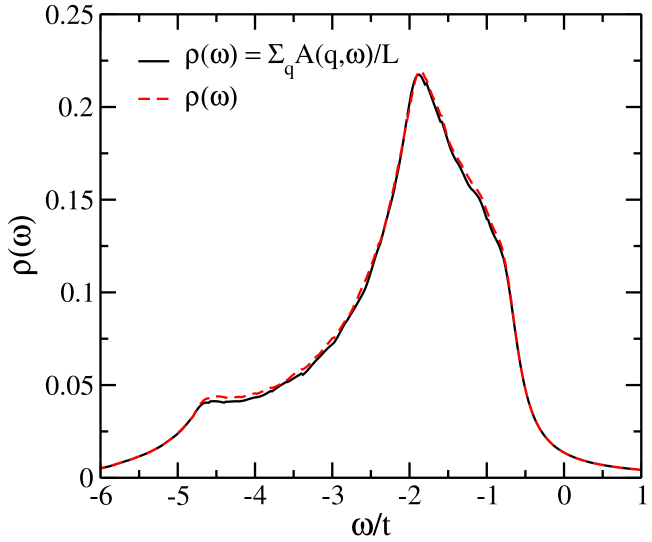

Figure 6.8: Local density of states $\rho(\omega)$ of the Hubbard model calculated directly by DDMRG (dashed red line). Momentum integrated one-particle spectral function $A(k,\omega)$ (black line). Open boundaries where used and $U/t = 4$, $L = 32$, $\eta/t = 0.2$. The curves are almost indistinguishable.

In figure 6.8 we show a plot of $\rho(\omega \leq 0)$ in the particle-hole symmetric half-filled Hubbard model with on-site interaction is $U/t = 4$. We use a resolution $\eta/t = 0.2$ for a system length $L = 32$. We use periodic boundary conditions and obtain $\rho(\omega)$ directly with DDMRG and, in addition, by performing the momentum sum (6.5). The resulting line shapes are close to indistinguishable and confirm our method for periodic boundaries.

Figure 6.9 shows $\rho(\omega \leq 0)$ for the Peierls-Hubbard model with on-site interaction $U/t = 3$ and a dimerization $\delta/t = 0.3$. The boundaries are both open and periodic for $L = 32$ and we have introduced a broadening of $\eta/t = 0.4$ in the calculations. The density of states was evaluated with $A(k, \omega)$ and then applying equation (6.5). Small deviations are visible only at the local maximum between $\omega/t = -1$ and $\omega/t = -2$. This result is another confirmation of our treatment of open boundary conditions.

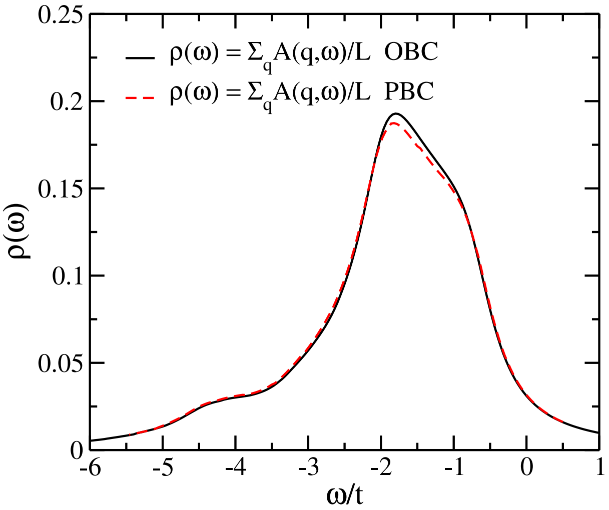

Figure 6.9: Local density of states $\rho(\omega)$ of the Peierls-Hubbard model calculated with $A(k, \omega)$ with open and periodic boundaries. Model parameters are $U/t = 3$, $\delta/t = 0.6$, $L = 32$, $\eta/t = 0.2$. The overall agreement is good except around the peak where small differences are visible.

6.2 Dynamical Density Structure Factor

In this section we verify our method for the dynamical density structure factor. The theoretical situation is difficult for dynamical density-density correlations since far less is known analytically here than in the case of photoemission spectra where we make use of the exact Bethe-Ansatz solution. We proceed by comparing with previous exact diagonalization studies of the extended Hubbard model and analytical strong-coupling expansions. Furthermore, we check that the $q \to 0$ limit of the density-density correlation function reproduces the optical conductivity, calculated independently with DDMRG.

6.2.1 Comparison with Exact Diagonalization

The dynamical density-density correlation function is given by

$$N(k, \omega) = \lim_{\eta \to 0} \frac{1}{\pi} \Im \langle \psi_0 | \hat{n}_k^+ \frac{1}{\hat{H} + \omega - E_0 - \mathrm{i}\eta} \hat{n}_k \, |\psi_0\rangle = \sum_f |\langle f | \hat{n}_k | 0 \rangle|^2 \delta \left(\omega - E_f + E_0\right) \tag{6.6}$$

with the momentum dependent density operator

$$\hat{n}_k = \sum_{p,\sigma} \hat{c}^{+}_{p-k,\sigma}\hat{c}_{p,\sigma} . \tag{6.7}$$

This correlation function describes the scattering of charged particles by the electronic density and is therefore relevant for experiments like electron-energy loss spectroscopy (EELS).

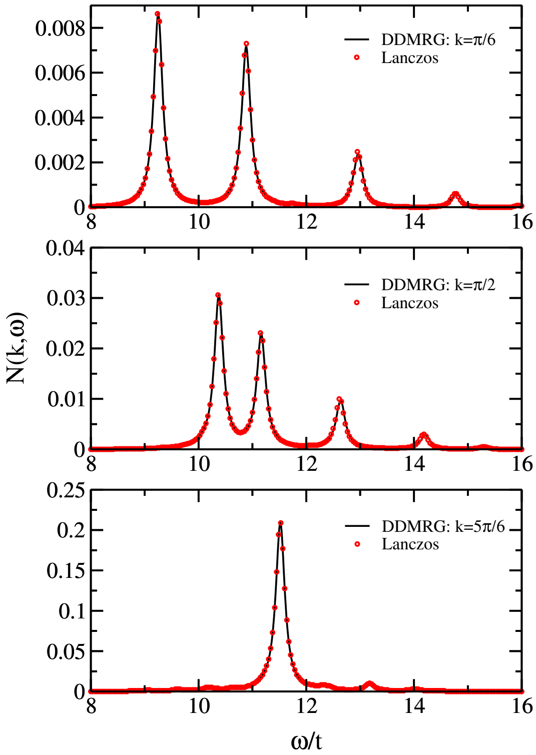

Figure 6.10: Comparison of $N(k,\omega)$ calculated with exact diagonalization (data extracted from [50]) and DDMRG. The system is periodic with $L = 12$ sites, $N = 12$ electrons, $U/t = 12$, $V/t = 1$. There are no visible differences between ED and DMRG.

We can test the accuracy of our method for small system sizes ($L = 12$) at half filling since there are exact diagonalization results for the dynamical density-density correlation function of the extended Hubbard model [50]. Despite the small system size this is a non-trivial problem for both methods.

We have extracted the data from the publication [50] and compare to our DDMRG results in figure 6.10. The system is a 12-site ring (periodic boundaries) and the interaction parameters are $U/t = 12$ and $V/t = 1$. There are no visible differences to the exact diagonalization data and we conclude that this independently verifies our method in a correlated system with periodic boundaries.

6.2.2 Limit $q \to 0$

The optical conductivity $\sigma_1(\omega)$ is related to the zero-momentum limit of the density-density correlation function $N(q,\omega)$ through

$$\frac{\sigma(\omega)}{\omega} = \lim_{q\to 0} \frac{N(q,\omega)}{(q/2)^2} \,. \tag{6.8}$$

We can use this relation to test our numerical results for $N(q \to 0, \omega)$. This is a valid procedure because we evaluate a different correlation function, namely the dynamical dipole-dipole or current-current correlation function (cf. chapter 8). The superior accuracy of DDMRG for $\sigma(\omega)$ for correlated one-dimensional lattice models, such as the extended Hubbard model, has been verified earlier [39]. We therefore have an independent source of verification.

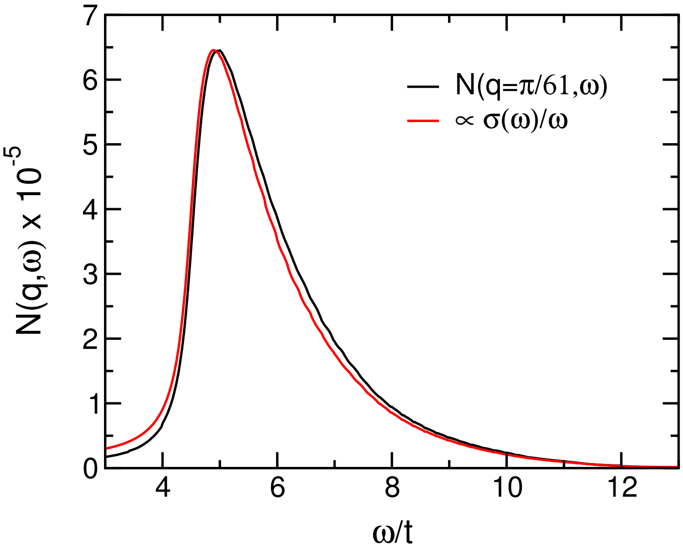

Figure 6.11: Comparison of $N(q=\pi/61,\omega)$ with $\sigma_1(\omega)/\omega$ for a 60-site system and a broadening $\eta/t = 0.2$. The peak position and overall line shape are in very good agreement.

A comparison of $\sigma(\omega)/\omega$ and $N(q \to 0, \omega)$ is shown in figure 6.11. We use open boundaries and $L = 64$ lattice sites keeping up to 200 density matrix eigenstates. The broadening is $\eta/t = 0.2$ for both correlation functions. Note that we have not used the q-dependent prefactor in equation (6.8) but we have used the peak height of $\sigma(\omega)$ as a fit parameter. Using open boundaries we cannot exactly reach the limit $q \to 0$. The pseudo-momentum $q = \pi/65 \approx 0.05$ is not yet small enough for (6.8) to hold precisely. Nevertheless, the overall line shape and the position of the peak agree remarkably well. This verifies the numerical calculation of $N(q,\omega)$ at the zone center and indicates that open boundaries can be used with good precision.

6.2.3 Strong-Coupling Theory

More details of the dynamic density structure factor are known in the limit of strong local Coulomb interaction $U \gg V, t$. In this limit the wavefunction factorizes into a charge and a spin part, $|\psi\rangle = |\phi_{\rm c}\rangle \otimes |\phi_{\rm s}\rangle$ [51]. Using this decomposition it is possible to calculate the structure factor $N(q, \omega)$ [50].

In order to test the DDMRG structure factor we calculate $N(q, \omega)$ for momenta close to the zone boundary, $q \to \pi$, and determine the total spectral weight and the position of the peak. Strictly in the limit $U/t \to \infty$, all weight at $q = \pi$ resides in an exciton peak with infinite lifetime at $\omega = U - V$. Its weight is given by [50]

$$\int N(q,\omega){\rm d}\omega \quad = \quad 16\ln(2)\left(\frac{t}{U}\right)^2 \sin^2\left(\frac{q}{2}\right) \ . \qquad (6.9)$$

One important consequence of this strong-coupling sum rule is that the total weight of $N(q, \omega) \sim U^{-2}$, i.e., the weight is strongly suppressed at large values of U.

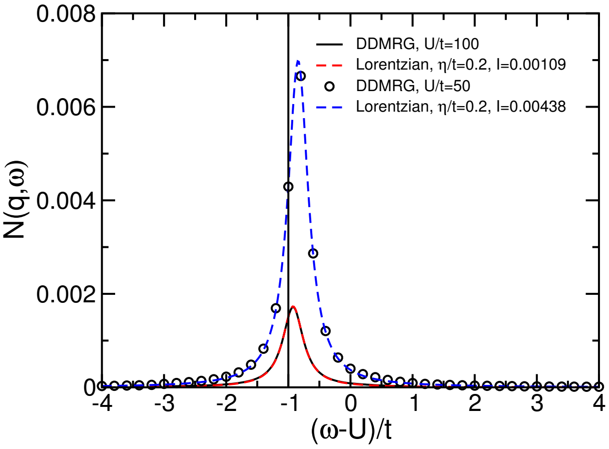

Figure 6.12: Spectral weight of the strong-coupling exciton at $q = \pi$ and $U/t = 50, 100$. The weight of the DDMRG peaks fitted with a Lorentzian are in excellent agreement with strong-coupling theory.

Consider figure 6.12 where we plot $N(q \approx \pi, \omega)$ for $U/t = 50$ and $U/t = 100$. The size of the open chain is $L = 30$ and we have introduced a broadening $\eta/t = 0.2$. We fit the peaks with Lorentzians and integrate the spectral weight I. The values I thus obtained agree excellently with the values derived from equation (6.9). In addition, the position of the peaks approaches $\omega = U - V$ with growing U, as expected. This, finally, proves the accuracy of our numerical method at momenta close to the zone boundary.

Having verified the accuracy of our numerical approach we digress at this point to discuss the question how long strong-coupling theory remains valid. The results we obtain here will be useful in chapter 9 where we present dynamical properties of the correlated chain cuprate $\rm SrCuO_2$ in conjunction with a recent RIXS experiment [52].

At very large couplings, $U/t = 50, 100$, it is safe to assume that strong-coupling theory holds. A simple way of addressing this issue is to check whether the resonance at $q = \pi$ is a strong-coupling exciton or whether it acquires an intrinsic life time. As long as strong-coupling theory is a good description, the height of the peak should therefore scale like a convolved δ-peak, i.e.,

$$h(\eta) \ \sim \eta^{-1} \ , \tag{6.10}$$

which indicates the presence of an exciton.

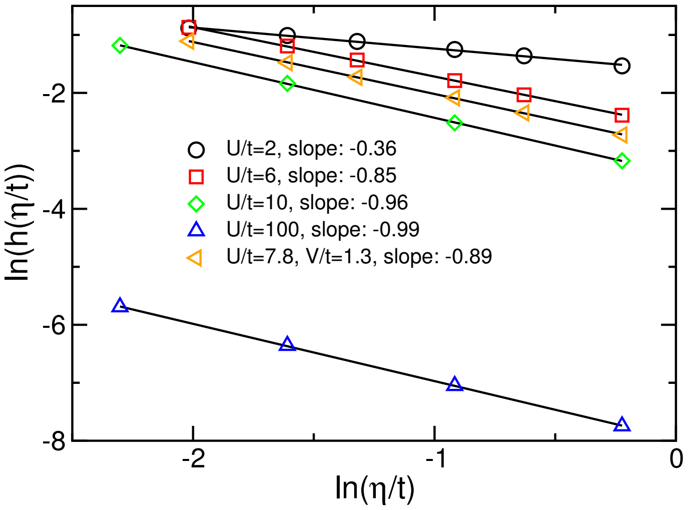

Figure 6.13: Finite-size scaling analysis of the resonance at $q = \pi$. At strong-coupling $U/t = 100$ the peak scales like an exciton-peak with an exponent close to one. Upon reducing the interaction to roughly twice the band width W, the peak broadens and yields power-law exponents smaller than one.

This can be efficiently achieved by performing a finite-size scaling analysis where the broadening $\eta \sim L^{-1}$. Figure 6.13 shows a double-logarithmic plot of $h(\eta)$ vs. $\eta \to 0$. At $U/t = 100$ the slope is very close to unity. However, as soon as we choose a Coulomb repulsion U/t comparable with twice the bare electron band width, the peak acquires an intrinsic width yielding power-law exponents smaller than one. This signals the breakdown of strong-coupling theory.

How much of the strong-coupling physics is still qualitatively correct for realistic parameters and can it be applied to the description of correlated charge-transfer insulators? The authors of [53] propose parameters $U/t = 7.64$, $V/t = 2.36$, $t = 0.55\,\mathrm{eV}$ for the description of the quasi one-dimensional chain cuprate Sr_2CuO_3. They then treat their strong-coupling $N(q, \omega)$ with a Random Phase Approximation (RPA). To check whether the input $N(q, \omega)$ from strong-coupling theory is justified we directly compare DDMRG with results from [50] in figure 6.14 a). There are gross qualitative and quantitative differences in the spectra. The parameters proposed by the authors of [53] can therefore *not* be treated in a strong-coupling approach.

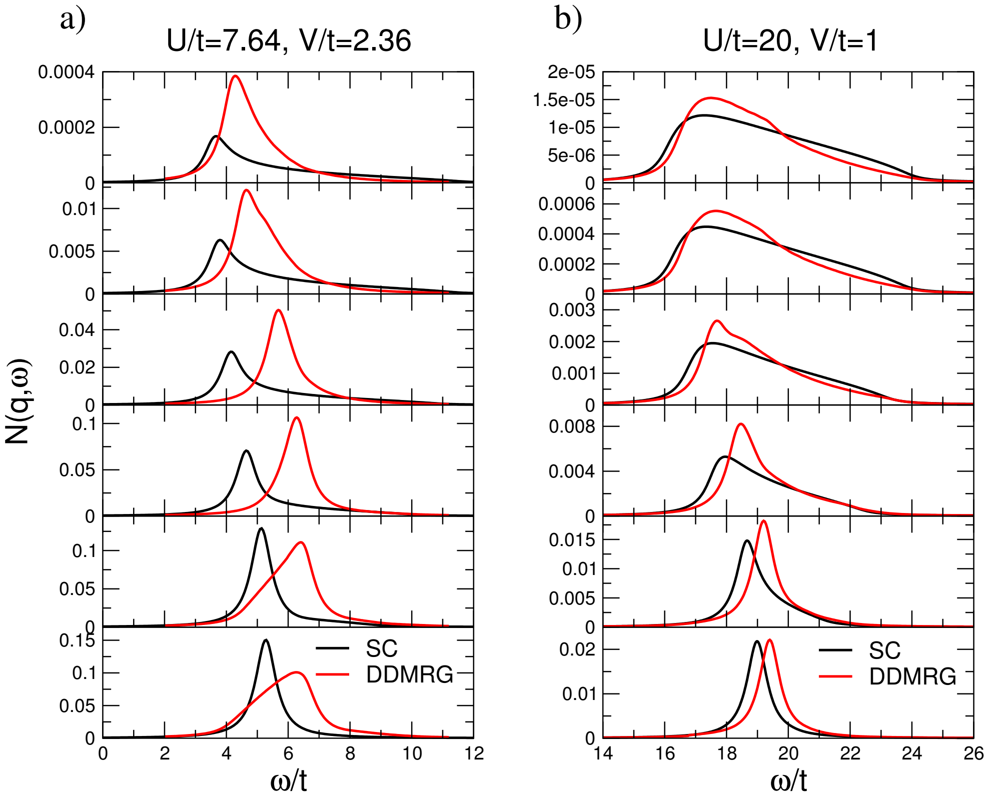

Figure 6.14: Panel a): Comparison of $N(q,\omega)$ from strong-coupling theory [50] and DDMRG. We use $U/t = 7.64$ and $V/t = 2.36$ [53] and introduce an appropriate broadening of $\eta/t = 0.4$ in the strong-coupling results. There are striking differences between the spectra. Panel b): Same for $U/t = 20$, $V/t = 1$. Although U/t is five times the band width there are significant differences between strong-coupling results and DDMRG.

It is surprising that the strong-coupling theory is, in fact, not even applicable for much larger U/t. We have calculated $N(q,\omega)$ for $U/t = 20 = 5W$ and $V/t = 1$ and compare directly with the strong-coupling structure factor, see figure 6.14 b). Both peak positions and line shapes differ significantly from the DDMRG results. This has an immediate bearing on the interpretation of electron-electron energy loss spectra (EELS) for $SrCu_2O_3$ presented in [53]. There, the authors suggest that the dispersion of the EELS spectral peak is related to a strong-coupling exciton at finite momenta. The theory proposed by the authors strongly relies on the applicability of strong-coupling theory. In view of the results in figure 6.14 we are forced to dismiss this interpretation. We remark that, besides the inapplicability of strong-coupling theory, the suggested parameter set yields too large optical gaps Δ_{opt} and incompatible values of the exchange parameter J. We conclude that $U/t = 7.64$ and $V/t = 2.36$ is inappropriate to describe the physics of the charge-transfer insulators $\mathrm{SrCuO_2}$ and $\mathrm{SrCu_2O_3}$.

6.3 Dynamical Spin Structure Factor

The last section of this chapter is devoted to the dynamical spin-spin correlation function, or dynamical spin structure factor. It is defined through

$$\begin{aligned} S(q,\omega) &= \lim_{\eta\to 0} \frac{1}{\pi} \Im \langle \psi_0 | \hat{S}_q^{z+} \frac{1}{\hat{H} + \omega - E_0 - \mathrm{i}\eta} \hat{S}_q^z | \psi_0 \rangle \\ &= \sum_n |\langle n | \hat{S}_q^z | 0 \rangle|^2 \delta \left(\omega - E_n + E_0 \right) \end{aligned} \quad (6.11)$$

where $\hat{S}_q^z$ is the Fourier transform of the local spin operator $\hat{S}_i^z = (\hat{n}_{i,\uparrow} - \hat{n}_{i,\downarrow})/2$. This correlation function is relevant for scattering experiments where the scattered particles couple to the spin-sector of the electronic system, such as inelastic neutron scattering.

As a test of DDMRG we have calculated $S(q,\omega)$ in a small system with $L = 30$ lattice sites for small on-site interaction $U/t = 1$. The broadening was chosen as $\eta/t = 0.4$ which is too large to resolve details of the spectrum. The result of this calculation is shown in figure 6.15. Despite the bad resolution we recognize the familiar shape of the two-spinon continuum (cf. figure 3.1 section 3.4.1). Most of the weight is distributed towards the upper onset as predicted from field theory calculations [54]. Thus, the rough features in figure 6.15 are compatible with our theoretical expectations.

In order to make a more quantitative evaluation of the data we extract the positions of the dominant peak in the DDMRG spectrum. It is a well-known fact that the compact support of the two-spinon continuum of the Hubbard model is well approximated by the *des Cloiseaux-Pearson* (dCP) dispersion relations of the spin-1/2 Heisenberg model. They are given by

$$\omega_{\mathrm{L}}(q) = \frac{\pi J}{2} |\sin(q)| \; , \quad (6.12)$$

$$\omega_{\mathrm{U}}(q) = \pi J |\sin(q/2)|, \quad (6.13)$$

where $\omega_{\mathrm{L}}(q)$ is the low-energy onset and $\omega_{\mathrm{U}}(q)$ is the onset at high energies. Figure 6.16 features a comparison of the DDMRG peak dispersion and the dCP-dispersion. Since the on-site interaction is weak, most weight resides in the high-energy peak. Accordingly, we cannot determine the lower onset, since it is concealed by the broadening of the data. We find that the dCP-onsets agree very well with our data for both periodic and open boundaries.

6.4 Conclusion

In conclusion, we have presented a variety of tests of DDMRG for the evaluation of momentum and frequency dependent dynamical correlation functions. Our presentation

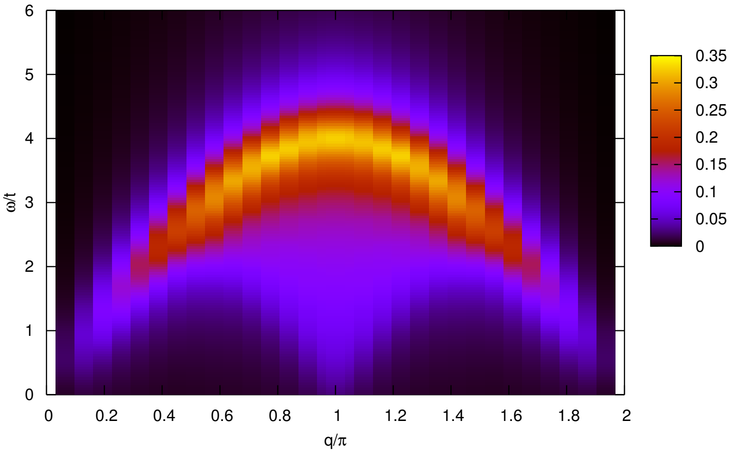

Figure 6.15: Spin structure factor $S(q, \omega)$ of the Hubbard model ($U/t = 1$) in a 30-site system with open boundaries and a large broadening $\eta/t = 0.4$. Due to the bad resolution all features are smeared out significantly. However, the enhancement of spectral weight at the upper boundary is consistent with expectations from field theory [54].

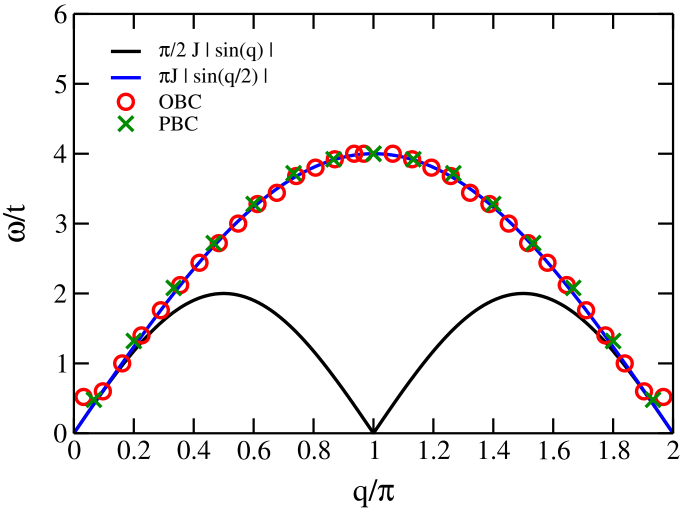

Figure 6.16: Peak dispersion of the spin structure factor of the Hubbard model ($U/t = 1$) in a 30-site system with open and periodic boundaries and resolution $\eta/t = 0.4$. Full lines are fits with the *des Cloiseaux-Pearson* dispersion relations (6.12) and (6.13).

included the one-particle spectral function, the dynamic charge structure factor and the dynamic spin structure factor. We have given a detailed discussion of the effect of open boundaries by comparing with periodic systems for non-trivial parameters of the models under consideration. Despite the small system sizes and the fairly low resolution of these test calculations we have good to excellent agreement with theoretical predictions (Bethe-Ansatz, strong-coupling theory) or independent numerical results (k-DMRG, ED).

This concludes the methodological part of this thesis. In Part III we present DDMRG results for dynamical correlation functions in different strongly correlated quasi one-dimensional materials. This permits us to explain recent experiments in these systems and shows that spin-charge separation can be detected spectroscopically at finite energies.

Part III

Results

Chapter 7

Angle-Resolved Photoemission in TTF-TCNQ

A number of organic charge transfer salts have proven to be an ideal testing ground for the quantum many-body problem in one dimension [55]. These materials comprise of planar organic molecules that order in linear stacks and charge is transferred from cationic to anionic complexes leading to strongly anisotropic transport behavior. In real materials, however, the low-energy properties are likely to be governed by three-dimensional physics. In three dimensions the Fermi liquid paradigm implies that the emergent low-energy excitations, the *quasi-electrons*, carry the quantum numbers of an electron with renormalized dispersion and an intrinsic lifetime.

One-dimensional physics is observed only above a crossover energy scale, even in the most strongly anisotropic materials. In this regime the low-energy excitations are expected to show dynamical decoupling into collective charge and spin excitations. In principle, these features can be observed in the one-particle spectral function [17, 18] which corresponds to the spectrum measured in angle-resolved photoemission spectroscopy (ARPES) experiments. Up to date, however, there has been little positive evidence from spectroscopy that such a decoupling occurs.

The Luttinger-liquid theory (cf. section 3.1) describes the ground state and asymptotic low-energy properties of one-dimensional correlated metals [15]. Within this framework all dynamical correlations can be evaluated analytically but the theory does not contain an intrinsic energy scale by its very construction. Just how much of the results can be carried on to *finite* energies is not known a priori. The photoemission spectral function at finite energies can only be calculated exactly in the limiting cases of noninteracting electrons or infinitely strong electron interaction [56, 57, 58] both of which are unphysical. Various numerical methods have provided a qualitative picture of spectral functions in the Hubbard model. Exact diagonalizations [58, 59] are limited to very small systems that do not allow an extrapolation to the thermodynamic limit. Other approaches [60, 61] are based on various approximations of uncertain accuracy. It has therefore been difficult for theory to make contact with experiments on the dynamical properties of correlated lattice models in one dimension.

In the following we give a brief introduction into the structure and the physics of the transfer salt TTF-TCNQ and report on recent angular resolved photoemission experiments [62] which show striking deviations from band theory. Then we present DDMRG calculations of the one-particle spectral function of the repulsive Hubbard model both above and below half-filling [63]. The data we obtain have an unprecedented accuracy. We argue that spin-charge separation occurs in TTF-TCNQ over an energy scale of the conduction band width and explain the ARPES excitation branches in terms of fractional excitations of the Hubbard model.

7.1 Experimental Situation

7.1.1 Structure of TTF-TCNQ

The conducting charge transfer salt TTF-TCNQ (tetrathiafulvalene tetracyanoquinodimethane) has a monoclinic crystal structure. At room temperature the lattice parameters are $a = 12.298\text{Å}$, $b = 3.819\text{Å}$, and $c = 18.468\text{Å}$, and the monoclinic angle is $\beta = 104.46^\circ$ [64]. The TTF and TCNQ molecules are oriented along linear stacks along the crystallographic **b** direction. Both molecules have π-type molecular orbitals that extend over the entire molecule. These orbitals have strong overlap with the neighboring orbitals belonging to molecules above or below. By tilting the plane of the molecules about the **a** axis, bonding is maximized and, due to alternating signs of the tilt angles θ_F and θ_Q between the stacks, a herringbone structure results as shown in figure 7.1.

On average there is a charge transfer of about 0.59 electrons from TTF to TNCQ molecules rendering both stacks metallic [64]. It can be seen from the strong anisotropic conductivity along the different directions

$$\sigma_b : \sigma_a \approx 1000 \qquad \sigma_b : \sigma_c \approx 1000 \tag{7.1}$$

that TTF-TCNQ is a quasi one-dimensional conductor. Below the transition temperature $T_\text{P} = 54\,\text{K}$ the systems is Peierls-insulating where a charge density wave (CDW) develops with wave vector $Q_\text{CDW} = 0.485\text{Å}^{-1} = 2k_\text{F}$. Accordingly, photoemission data were taken at higher temperatures.

7.1.2 Angular Resolved Photoemission (ARPES) of TTF-TCNQ

A recent ARPES experiment for the quasi-one-dimensional organic conductor TTF-TCNQ has revealed significant discrepancies from the predictions of Fermi liquid theory and conventional band structure calculations [62, 65]. The experimental dispersion can be consistently mapped over the scale of the conduction band width onto separated spin and charge excitation bands of the one-dimensional Hubbard model away from half filling. This is one of the strongest pieces of experimental evidence for spin-charge separation and thus for Luttinger-liquid physics in low-dimensional materials.

Figure 7.2 shows the angle-resolved photoemission data for TTF-TCNQ in the quasi-1D direction **b** where well-defined features are observed that disperse significantly (structures (a)–(d)). The corresponding results for the other crystallographic directions (not

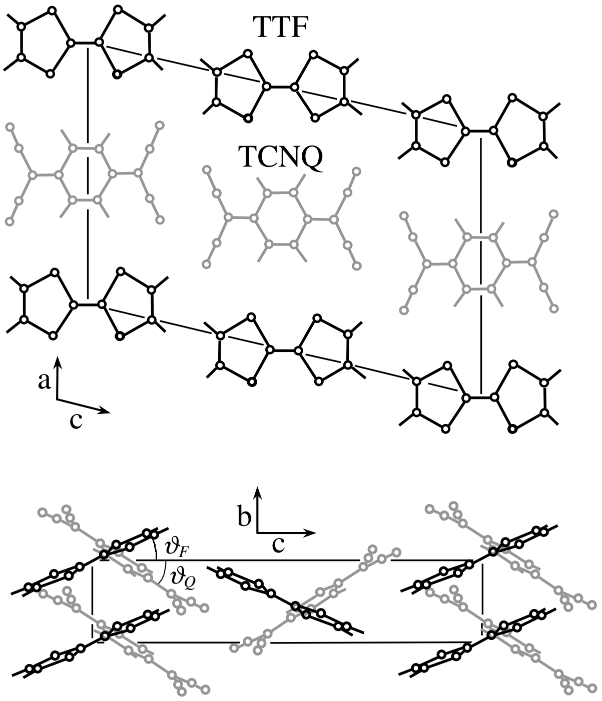

Figure 7.1: Crystal structure of TTF-TCNQ [65]. The extended π-type molecular orbitals overlap in the crystallographic **b** direction which leads to strongly anisotropic transport.

shown) display no dispersion at all, as expected for a quasi-1D system. The point where the spectral features labeled (a) and (b) merge and where they most closely approach the Fermi level is used to define the Fermi momentum $k_\mathrm{F} = 0.24\text{Å}^{-1}$, in good agreement with the CDW vector $Q_\mathrm{CDW} = 0.485\text{Å}^{-1} = 2k_\mathrm{F}$. Despite the fact that TTF-TCNQ is highly conductive it does not show a metallic Fermi edge. Instead, the spectral weight diminishes in a linear fashion as the energy approaches E_F.

In figure 7.3 we see a density plot of the second derivative of the ARPES data clipped at negative energies. Such a plot provides an unbiased depiction of the dispersive structures. In addition, the full lines show the results of a band structure calculation using density functional theory (DFT). According to DFT, the molecular orbitals of TTF-TCNQ are strongly localized except along the stacking direction where small but significant bonding is present. This bonding forms two sets of quasi one-dimensional conduction band doublets with a band width of $\sim 0.7\,\mathrm{eV}$. The band just below the Fermi energy that becomes unoccupied at the zone boundary (Z point) is due to the overlapping π-bonded orbitals of carbon atoms and can therefore be attributed to TCNQ. The splitting at zero momentum is due to weak interactions between TCNQ stacks. The other nearly degenerate doublet can be mainly derived from the $3p$-orbitals with π-symmetry originating from sulphur atoms. It is thus related to the TTF stacks.

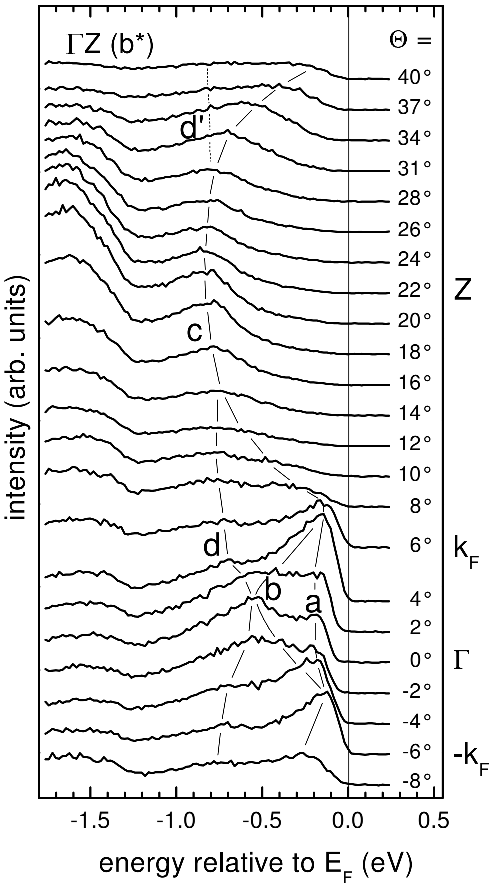

Figure 7.2: Energy distribution curves measured at $T = 61\,\mathrm{K}$ [62] along the quasi one-dimensional direction **b**. Thin lines indicate the dispersion of spectral features.

When we compare the DFT conduction bands with the ARPES data we find both qualitative agreement and significant deviations. The band doublet associated with TCNQ can account for the structures (a) and (b) in figure 7.3 if we approximately *double* the band width. This band width enhancement could be justified by surface relaxation involving tilt angles [65]. Structure (c) could be explained by the TTF band dispersing below E_F if one renormalizes the band width by a factor of two. This leaves structure (d) completely unaccounted for since there is no corresponding counterpart in the DFT band structure. One could of course argue that (d) is a surface state. But since (d) lies well below the Fermi surface it should be occupied throughout the entire Brillouin zone. This would severely affect the charge balance between TTF and TCNQ bands, shifting the surface Fermi vector away from its bulk value. This is not observed.

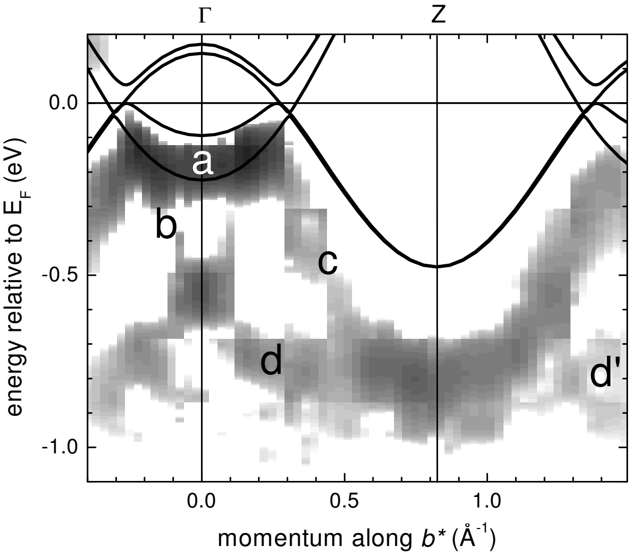

Figure 7.3: Density plot of the second derivative of the ARPES data clipped at negative energies [62]. The dispersive gray shaded features correspond to excitation branches in the ARPES data. The black lines are results from band structure calculations. Features (a), (b) and (c) can be qualitatively explained by band theory if one assumes a band width approximately twice the predicted value. Structure (d) does not resemble anything seen in the band theory picture.

We conclude that band theory can not explain important details of the ARPES data. The next two sections will show that this is due to the breakdown of Fermi-liquid physics in one dimension and the emergence of a new quantum liquid that can be described in terms of fractional excitations of an electron. We will refer to the "bands" of the ARPES spectrum as branches of these excitations since they are no longer quasi particles akin to an electron.

7.2 TCNQ Band

In this section we determine the photoemission spectral function of the one-dimensional Hubbard model with parameters appropriate for TTF-TCNQ using the dynamical density-matrix renormalization group (DDMRG) method [39]. This allows us to investigate large systems almost exactly. Thereby, a direct comparison of the Hubbard model spectral weight distribution with the experimental TTF-TCNQ spectrum becomes meaningful. In order to demonstrate the accuracy of our method and to identify excitations which contribute to the photoemission spectral function, we compare our numerical data with exact Bethe-Ansatz results introduced in section 3.2. We first discuss the photoemission spectrum of the TCNQ band and then address the photoemission of the TTF band. We show that the electron-removal spectrum of TTF-TCNQ can be described in terms of the one-particle spectral function of independent Hubbard chains with filling $n = 0.6$ and $n = 1.4$ for TCNQ chains and TTF chains, respectively.

7.2.1 Methods

A minimal model to describe the electronic properties of TTF-TCNQ is the one-dimensional Hubbard model defined by the Hamiltonian

$$\hat{H} \;=\; -t \sum_{l;\sigma} \left(\hat{c}^{+}_{l,\sigma} \hat{c}_{l+1,\sigma} + \hat{c}^{+}_{l+1,\sigma} \hat{c}_{l,\sigma} \right) + U \sum_{l} \hat{n}_{l,\uparrow} \hat{n}_{l,\downarrow} - \mu \sum_{l} \hat{n}_{l} \tag{7.2}$$

Here, $\hat{c}^{+}_{l,\sigma}$, $\hat{c}_{l,\sigma}$ represent the creation and annihilation operators for electrons with spin $\sigma = \uparrow, \downarrow$ at site $l = 1, \ldots, L$ in a π-type Wannier orbital centered on a TCNQ molecule. Appropriate parameters for the TCNQ band are an on-site Coulomb repulsion $U = 4.9t$ and a hopping integral $t = 0.4\,\mathrm{eV}$ [62, 65]. These values are appropriate for the TTF-TCNQ surface which is probed in ARPES experiments, not for bulk TTF-TCNQ. Although the filling of the TCNQ band is $n = 0.59$, we use a slightly different filling $n = 0.6$ in our simulations to facilitate the finite-size-scaling analysis. For a chain with L sites and $N = nL$ electrons the chemical potential μ is chosen so that $E_0(N-1) = E_0(N+1)$, where $E_0(N \pm 1)$ is the ground state energy with $N \pm 1$ electrons. Thus the Fermi energy is $E_{\mathrm{F}} = 0$ in the thermodynamic limit $L \to \infty$.

The photoemission spectral function $A(k, \omega)$ is the imaginary part of the one-particle Green's function

$$A(k, \omega) = \frac{1}{\pi} \Im \langle \psi_0 | \hat{c}^{+}_{k,\sigma} \frac{1}{\hat{H} + \omega - E_0 - \mathrm{i}\eta} \hat{c}_{k,\sigma} | \psi_0 \rangle, \tag{7.3}$$

where $|\psi_0\rangle$ and E_0 are the ground state wavefunction and the energy of the Hamiltonian (7.2). As explained in detail in chapter 5, this function can be calculated for finite broadening η and system sizes L using the dynamical DMRG method. The spectral properties in the thermodynamic limit can be determined using a finite-size-scaling analysis with an appropriate broadening $\eta(L)$, as discussed in section 5.1.6. Here, we have used $\eta L = 9t$ and system sizes up to $L = 150$ sites. We have kept up to $m = 400$ density-matrix eigenstates per block in our calculations and DMRG truncation errors are negligible for all results presented here.

We use the quasi-momentum $k = \pi z/(L+1)$ for integers $1 \leq z \leq L$ introduced in section 5.2.2 to express the momentum dependent operators $\hat{c}_{k,\sigma}$. This allows us to expand the definition of $A(k, \omega)$ to open boundary conditions, see section 5.2.2. Therefore, open chains can be used to investigate the spectral function $A(k, \omega)$. In the following sections we consider only open boundaries unless stated otherwise.

7.2.2 ARPES Spectrum at Filling $n = 0.6$

Figures 7.4 and 7.5 show the spectral function calculated with DDMRG in a chain with $L = 90$ sites. Since the spectrum is symmetric, $A(-k, \omega) = A(k, \omega)$, we show results for

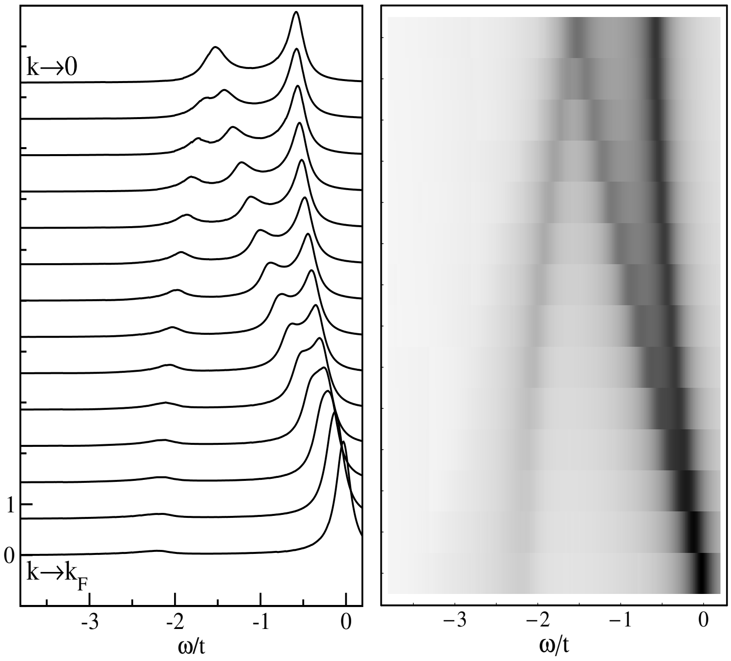

Figure 7.4: Line shapes (left) and gray-scale plot (right) of the spectral function $A(k, \omega)$ for $0 < k < k_{\mathrm{F}}$ calculated with a broadening $\eta = 0.1t$ using DDMRG on $L = 90$ lattice sites.

$k \geq 0$ only. We distinguish between $0 < k < k_{\mathrm{F}} = n\pi/2$ and $k_{\mathrm{F}} < k < \pi$.

Three dispersing features are clearly visible in the spectrum for $|k| < k_{\mathrm{F}}$ in Fig 7.4. At small binding energy $(-\omega)$ there are intense peaks with a narrow dispersion, from $\omega \approx 0$ at $k = \pm k_{\mathrm{F}}$ to $\omega \approx -0.5t$ at $k = 0$. This feature corresponds to the spinon branches in the Luttinger-liquid regime. Note that both spinon branches (for $k < 0$ and $k > 0$) join at $k = 0$ and thus form just one spinon band. At energies ω lower than the spinon band there is a second spectral feature made of peaks with less spectral weight and a wider dispersion from $\omega \approx 0$ at $k = \pm k_{\mathrm{F}}$ to $\omega \approx -1.5t$ at $k = 0$. It merges with the spinon band for $k \to \pm k_{\mathrm{F}}$ because of the finite broadening. This feature corresponds to the two holon branches of Luttinger-liquid theory. The third spectral feature is made of weaker peaks and has an (apparently) inverted dispersion, starting at $\omega \approx -1.5t$ for $k = 0$ and reaching $\omega \approx -2.2t$ at $k = \pm k_{\mathrm{F}}$. These so-called shadow bands [57] are actually the continuation of the holon bands. Thus, the second and third features correspond to two holon/shadow bands crossing at $k = 0$. While the spectral weight of the structure associated with the spinon and holon bands remains relatively constant for all $|k| < k_{\mathrm{F}}$, the shadow bands rapidly loose intensity with increasing k.

Figure 7.5 shows the spectral weight for $|k| > k_{\mathrm{F}}$. It is much smaller than for $|k| < k_{\mathrm{F}}$. Nevertheless, one can observe four dispersive structures in the spectral function. First, the shadow band continues from $k = \pm k_{\mathrm{F}}$ to $\pm 3k_{\mathrm{F}}$, but its energy increases with $|k|$ and approaches zero for $|k| = 3k_{\mathrm{F}}$. Weaker peaks are also visible at higher energies than the shadow band for $k_{\mathrm{F}} < |k| < 2k_{\mathrm{F}}$. The corresponding binding energy $(-\omega)$ increases from about zero at $k = \pm k_{\mathrm{F}}$ to about $1.7t$ at $k = \pm 2k_{\mathrm{F}}$, where this second feature meets the shadow band and apparently disappears. The third dispersing feature corresponds to very weak peaks not visible on the scale of figure 7.5 with energies from $\omega \approx -3.7t$ at $k = \pi$ to $\omega \approx -2.2t$ at $|k| \approx 2k_{\mathrm{F}}$. Note that, despite its weakness, this feature corresponds to the spectrum maximum for $k \approx \pi$. The last feature is a sharp drop of the spectral weight at low energy. It goes from $\omega \approx -3.25t$ at $|k| \approx k_{\mathrm{F}}$ to $\omega \approx -4.6t$ at $k = \pi$. We interpret this drop as the lower edge of the photoemission spectrum. The little spectral weight found at lower energies is due to the finite broadening η used in our DDMRG calculations. Note that the third and fourth spectral features are not visible for small $|k|$ because they are too close to the broadened and comparably much stronger peaks belonging to other structures.

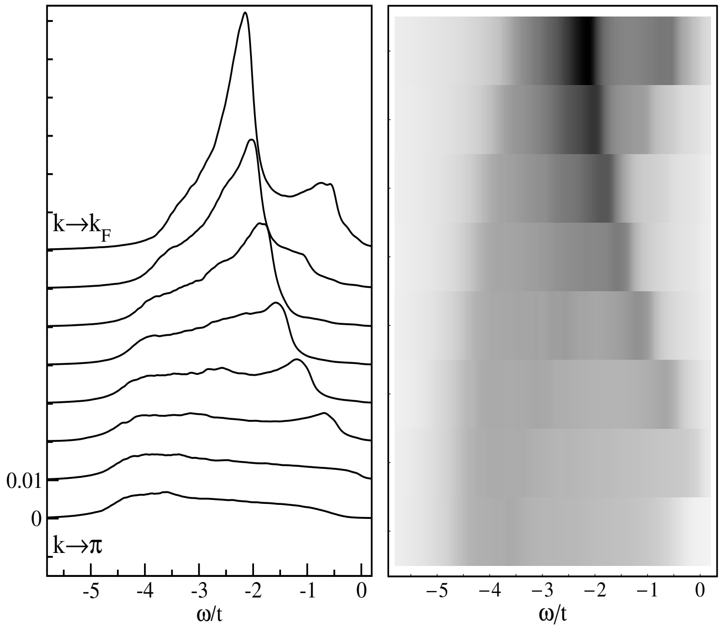

Figure 7.5: Line shapes (left) and gray-scale plot (right) of the spectral function $A(k, \omega)$ for $k_{\mathrm{F}} < k < \pi$ calculated with a broadening $\eta = 0.1t$ using DDMRG on $L = 90$ lattice sites.

7.2.3 Comparison with Bethe-Ansatz Energies

Figure 7.6 shows the dispersion $\omega(k)$ of the various features found in the DDMRG spectrum for the 90-site chain. One clearly sees that the shadow bands are just the continuation of the holon bands. The dispersions $\omega(k)$ should naturally correspond to specific excitation bands $\epsilon(k)$ of the Hubbard model. To identify these excitations we have calculated the excitation energies $\epsilon(k)$ for the removal of an electron in the Hubbard model on a 90-site chain using the Bethe-Ansatz solution introduced in section 3.4. There, we have seen that physical excitations of the Hubbard Hamiltonian comprise of an even number of holons and spinons. In particular, the holon-spinon excitation (section 3.4.2) corresponds the removal of an electron. In figure 7.6 we show those excitation bands $\epsilon(k)$ which correspond to the dispersing features found in the DDMRG spectral function. The excellent quantitative agreement between the Bethe-Ansatz results calculated for periodic boundary conditions and our numerical data confirms that the open chains used in our DDMRG calculations do not affect the spectral properties significantly.

Due to the separation of spin and charge dynamics, electron-removal excitations with momentum k are made of independent spin and charge excitations with momenta k_s and $k_\mathrm{c} = k - k_\mathrm{s}$, respectively. The spinon band between $-k_\mathrm{F}$ and k_F is related to excitations with the lowest possible binding energy for $k_\mathrm{c} = 0$ and $|k_\mathrm{s}| \leq k_\mathrm{F}$. This defines the spinon dispersion $\epsilon_\mathrm{s}(k_\mathrm{s})$, which has a width of about $0.5t$ and gives the spectral onset for $|k| < k_\mathrm{F}$. The holon/shadow bands going from $-k_\mathrm{F}$ to $3k_\mathrm{F}$ and from $-3k_\mathrm{F}$ to k_F correspond to excitations with the lowest possible binding energy for $|k_\mathrm{s}| = k_\mathrm{F}$, $0 \leq |k_\mathrm{c}| \leq 4k_\mathrm{F}$, and $k_\mathrm{s}k_\mathrm{c} < 0$. This defines the holon dispersion $\epsilon_\mathrm{c}(k_\mathrm{c})$ with a width of about $2t$. It gives the spectral onset for $2k_\mathrm{F} \leq |k| \leq 3k_\mathrm{F}$. The peaks found at low binding energy for $k_\mathrm{F} \leq |k| \leq 2k_\mathrm{F}$ correspond to secondary holon bands made of similar excitations as the holon-shadow bands but with parallel spin and charge momenta ($k_\mathrm{s}k_\mathrm{c} > 0$). They give the spectral onset for $k_\mathrm{F} \leq |k| \leq 2k_\mathrm{F}$. For $3k_\mathrm{F} < |k| < \pi$ this onset corresponds to a secondary spinon band with $k_\mathrm{c} = \pm 4k_\mathrm{F}$ and $|k_\mathrm{s}| < k_\mathrm{F}$.

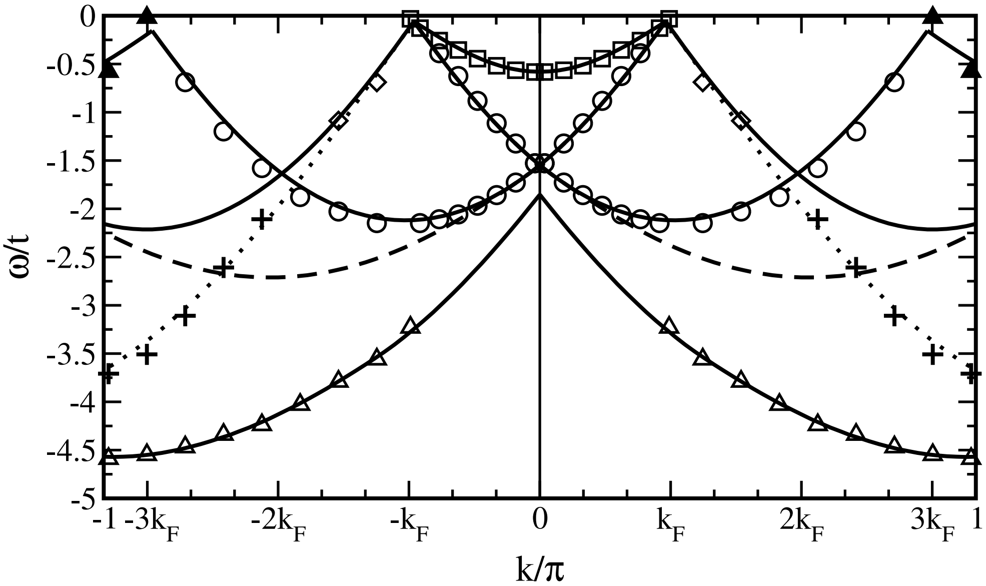

Figure 7.6: Dispersion $\omega(k)$ of the structures observed in the DDMRG spectral function: spinon band (square), holon-shadow bands (circle), secondary holon bands (diamond), lowest "$4k_\mathrm{F}$"-singlet excitations (plus), and lower (open triangle) and upper (solid triangle) spectral edges. Lines show dispersions $\epsilon(k)$ obtained from the Bethe-Ansatz solution.

In figure 7.6, a dashed line shows the dispersion of the lowest possible excitations made of one spinon and one holon, i.e., the minimum of $\epsilon_{\mathrm{c}}(k_{\mathrm{c}}) + \epsilon_{\mathrm{s}}(k_{\mathrm{s}})$ for a given $k = k_{\mathrm{c}} + k_{\mathrm{s}}$. This lower edge of the spinon-holon continuum is not related to any feature in the DDMRG spectral function and one finds spectral weight at lower energy ω. Therefore, the Hubbard model spectral function cannot be explained with spinon-holon excitations only. Actually, the lower edge of the spectrum follows the dispersion of the lowest states made of one spinon and a single charge excitation called "$4k_{\mathrm{F}}$"-singlet excitation in Ref. [19]. Finally, the very weak peaks found for $-2t > \omega > -4t$ and $|k| \gtrsim 2k_{\mathrm{F}}$ seem to be related to the lowest possible "$4k_{\mathrm{F}}$"-singlet charge excitations with $k_{\mathrm{s}} = \pm k_{\mathrm{F}}$ and $k_{\mathrm{c}}k_{\mathrm{s}} > 0$.

In Ref. [65] it was shown that the dispersion of the TCNQ related peaks in the ARPES spectrum of TTF-TCNQ could be mapped onto excitation bands of a one-dimensional Hubbard model. Our DDMRG calculations show that the Hubbard model also explains qualitatively the experimental spectral weight distribution. However, a quantitative comparison is not possible because of the strong background contribution in the ARPES data. The ARPES spectrum features labeled (a), (b), and (d) in figure 7.3 perfectly match the (singular) features found in the Hubbard model spectral function for momenta $k < k_{\mathrm{F}}$, the spinon, holon, and shadow bands, respectively. The agreement confirms that the ARPES spectrum of TTF-TCNQ shows the signature of spin-charge separation over the scale of the conduction band width, of the order of 1 eV. In the next section we discuss how the spectral features (c) and (d) for momenta $k > k_{\mathrm{F}}$ can be understood in terms of the electron-removal spectrum of the TTF band which we have not discussed so far.

7.2.4 Exponents

In Luttinger-liquid theory, cf. section 3.1, the spectral functions have singularities

$$A(k,\omega) \sim |\omega - \epsilon(k)|^{-\alpha} \tag{7.4}$$

for energies $\epsilon(k) \propto |k \pm k_{\mathrm{F}}|$ given by the spinon and holon linear dispersions [17, 18]. For a system which is invariant under spin rotation the exponents α are related to the Luttinger-liquid parameter K_ρ through $\alpha_{\mathrm{s}} = (4 - K_\rho - K_\rho^{-1})/4$ on the spinon branch and $\alpha_{\mathrm{c}} = (6 - K_\rho - K_\rho^{-1})/8$ on the holon branch. The parameter K_ρ can be calculated in the one-dimensional Hubbard model [66]. One finds $K_\rho \approx 0.68$ for $U = 4.9t$ and $n = 0.6$, which corresponds to exponents $\alpha_{\mathrm{s}} = 0.46$ and $\alpha_{\mathrm{c}} = 0.48$.

In view of the results from Luttinger-liquid theory, it is natural to ask whether the broadened peaks found in our DDMRG calculations become singularities of the spectral function in the thermodynamic limit. It was recently pointed out by [67] that if a microscopic model belongs to the Luttinger-liquid universality class we cannot expect $A(k,\omega)$ to show algebraic singularities apriori: Whether the model displays power-law divergences *away* from the limits $|k \pm k_{\mathrm{F}}| \to 0$ and $\omega \to 0$ has to be seen from case to case. Furthermore, given there are divergences it is not clear how these are related to the Luttinger-liquid parameters K_ρ and K_σ or, indeed, if they are related at all.

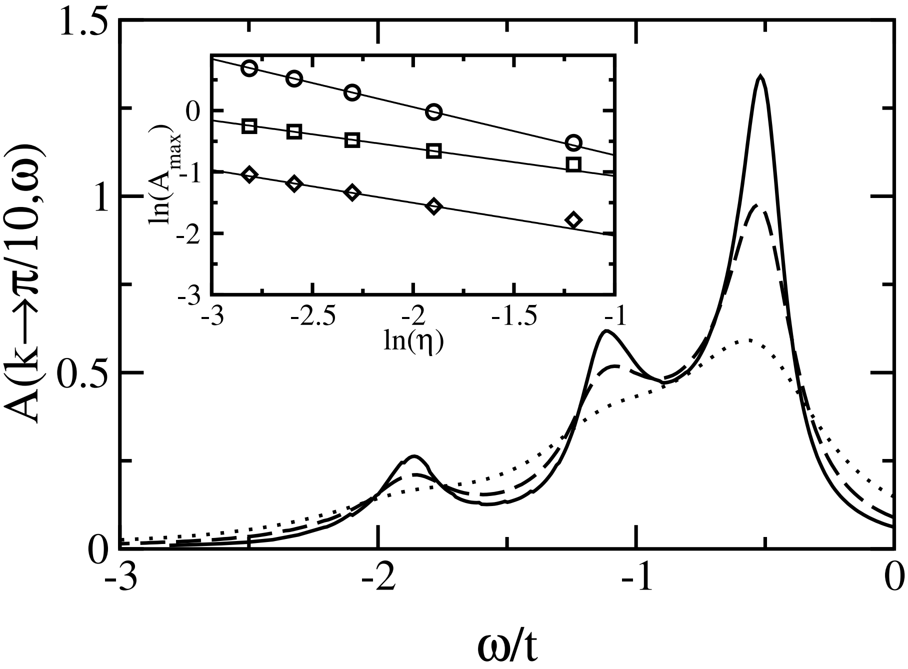

Figure 7.7: Spectral functions $A(k \approx \pi/10 = k_F/3, \omega)$ calculated with DDMRG for system sizes $L = 30$ (dotted), 60 (dashed), and 90 (solid). Inset: scaling of the peak maxima for $0.3 \le \eta/t \le 0.06$ $(30 \le L \le 150)$. Solid lines are fits.

In order to answer this question and to estimate the exponents α, we have performed a finite-size-scaling analysis [39]. The spectral function $A(k, \omega)$ is calculated for several system sizes L with a broadening scaling as $\eta = 9t/L$. Some spectra for $k \approx \pi/10 = k_F/3$ are shown in figure 7.7. The scaling of the peak maxima $A_{\max}$ with η can then be analyzed, see the inset of figure 7.7. If $A_{\max}$ diverges as $\eta^{-\alpha}$ $(0 < \alpha < 1)$ for $\eta \to 0$, the spectral function has a singularity with exponent α in the thermodynamic limit. A Landau quasi-particle corresponds to a Dirac δ-function and thus to a peak diverging as η^{-1}, see section 5.1.6.

From this scaling analysis we find that the spinon, holon, and shadow band peaks become singularities in the thermodynamic limit. We do not find any diverging peak with an exponent larger than 0.86 which confirms the absence of Landau quasi-particles. For $k = \pi/10$, the spinon, holon, and shadow-band exponents are $\alpha = 0.78$, 0.44, and 0.56, respectively. For $k = 0$, we obtain $\alpha = 0.86$ for the spinon band and $\alpha = 0.70$ for the holon/shadow band. Therefore, the exponents α are momentum-dependent and for finite $|k \pm k_F|$ they significantly differ from the Luttinger-liquid predictions for $|k| \to k_F$. A recent analytical study [68] has also shown that these exponents are strongly k-dependent. It is not possible to determine the exponents α in the asymptotic Luttinger-liquid regime, $k \to k_F$ and $\omega \to 0$, with DDMRG because the finite-size effects are not under control in that limit.

7.2.5 Density of States at Filling $n = 0.6$

The local density of states of the Hubbard model varies as

$$\rho(\omega) \sim |\omega|^{\alpha} \tag{7.5}$$

close to $\omega = 0$. The exponent α ranges from $\alpha = 0$ to $\alpha = 1/8$ for $U/t \to 0$ and $U/t \to \infty$, respectively. As noted in section 7.1.2, the experimental onset of the angle-integrated ARPES (PES) spectrum at E_F varies as in (7.5), however, with an exponent of $\alpha_{\text{exp}} \approx 1$. The simple Hubbard model is therefore not adequate to describe the low-energy ($\omega < 200\,\text{meV}$) range of the angle-integrated ARPES spectra.

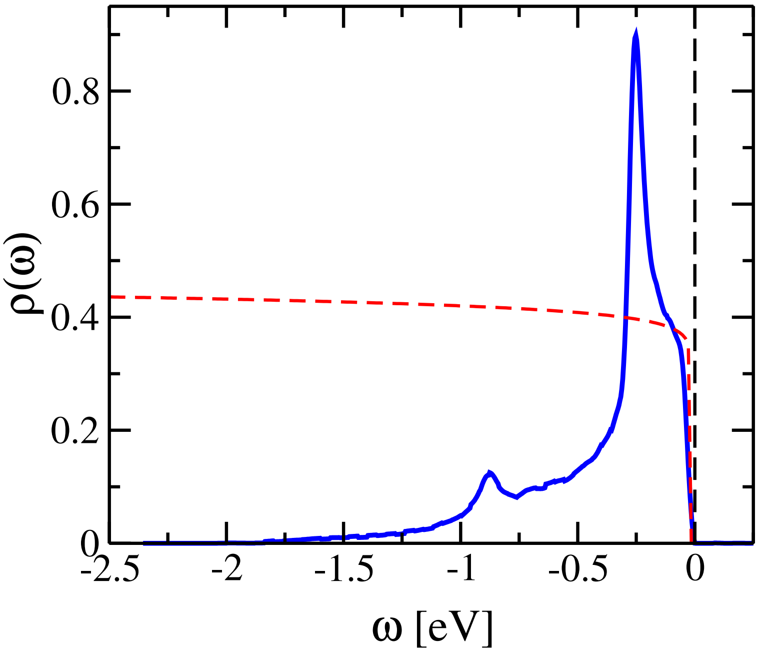

Figure 7.8: Local density of states $\rho(\omega)$ of the Hubbard model with parameters $U/t = 4.9$ and filling factor $n = 0.6$. The solid blue line is the result of a DDMRG calculation and the dashed red line indicates an onset of $|\omega|^{1/8}$ as discussed in the text.

How does this discrepancy fit in to the theoretical picture presented so far? It is known that the inclusion of longer-range interactions in the microscopic model yields exponents of the onset up to $\alpha \sim 1$ [69]. Thus, nearest- and next-nearest-neighbor interactions in the Hamiltonian can reconcile this apparent discrepancy [70]. This, however, may change the spectral properties considerably. It must be kept in mind though that other mechanisms may equally contribute to the experiment which we discuss in the following paragraphs.

Impurities which will be inevitably present in real systems, including the surface, will strongly influence the low energy physics in one dimension. In fact, it has been argued that defects on the surface of an organic conductor can give rise to an exponent α close to unity [71] through the formation of finite strands of electrons. These systems belong to a universality class of “bounded Luttinger liquids”. Again, we face the problem that the Luttinger-liquid results are valid only in the limit $\omega \to 0$ whereas the observed linear onset has a range of $\sim 0.1\,\mathrm{eV}$. For example, consider the local density of states of the open Hubbard chain in figure 7.8 with system length of $L = 90$ lattice sites.

In the energy range of interest the onset appears to follow the form (7.5) but with a smaller exponent close to 1/8 as in the periodic case. In the limit $\omega \to 0$ the open Hubbard chain belongs to the aforementioned bounded Luttinger-liquid universality class and we should observe an exponent close to unity. This is not the case. Of course, due to the finite resolution of the DDMRG method we cannot make definite statements about the Luttinger-liquid limit. Nevertheless the given resolution allows us to rule out the explanation of the linear onset due to a bounded Luttinger liquid at *finite* energies.

Below $T = 54\,\mathrm{K}$ TTF-TCNQ becomes Peierls insulating and consequently there is a coupling to phonon degrees of freedom that drive the Peierls transition. The resulting Peierls gap has been reported as 20 meV [55] which is smaller than the region of the linear onset of $\rho(\omega)$. Indeed the phonon spectrum of TTF-TCNQ reaches up to 200 meV [72] which indicates that coupling to other phonons than those involved in the transition could play an important rôle in this material, too. Therefore the exponent enhancement could partly be due to electron-phonon coupling.

7.3 TTF Band

So far we have only discussed the electron removal spectrum of the 1D Hubbard chain at filling $n = 0.6$ that describes photoemission from the TCNQ Band. In this section we discuss results for the photoemission spectral function of the TTF chain at filling $n' = n - 0.6 = 1.4$, and point out their relevance for the TTF-TCNQ ARPES data. The DFT-Bandstructure calculation indicates that the TTF band is located around the Z-point or, equivalently, $k = \pi$ in our one-dimensional Brillouin zone. We have seen in the previous section that the spectral weight of the TCNQ band is suppressed strongly, up to two orders of magnitude, above its Fermi momentum $k_{\mathrm{F}}^{\mathrm{TCNQ}} = 0.3\pi$. The ARPES spectral weight at $k > k_{\mathrm{F}}^{\mathrm{TCNQ}}$ should therefore be dominated by the TTF band if it shows significant weight.

Our choice of parameters for the TCNQ band is justified by the agreement of the holon and spinon dispersion with the dispersion of ARPES bands below $k_{\mathrm{F}}^{\mathrm{TCNQ}}$. In the TTF band we suggest that the same values of U and t should be adequate. This is corroborated by the fact that the DFT bandstructure yields the same total band-width which suggest that the ratio U/t should be comparable in both TTF and TCNQ chains. Figure 7.9 shows a density plot of the electron-removal spectrum $A(k, \omega)$ of a Hubbard chain with $U/t = 4.9$ and filling factor $n = 1.4$. There are two distinct energy scales at which we observe spectral weight with no significant spectral weight in-between. We first discuss the structures at low binding energies and then we consider the features at high binding energies.

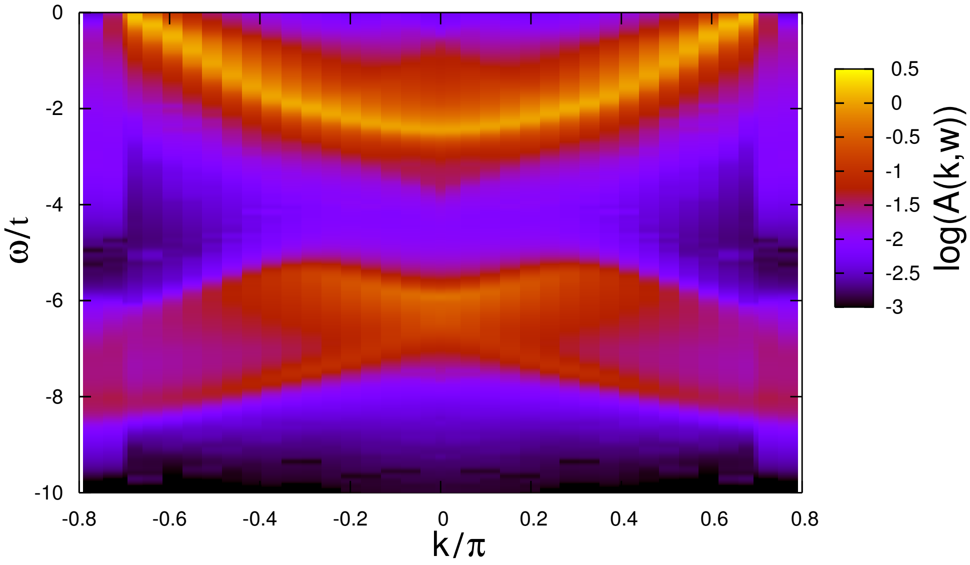

Figure 7.9: Density plot of the electron-removal spectrum of the Hubbard chain with parameters $U/t = 4.9$ and band filling $n = 1.4$. The two-particle continuum between $\omega = 0$ and $\omega = -5t$ is less structured than in the case of $n = 0.6$ band filling. Well below the two-particle continuum we find significant spectral weight dispersing down to more than twice the free electron band width displaying rich internal structure.

7.3.1 ARPES Spectrum at Filling $n = 1.4$: Small Binding Energies

The electron-removal spectrum of the Hubbard chain with band filling $n = 1.4$ is shown in figure 7.9. The low binding-energy part is dominated by a broad peak that disperses from $k = k_{\mathrm{F}}^{\mathrm{TTF}} = 0.7\pi$ to $k = -k_{\mathrm{F}}^{\mathrm{TTF}} = 0.7\pi$. Some structures are present close to $k = \pm k_{\mathrm{F}}^{\mathrm{TTF}}$ and $k = 0$. However, they are not visible on the scale of the figure, since their spectral weight is to small. They can be identified by investigating the first and second derivative of the DDMRG data. For the rest of this section we restrict our discussion to the lower part of the DDMRG spectrum. We consider the spectrum at energies below $\approx -5t$ in subsection 7.3.2.

What are the elementary excitations of the Hubbard model that can account for the spectral weight in the range down to $-2.5\,t$ in figure 7.9? It turns out that we can answer this question in the same spirit as in the case of the TCNQ chain. To this end, consider figure 7.10 where we can see a plot of both the DDMRG structures and the exact excitation energies from the Bethe Ansatz. Specifically, we consider an *antiholon-spinon* excitation described in section 3.2 of the Hubbard model with band filling $n = 0.6$. This is the excitation relevant for the *inverse* photoemission spectral function. Nevertheless, everything discussed there can be directly applied to the photoemission spectral function of the chain with filling $n = 1.4$ since the Hubbard model is particle-hole symmetric.

Thus, when we speak of an antiholon-spinon excitation at band filling $n = 0.6$ this is equivalent to a holon-spinon excitation at band filling $n = 1.4$. To avoid confusion we stick to the latter manner of speaking since it corresponds to the physical situation at hand. Note, however, that the integral equations of section 3.3 are defined for $n < 1$ and we have transformed the results accordingly.

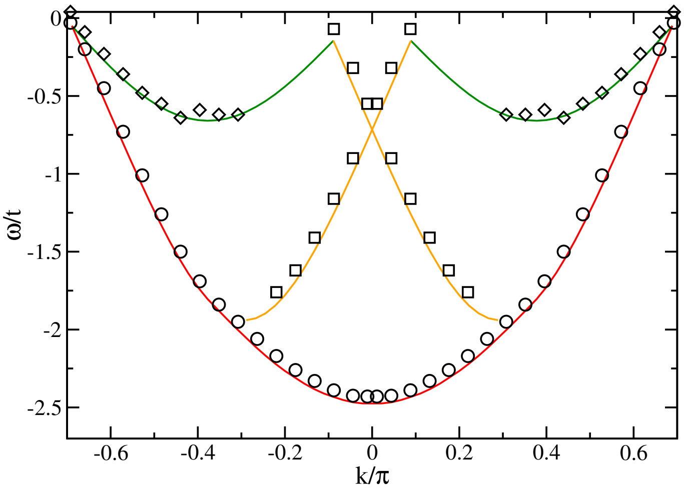

Figure 7.10: Comparison of the peak positions in the DDMRG photoemission spectrum at low binding energies with the exact excitation energies from the Bethe-Ansatz solution. The filling is $n = 1.4$, as appropriate for the TTF chain. The most prominent structure in the spectrum is associated with the lower boundary of the particle-hole transformed antiholon-spinon continuum (red). Steps in $A(k, \omega)$ (squares) follow the holon branch (orange) and peaks in the second derivative follow the spinon branch (green).

The upper onset (diamonds) at low binding energies follows the spinon branch (green) from $\pm k_F^{\mathrm{TTF}} = \pm 0.7\pi$ to smaller momenta. This branch can be identified in the DDMRG spectrum as a peak in the first derivative of $A(k, \omega)$. These peaks in $A'(k, \omega)$ become indistinguishable from the broadened background at approximately $k = \pm 0.4\pi$. The lower onset of the two-particle continuum is defined through the lower boundary of all possible holon-spinon excitations, or, upon transforming $n \rightarrow 2 - n$, by the onset of *antiholon-spinon* excitations. In addition to the dispersing peaks, we also observe structures that are steps (squares) rather than divergences. Around $k = 0$ these steps are consistently described by the holon dispersion. Altogether, the low-energy part of the one-particle spectral function $A(k, \omega)$ at band-filling $n = 1.4$ shows a less rich structure than the photoemission spectrum at filling $n = 0.6$. Moreover, the observed weight of the spinon branch is very small, visible only in $A'(k, \omega)$, in contrast to the observation of a strong spinon weight in the TCNQ band. The strong peak at high binding energies is associated with both spinon and holon branches because the onset is given by either excitation depending on momentum, as indicated in figure 7.10. We expect that this broadened peak turns into an algebraic singularity in the thermodynamic limit.

7.3.2 ARPES Spectrum at Filling $n = 1.4$: Large Binding Energies

It remains to discuss the photoemission spectrum shown in figure 7.9 at binding energies in the interval $-5t$ to $-9t$. It cannot be explained with two-particle excitations built from (anti)holons and spinons. In fact, the two-particle continuum is well-separated from this range of energies. It would be tempting to interpret this excitation in terms of higher-order excitations containing m-pairs of holon-spinon or antiholon-spinon excitations plus any number of $4k_{\mathrm{F}}$-singlet excitations. All these possibilities are ruled out, however, since all these combinations are gapless. While logically it could be possible that matrix element effects cause the spectral weight to be very small or zero between energies of $-2.5t$ to about $-5t$, this argument appears to be somewhat artificial.

A more natural explanation can be found in terms of a different type of excitation that was introduced in section 3.2. It is called a k-Λ-string, a bound state of the charge degrees of freedom, which is separated from the two-particle continuum by a gap. Some aspects of the spectrum at high binding-energies fit nicely with this explanation. Consider an excitation with occupation numbers $N = N_{\mathrm{GS}} + 1$, $M_1 = N_{\mathrm{GS}}/2 - 1$, ${M_1}' = 1$, $\mathcal{M}_e = N - 1$. This corresponds to adding an electron with spin up to the system and forming a k-Λ-string of length $m = 1$ as described in section 3.2. This excitation is compatible with the sum rules (3.45)-(3.46) and, according to (3.51)-(3.56), there is no hole in the sequence of spin quantum numbers and hence no spinon. Nevertheless, we have an excited state with the quantum numbers of an *additional* electron. As before, we apply a particle-hole transformation to all results to get the contribution relevant to *photoemission* in the chain with filling $n = 1.4$.

The dispersion of the peaks in the DDMRG spectral function and the excitation energies of the k-Λ-string are plotted together in figure 7.11. First, let us focus on the region around $-0.4\pi < k < 0.4\pi$. The red line denotes the dispersion of a single k-Λ-string with length $m = 1$, as described in section 3.4. This line very closely resembles the dispersion of the strong peaks (black squares) in the DDMRG data. At $|k| \approx 0.4\pi$ the k-Λ-string disperses down towards slightly lower binding energies than the DDMRG peaks. This could be attributed to the finite size of the system. We have learnt in section 3.2 that the exact solution of the discrete Bethe-Ansatz equations may exhibit substantial finite-size gaps (there with respect to $\omega = 0$) which vanish only as the system size approaches the thermodynamic limit. The energy continuum in which the k-Λ-string plus holon excitation reside is indicated in figure 7.11 by the blue points. When $|k|$ becomes larger than 0.4π the DDMRG peaks disperse down to smaller ω and closely follow the onset of the holon-spinon continuum. This scenario is supported by the intuition that a divergence in the density of states and thus also in the spectral function should occur along the onsets of excitation continua. In this case, the onset is defined precisely by the holon branch where the k-Λ-string supplies only a constant to the energy, namely $\Delta_{k\Lambda} = -2\mu - U$. The second dispersive feature in the DDMRG spectral function is shown by the orange circles. This excitation begins to disperse from $\omega \approx -6.5t$ at the center of the zone up to $\omega \approx -8t$ at the zone boundary. This behavior is roughly mimicked by the lower onset of the k-Λ-string plus holon continuum. The difference is so large, however, that it cannot be simply explained by a finite-size effect.

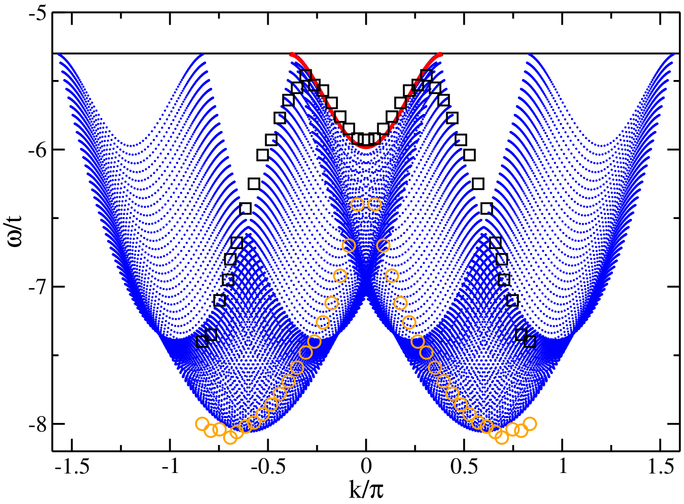

Figure 7.11: Dispersion of structures at high binding energies in the photoemission spectrum of the Hubbard model with $U/t = 4.9$ and $n = 1.4$. Symbols indicate peaks in the DDMRG data. Also shown is the continuum of excitations made of one k-Λ string of length $m = 1$ and a holon. The onset of this combination of elementary excitations for small momenta is shown as a red line. The DDMRG peaks follow this onset in a substantial part of the Brillouin zone.

Upon closer inspection there seems to be a shift of approximately 0.15π in the dispersion of the peaks and the dispersion of the holon branch. The shift in momentum could be attributed to the excitation of soft modes that carry this additional momentum.

There is an apparent discrepancy of our explanation of figure 7.11. There is no branch visible in the DDMRG data that disperses to higher binding energies for momenta $|k| > k_F^{\mathrm{TCNQ}} = 0.7\pi$, analogously to the secondary holon band in TCNQ. Within our energy resolution of $\eta/t = 0.1$ we cannot discern a dispersive peak that follows upwards from k_F^{TCNQ}. We have to conclude that the spectral weight in the lower Hubbard band can no longer be explained in an equally simple kinematic approach as the two-particle (holon-spinon) spectrum at lower binding energies. Matrix element effects must play a dominant rôle in the lower Hubbard band.

From an experimental point of view is is difficult to detect the lower Hubbard band because of background noise and other bands lying below the Fermi surface. Still, future experiments may find evidence of the lower Hubbard band.

7.3.3 Density of States at Filling $n = 1.4$

In order to quantify how much total weight the excitations in the lower Hubbard band carry compared to the two-particle continuum (upper Hubbard band), we have calculated the local density of states for filling $n = 1.4$. This is shown in figure 7.12. Clearly, the lower Hubbard band carries a significant amount of spectral weight. Furthermore, the onset of the lower Hubbard band that we determine by a deconvolution of the data starts at $\omega/t = -5.3 = -2\mu - U$. This coincides precisely with the lowest binding energy (3.81) of a k-Λ-string. The peak of $\rho(\omega)$ at $\omega/t \approx -6$ can be explained by the energy of the k-Λ-string at zero momentum which further corroborates our particular interpretation of the spectral weight with this bound state.

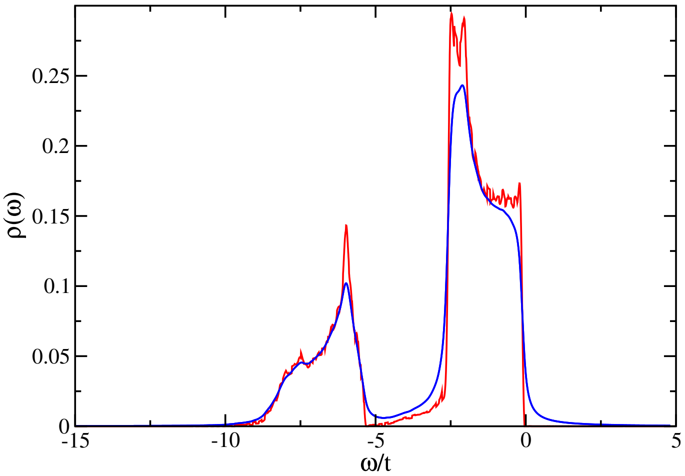

Figure 7.12: Local density of states of the Hubbard model with $U/t = 4.9$ and $n = 1.4$ calculated with DMRG (blue line). Also shown is the deconvolution of the DDMRG data (red line). Most weight resides in the energy ranges that corresponds to spinon-holon excitations (upper Hubbard band). Despite the noise in the deconvolved data, we recognize that the onset of the lower Hubbard band ($\Delta_{k\Lambda} = -2\mu - U = -5.3t$) lies well above the prominent peak ($\approx -6t$). As discussed in the text, the onset corresponds to the minimum in the binding energy of a $k - \Lambda$-string of length $m = 1$ when no additional holon is excited. The peak is consistently explained by the energy of the same excitation at momentum $k = 0$.

Now that we have the density of states of the Hubbard chain at band filling $n = 1.4$ we can plot the total density of states of the Hubbard model both for the creation ($\rho^{>}$) and annihilation ($\rho^{<}$) of a particle at band filling $n = 0.6$. A plot of the total density of states is given in figure 7.13. The electron-removal part of the density states and the electron-addition part are separated by a pseudo-gap at $\omega/t = 0$ which can be seen in the deconvolution of the DDMRG data. This is of course exactly the expectation from Luttinger-liquid theory. We can now check the accuracy of the DDMRG results by invoking a sum-rule for the density of states, namely

$$\int_{-\infty}^{\infty} \mathrm{d}\omega \left(\rho_\sigma^{>}(\omega)) + \rho_\sigma^{<}(\omega)\right) = 1 \; . \tag{7.6}$$

Here $\rho_\sigma^{>}(\omega)$ and $\rho_\sigma^{<}(\omega)$ refers to photoemission and inverse photoemission density of states for electrons with spin σ. The sum-rule is fulfilled within an error of less than two percent, indicating that we have not missed any significant spectral weight. This independently confirms the accuracy of the DDMRG spectra.

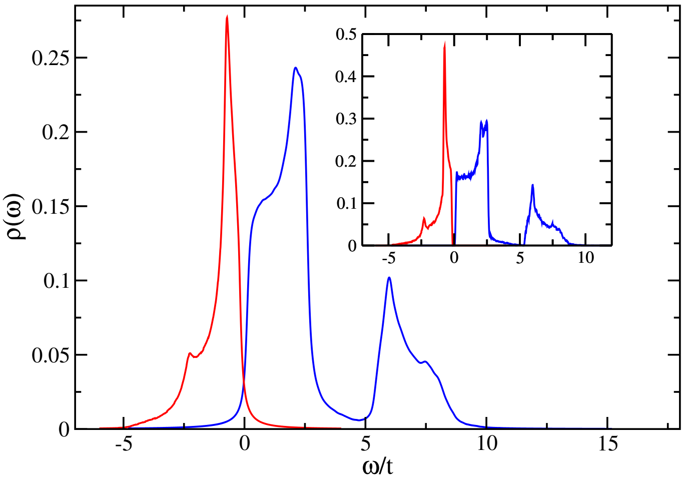

Figure 7.13: Density of states of the Hubbard model with $U/t = 4.9$ and $n = 0.6$ for the annihilation (red) and creation (blue) of a particle. The sum rule (7.6)is fulfilled within a relative error of less than two percent. Both parts of the density of states are separated by a pseudo-gap at zero frequency which can be easily seen in the deconvolved data (inset).

7.4 Interpretation of TTF-TCNQ ARPES Spectra

According to our discussion in section 7.3.1, there is an intense peak following the holon-spinon onset in the photoemission spectrum at band filling $n = 1.4$. This dispersive structure should be observable in the ARPES spectrum of TTF-TCNQ. According to band theory, see section 7.1.2, this spectral weight should be centered around $k = \pi$. Assuming that our initial assumption for the choice of parameters of the TTF band is correct we consider again figure 7.3 with the experimental ARPES data. If the spectral feature (c) is associated with the secondary holon band, it should cross (d), the shadow band, at $2k_{\mathrm{F}}^{\mathrm{TCNQ}}$ which is not observed. Instead the peak labeled (d) vanishes above roughly $2k_{\mathrm{F}}^{\mathrm{TCNQ}}$ and (c) continues to disperse to higher binding energies. The disappearance of (d) is compatible with its diminishing spectral weight in the DDMRG spectrum. While it appears in figure 7.3 that (d) remains strong up to the crossing point with (c) we recall that it does not show the absolute intensity but the second derivative of the ARPES data. The dispersion of (c) rules out the interpretation of (c) as a secondary holon branch. Instead, we interpret (c) as the onset of the holon-spinon spectrum of the TTF band centered around $k = \pi$ which resolves the above discrepancy. Moreover, this interpretation also explains that (c) tends to slightly higher binding energies than structure (d): The minimum of the TCNQ secondary holon band in the DDMRG spectral function is $\omega = -0.84$eV whereas the minimum of the TTF spinon-holon continuum is $\omega/t = -0.96$eV, in agreement with the trends in figure 7.3. Qualitatively, this interpretation also reflects the trend of the total weight in figure 7.2. A direct comparison of lineshapes is not possible due to the strong background in the experimental data.

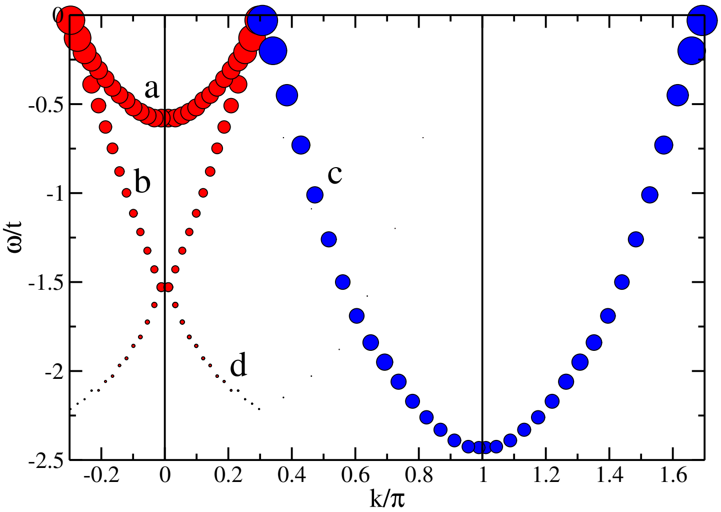

Figure 7.14: Dispersive structures of the Hubbard model with filling $n = 0.6$ and $n = 1.4$. The size of the symbols is directly proportional to the spectral weight. Only the TCNQ holon and spinon branches (red) and the TTF holon-spinon onset (blue) are visible on this scale. This reflects the experimental situation (see figure 7.3).

The experimental setup introduces a finite broadening which amounts to a convolution of the divergences with a Lorentzian distribution. Hence, some TTF and TCNQ excitation branches can not be observed experimentally due to their little spectral weight. For example, we expect a dispersing holon divergence that has a soft mode close to $k = \pi$, see, e.g., figure 7.6, which is not present in the ARPES spectrum.

In figure 7.14 we summarize the situation for TTF-TCNQ. There, we plot the dispersion of the strongest DDMRG spectral features. We omit very weak peaks since they are not visible on this scale. The size of the symbols is *directly proportional* to the spectral weight of the peak. This makes very clear how strongly the TCNQ holon and spinon branch and the TTF holon-spinon onset dominate the one-particle spectral function.

7.5 Conclusion

In summary, we have used a novel approach to compute the photoemission spectral function of the Hubbard model in open chains using DDMRG. We have shown the unprecedented accuracy of our method and addressed the influence of the boundary conditions by comparison with the exact Bethe-Ansatz solution of a periodic system.

The finite-energy structure of the electron removal spectrum is significantly richer than the Luttinger-liquid picture. The comparison between theory and experiment shows that we can quantitatively interpret the dispersion of excitations in the ARPES spectrum of the quasi-1D charge transfer salt TTF-TCNQ in terms of the one-particle spectral function of Hubbard chains with filling $n_{\mathrm{TCNQ}} = 0.6$ and $n_{\mathrm{TTF}} = 1.4$. The agreement gives striking evidence for spin-charge separation over an energy range of 1 eV in TTF-TCNQ. Furthermore, we can give the experimental structures a precise meaning in terms of holons and spinons. A careful finite-size scaling analysis enables us to extract the momentum-dependent exponents of dispersive divergent structures.

Chapter 8

Optical Properties of Quarter Filled Chains

In chapter 7 we presented results for the charge-transfer salt TTF-TCNQ. In this chapter we consider another important example of such compounds, the family of Bechgaard salts $(\mathrm{TM})_2X$, where TM is the organic molecule TMTSF (tetramethyltetraselenafulvalene) or TMTTF (tetramethyltetrathiafulvalene), and X denotes an anion such as ClO_4^-, PF_6^-, Br^-, etc. These organic compounds exhibit strongly anisotropic behavior. Their electronic properties are generally believed to be describable by one-dimensional models above an energy scale of a few meV.

It has been proposed that the extended Peierls-Hubbard Hamiltonian (cf. section 2.1) is appropriate to model various aspects of the Bechgaard salts [73, 74, 75, 76, 77, 78]. In particular, it is believed that it can model their unusual optical properties [79, 80, 81, 82, 83]. The model captures both the physics of the Mott-insulating ground state and the electron-phonon coupling since it explicitely includes a lattice dimerization. The competition between these two energy scales may be relevant to explain optics in the Bechgaard salts.

While the low-energy part of the optical conductivity of one-dimensional Mott-insulators is thoroughly understood [39, 84, 85] the optical properties of the Peierls-Hubbard model are not known well. Accordingly, there has been no decisive comparison between experimental and theoretical results so far. We analyze the optical conductivity of the extended Peierls-Hubbard model at quarter band filling in this chapter and discuss the relevance of these results for the Bechgaard salts.

8.1 Model and Method

In this section we remind the reader of the extended Peierls-Hubbard model which we introduced in chapter 2 and list values for the model parameters which are deemed appropriate for the family of Bechgaard salts. Then we discuss the optical conductivity and how it is calculated with DDMRG.

8.1.1 Extended Peierls-Hubbard Model

The one-dimensional extended Peierls-Hubbard model is defined by the Hamiltonian (cf. section 2.1)

$$\begin{aligned}\hat{H} &= -t_1 \sum_{\text{odd } l;\sigma} \left(\hat{c}^{+}_{l,\sigma}\hat{c}_{l+1,\sigma} + \hat{c}^{+}_{l+1,\sigma}\hat{c}_{l,\sigma} \right) \\ &\quad -t_2 \sum_{\text{even } l;\sigma} \left(\hat{c}^{+}_{l,\sigma}\hat{c}_{l+1,\sigma} + \hat{c}^{+}_{l+1,\sigma}\hat{c}_{l,\sigma} \right) \\ &\quad +U \sum_{l} \hat{n}_{l,\uparrow}\hat{n}_{l,\downarrow} + V \sum_{l} (\hat{n}_l - \rho)(\hat{n}_{l+1} - \rho) \end{aligned} \tag{8.1}$$

with $t_1 = t(1+\delta/2)$ and $t_2 = t(1-\delta/2)$. It describes electrons (or holes) with spin $\sigma = \uparrow, \downarrow$ which can hop between nearest-neighbor sites, where the highest occupied molecular orbital (HOMO) of each TM molecule is centered.

It is known from stoichiometry that there are three electrons in the HOMOs of each pair $(\text{TM})_2$. Accordingly, the band comprising of the HOMOs is quarter filled in terms of holes or three-quarter filled in terms of electrons. In our analysis we use the hole representation and keep the number of particles N such that we have a density $\rho = N/L = 1/2$ for an even number of lattice sites L. The alternating hopping integrals $t_1 \geq t_2 \geq 0$ give rise to a single-particle dispersion (see section 2.1)

$$\epsilon(k) = \pm\sqrt{(\delta t)^2 \sin^2(k) + (2t)^2 \cos^2(k)} \tag{8.2}$$

with a total band width $4t$ and a (dimerization) gap $2\delta t = 2(t_1 - t_2)$. The Coulomb repulsion is mimicked by a local Hubbard interaction U, and a nearest-neighbor interaction V. The physically relevant parameter regime for Bechgaard salts is $U > 2V \geq 0$. In Table 8.1 we show some values of the model parameters t_1, t_2, U, and V which have been proposed to describe various $(\text{TM})_2\text{X}$ salts.

		t_1	t_2	U	V
$(\text{TMTTF})_2\text{PF}_6$	(Ref. [76])	130	90	910	180
$(\text{TMTSF})_2\text{PF}_6$	(Ref. [75])	250	225	1250	0
$(\text{TMTSF})_2\text{ClO}_4$	(Ref. [76])	290	260	1450	210

Table 8.1: Model parameters (in meV) for various Bechgaard salts from Refs. [75, 76].

Throughout the entire chapter we use open boundary conditions. In the presence of open boundaries it is important to work with the appropriate form of the nearest-neighbor repulsion. If we had set $\rho = 0$ in (8.1), we would observe surface effects at the system boundary. For $\rho = 0$, we find localized excitations at the end of the chains which are visible in the local charge densities, $\langle \hat{n}_l \rangle$, or spin densities, $\left\langle \hat{S}^z_l \right\rangle$.

At quarter filling the lower Peierls-band in equation (8.2) is effectively half filled. The Umklapp scattering in this band drives the system into an insulating ground state [77, 78]. This Mott-insulating state is accompanied by a $4k_{\mathrm{F}}$ bond order wave (BOW), where $k_{\mathrm{F}} = \pi\rho/2 = \pi/4$ is the Fermi momentum. However, another mechanism may render the system an insulator. When U and V are sufficiently large the system spontaneously breaks the translational symmetry and exhibits a $4k_{\mathrm{F}}$ charge density wave (CDW) [77, 86, 87]. The TMTSF compounds are considered to be realizations of one-dimensional Mott insulators [84] while the TMTTF compounds are believed to be charge ordered [78] as in a CDW-like state. For realistic parameters (see Table 8.1) of the model (8.1), however, the system is always Mott insulating [77]. We accordingly restrict ourselves to the Mott-insulating phase of the parameter space.

In our investigation we use open boundary conditions which result in rapidly decaying $2k_{\mathrm{F}}$-BOW and $2k_{\mathrm{F}}$- and $4k_{\mathrm{F}}$-CDW fluctuations in the ground state induced by the chain ends (Friedel charge oscillations). Note that for all parameters (δ,U,V) used in this chapter there is no long-range order or broken symmetry in the ground state, except for the $4k_{\mathrm{F}}$-BOW caused by the alternating hopping term in the Hamiltonian (8.1).

8.1.2 Optical Conductivity

The linear optical absorption is proportional to the real part $\sigma_1(\omega)$ of the optical conductivity, which is related to the imaginary part of the current-current correlation function by

$$\sigma_1(\omega > 0) = \lim_{\eta \to 0} \frac{-1}{L\omega} \Im \langle \psi_0 | \hat{J} \frac{1}{E_0 + \omega + \mathrm{i}\eta - \hat{H}} \hat{J} | \psi_0 \rangle \, . \tag{8.3}$$

Here $|\psi_0\rangle$ is the ground state of the Hamiltonian $\hat{H}$ and E_0 is the ground state energy. Assuming that the sites are equidistant, the current operator $\hat{J}$ is

$$\begin{aligned} \hat{J} &= -\mathrm{i}t_1 \sum_{\text{odd } l;\sigma} \left(\hat{c}^{+}_{l,\sigma} \hat{c}_{l+1,\sigma} - \hat{c}^{+}_{l+1,\sigma} \hat{c}_{l,\sigma} \right) \\ &\quad -\mathrm{i}t_2 \sum_{\text{even } l;\sigma} \left(\hat{c}^{+}_{l,\sigma} \hat{c}_{l+1,\sigma} - \hat{c}^{+}_{l+1,\sigma} \hat{c}_{l,\sigma} \right) \, . \end{aligned} \tag{8.4}$$

With these definitions the optical conductivity $\sigma_1(\omega)$ is given in units of $e^2 a/\hbar$, where $2a$ is the lattice constant and e the charge of a hole. The frequency ω is given in units of $t/\hbar$.

In an open chain the optical conductivity is also related to the imaginary part of the dipole-dipole correlation function

$$\sigma_1(\omega) = \frac{-\omega}{L} \Im \langle \psi_0 | \hat{D} \frac{1}{E_0 + \omega + \mathrm{i}\eta - \hat{H}} \hat{D} | \psi_0 \rangle \, , \tag{8.5}$$

where the dipole operator is

$$\hat{D} = \sum_{l=1}^{L} l \left(\hat{n}_l - \rho \right) = \sum_{l=1}^{L} \left(l - \frac{L+1}{2} \right) \hat{n}_l . \tag{8.6}$$

The application of DDMRG to optical properties has been shown to be very successful in simple one-dimensional Mott insulators, i.e., in the extended Hubbard model at half filling [39, 88, 10]. Here, we use the methods described in section 5.1.5 to calculate the excited states of the Hamiltonian which contribute to the optical spectrum (8.3). We thus determine the excitation energy ω_1 of the lowest eigenstate $|\psi_1\rangle$ with a finite matrix element $\langle\psi_1|\hat{J}|\psi_0\rangle$ in finite chains very accurately. Up to $m = 320$ density-matrix eigenstates are kept per block in DDMRG calculations and up to $m = 768$ in ground state DMRG calculations. Truncation errors are negligible for all results presented here. Thus, the accuracy of our calculations is mostly limited by the finite broadening or resolution $\eta \sim 1/L$ imposed by finite system lengths.

8.2 Results

Our analysis of the model (8.1) begins with the investigation of three limiting cases [73] for which the main features in the optical conductivity $\sigma_1(\omega)$ can be easily understood. Neglecting the nearest-neighbor coulomb repulsion V the model reduces to the Peierls-Hubbard model (2.13) that depends on the parameters U and δ only. We then consider the following limits.

1. Large-dimerization limit: $\delta \to 2$ or $t_2 \ll t_1$, $U \leq 4t_1$ (section 8.2.1).
2. Strong-coupling limit: $U \gg t_1 > t_2$ (section 8.2.2).
3. Weak-coupling limit: $U \ll t_2 < t_1$ (section 8.2.3).

We proceed by discussing the evolution of the optical spectrum between these limits in sections 8.2.4 and 8.2.5. Finally, in section 8.2.6 we take into account the effect of the non-local electron-electron interaction V (exciton formation) and determine the optical properties of (8.1) for parameters δ, U, and V which are believed to be appropriate for $(\mathrm{TM})_2X$ salts.

8.2.1 Large Dimerization

In the dimer limit $\delta = 2$ and $V = 0$ the system (8.1) breaks down into independent pairs of sites, *dimers*, with no hopping between dimers and hopping $t_1 = 2t$ within the dimer [73]. Thus, any eigenstate of the system is a direct product of the dimer eigenstates which correspond to solutions of the two-site Hubbard model. At quarter filling there is one localized hole per dimer. Since the current operator $\hat{J}$ defined by equation (8.4) does not couple the dimers ($t_2 = 0$) only *intra-dimer* excitations contribute spectral weight in this limit. These excitations correspond to the transition from the bonding to the anti-bonding orbital of the two-site Hubbard model with an energy difference of $\Delta E = 2t_1$. Thus $\sigma_1(\omega)$ consist of a single δ-peak at

$$\omega = 2t_1 = 4t = 2\delta t \; . \tag{8.7}$$

In this limit it is possible to make charge excitations that have energies *below* the optical gap $\omega_1 = 2\delta t$. This involves processes where a hole is moved from one dimer to its nearest-neighbor. The corresponding excitation energies can be lower than ω_1 and we have $E_c < \omega_1$. Setting $U = 0$, for instance, yields $E_c = 0$. Note, that ($\delta = 2$, $U \geq 0$, $V = 0$) is the only part of full parameter regime where this is possible.

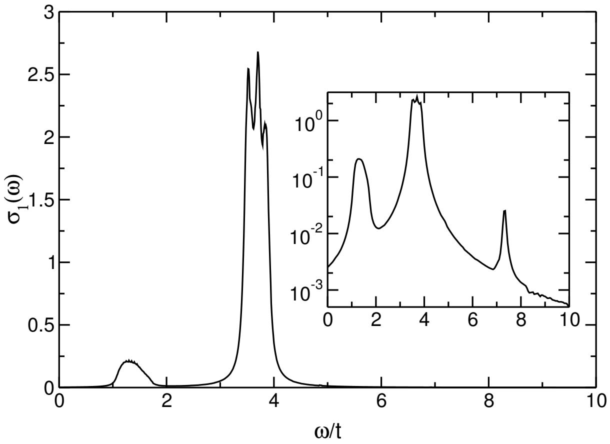

Figure 8.1: Optical conductivity $\sigma_1(\omega)$ in the large-dimerization limit ($\delta = 1.64$) for a strong effective coupling ($U = 3.64t \approx 20t_2$) with a broadening $\eta = 0.05t$ ($L = 128$ sites). Inset: same data on a logarithmic scale.

We now consider the case of intermediate Coulomb repulsion $U < 4t_1$ and small but finite $t_2 > 0$, because for larger values of U the strong-coupling limit $U \gg t_1$ is a more appropriate starting point. Any $t_2 > 0$ leads to the hybridization of dimer eigenstates which in turn yields bands of delocalized electronic states with a bandwidth $\propto t_2$. How does this affect the optical excitations? The intra-dimer δ-peak at $\omega = 2t_1$ is now broadened to an absorption band (*intra-dimer* band) of width $\propto t_2$ at approximately $\omega = 2t_1$. This situation is shown in figures 8.1 and 8.2 where we have calculated the optical conductivity for a dimerization $\delta = 1.64$ (or equivalently $t_2 = 0.18t$ and $t_1/t_2 \approx 10$) and two different coupling strengths $U = 3.64t$ and $U = 0.546t$, respectively. The intra-dimer band is the dominant spectral feature at $3.4 < \omega < 4.2$ which contains most of the spectral weight.

The finite value of t_2 also allows for *inter-dimer* excitations since $\hat{J}$ now couples dimers with a term $\propto t_2$. The inter-dimer excitations involve the transfer of a hole between nearest-neighbor dimers which can again be understood by excitations between two-site Hubbard models. These excitations give rise to small peaks at higher energies ($\omega \geq 2\delta t$) around $\omega = 2t_1$ and $\omega = U + 2t_1$. Since we consider t_2 a weak perturbation away from the dimer limit, the spectral weight of those peaks should be small, namely $t_2^2/\omega = t_2^2/t_1$ and $t_2^2/(2t_1 + U)$, respectively. The first inter-dimer peak is visible on the top of the intra-dimer band in figure 8.1 and the second peak in the inset of that figure at $\omega \approx 7.5$. Note, that the inter-dimer excitation at $\omega = 2t_1$ involves both spin

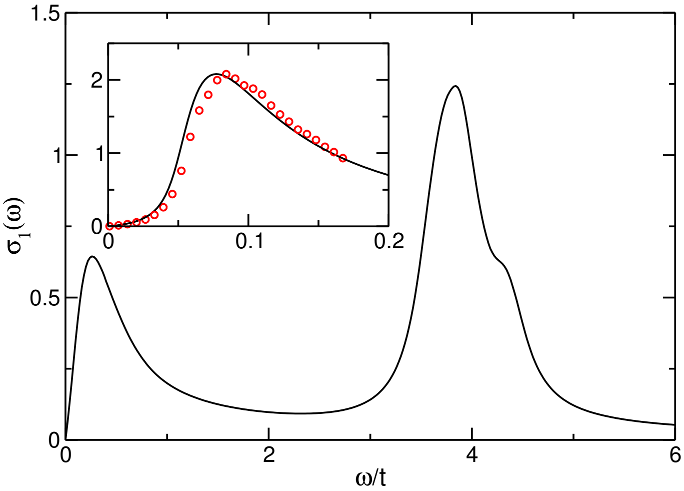

Figure 8.2: Optical conductivity $\sigma_1(\omega)$ in the large-dimerization limit ($\delta = 1.64$) for a weak effective coupling ($U = 0.546t \approx 3t_2$) with a broadening $\eta = 0.2t$ ($L = 64$ sites). Inset: high-resolution and expanded view of $\sigma_1(\omega)$ in the low-energy region $\omega \leq 0.2t$. DDMRG results (circles) for $\eta = 0.0128t$ ($L = 200$ sites) and field-theoretical result [39] (line) for a gap $E_c = 0.049t$ and the same broadening η.

and charge degrees of freedom because it requires the formation of a triplet state on the second dimer.

So far we have only considered the high energy spectrum ($\omega \geq 2\delta t$). At low excitation energies ($\omega < 2\delta t$) and $\delta \to 2$ we can neglect transitions to the upper Peierls-band and map the model (8.1) onto an (effective) half-filled Hubbard model with renormalized parameters $t_{\text{eff}} = t_2/2$ and $U_{\text{eff}} = U/2$ under the assumption that U remains small against $4t_1$ [73]. We therefore expect that the optical conductivity of the half-filled Hubbard model gives a good description of optical excitations at low energies.

The first set of parameters $\delta = 1.64$ and $U = 3.64t$ (cf. figure 8.1) corresponds to a renormalized interaction of the effective model $U_{\text{eff}}/t_{\text{eff}} = U/t_2 \approx 20$. This strong effective coupling leads to a shape of the low-energy band below $\omega = 2t$ which is reminiscent of the semi-elliptic absorption band centered around $\omega = U_{\text{eff}} = 1.82t$ found in the strong-coupling limit of the half-filled Hubbard model [89]. As expected, the optical weight $\propto t_{\text{eff}}^2/U_{\text{eff}}$ is significantly smaller than the intra-dimer band.

For the second parameter set, $\delta = 1.64$ and $U = 0.54t$, the situation is entirely different, since the effective interaction is relatively weak $U_{\text{eff}}/t_{\text{eff}} = U/t_2 \approx 3.3$. This corresponds to a small Mott gap $E_c \approx 0.049t \approx 0.54t_{\text{eff}}$ where the optical conductivity is amenable to field-theoretical approaches. In fact, the high-resolution inset of figure 8.2 clearly shows that the low-energy spectrum agrees very well with field-theory results in the limit of small Mott gaps [39]. Of course, the optical weight is much less suppressed than in the effective strong-coupling case and thus comparable to that of the intra-dimer band.

8.2.2 Strong Coupling

In the limit of strong electron-electron interaction, $U \gg t_1 > t_2$, and without dimerization, two bands, lower and upper Hubbard band, separated by an energy scale of U with band width $4t$ appear [8]. Upon turning on the dimerization these bands are split by a dimerization gap $2\delta t$ [73]. For quarter band filling the excitations in the lower Hubbard band have the dispersion (8.2) of a half-filled Peierls insulator. The energy required for the creation of an unbound pair of excitation, the Mott-gap, is $E_c = 2\delta t$. If we neglect the contribution of the spin sector to the matrix elements in (8.3) we therefore expect [79] that the optical conductivity is well approximated by the Peierls spectrum [8]

$$\sigma_1(\omega) = \frac{(2\delta t)^2 (4t)^2}{4\omega^2 \sqrt{[\omega^2 - (2\delta t)^2][(4t)^2 - \omega^2]}} \; . \tag{8.8}$$

This should hold in the range of energies $\omega < U$ when no transitions from lower to upper Hubbard band are possible. In figure 8.3 we present a comparison between DDMRG data and the theoretical prediction (8.8) for parameters $U = 40t$ and $\delta = 0.6$. The Peierls insulator spectrum has been broadened by the same value of $\eta/t = 0.2$ that we use in the numerical calculation. We find excellent agreement. The small differences are due to the finite Hubbard interaction U which is not present in the effective free solution (8.8). The transitions to the upper Hubbard band are visible at $\omega > U$ as expected and can be seen as the weak absorption band with spectral weight $\propto t^2/U$ in the inset of figure 8.3.

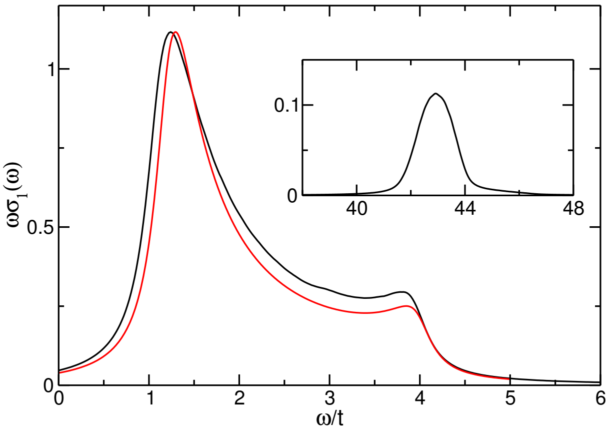

Figure 8.3: Reduced optical conductivity $\omega\sigma_1(\omega)$ in the strong-coupling limit ($U = 40t$) calculated with $\delta = 0.6$ and a broadening $\eta = 0.2t$ ($L = 64$ sites). The red line is the Peierls insulator spectrum for the same values of δ and η. Inset: expanded view of the high-energy spectrum.

This strong-coupling scenario remains qualitatively valid even for moderate couplings U. In figure 8.4 we show $\sigma_1(\omega)$ for parameters $U = 5t_1$ and $t_1/t_2 = 2$, or equivalently, $U/t = 20/3$ and $\delta = 2/3$. We can still recognize the form of the Peierls

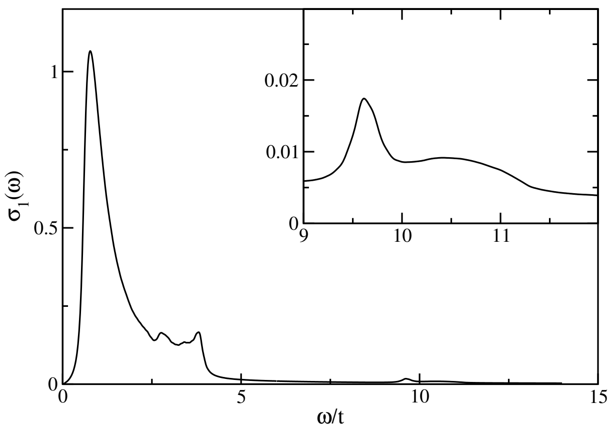

Figure 8.4: Optical conductivity $\sigma_1(\omega)$ for $\delta = 2/3$, $U/t = 20/3$, and a broadening $\eta = 0.1t$ ($L = 128$ sites). Inset: expanded view of the high-energy spectrum.

spectrum (8.8) although U is far from the strong-coupling limit. This fact is surprising since other physical quantities are no longer well approximated by strong-coupling theory. For instance, the Mott gap is $E_c = 0.53t$ in agreement with [73] while the strong-coupling result $2\delta t \approx 1.33t$ is significantly larger.

In previous work [89, 39] it has been observed that there are small deviations from the simple Peierls spectrum (8.8) in the large-U limit which involve excitations in the charge and the spin sector. We argue that the small features visible around $\omega = 3$ in figure 8.3 and more clearly around $\omega = 2.8$ in figure 8.4 are also due to spin excitations. To this end, we discuss how the spectrum in the large-U limit evolves with δ. For very small dimerization ($\delta \ll 1$) most of the spectral weight resides in the low-energy peak which for $\delta \to 0$ turns into the Drude peak of the effective free model. With growing δ the low-energy peak is shifted towards the high-energy divergence at $4t$ and spectral weight is transferred from the lower to the upper peak. When we have $\delta \to 2$ this results in a very narrow band between $\omega = 2\delta t \lesssim 4t$ and $\omega = 4t$. This band corresponds to the intra-dimer band around $\omega = 2t_1 = 4t$ in the strong-dimerization limit discussed in the previous section. Therefore, the strongly dimerized strong-coupling limit ($U \gg t$ and $\delta \approx 2$) and the large-dimerization limit ($\delta \approx 2$ and $U < 4t_1$) are dominated by a similar structure. We noted in section 8.2.1 that spin excitations contribute to the spectrum in the large-dimerization limit which suggests that the deviations from the Peierls form (8.8) are also caused by excitations involving both spin and charge degrees of freedom.

8.2.3 Weak Coupling

In the weak-coupling limit $U \ll t_2 < t_1$ the largest energy scale is the dimerization gap $2\delta t$ between the Peierls bands (8.8). The low-energy sector of the model can therefore be mapped onto an effectively half-filled Hubbard chain with renormalized hopping $2t_2$ and an effective (long-ranged) interaction $\propto U$ and a small Mott gap $E_c \ll t_2$ [73].

Accordingly, the low-energy part of $\sigma_1(\omega)$ should be described well by field-theory [39, 84]. Since most of the weight resides in the Drude peak at $\omega = 0$ for vanishing Mott gaps field-theory captures the relevant part of the spectrum.

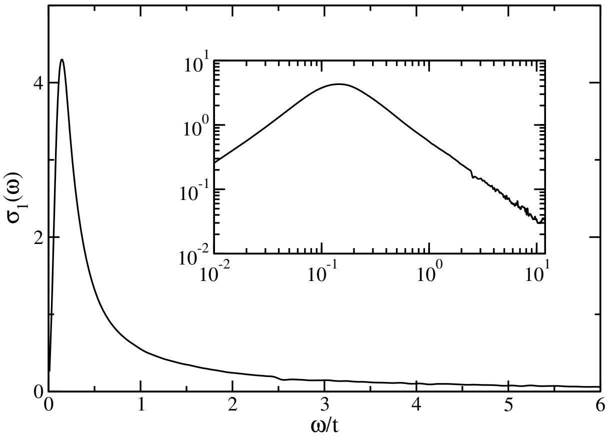

Figure 8.5: Optical conductivity for $\delta = 0.105$, $U = 5.263t$, and $\eta = 0.1t$ ($L = 128$ sites). Inset: same data on a double logarithmic scale.

This situation is shown in figure 8.5 where we have calculated $\sigma_1(\omega)$ for parameters $U = 5.263t$ and $\delta = 0.105$ (corresponding to $t_2/t_1 = 0.9$). Most spectral weight is concentrated in the sharp low-energy peak. The long high-frequency tail is due to the finite broadening $\eta/t = 0.1$ introduced in the calculations. In addition, we have used the standard DMRG method to determine the Mott gap $E_c = 0.03t$, the optical gap $\omega_1 \approx E_c$ and the position $\omega_{\max} = 0.04t$ of the maximum $\sigma_1^{\max}(\omega)$. All results are extrapolated to the thermodynamic limit as seen in figure 8.6. The fact that E_c and ω_1 extrapolate to the same value in the thermodynamic limit is consistent with field-theory [39, 84]. This is also true for our finding $\omega_1 \approx E_c$.

While our results for excitation gaps and the spectrum are fully compatible with field-theory, a direct comparison of the DDMRG line-shapes is not possible. We cannot sufficiently resolve the spectrum since the energy scale $\omega \sim E_c$ on which most spectral weight is concentrated is comparable or smaller than the resolution η of our calculations. An important result from field-theory is the power-law behavior of the optical conductivity of one-dimensional Mott insulators in the range of frequencies $\omega \gg E_c$

$$\sigma_1(\omega) \sim \omega^{-\alpha}, \tag{8.9}$$

with an interaction-dependent exponent $\alpha \geq 1$. The field-theory approach, by construction, is only valid for energies much smaller than the band width $\sim 2t$. On the other hand, the power law (8.9) is known to be valid only at very high frequencies $\omega \sim 10^2 E_c$ [84]. This poses a restriction on the parameter range of the underlying microscopic Hamiltonian because very small Mott gaps are required to simultaneously fulfill both conditions $E_c \ll \omega \ll t$. In addition, no other optical excitations must be present

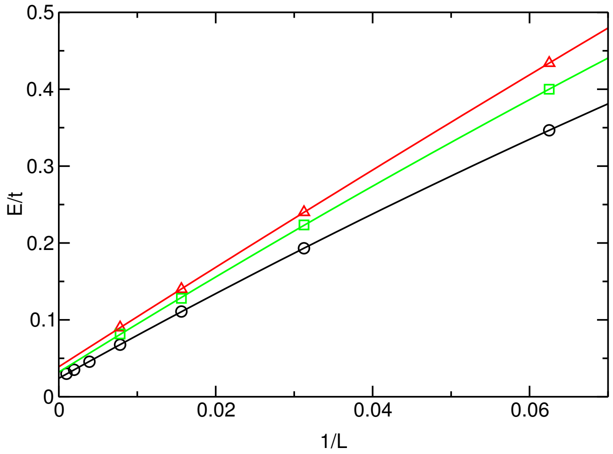

Figure 8.6: Mott gap E_c (circle), optical gap ω_1 (square), and position $\omega_{\max}$ of the conductivity maximum (triangle) as a function of the inverse system size for $\delta = 0.105, U = 5.263t$, and $V = 0$. Lines are quadratic fits.

in the frequency range of interest because it would spoil the form (8.9). This cannot be judged from the perspective of field-theory only, because the underlying assumptions neglect excitations which are present in the lattice model. We have seen in section 8.2.1 that this situation occurs in the weak-coupling regime of the dimer-limit. There, the low-energy spectrum ($\omega \ll t$) is in good agreement with field-theory whereas the high-energy spectrum ($\omega > 2\delta t$) is dominated by inter-dimer and inter-band transitions at energies $\omega = 2\delta t$ and $\omega = 2t_1 + U$, respectively. For the model (8.1) at hand this line of reasoning can be summarized: (i) only the weak-coupling regime yields sufficiently small Mott gaps $E_c \ll t$ and (ii) no other optical excitations of the lattice model are allowed in the energy range of interest.

The DDMRG spectra calculated in the small-Mott-gap limit often show a power-law decay as seen in the inset of figure 8.5. There, we plot $\sigma_1(\omega)$ on a double-logarithmic scale and the power-law form is visible in the interval $0.2t < \omega < 10t$ corresponding to $7E_c < \omega < 330E_c$, with an exponent $\alpha \approx 1.2$. However, this may well be an artefact of the finite broadening η used in the calculations. We find that the exponent α depends on the method used to determine $\sigma_1(\omega)$, see section 8.1, and also the system size L. How can this be understood? Assume that most of the weight is concentrated in the sharp peak at $\omega \sim E_c$. The convolution of this structure with a Lorentzian yields a slowly decaying high-energy tail which decays as $\eta A_1 \omega^{-\beta}$ for $\omega \gg E_c$. The pre-factor A_1 is proportional to the total spectral weight of the structure at E_c. Thus, the true power-law behavior $\sigma_1(\omega) \sim A_2 \omega^{-\alpha}$ will be concealed in numerical calculations: (i) when $\beta/\alpha > 1$ or (ii) the pre-factor A_1 is significantly larger than A_2, irrespective of the ratio β/α.

We have also tried to assess the spectrum in the thermodynamic limit by a deconvolution of the DDMRG data. The resulting spectra do *not* show a power-law behavior in any significant range of frequencies. Unfortunately, the deconvolution approach does not work well when the spectrum is dominated by sharp structures as in figure 8.5 and the accuracy of the deconvolved spectra is very poor at high frequencies.

In summary, we have not been able to find convincing numerical evidence for the power-law behavior (8.9) in the weak-coupling regime of the lattice model (8.1). Based on our considerations we can, however, conclude that if (8.9) is the true asymptotic form of $\sigma_1(\omega)$ then the spectral weight in the power-law tail can only contain a *small* fraction of the total spectral weight.

8.2.4 From Small to Large Dimerization

How does $\sigma_1(\omega)$ evolve with the dimerization δ when we keep the Coulomb repulsion fixed? We find that the spectrum evolves continuously from small to large dimerization. Most notably, the qualitative form of $\sigma_1(\omega)$ is similar for all values of $U > 0$ even though the nature of the excitations is very different. We have described the evolution of the spectrum in the strong-coupling limit earlier, see section 8.2.2, but reiterate the salient points. The low-energy structure at $2\delta t$ moves towards higher energies with larger dimerization. At the same time, spectral weight is progressively transferred from the low-energy singularity to the high-energy divergence at $\omega = 4t$. In the limit $\delta \to 2$ both peaks finally merge into a single singularity at $\omega = 4t$.

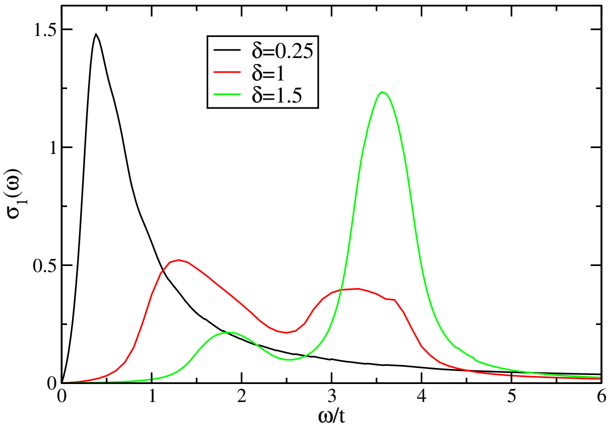

Figure 8.7: Optical conductivity $\sigma_1(\omega)$ for $U = 6t$ and $\eta = 0.2t$ ($L = 32$) for various dimerizations δ.

Away from strong-coupling we may no longer expect that the Peierls spectrum (8.8) is a decent description of the optical properties. Our DDMRG results nevertheless indicate that the evolution of the spectrum is similar to the strong-coupling case even for small interaction, down to $U/t = 1$. Consider, for instance, figure 8.7 which shows the δ-dependent evolution of the spectrum for $U = 6t$. We can clearly discern that optical weight is transferred from the low-energy peak to the high-energy structure and that the low-energy peak shifts towards higher energies as δ increases. The high-energy structure always lies close to $\omega = 4t$ for all U and δ. Its weight, however, can become so small that it is no longer visible. This happens, for example, in the weak-coupling limit, see figure 8.5. Note that the low-energy peak is close to the Mott gap E_c only for small dimerization δ. For moderate U it moves away from E_c with larger δ, in contrast to the strong-coupling result (8.8) where $E_c = 2\delta t$.

8.2.5 From Weak to Strong Coupling

In the previous section 8.2.4 we have learnt that U has only a small effect on the optical spectrum as δ is varied. We now strengthen this point by presenting results at fixed $\delta = 1.64$ when we vary the interaction from $U = 6t$ to $U = 100$. This is shown in figure 8.8 where we plot the reduced optical conductivity $\omega\sigma_1(\omega)$. For $U \leq 4$ the spectrum can be explained in terms of the large-dimerization limit, see section 8.2.1. There is a strong peak at $\omega \approx 2t_1 = 3.64t$ and two weaker structures at $\omega \approx E_c$ and $\omega \approx 2t_1 + U$, see also figure 8.1. For fixed $\delta < 2$ the on-site interaction U significantly enhances the Mott gap E_c which is equal to the optical gap ω_1 for all values of $\delta < 2$ and $V = 0$. Accordingly, the low-energy absorption band is shifted towards the main peak at $\omega = 2t_1$. At the same time the high-energy peak moves to higher energies in agreement with the expression $\omega = 2t_1 + U$. This is visible in the inset of figure 8.8. The main structure of the optical spectrum at $\omega = 2t_1$ remains mostly unaffected when we vary the interaction U.

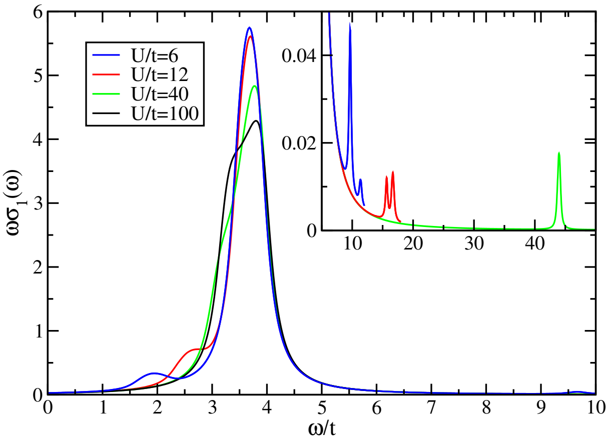

Figure 8.8: Reduced optical conductivity $\omega\sigma_1(\omega)$ calculated with $\eta = 0.2t$ ($L = 64$) for $\delta = 1.64$ and various values of U. Inset: expanded view of the high-frequency conductivity spectrum.

A remark is in order at this point. We have seen in section 8.2.3 that for weak coupling the effective interaction splits the lower Peierls band in a lower and a upper Hubbard band. The gap between these effective Hubbard bands is E_c and therefore transitions with $\omega = E_c$ contribute to the optical spectrum. In the strong-coupling limit the largest energy scale is the on-site interaction which creates two Hubbard bands separated by a gap $\propto U$. The effect of the dimerization is to split the lower band into an effectively half-filled Peierls-band (8.8). Transitions from the (full) lower to the upper

Hubbard band thus contribute spectral weight at energies $\omega \approx U$. Our calculations show that there is a domain in the parameter space (δ, U) of the model (8.1) where both features can be seen simultaneously. In other words, the low-energy part of $\sigma_1(\omega)$ is described by weak-coupling, i.e., field-theoretical approaches, whereas the high-energy part is explained by a strong-coupling analysis. Examples are the spectra shown in figures 8.1 and 8.8.

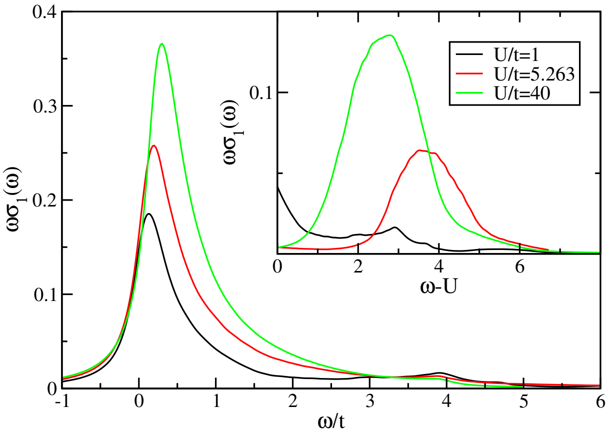

Figure 8.9: Reduced optical conductivity $\omega\sigma_1(\omega)$ calculated with $\eta = 0.2t$ $(L = 64)$ for $\delta = 0.105$ and various values of U. Inset: expanded view of the high-frequency conductivity spectrum as a function of $\omega - U$.

As a second example of the optical spectrum evolution with U, we show the reduced optical conductivity calculated with DDMRG for small dimerization $\delta = 0.105$ and various interaction strengths U in figure 8.9. We begin with the weak-coupling limit $U = t$ where most of the spectral weight is found in the peak close to $\omega = E_c$. There is a second peak close to $\omega = 4t$ which corresponds to transitions from the lower to the upper Peierls band (8.2). The lower peak moves to higher energies as E_c increases with larger U. Once $U \gg t$ we have $E_c = 2\delta t$ and recover the strong-coupling limit, see section 8.2.2. Despite the drastic change of U, the overall shape of the peak is not significantly altered. The effect of larger interaction U leads to the vanishing of the structure at $\omega = 4t$. Instead we find optical weight at $\omega \approx U$ which again corresponds to transitions between the (full) lower and upper Hubbard bands, see the inset of figure 8.9. These transitions can already be seen at $U = 5.263t$ close to $\omega - U = 4t$ in the inset of figure 8.9. This is in direct contradiction of the power-law decay (8.9) that we have found in figure 8.5 for the same parameters. As in section 8.2.3, we conclude that the power-law we observe in figure 8.5 is an artefact of the broadening used in the DDMRG calculations. Furthermore, this observation sheds some light on the difficulty to observe the asymptotic form (8.9) in a lattice Hamiltonian since field-theory neglects optical transitions at higher energy scales.

In summary, we have calculated the optical conductivity of the model (8.1) for $V = 0$ and various parameters (U, δ). We have included the relevant limiting cases where the spectrum can be understood in simple terms and we have related these findings to the transition of the spectrum between these limits. The spectral properties of the Peierls-Hubbard Hamiltonian are mostly determined by the dimerization δ. The on-site repulsion U affects only the weaker details of the spectrum which directly relate to the gap E_c and the energy scale U itself.

8.2.6 Nearest-Neighbor Coulomb Interaction: Excitons

So far we have neglected the nearest-neighbor electron-electron interaction V in the extended Peierls-Hamiltonian (8.1). In an insulator this is difficult to justify because screening is less effective. Moreover, the nearest-neighbor repulsion introduces a new energy scale in the system that drives the ground state from a Mott insulator to a charge-density wave (CDW) insulator [77] for large enough values of V. We restrict the following discussion to the Mott insulating phase $U/2 > V$.

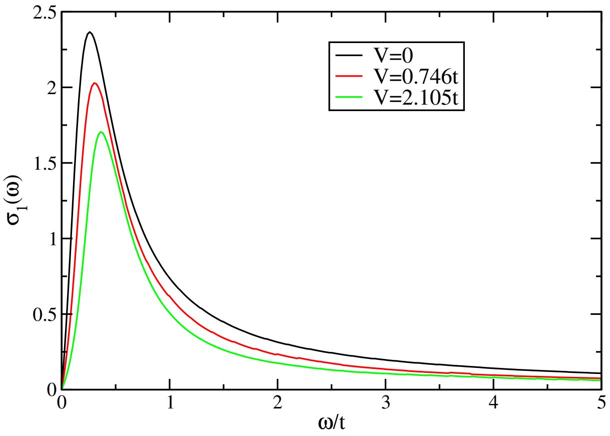

Figure 8.10: Optical conductivity $\sigma_1(\omega)$ for $\delta = 0.105$, $U = 5.263t$, $\eta = 0.2t$ ($L = 64$), and various nearest-neighbor interactions V.

It is known from previous DMRG investigations [76] that the charge gap E_c is strongly affected by the non-local Coulomb repulsion V. Our findings confirm this result. We have shown in figure 8.6 that the optical gap ω_1 is equal to the Mott gap E_c for $V = 0$ in the thermodynamic limit. It is only for energies larger than E_c that unbound pairs of elementary excitations may be formed. In the language of field-theory these are unbound holon-antiholon pairs which are responsible for the onset of the low-energy absorption band. In contrast to a naive Wannier theory, we find that $\omega_1 = E_c$ for small nearest-neighbor interaction V. This indicates that the low-energy spectrum is *still* determined by unbound pairs of elementary excitations.

The influence of small V on the optical spectrum is shown in figure 8.10. The low-energy peak above the Mott gap E_c is shifted to higher frequencies as V increases. Moreover, the total weight decreases with larger V in accordance with other investigations [74]. Finally, when we tune V to larger values, the nature of the excitations

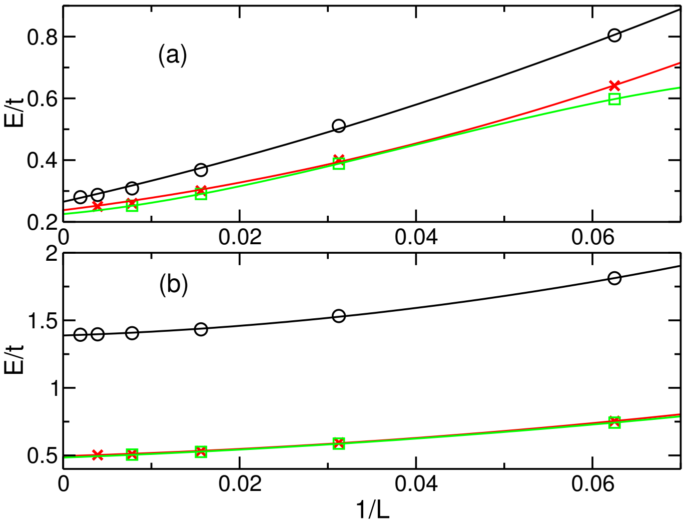

Figure 8.11: Mott gap E_c (circle), optical gap ω_1 (square), and position $\omega_{\max}$ of the spectrum maximum (cross) as a function of the inverse system size for (a) $\delta = 0.105, U = 5.263t$, and $V = 2.105t$, and (b) $\delta = 0.353, U = 8.235t, V = 3.294t$. Lines are quadratic fits.

that contribute to the optical spectrum changes fundamentally. Consider the extrapolation of the gaps E_c, ω_1 and the position of the maximum $\omega_{\max}$ in figure 8.11. The first set (a) of parameters ($\delta = 0.105, U = 5.263t$, and $V = 2.105t$) gives a difference $E_b = \omega_1 - E_c = 0.04t$. The second set (b) ($\delta = 0.353, U = 8.235t$, and $V = 3.294t$) yields larger $E_b \approx 0.9t$. Thus, in both cases with $V > 2t$ the onset of the optical spectrum lies *below* the Mott gap. In addition, the position of the maximum scales as $\omega_{\max} \to \omega_1$ for $L \to \infty$. This identifies the low-energy peak in figure 8.10 as an excitonic δ-peak in both cases. The presence of an excitonic δ-peak can also be identified through the finite-size-scaling procedure discussed in section 5.1.6. The low-lying optical excitations of the model 8.1 are now neutral bound states of elementary excitations, e.g., bound holon-antiholon pairs in the field-theory picture. These excitations are called Mott-Hubbard excitons and their properties have been recently analyzed both numerically and analytically [88]. The size or binding strength of the exciton is related to its binding energy E_b which implies that for parameter set a) we have a small or weakly bound Mott-Hubbard exciton, and a small or strongly bound Mott-Hubbard exciton for parameter set (b). We emphasize again that excitons are not formed in the gap for all $V > 0$. On the contrary, a finite value $V > V_c \simeq 2t$ is necessary to find bound excitonic states in the optical conductivity below the singe-particle gap.

With increasing V the exciton becomes more tightly bound and the binding energy E_b becomes larger. Accordingly, the position $\omega = \omega_1 < E_c$ of the δ-peak is shifted towards lower energies. This effect takes place only for large enough V when excitons have been formed. An interaction V which is less than this threshold will cause the opposite shift of the peak by enhancing E_c. This is shown in figure 8.12. At first, when

V increases from zero to $1.636t$, the peak shifts upwards and then downwards again for $V = 3.294t$ when spectral weight is transferred from the continuum onset at $E_c = 1.4t$. Due to the finite resolution in figure 8.12 we cannot resolve the gap between the excitonic peak at $\omega_1 \approx 0.5t$ and the onset of the continuum. Another effect of increasing V is that the weak structure at $\omega \approx 4t$ rapidly vanishes.

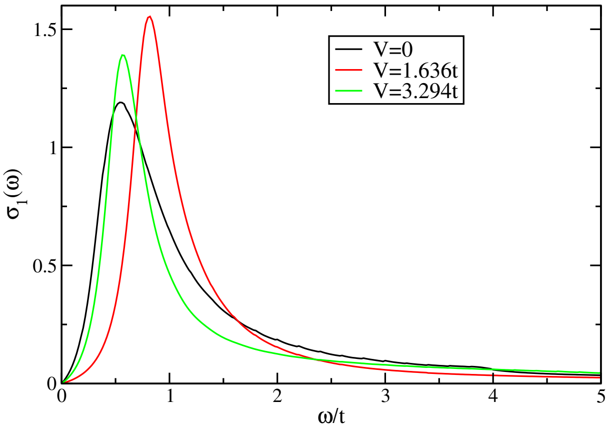

Figure 8.12: Optical conductivity $\sigma_1(\omega)$ for $\delta = 0.353$, $U = 8.235t$, $\eta = 0.2t$ ($L = 64$), and various nearest-neighbor interactions V.

In summary, our investigations show that, contrary to the on-site repulsion, the nearest-neighbor repulsion V has a significant impact on the shape of the optical spectrum, but only if it is large enough to generate an excitonic bound state below the Mott gap.

8.3 Discussion

What are the implications of our numerical results for the theoretical description of the Bechgaard salts?

During the past ten years different parameter sets for the extended Peierls-Hubbard model have been proposed. F. Mila [74] analyzed the reduction of infrared oscillator strength found experimentally in the Bechgaard salts. His investigation indicates that large values V are necessary to explain the reduction of the electron kinetic energy due to correlation effects. The resulting parameter set is $t_2/t_1 = 0.9$, $U = 5t_1$, and $V = 2t_1$, which correspond to $\delta = 0.105$, $U = 5.263t$, and $V = 2.105t$, for (TMTSF)$_2$ClO$_4$ and $t_2/t_1 = 0.7$, $U = 7t_1$, and $V = 2.8t_1$, which correspond to $\delta = 0.353$, $U = 8.235t$, and $V = 3.294t$, for (TMTTF)$_2$PF$_6$. The corresponding DDMRG spectra are shown in figures 8.11 and 8.12, respectively. In both cases our finite-size-scaling analysis proves the existence of an excitonic bound state with energy $\omega_1 < E_c$, cf. figure 8.10.

A different analysis by S. Nishimoto *et al.* [76] used a fit of the Mott gap of (8.1) to the optical gap from experiments in order to find a suitable set of parameters. They propose that smaller values V are adequate to describe the Mott gap while they use the same ratios t_2/t_1 and U/t_1 as F. Mila. Specifically, they find $V = 0.764t$ for (TMTSF)$_2$ClO$_4$ and $V = 1.636t$ for (TMTTF)$_2$PF$_6$. The optical spectra for these parameters are also shown in figures 8.11 and 8.12, respectively. In contrast to F. Mila's parameters, no exciton is present in the spectrum and the onset of the optical conductivity coincides with the Mott gap E_c.

How can we explain the discrepancy of the proposed parameters? Let us discuss the case of (TMTSF)$_2$ClO$_4$ first. According to F. Mila, the kinetic energy is quite flat as a function of V while the Mott gap E_c changes rapidly with V. This results in a large uncertainty of F. Mila's value. In fact, the value $V = 0.764t$ proposed by S. Nishimoto *et al.* is also consistent with the reduction of infrared oscillator strength. For consistency reasons we conclude that S. Nishimoto's value $V = 0.764t$ is appropriate for (TMTSF)$_2$ClO$_4$ and, accordingly, no excitons contribute to the low-energy spectrum.

For the salt (TMTTF)$_2$PF$_6$ the case is altogether different. The kinetic energy now depends strongly on V in the range of parameters (U, δ) used by F. Mila. The nearest-neighbor interaction $V = 1.636t$ reported by S. Nishimoto *et al.*, however, is consistent with the reduced oscillator strength only if unrealistically large values of U are chosen. How can this be explained? In their work S. Nishimoto *et al.* fitted the Mott gap E_c directly to the onset of the optical spectrum ω_1. Thereby, they neglect the possibility of exciton formation. This, in turn, yields too small values of V since the Mott gap may lie well above the optical gap in the presence of an exciton. For consistency reasons, we now conclude that F. Mila's value $V = 3.294t$ is appropriate for (TMTTF)$_2$PF$_6$. Within the theoretical description of the material by the extended Peierls-Hubbard model, we expect that excitons make a significant contribution to the optical spectrum.

To summarize the argument above, we restore absolute units with $t \approx 0.275$ eV for (TMTSF)$_2$ClO$_4$ and $t = 0.11$ eV for (TMTTF)$_2$PF$_6$, cf. Table 8.1. This yields nearest-neighbor repulsions

$$V = 0.764t = 0.21\,\mathrm{eV} \quad \text{for (TMTSF)}_2\text{ClO}_4 \tag{8.10}$$

and

$$V = 3.294t = 0.36\,\mathrm{eV} \quad \text{for (TMTTF)}_2\text{PF}_6\ . \tag{8.11}$$

The most salient feature of the optical conductivity of the (TMTSF)$_2$X salts is the narrow Drude peak at $\omega = 0$ which contains only a small fraction (about 1%) of the spectral weight that resides in the strong absorption band at mid-infrared frequencies [80, 81, 82, 83]. The energy of the second feature lies above the energy beyond which excitations are effectively confined to a single stack of (TM) molecules. It is therefore widely believed that the mid-infrared structure can be adequately treated within one-dimensional models. Specifically, it is argued that the absorption band at finite energies is described by the physics of one-dimensional Mott insulators. The most remarkable property of the mid-infrared spectrum is the power-law dependence of the rescaled optical conductivity [82]

$$\frac{\sigma_1(\omega)}{\sigma_1(\omega_{\max})} = C\left(\frac{\omega}{\omega_{\max}}\right)^{-1.3} . \tag{8.12}$$

This relation is obeyed astonishingly well by various $(\mathrm{TMTSF})_2\mathrm{X}$ salts over a large range of energies $2\omega_{\mathrm{peak}} < \omega < 20\omega_{\mathrm{peak}}$.

As detailed in section 8.2.3, our numerical method does not resolve the spectrum well enough to either confirm or refute the presence of a power-law decay in the optical conductivity of the extended Peierls-Hubbard Hamiltonian. Despite this shortcoming, our analysis implies that if a power-law of the form (8.12) exists in the extended Peierls-Hubbard model then its weight must be very small compared to the weight of the low-energy peak. This is clearly at variance with the experimental situation where the largest fraction of optical weight belongs to the mid-infrared absorption band. We therefore conclude that the feature (8.12) of the optical spectrum in $(\mathrm{TMTSF})_2\mathrm{X}$ salts cannot be explained within the extended Peierls-Hubbard model (8.1).

An idea put forth by J. Favand and F. Mila [75] is that the observed optical gap ω_1 is substantially larger than the Mott gap E_c. They base their argument on the exact diagonalizations of small quarter-filled dimerized Hubbard chains ($V = 0$). In contrast, we have found that for all values ($\delta < 2$, U) the Mott gap is equal to the optical gap, $E_c = \omega_1$. The only exception is the extreme and unphysical limit $\delta = 2$ when the system comprises of non-interacting dimers. Experimentally, it could be possible that the absorption band with onset at E_c is not detected if its spectral weight is very small compared to higher-energy structures. This occurs, for instance, in the larger-dimerization limit, cf. figure 8.1. In this situation one could falsely assume that the optical gap ω_1 is larger than the gap for charge excitations E_c. In our calculations for realistic parameters we always find that there is substantial weight close to the Mott gap. Indeed, for those parameters suggested by J. Favand and F. Mila for $(\mathrm{TMTSF})_2\mathrm{PF}_6$ ($\delta = 0.105$ and $U = 5.263t$, see Table 8.1) we find that the Mott gap, the optical gap, and the maximum of the spectrum extrapolate to very close values in the thermodynamic limit, cf. figure 8.6. In conclusion, we assume that the differences between the gaps found in conductivity measurements and the optical conductivity in the Bechgaard salt $(\mathrm{TMTSF})_2\mathrm{PF}_6$ cannot be explained by the extended Peierls-Hubbard model (8.1).

The situation in the $(\mathrm{TMTTF})_2\mathrm{X}$ salts is reversed. They show an optical conductivity in the quasi one-dimensional direction akin to semiconductors [81, 83]. An experimental riddle is the observation of a strong structure in the optical spectrum, around 100 meV, which is twice as small as the Mott gap found in photoemission experiments, at around 200 meV. We interpret this as evidence for exciton formation in $(\mathrm{TMTTF})_2\mathrm{PF}_6$. This interpretation is corroborated by the fact that for the nearest-neighbor interaction V suggested by F. Mila [74] ($\delta = 0.353, U = 8.235t, V = 3.294t$) we find a charge gap

$$E_c \approx 160\,\mathrm{meV} \tag{8.13}$$

and an exciton at

$$\omega_1 \approx 60\,\mathrm{meV} \tag{8.14}$$

This is in good agreement with the experiment. We therefore suggest that excitons are present in $(\mathrm{TMTTF})_2\mathrm{PF}_6$ and probably also in other $(\mathrm{TMTTF})_2\mathrm{X}$ salts. It would be interesting to perform an experiment that can detect possible excitonic bound states in

$(\mathrm{TMTTF})_2\mathrm{PF}_6$. This might be achieved, for instance, by electro-absorption which has been used to detect excitons in the quasi one-dimensional material polydiacetylene [90].

8.4 Conclusion

In this chapter we have presented a detailed analysis of the optical conductivity of the quarter-filled extended Peierls-Hubbard model in various regimes of the parameter space using DDMRG. We find that the dimerization δ and the nearest-neighbor interaction V have a strong influence on the salient features of the spectrum. Sufficiently large values of V allow for the formation of excitons. In contrast, the on-site repulsion determines only the finer spectral structure and changes the spectrum mostly by influencing the value of the charge gap. While our calculations could not directly find an asymptotic power-law decay in the optical conductivity, we argue that the extended Peierls-Hubbard model may be too simplistic for a complete description of the Bechgaard salts $(\mathrm{TMTSF})_2\mathrm{X}$. Based on our arguments, excitons may play a significant rôle in the optical spectrum of the $(\mathrm{TMTTF})_2\mathrm{X}$ salts.

Chapter 9

Dynamical Properties of $SrCuO_2$

The one-dimensional chain cuprates Sr_2CuO_3 and $SrCuO_2$ are among the best realizations of quasi one-dimensional systems. They have attracted significant theoretical and experimental interest in recent years. A good part of this interest stems from the fact that their two-dimensional relatives – the superconducting cuprates – basically consist of the same building blocks, namely, a copper atom surrounded by four oxygen atoms. Therefore it is interesting to study one-dimensional relatives.

This chapter begins with an introduction into the chemistry and electronic structure of the corner-sharing cuprates Sr_2CuO_3 and $SrCuO_2$. Then we discuss the optical conductivity and argue that the low-energy part of the experimental spectra can be described by the optical conductivity of the extended Hubbard model. We then move on to include a particle-hole probe, resonant inelastic x-ray scattering or RIXS. We show DDMRG results which indicate that the dispersion of RIXS peaks can be explained by the dynamical charge structure factor $N(q, \omega)$ of the extended Hubbard model. Finally, we conclude by presenting the dynamical spin structure factor $S(q, \omega)$ of the extended Hubbard model and compare it with recent neutron-scattering experiments.

9.1 Electronic Structure of $SrCuO_2$

The quasi one-dimensional cuprate $SrCuO_2$ consists of two corner-sharing chains that share their edges to build a ladder-like structure. This is shown in figure 9.1. The two chains are essentially decoupled since the Cu-O-Cu bonding angle is nearly 90°. The resulting single copper-oxide chains show the same physical properties as two single Sr_2CuO_3 chains. This expectation is supported by measurements of the magnetic susceptibility over a large range of temperatures [91]. When the copper-oxide chains are doped with holes, the extra holes go into the oxygen 2p orbitals. There, they form singlet states with the localized hole in the Cu 3d orbital. These states are referred to as "Zhang-Rice singlets" [92].

It is clear that we need a correlated three band model to give a complete description of the dynamical properties of $SrCuO_2$. The oxygen $2p_{x,y}$ and the copper $3d_{x^2-y^2}$ orbitals

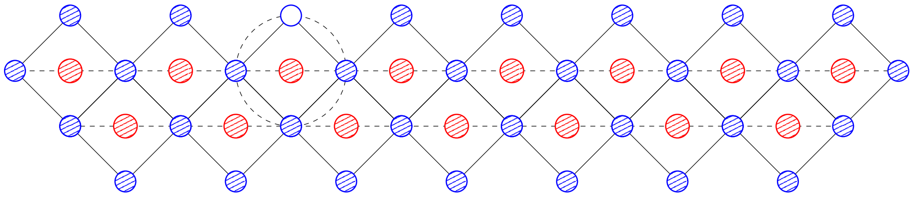

Figure 9.1: Copper oxide chain in SrCuO$_2$. Oxygen atoms are shown as blue circles and the copper atoms by red circles. Doped holes predominantly go in to the oxygen 2d orbitals. This gives rise to a localized singlet on a CuO$_4$-plaquette, the so called Zhang-Rice singlets [92]. The ladder is essentially decoupled into two one-dimensional corner-sharing chains due to the 90° Cu-O-Cu bonding angle between copper atoms on different chains.

are included in the Emery model

$$\hat{H} = \varepsilon_\mathrm{d} \sum_{i,\sigma} \hat{n}^d_{i,\sigma} + \varepsilon_\mathrm{p} \sum_{l,\sigma} \hat{n}^p_{l,\sigma} + t_\mathrm{pd} {\sum_{i,l,\sigma}}' \left(\hat{d}^+_{i,\sigma} \hat{p}_{l,\sigma} + \mathrm{h.c.} \right) + U_\mathrm{d} \sum_i \hat{n}^d_{i,\uparrow} \hat{n}^d_{i,\downarrow} \tag{9.1}$$

The operators $\hat{d}^+_{i,\sigma}$ create a hole on a copper site located at i, the operators $\hat{p}^+_{l,\sigma}$ create a hole in an oxygen 2p orbital located at l, $\hat{n}^d_{i,\sigma} = \hat{d}^+_{i,\sigma} \hat{d}_{i,\sigma}$ and $\hat{n}^p_{l,\sigma} = \hat{p}^+_{l,\sigma} \hat{p}_{l,\sigma}$. The index i runs over the copper sites and the index l runs over all O 2p orbitals. The primed sum in the last line indicates that the summation is restricted to the O 2p orbitals surrounding the copper atom at i. The first two terms are the chemical potentials for adding a hole to Cu 3d or O 2p. The difference $\varepsilon_\mathrm{p} - \varepsilon_\mathrm{d} \equiv \Delta > 0$ ensures that the holes are located in the Cu 3d orbitals with one hole per unit cell at half filling. The choice $\Delta > 0$ makes sure that doped holes predominantly go into the O 2p orbitals. The hopping of electrons from Cu 3d to O 2p orbitals is modeled by the third term in (9.1). The last term corresponds to the intra-site Coulomb repulsion of two holes on a copper site.

The model (9.1) of a charge transfer insulator cannot be solved exactly. Nevertheless there are limits in which the model can be mapped to effective models. To this end, consider figure 9.2 where we have sketched the local density of states for the electrons. Part (a) shows the lower Hubbard band of the correlated Cu 3d bands. This band is separated from the empty upper Hubbard band by a gap of order U_d. In between the Hubbard bands is the O 2p band which is separated from the upper Hubbard band by the charge transfer energy Δ. We can now map this three-band model onto a one-band model by discarding all occupied Cu 3d states and defining an effective interaction U of the order of Δ between an effective lower and upper Hubbard band as shown in figure 9.2 (b) [93]. The effective model is a Hubbard Hamiltonian at half band-filling in which we may include a next-neighbor interaction term

$$\hat{H} = -t \sum_{l,\sigma} \left(\hat{c}^+_{l,\sigma} \hat{c}_{l+1,\sigma} + \mathrm{h.c.} \right) + U \sum_l \hat{n}_{l,\uparrow} \hat{n}_{l,\downarrow} + V \sum_l \hat{n}_l \; \hat{n}_{l+1} \,. \tag{9.2}$$

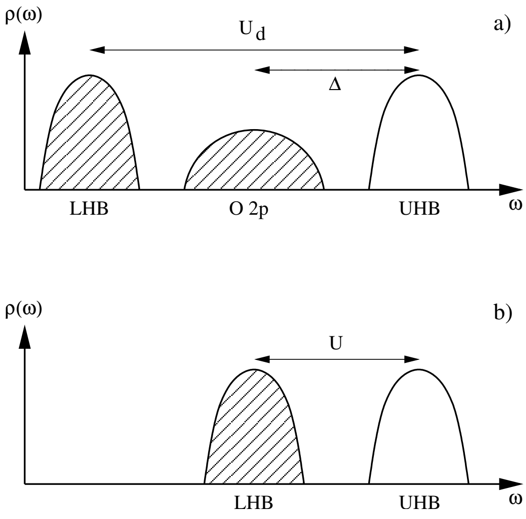

Figure 9.2: a) Electron density of states of SrCuO$_2$. The upper and lower Cu 3d Hubbard bands are separated by U_d. The O 2p band is located in between and is separated from the upper Hubbard band by Δ. b) Effective model for SrCuO$_2$. The O 2p band is mapped to an effective lower Hubbard band. The effective Model has an effective local interaction $U \sim \Delta$ [93].

It is important to note that this is not a rigorous mapping in the sense that it becomes valid in some regime of the model parameters. However, as long as the energy scales U_d and Δ are sufficiently well separated, we may assume that this procedure has some merit. We can justify this mapping onto a one-band Hamiltonian *a posteriori* by comparing with experimental data. Measurements of the static spin-susceptibility show that the spin properties of SrCuO$_2$ can be described by a one-dimensional antiferromagnetic Heisenberg model [91]. This is strongly indicative that the effective model of SrCuO$_2$ is a Mott-insulator that can be modeled by the Hamiltonian (9.2). Other theoretical and experimental studies suggest the same [93]. In the following sections we present evidence that (9.2) gives qualitatively and quantitatively correct results for the dynamics of SrCuO$_2$, namely, the optical conductivity in section 9.2, the dynamical spin-structure factor in section 9.3, and the dynamical charge-structure factor in section 9.4.

9.2 Optical Conductivity of SrCuO$_2$

In this section we show data for the optical conductivity $\sigma_1(\omega)$ of the extended Hubbard model and experimental data in SrCuO$_2$. The experimental resolution is very good, $\eta_\mathrm{exp} \approx 40\,\mathrm{meV}$ or $\eta_\mathrm{exp} \approx 0.1t$. The DDMRG calculations were performed on an open 128-site lattice using up to 200 density-matrix eigenstates. The units of $\sigma_1(\omega)$ are $e^2c/(\hbar\mathcal{V}) = 1643.54\,\Omega^{-1}\mathrm{m}^{-1}$ per copper-oxide chain and unit cell, cf. section 8.1.2, where $c = 3.9042\text{Å}$ is the lattice constant in the chain direction and $\mathcal{V} = 225.95\text{Å}^3$ is the volume of the unit cell [94]. We determine the parameters of the extended Hubbard model (9.2) such as to give the best agreement with the position, height, and width of the peak in $\sigma_1(\omega)_{\text{exp}}$. The results are shown in figure 9.3.

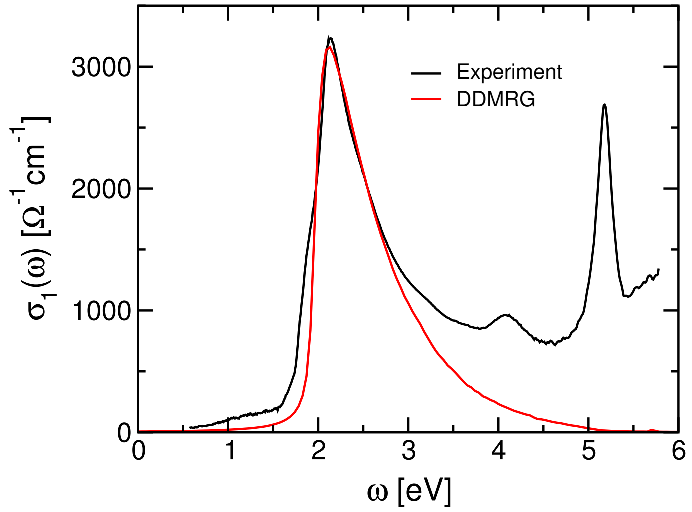

Figure 9.3: Optical conductivity $\sigma_1(\omega)$ calculated with DDMRG and experimental results. The broadening of the DDMRG data is $\eta/t = 0.1$ as in the experiment. We use parameters $U/t = 7.8$, $V/t = 1.3$, and $t = 0.435\,\text{eV}$ in the extended Hubbard model. For this choice of parameters both the peak height of $\sigma_1(\omega)$ and the peak position agree with the experimental data. There are no other free parameters. At energies larger than 4 eV the experimental data show the presence of transitions to other bands.

The set of parameters

$$U/t = 7.8, \qquad V/t = 1.3, \qquad t = 0.435\,\text{eV}, \tag{9.3}$$

gives the best overall agreement with the low-energy part of $\sigma_1(\omega)_{\text{exp}}$. Other than the model parameters of the effective Hamiltonian we did *not* introduce any further fit parameters to adjust the height of the peak. It is an unbiased property of the Hamiltonian. The onset and the peak of the optical conductivity in the extended Hubbard model are determined by the ratio U/t while the width of the peak is mostly affected by V/t. This fixes both interaction parameters. The exchange coupling finally fixes t, see below, and we are left with no free parameter.

What are the ground-state properties of the system in this parameter region? The one-particle gap Δ_c extrapolated to the limit $1/L \to 0$ is $\Delta_c = 1.94\,\text{eV}$ as shown in figure 9.4. This agrees well with the onset of the optical conductivity in figure 9.3 of $\Delta_1 = 1.96\,\text{eV}$. Since $V < 2t$ there is no exciton present in the system, or $\Delta_1 \geq \Delta_c$ as shown above. The spin gap for the lowest possible spin-excitation Δ_s approaches zero as expected for a spin-liquid.

Consider again figure 9.3. It is clear that excitations involving other bands are present. Nevertheless, we emphasize that (9.2) appears to model the optical spectrum

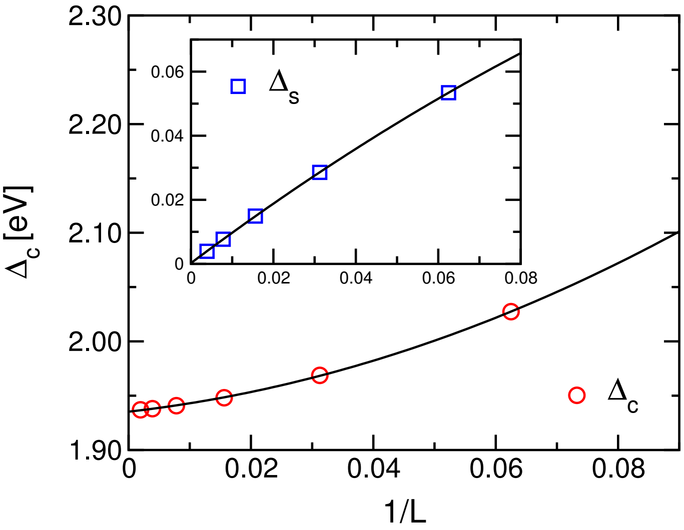

Figure 9.4: Extrapolation of charge- and spin gaps to the thermodynamic limit. The charge gap is finite and the spin gap vanishes, as expected for a Mott-insulator.

reasonably at energies lower than $\approx 4\,\mathrm{eV}$. It is not our intention to make any statements about the dynamics beyond this range since the effective model is a one-band model. But how can we claim that the extended Hubbard model gives us more at hand than just a simple and naïve fit procedure? The answer relies on the possibility to either predict or explain different unrelated experimental observables. An observable that is known with good precision for SrCuO$_2$ is the value of the spin-exchange coupling

$$J = 0.226\,\mathrm{eV} \tag{9.4}$$

from neutron scattering [94]. We can extract this value for our parameter set (9.3) by a perturbative expansion [95]

$$J = \frac{4t^2}{U(1-v)} - \frac{16t^4}{U^3}\frac{(1+v)}{(1-v)^3}\,, \tag{9.5}$$

$$v = \frac{V}{U}. \tag{9.6}$$

We obtain $J = 0.24\,\mathrm{eV}$ in good agreement with (9.4). Of course, we can not be sure if the agreement is an artefact of the perturbation theory.

A direct and non-perturbative way to obtain J is to calculate the spinon dispersion in the one-particle spectral function $A(k,\omega)$. This can be done efficiently because we do not need the full frequency and momentum dependence. Instead, we identify the position of the low-energy peak in $A(k \to 0,\omega)$ and $A(k \to \pi/2,\omega)$ for different system lengths L and extrapolate the spinon band width W_s to the limit $1/L \to 0$. This extrapolation is shown in figure 9.5. More precisely, we plotted $J = 2W_s/\pi$ versus the broadening

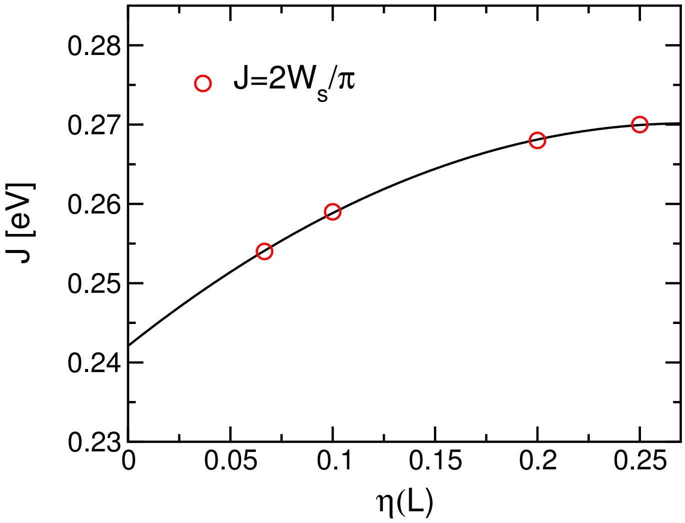

Figure 9.5: Extrapolation of the exchange coupling J obtained directly from the spinon band width $W_s = J\pi/2$ in $A(k,\omega)$. The extrapolation is performed with respect to $\eta/t = 6/L \to 0$.

$\eta/t = 6/L$ and let η approach zero. The extrapolation yields a value $J \approx 0.24\,\text{eV}$ which again is in good agreement with the experimental and perturbative results.

We can now safely conclude that the fit of the low-energy part of the optical conductivity is not merely accidental. On one hand, the effective model (9.2) describes a property of the electronic density, $\sigma_1(\omega)$, and, on the other hand, a property of the electronic spins, namely, the exchange coupling J. Sections 9.3 and 9.4 provide further evidence that the complete momentum dependent dynamical spin and charge structure factors are adequately modeled by an extended Hubbard Hamiltonian.

9.3 Dynamical Spin Structure Factor

In this section we present calculations of the dynamical spin-spin correlation function $S(q,\omega)$ of the extended Hubbard model (9.2). The spin structure factor can be measured by neutron scattering experiments and well resolved data have been published [94] very recently.

So far we have seen that quantitative and qualitative aspects of SrCuO$_2$ can be understood using the extended Hubbard model with $U/t = 7.8$, $V/t = 1.3$ and $t = 0.435\,\text{eV}$. Here, we argue that the neutron scattering intensity can also be modeled with this approach. Figure 9.6 shows the lineshapes of $S(q,\omega)$ calculated on a 100-site extended Hubbard chain. Starting from $q = 0$ a peak develops at low energies. The peak disperses to higher ω until $q/\pi = 0.5$ and then disperses downwards until it becomes soft at $q/\pi = 1$. As the peak approaches the zone boundary it gathers spectral weight at its lower onset. We also observe that there is a growing region of small but

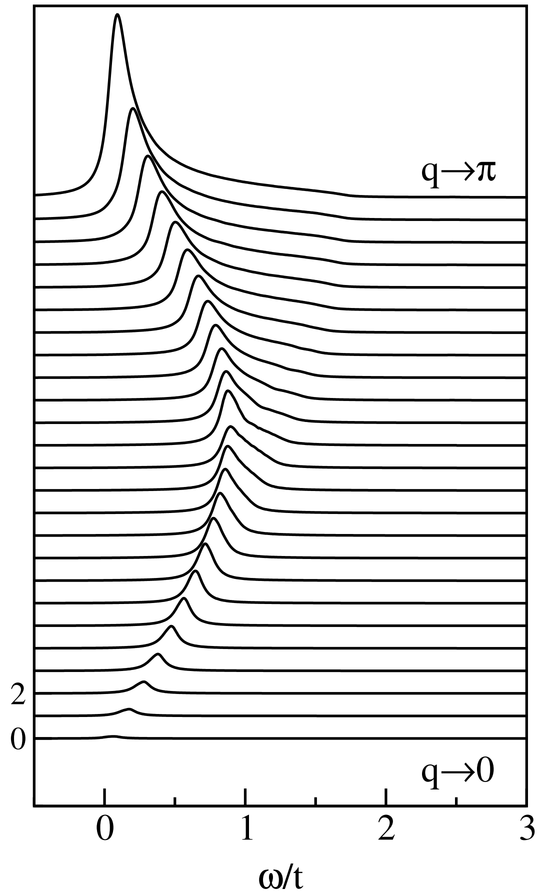

Figure 9.6: Lineshapes of $S(q, \omega)$. Parameters: $U/t = 7.8$, $V/t = 1.3$, $L = 100$ and $\eta/t = 0.05$. Different momenta have been offset vertically.

noticeable spectral weight at higher ω. This can be seen more clearly in figure 9.7 where show a density plot of the same data. The spectrum is very similar to that of the antiferromagnetic Heisenberg model.

In figure 9.8 we present the upper and lower onsets of the spin structure factor. The spin-exchange coupling $J \approx 0.23$ determined by [94] can again be used as a benchmark for the validity of the effective Hamiltonian (9.2). We therefore fit the upper and lower onsets with the des Cloiseaux-Pearson dispersion relations, which describe the compact support of the two-spinon continuum of the spin-1/2 Heisenberg model

$$\omega_{\mathrm{L}}(q) = \frac{\pi J}{2} |\sin(q)| \ , \tag{9.7}$$

$$\omega_{\mathrm{U}}(q) = \pi J |\sin(q/2)| \ . \tag{9.8}$$

The agreement of the onsets with these dispersion relations is excellent and we can directly read off $\pi J/2$ from the lower onset $\omega_{\mathrm{L}}(q)$ and πJ from the upper onset $\omega_{\mathrm{U}}(q)$.

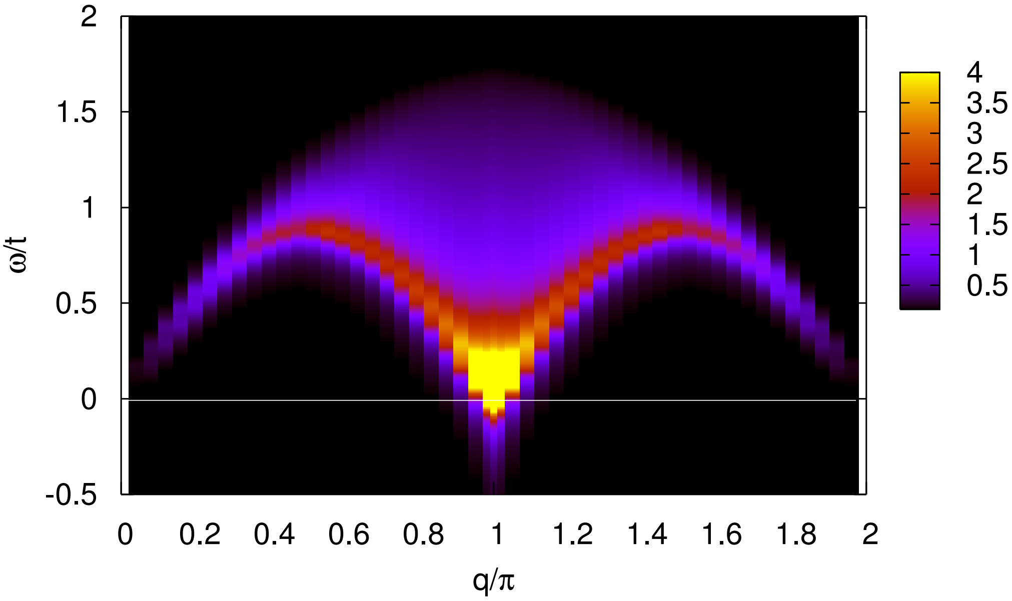

Figure 9.7: Density plot of $S(q,\omega)$. Parameters: $U/t = 7.8$, $V/t = 1.3$, $L = 100$, and energy resolution $\eta/t = 0.05$. The spectrum is very similar to that of the antiferromagnetic Heisenberg model. The spectral weight below $\omega = 0$ is due to broadening of strong peaks at the lower onset of the data.

This yields $J = 0.242\,\mathrm{eV}$ and $J = 0.246\,\mathrm{eV}$, respectively, in good agreement with both the experimental value and the theoretical considerations in section 9.2 where we independently obtained $J = 0.24\,\mathrm{eV}$.

The overall form of $S(q,\omega)$ is compatible with the neutron-scattering results which further corroborates our approach to the dynamics of SrCuO$_2$. It was proposed in [94] that the neutron-scattering spectra can be completely understood in terms of the Müller-Ansatz, which is a good approximation for the two-spinon contribution of the spin structure factor of the antiferromagnetic Heisenberg model [96, 97]. Note, however, that the Müller-Ansatz is known to significantly *overestimate* the two-spinon contribution close to the upper onset [97]. The Müller-Ansatz structure factor is given by

$$S_{\mathrm{MA}}(q,\omega) = A\frac{\theta(\omega-\omega_{\mathrm{L}}(q))\theta(\omega-\omega_{\mathrm{U}}(q))}{\sqrt{\omega_{\mathrm{U}}(q)^2-\omega^2}} \tag{9.9}$$

where A is a prefactor that we use to fit the peak heights and $\omega_{\mathrm{U,L}}(q)$ are the des

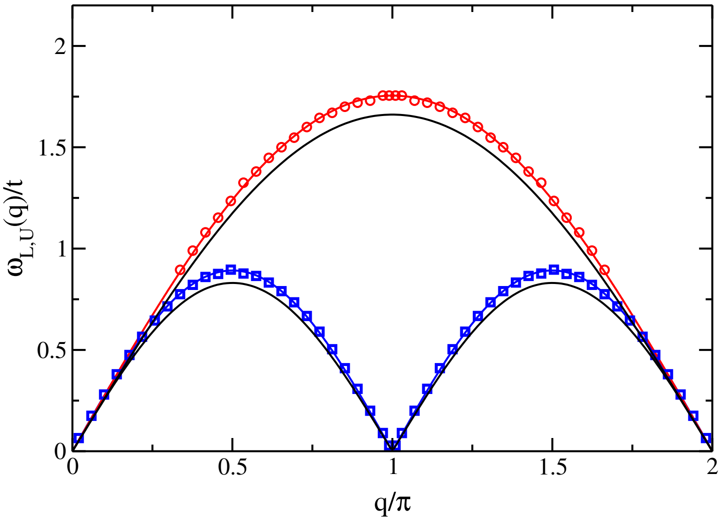

Figure 9.8: The lower onset $\omega_L(q)$ (blue) and upper onset $\omega_U(q)$ of $S(q,\omega)$ (red). Colored lines are fits with the des Cloiseaux-Pearson (dCP) dispersion relations (9.7)–(9.8) which directly yield the value of the antiferromagnetic exchange coupling $J = 0.242\,\mathrm{eV}$ and $J = 0.248\,\mathrm{eV}$, respectively. Black lines show the dCP dispersion for the exchange $J \approx 0.23\,\mathrm{eV}$ derived from neutron scattering [94].

Cloiseaux-Pearson dispersion relations (9.7)–(9.8). The Müller-Ansatz structure factor is non-zero only within the bounds of $\omega_{U,L}(q)$ and there is a square-root divergence at the low-energy onset. It is believed that the Müller-Ansatz is a reasonable starting point for the understanding of the spin structure factor of the Hubbard model. In a recent field-theoretical study of the spin-structure factor of the Hubbard model, however, it is shown that there are significant contributions in $S(q,\omega)$ due to itinerancy effects at intermediate values of the Coulomb interaction.

Following [94] we fit $S(q,\omega)$ with the Müller-Ansatz structure factor (9.9). We take into account the finite broadening of our data by convolving (9.9) with a Lorentzian distribution of width $\eta/t = 0.05$. In order to compare the spectra we fit the peak heights of $S_{\mathrm{MA}}(q,\omega)$ to our numerical result. This is shown in figure 9.9 for momentum $q = 100/101\pi \approx \pi$. In addition, we show the exact result $S_{2\mathrm{s}}(q,\omega)$ for the two-spinon contribution of the spin structure factor [97]. As expected, the Müller-Ansatz $S_{\mathrm{MA}}(q,\omega)$ overestimates the two-spinon contribution $S_{2\mathrm{s}}(q,\omega)$ close to the upper onset. The DDMRG result $S(q,\omega)$ lies in between both approximations. It is nevertheless surprising to see, how well the spin structure factor of the extended Hubbard model is captured by the spin dynamics of the antiferromagnetic Heisenberg model which we already documented in figure 9.8. Towards higher frequencies there are deviations from the two-spinon contribution which indicates that itinerancy effects are relevant. It would therefore be very interesting to compare the DDMRG data with neutron scattering data in $\mathrm{SrCuO_2}$ to check whether or not itinerancy effects are relevant for the spin dynamics.

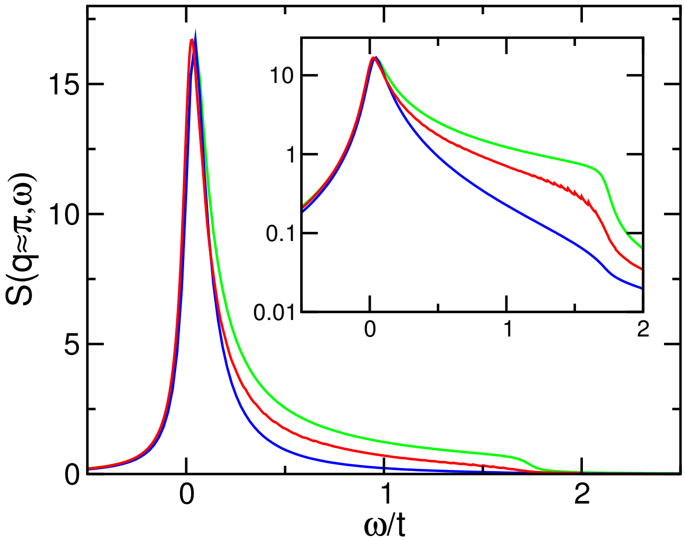

Figure 9.9: Plot of $S(q \approx \pi, \omega)$ of the extended Hubbard model calculated with DDMRG (red line). We also show the exact two-spinon contribution to the spin structure factor of the antiferromagnetic Heisenberg model $S_{2\mathrm{s}}(q,\omega)$ (blue line) and the Müller-Ansatz $S_{\mathrm{MA}}(q,\omega)$ (green line). Parameters: $U/t = 7.8$, $V/t = 1.3$, $L = 100$, and $\eta/t = 0.05$. The spectral weight is mainly concentrated in the peak at $\omega = 0$. $S_{\mathrm{MA}}(q,\omega)$ overestimates the two-spinon contribution $S_{2\mathrm{s}}(q,\omega)$. The DDMRG result lies in between both approximate expressions.

9.4 Resonant Inelastic X-Ray Scattering (RIXS) in SrCuO$_2$

In chapter 7 we have seen how the electronic structure of correlated materials can be directly measured with angle-resolved photoemission. For TTF-TCNQ the photo-hole decays into two new particles, the spinon and the holon. This kind of experiment is a "one-particle" probe. What happens in a correlated one-dimensional material when we introduce an electron-hole pair? We should expect that the hole decays into a holon-spinon pair while the electron, or double occupancy, decays into into an antiholon-spinon pair. Examples of such "particle-hole" probes are measurements of the optical conductivity, electron-energy loss spectroscopy (EELS), and resonant inelastic x-ray scattering (RIXS). The first two experiments probe the dynamical density structure factor for vanishing momentum (optics) or in the entire Brillouin-zone (EELS). It is accepted that RIXS also probes the dynamical density structure factor but this fact is not as well established as for optical or EELS experiments. In this section we compare data of a recent high resolution RIXS experiment in SrCuO$_2$ with DDMRG calculations of the dynamical structure factor of the extended Hubbard model [52]. We obtain both qualitative and quantitative agreement for the dispersion of RIXS features. This strongly indicates that the model (9.2) is the valid effective model of the quasi one-dimensional chain cuprate SrCuO$_2$.

9.4.1 RIXS Technique

Which correlation function is probed with resonant inelastic x-ray scattering experiments? Figure 9.10 depicts a cartoon of the electronic transitions involved in the RIXS process. The incoming x-ray photons have Energy $E = E_i$ and momentum $q = q_i$ and excite a strongly localized Cu 1s core electron to the delocalized Cu 4p band. The 1s core hole and the 4p electron form a highly excited intermediate state, ($\overline{\text{1s}}$4p). When the intermediate state relaxes back a photon with final energy $E' = E_f$ and momentum $k = q_f$ is emitted. The energy loss $E_i - E_f$ and momentum $q_i - q_f$ are transferred to the correlated lower and upper Hubbard band by exciting particle-hole excitations. On qualitative grounds we should therefore expect that the dynamical density-density correlation function,

$$N(q,\omega) = \sum_f |\langle f|\hat{n}_q|0\rangle|^2 \delta\left(\omega - E_n + E_0\right) \ , \qquad (9.10)$$

$$\hat{n}_q = \sum_{p,\sigma} \hat{c}^\dagger_{p-q,\sigma}\hat{c}_{p,\sigma} \qquad (9.11)$$

of the correlated electron bands is related to the RIXS intensity. This argument is made more precise in [98, 99, 100, 101]. At present, however, there is no satisfactory theory of the RIXS correlation function. In the following we therefore *assume* that the density structure factor (9.10) gives us a first understanding of the RIXS intensity.

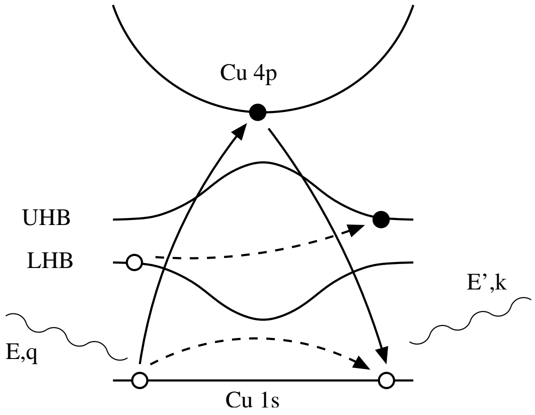

Figure 9.10: Cartoon of the electronic processes involved in resonant inelastic x-ray scattering. A strongly localized Cu 1s electron is excited to the delocalized Cu 4p band by an x-ray photon with energy E and momentum q. The correlated bands (LHB, UHB) lie in between the Cu 1s and Cu 4p bands. Energy E' and momentum k of the outgoing photon are detected. The energy loss $E - E'$ and momentum transfer $q - k$ depend on the charge density excitations in the correlated LHB and UHB.

9.4.2 Experimental Results for SrCuO$_2$

In RIXS experiments the sample is exposed to x-rays that are tuned close to an absorption edge of a particular element. For SrCuO$_2$ the energy of the x-ray photons singles out the copper atoms of the one-dimensional chains. This is a great advantage of the method since only specific electronic excitations are resonantly enhanced. In the setup described here the incoming x-rays are fixed to $E_\mathrm{i} = 8982\,\mathrm{eV}$ near the Cu K-edge and thereby resonantly enhance a feature at $\omega \sim 3\,\mathrm{eV}$. The measurement is then performed by detecting the momentum transfer $q = q_\mathrm{i} - q_\mathrm{f}$ and energy transfer $\omega = \omega_\mathrm{i} - \omega_\mathrm{i}$ of the scattered x-ray photons together with their counts per second. The energy of incoming photons is kept constant at E_i while their momentum is controlled through their angle of incidence.

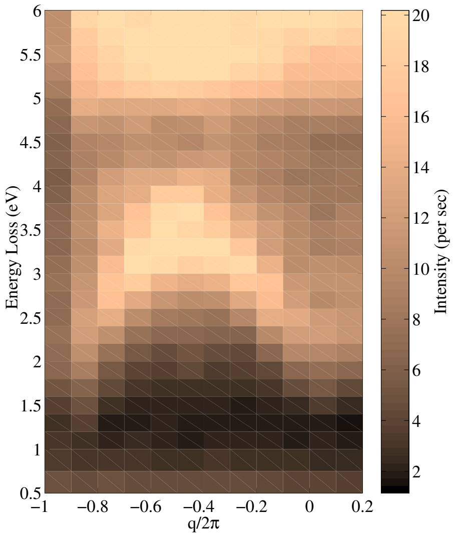

Figure 9.11: Pseudo-color density plot of the RIXS intensity as a function of momentum and energy transfer $E_\mathrm{i} = 8982\,\mathrm{eV}$ (from [52]).

The results of this measurement are shown as a density plot in figure 9.11. The most prominent feature there is a highly dispersive peak at $\omega \approx 3\,\mathrm{eV}$ centered at the zone boundary $q/2\pi = -0.5$. Its band width is 1.1 eV. Upon closer inspection of figure 9.11 we find additional spectral weight also on the low-energy side of this structure. This suggests that the dispersive peak resides in a continuum of excitations. This is in contrast to previous EELS and RIXS results. A recent EELS study [53] proposed that the sharp spectral feature close to the zone boundary is an excitonic bound state which is due to strong onsite Coulomb repulsion. The observation of a low-energy continuum does not permit this interpretation. We can, in fact, completely rule out the applicability of strong-coupling theory to the parameters relevant for SrCuO$_2$ as shown in section 6.2.3. We conclude that the particle-hole excitations do not form a bound exciton at $q = \pi$. An earlier RIXS study [102] interprets the dispersion by the q-dependence of the Mott-gap, or in other words, as the onset of transitions from the lower, effective, Hubbard band to the unoccupied upper Hubbard band. Again, this interpretation is not compatible with the presence of a low-energy continuum below the dispersive peak. The onset dispersion of about 0.4 eV is smaller than the dispersion of the main structure.

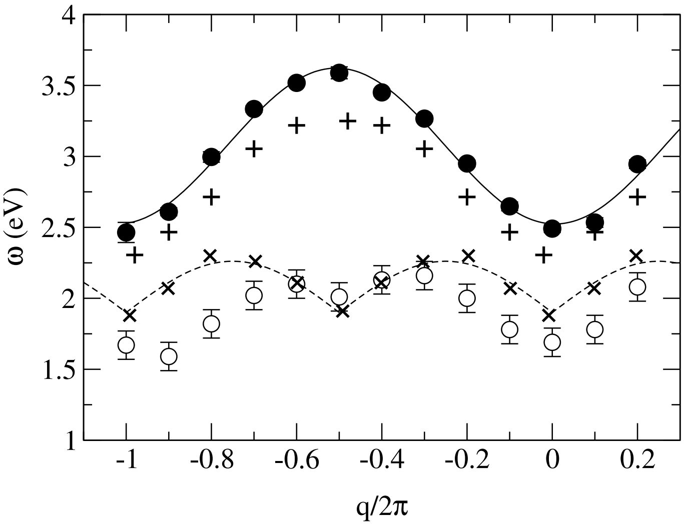

Figure 9.12: Dispersion relation of the peak position (filled symbols) and the onset energy (open symbol) of the RIXS spectra. The solid line is $\omega(q) = 3.07 - 0.55\cos(q)$. The peaks (+) and onsets (×) of $N(q,\omega)$ are also plotted. The dashed line is the spinon dispersion as discussed in the text (from [52]).

We propose that the dispersive structures observed in RIXS can be explained in terms of the charge structure factor of the extended Hubbard model. To this end, calculate $N(q,\omega)$ for chains up to 128 lattice sites using DDMRG. The parameters used are the same as those extracted from the fit of the optical conductivity in section 9.2

Figure 9.12 shows the peak dispersion and the onsets of $N(q,\omega)$, compared with the experimental dispersion. The dispersion of the onset of $N(q,\omega)$ closely follow the spinon-like dispersion which is offset by a constant that corresponds to the charge gap $\Delta_c = 1.94\,\text{eV}$ of the system. Specifically, the onset is described by

$$\frac{\omega_1(q)}{\text{eV}} = \frac{\pi}{2} J|\sin(q)| + 1.9\,. \tag{9.12}$$

The spinon-like dispersion of $\omega_1(q)$ is consistent with the low-energy field theory prediction [103], see also section 9.3. The RIXS data appear to follow this behavior. Firstly, the band width of the onset agrees well with $\pi J/2$ as for $N(q,\omega)$ and, secondly, the energies appear to be compatible. In addition, the overall behavior of the peak dispersion fits the peaks of $N(q,\omega)$. Altogether, we find quantitative and qualitative agreement of RIXS dispersion and $N(q,\omega)$.

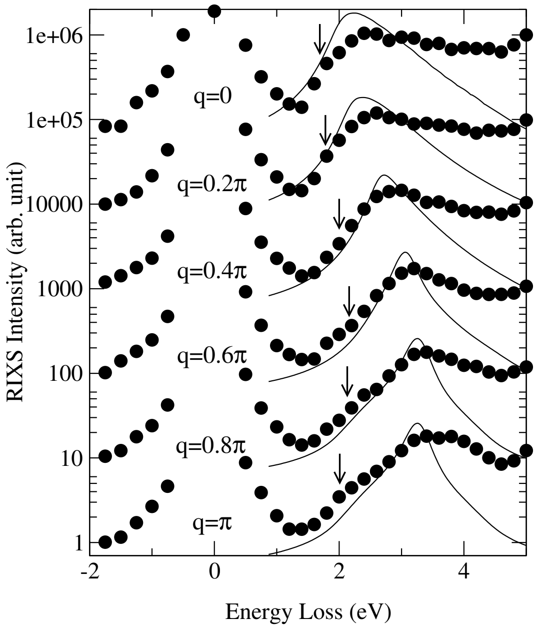

Figure 9.13: RIXS lineshapes and $N(q,\omega)$. The theoretical curves are normalized by a factor $\sin^2(q/2)$ (from [52]). Arrows indicate the onset of the RIXS spectra.

Can we also model the lineshapes with this approach? The problem with this question is, again, the incomplete knowledge of the RIXS response function. In figure 9.13 we plot the RIXS spectra directly together with $N(q,\omega)$. In order to compare both spectra we broadened $N(q,\omega)$ with the experimental resolution, $\eta/t = 0.5$, and normalized $N(q,\omega)$ with a phenomenological q-dependent factor

$$C \sim \sin^2(q/2). \tag{9.13}$$

At $q = 0$ there is a broad band with a peak at $\omega = 2.3\,\text{eV}$. Its spectral weight is almost entirely due to holon-antiholon scattering states [88]. With growing momentum the peaks narrows and becomes sharpest at $q = \pi$. Clearly, noticeable spectral weight accumulates below the peak energy when we approach the zone boundary. As outlined in section 6.2.3, we perform a careful finite-size scaling analysis of the strength of the divergence at $q = \pi$, and find no evidence of a strong-coupling exciton. Our conclusion is that the RIXS peak at the zone boundary is a holon-antiholon resonance that acquires a finite life-time through scattering off spin excitations.

To support this explanation we have calculate $N(q \approx \pi, \omega)$ with higher accuracy and for larger system sizes. Consider figure 9.14 where we have plot $N(q,\omega)$ for $L = 120$ on a logarithmic scale together with a deconvolution of the data. We observe a considerable asymmetry of the peak which is reminiscent of the situation that occurs when a single resonance is coupled to a continuum. Such a *Fano resonance* [104] could well be the explanation of the asymmetrical peak and its intrinsic width. It also points towards a

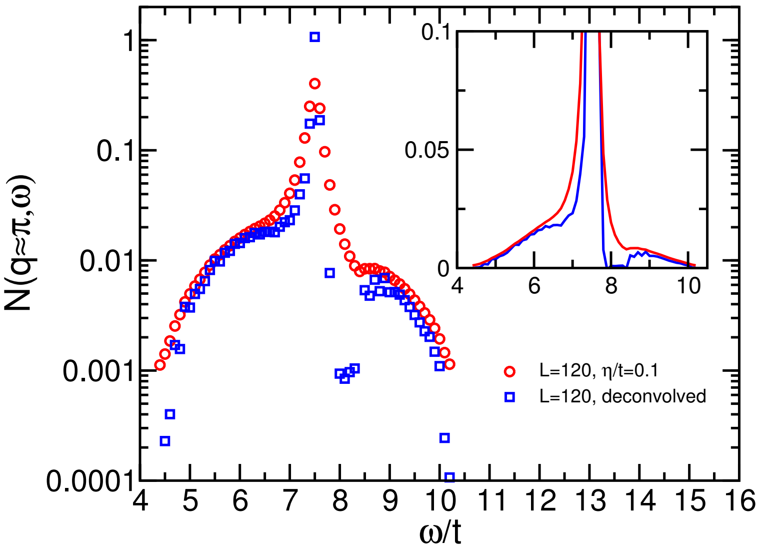

Figure 9.14: Resonance at $q \to \pi$ on a 120-site lattice and a broadening $\eta/t = 0.05$. Both the broadened and the deconvolved data are shown. There is a considerable asymmetry in the peak, reminiscent of a Fano resonance, where a single level (resonance) couples to a continuum of states.

possible explanation of the physics behind the resonance. Let us start from the strong-coupling limit were a long-lived holon-antiholon bound state occurs *below* the continuum. Tuning down U now places the bound state in a continuum of states that was formerly integrated out from the Hilbert space. The hybridization between the bound holon-antiholon resonance and the continuum then leads to a finite life-time of the single mode. Part of the spectral weight is redistributed to the lower onset of the continuum, given through the spinon-like dispersion (9.12).

Let us return to the problem of normalizing the theoretical spectra. The spectral weight of $N(q, \omega)$ vanishes like q^2 for small momenta. Moreover, we know that the integrated weight of $N(q, \omega)$ behaves like $\sin^2(q/2)$ in the limit $U \to \infty$ [50]. In order to see whether or not the similarity with the phenomenological normalization (9.13) is accidental we have determined $\int N(q, \omega)\mathrm{d}\omega$ for various parameters and momenta. The result is shown in figure 9.15. Albeit strong-coupling theory should no longer be a valid description of $N(q, \omega)$ at these interaction strengths, the sum-rule

$$\int \mathrm{d}\omega N(q, \omega) \propto \sin^2(q/2) \tag{9.14}$$

apparently holds. Even though we have no microscopic justification for normalizing with (9.13) we can relate this normalization to the first moment of the charge structure factor (9.14).

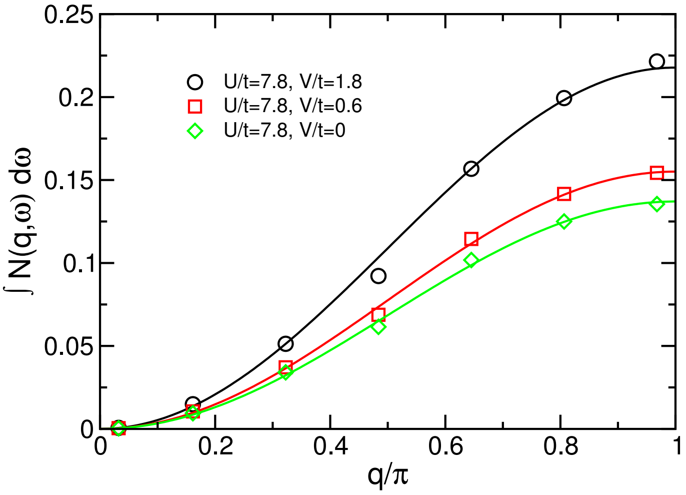

Figure 9.15: Frequency integrated $N(q,\omega)$ for three different sets of parameters. The lines are fits with $\sin^2(q/2)$. We find $\int \mathrm{d}\omega N(q,\omega) \propto \sin^2(q/2)$.

9.5 Conclusion

In this chapter we presented DDMRG calculations of three different dynamical correlation functions of the extended Hubbard model and compared them to experimental results for $\mathrm{SrCuO_2}$.

First, we calculated the optical conductivity $\sigma(\omega)$ and showed that the parameter set (9.3) describes the low-energy part of the experimental data.

Next, we discussed simulations of the dynamical spin structure factor $S(q,\omega)$ of the extended Hubbard model. We found good agreement of the experimental spin-exchange coupling J with our calculations, independently through $S(q,\omega)$ and the one-particle spectral function $A(q,\omega)$. The overall dispersion of features in $S(q,\omega)$ is consistent with the experiment and it would be desirable to make a direct comparison of the lineshapes in the future. Although well resolved ARPES data of insulating systems are difficult to obtain it would be of great interest to compare with $A(q,\omega)$.

Finally, we suggested that the RIXS intensity of $\mathrm{SrCuO_2}$ can be described in terms of the dynamical charge structure factor $N(q,\omega)$. We presented results which quantitatively and qualitatively agree with the RIXS dispersion and argued that there is no excitonic bound state anywhere in the Brillouin zone. Instead, we find a dispersing holon-antiholon resonance with an intrinsic life-time due to scattering of spin excitations. The coupling to this continuum also explains the observed asymmetry of $N(q \approx \pi,\omega)$ in terms of a Fano resonance.

We conclude that the consistent description of these three different probes of the spin and charge dynamics makes a strong case for spin-charge separation in $\mathrm{SrCuO_2}$. Moreover, it provides ample evidence that the extended Hubbard model is indeed the correct one-band effective Hamiltonian of the corner sharing one-dimensional cuprate $\mathrm{SrCuO_2}$.

Chapter 10

Quantum Phase Transition in the Extended Peierls-Hubbard Model

Quasi one-dimensional gapless electron systems have an instability towards the formation of a Peierls dimerized ground state [7]. This symmetry breaking state lowers the total energy of the system and can therefore occur spontaneously. In a half filled Peierls-insulator the expectation value of the bond-order shows a periodic variation with wavevector $2k_{\mathrm{F}} = \pi$. This bond alternation can be modeled with an alternating hopping amplitude between nearest-neighbor sites. When we include local and nearest-neighbor electron-electron interactions this leads to the extended Peierls-Hubbard model which we already encountered in chapters 2 and 8. This explicit bond-alternation introduces a new energy scale into the system which may therefore lead to new quantum critical behavior at $T = 0$.

In a recent field theoretical study by A. Grage [105] and the author of this thesis [106] it is shown that this is indeed the case. Above a critical dimerization the system undergoes a phase transition from a charge density wave insulator (CDW) with coexisting bond-order (BOW) to a phase where only a BOW is present. In this chapter we give numerical evidence for this quantum phase transition and present strong evidence that it belongs to the same universality class as the classical Ising model in two spatial dimensions.

Our analysis of the quantum phase transition in the extended Peierls-Hubbard model begins with the calculation of the CDW and BOW order parameters in open chains. From this we derive the critical exponent β of the CDW order parameter. We determine the dimerization dependence of spin and charge excitations and find an excitation whose energy goes to zero at the quantum critical point. We identify the gap, Δ_2, of this critical mode with the characteristic energy scale of the quantum phase transition. This allows us to determine the product of critical exponents $z\nu$. A scaling analysis of the characteristic correlation length ξ fixes the dynamical critical exponent z. The exponent z relates the vanishing characteristic energy scale to the divergence of the characteristic length scale via $\Delta_2 \sim \xi^{-z}$ which in turn fixes ν. In addition, we calculate ν independently by analyzing the electric susceptibility χ with a hyperscaling Ansatz.

10.1 CDW and BOW Order Parameters

We define the order parameter for the charge-density wave phase as

$$m_{\mathrm{CDW}}(L) = \frac{1}{L} \sum_{\sigma} \sum_{l=1}^{L} (-1)^l \left\langle \hat{n}_{l,\sigma} \right\rangle \ . \tag{10.1}$$

For particle-hole symmetric Hamiltonians $\langle \hat{n}_{l,\sigma} \rangle = 1/2$ at half band filling if the ground state is non-degenerate. In a symmetry-breaking ground state like in the CDW or BOW-phase the ground state is degenerate and the order parameter can take finite values in the thermodynamic limit.

The formation of a bond-ordered ground state can be detected by measuring the value of the bond-order parameter

$$m_{\mathrm{BOW}}(L) = \frac{1}{L} \sum_{\sigma} \sum_{l=1}^{L} (-1)^l \left\langle \hat{c}^{+}_{l,\sigma} \hat{c}_{l+1,\sigma} + \hat{c}^{+}_{l+1,\sigma} \hat{c}_{l,\sigma} \right\rangle \ . \tag{10.2}$$

A finite value of m_{BOW} signals that the kinetic energy of an electron alternates locally, which corresponds to forming a pattern of stronger and weaker bonds. Such a state is referred as a bond-order wave.

In practice, it is more convenient not to perform the averages defined in (10.1) and (10.2). The boundaries induce Friedel-oscillations that decay towards the middle of the chain [107]. When we measure the charge-density and bond-order alternation at the chain center, we find results which are less affected by boundary effects and are equivalent to (10.1) and (10.2) in the thermodynamic limit.

The calculations were performed on open chains with up to $L = 1024$ lattice sites and we used up to $m = 1024$ density-matrix eigenstates in the truncation of the superblock Hamiltonian. The results are summarized in figure 10.1. In the absence of the Peierls dimerization, the system is a CDW-insulator for any value $V > U/2$. When we turn on the dimerization, the BOW order parameter m_{BOW} grows linearly with δ. This trivial dependence is due to the fact that we explicitely introduce the bond-order into the system through the alternating hopping term in the Hamiltonian (2.23). While m_{BOW} is enhanced, the charge-density wave parameter m_{CDW} is reduced until it rapidly decays at the quantum critical point

$$\delta_{\mathrm{c}} = 1.28 \ . \tag{10.3}$$

Beyond this point m_{CDW} vanishes, whereas m_{BOW} deviates non-trivially from the line $m_{\mathrm{BOW}} \approx 0.25\delta$.

This behavior reflects the fact that both types of order compete with each other. For $\delta < \delta_{\mathrm{c}}$ the CDW phase dominates and the coexisting BOW order results from the explicit alternation of the hopping amplitude. When $\delta \geq \delta_{\mathrm{c}}$, the BOW phase wins the energetic tug-of-war and the CDW order parameter vanishes.

What is the nature of the phase transition that we observe in figure 10.1? The onset of $m_{\mathrm{CDW}}(\delta)$ as a function of δ close to the critical point is strikingly similar to the onset

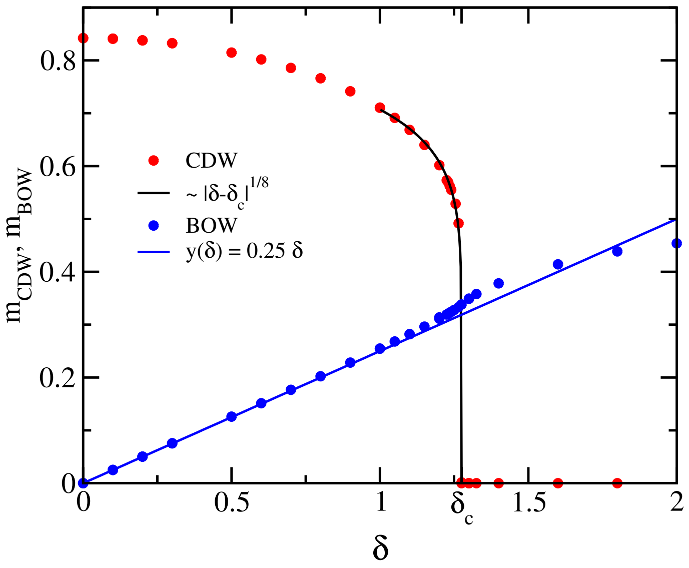

Figure 10.1: Bond-order wave (BOW) and charge density wave (CDW) order parameters of the extended Peierls-Hubbard model with $U/t = 4$, $V/t = 3$, and varying dimerization δ. Open chains with up to $L = 1024$ lattice sites were used and up to $m = 1024$ density-matrix eigenstates. The transition occurs at $\delta_{\rm c} = 1.28$.

of the magnetization in the Ising model where it is well-known that $\langle S_z \rangle \sim |T - T_c|^\beta$. We therefore attempt a fit of the data with a power-law onset $m_{\rm CDW}(\delta - \delta_{\rm c}) \sim |\delta - \delta_{\rm c}|^\beta$ in the vicinity of the critical point. We find that the exponent thus obtained is very close to $\beta = 1/8$ which is precisely the exponent that governs the power-law onset in the Ising model. The logarithmic plot figure 10.2 shows the good agreement of this fit with our data. This leads us to suggest that the transition belongs to the Ising universality class. A finite-size scaling analysis of spin and charge excitation gaps corroborates this interpretation.

10.2 Spin and Charge Gaps

To deepen our understanding of the quantum phase transition we perform an analysis of the size-dependence of the spin and charge excitation gaps. We define the gaps as follows:

$$\begin{aligned} \Delta_{\rm s} &= E_0(N, S_z = 1/2) - E_0(N, S_z = 0) \ , && (10.4) \\ \Delta_1 &= E_1(N, S_z = 0) - E_0(N, S_z = 0) \ , && (10.5) \\ \Delta_2 &= E_2(N, S_z = 0) - E_0(N, S_z = 0) \ . && (10.6) \end{aligned}$$

In these definitions E_0 is the ground state in the subspace under consideration and E_1 and E_2 are the first and second highest excited states, respectively. Note that in a finite

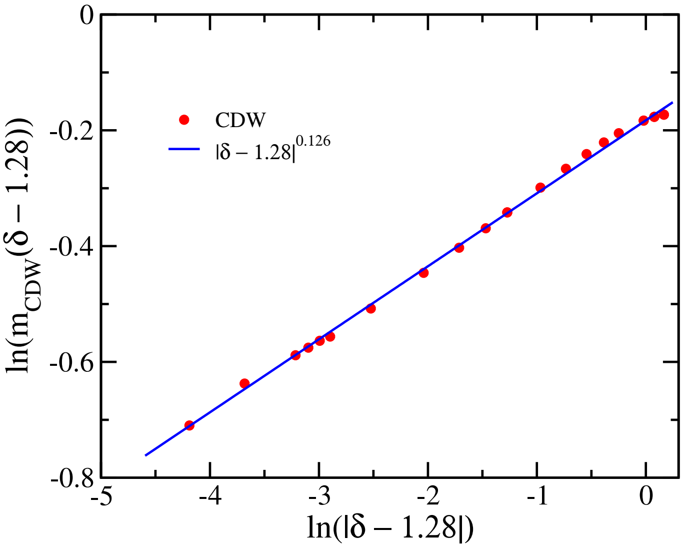

Figure 10.2: Fit of the CDW order parameter m_{CDW} with the power law $|\delta-\delta_{\mathrm{c}}|^{\beta}$ plotted on a logarithmic scale. The best fit is obtained with $\delta_{\mathrm{c}}=1.28$ and $\beta=0.126\approx 1/8$ which is very close to the critical exponent of the classical two-dimensional Ising model.

system states that are degenerate in the thermodynamic limit acquire a non-zero energy difference. The boundaries act as a perturbation that split the levels which will become exactly degenerate in the limit $L\to\infty$. This is true also for periodic systems.

To determine the excitation gaps Δ_1 and Δ_2, the three lowest-lying eigenstates are included as targets in the reduced density-matrix of the subsystem. The spin gap Δ_{s} is determined similarly by targeting the ground states of the $S_z=0$ and $S_z=1/2$ sectors of the Hilbert space.

In contrast to the previous section, we do not employ open boundaries to calculate the excitation gaps. It turns out that localized bound states occur at the system boundaries when we use open boundary conditions. These oscillations of the local spin and charge densities are localized at one chain end. This indicates that charge and spin is localized at the system boundary, or in other words, that a charged bound state forms at the chain ends. Since we are not interested in the energy of such surface effects we have to use periodic boundaries. This makes the simulations considerably more difficult as DMRG is most efficient on open chains. In this study it was possible to determine the excitation gaps in periodic chains with lengths up to $L=128$. Computationally this is very costly since it requires keeping as much as $m=3072$ density-matrix eigenstates. We verified our DMRG results for spin and charge gaps by exact diagonalizations of small systems $(L\le 14)$.

Figure 10.3 shows a plot of the gaps as a function of the dimerization. For clarity, results for small systems are omitted. The gaps Δ_1 and Δ_2 are strongly size dependent. Below the critical value of the dimerization the gap Δ_1 extrapolates to values very

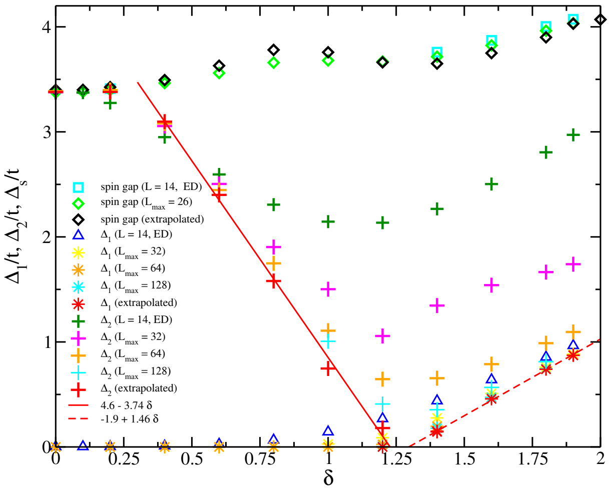

Figure 10.3: Dimerization dependent gaps Δ_1, Δ_2, and Δ_s for different system sizes ($L = 14, 64, 128$). Other system sizes have been omitted for clarity. In the region $\delta < \delta_c$ the ground state is degenerate and $\Delta_1 = 0$. The gap Δ_2 is reduced linearly (red line) as we approach δ_c and extrapolates to zero at the critical point. Above the transition the gap to the first excited state, Δ_1, opens linearly (dashed red line). The spin gap Δ_s is non-zero for all δ and is equal to Δ_2 for very small dimerization, as expected. Note that the one-particle gap (not shown) is finite with values between $\Delta_c/t \approx 5 - 6$. The $L = 14$ data were obtained using exact diagonalizations and agree perfectly with the DMRG data.

close to zero in the thermodynamic limit. This means that the ground-state is twofold degenerate in this dimerization regime. This corresponds to our expectation that the CDW state in the classical picture is invariant under the translation $l \to l + 2$. Above the critical dimerization the gap Δ_1 opens linearly and the ground state is no longer degenerate and has no long-range CDW order.

At $\delta = 0$ the extrapolated gap to the second excited state Δ_2 is very close to the value of the spin gap Δ_s since both are expected to be equal in a CDW insulator. They stay close also for small dimerizations which indicates that the CDW phase of the extended Hubbard model is not strongly perturbed by a small dimerization. This is true only on a lattice, since it is known that in the low-energy continuum limit [105, 106] any non-zero dimerization is a relevant perturbation. Tuning δ to larger values the spin gap Δ_s is not much affected in contrast to Δ_2 which is now linearly reduced with growing dimerization (cf. figure 10.3). Above the critical dimerization Δ_2 increases with the dimerization. It is difficult to reliably extrapolate Δ_2 to $L \to \infty$ numerically because of the strong size dependence of the gap. However, figure 10.3 suggests that Δ_2 is at most slightly larger than Δ_1 in the thermodynamic limit or possibly degenerate.

In the previous section we argued that the onset of the CDW order parameter m_{CDW} is compatible with an Ising-type phase transition. Now, we can go further to show that the excitation of the system that becomes critical at δ_c also suggests this interpretation.

As δ approaches δ_c we expect that the gap to the lowest excitation vanishes like [108]

$$\Delta^{\pm} \sim A^{\pm}|\delta - \delta_\mathrm{c}|^{z\nu} \;, \tag{10.7}$$

below (−) and above (+) the critical point. The non-universal constant $A^{\pm}$ is a typical energy scale of the system and $z\nu$ is a universal critical exponent. This gap is the characteristic energy scale of the quantum phase transition. In figure 10.3 we show a linear fit of the extrapolated gap to the lowest excited state above ($\Delta^{+} = \Delta_1$) and below ($\Delta^{-} = \Delta_2$) the transition point. We obtain

$$\Delta_2(\delta)/t \;=\; 4.6 - 3.74\delta \;, \tag{10.8}$$

$$\Delta_1(\delta)/t \;=\; -1.9 + 1.46\delta \;. \tag{10.9}$$

Both fits are a good description of our data since we can derive a critical dimerization

$$\delta_\mathrm{c} \approx 1.25 \;, \tag{10.10}$$

which is consistent with our estimate (10.3) for the open chains. This suggest that the gap to the lowest excitation indeed vanishes as in equation (10.7). We can now infer that

$$z\nu \approx 1 \;. \tag{10.11}$$

In order to fix z we note that the characteristic length scale $\xi(\delta)$ of the critical fluctuations diverges at the critical point such that

$$\xi \sim |\delta - \delta_\mathrm{c}|^{-\nu} \tag{10.12}$$

holds [108]. The length scale $\xi(\delta)$ can be estimated by considering the critical dimerization $\delta_\mathrm{c}(L)$ as a function of the system length L. By inverting this relation we obtain a critical system size $L_\mathrm{c}(\delta)$ which is an estimate of of the length scale $\xi(\delta)$ of the critical fluctuations. We find that $\nu = 0.98 \approx 1$ in equation (10.12). Comparing with the vanishing characteristic energy scale in (10.7) we conclude that the dynamical critical exponent

$$z = 1 \;. \tag{10.13}$$

Of course, this is what we expected for a critical quantum system that belongs the universality class of a (1 + 1)-dimensional classical system.

Since we could only access system sizes of $L = 128$ lattice sites with periodic boundary conditions the extrapolations to $L \to \infty$ were difficult. We therefore extrapolate a more robust quantity in order to extract the critical value of δ in a periodic system. To this end we calculate the dimerization dependence of Δ_2 for many different system sizes. The results are shown in figure 10.4. We determine the minimum $\Delta_2(\delta_\mathrm{min})$ by fitting second order polynomials to the curves $\Delta_2(\delta)$ to obtain $\delta_\mathrm{min}(L)$ as a function of L. Extrapolating this quantity to $L \to \infty$ should yield the critical value of the dimerization in the thermodynamic limit. This is shown in figure 10.5 where observe that $\Delta_2(\delta_\mathrm{min}) = 0$

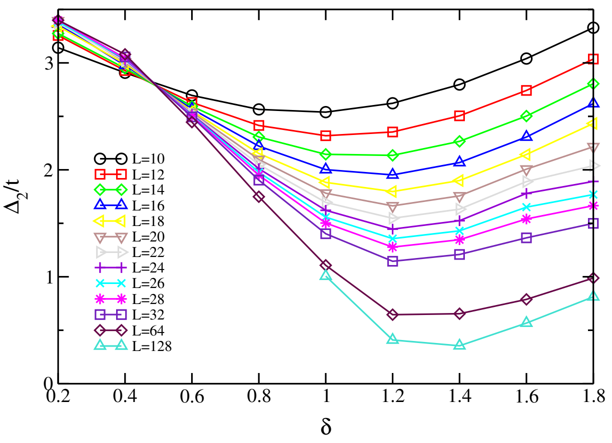

Figure 10.4: Dimerization dependence of the gap $\Delta_2(\delta)$ for periodic systems with ring lengths $L = 10, \ldots, 128$. The position and value of the gap minimum is strongly size-dependent.

within the numerical precision of our extrapolation. An extrapolation yields a critical dimerization

$$\delta_{\mathrm{c}}^{\mathrm{PBC}} = 1.3 \ , \tag{10.14}$$

of the periodic system. This value agrees well with the result in the open chains $\delta_{\mathrm{c}}^{\mathrm{OBC}} = 1.28$ obtained in (10.3) with open boundary conditions and is consistent with the result (10.10) for the periodic system.

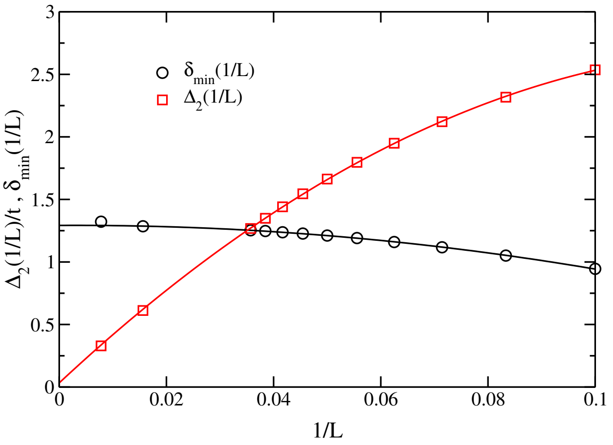

Figure 10.5: Extrapolation of the position $\delta_{\min}$ and value of the minimum of the gap Δ_2 to the limit $1/L \to 0$. Within numerical precision $\Delta_2(L \to \infty) = 0$ at $\delta_{\mathrm{c}}^{\mathrm{PBC}}(L \to \infty) = 1.3$ in good agreement with open boundary conditions.

10.3 Electric Susceptibility

In the previous section we identified the mode that becomes critical at the transition point δ_c. This state is related to the charge degrees of freedom of the system. We therefore consider the static electric susceptibility of the system in the ground state in an open-chain geometry. To this end we apply small electric fields along the chain direction by adding a term

$$F \sum_l \hat{n}_l x_l \tag{10.15}$$

to the Hamiltonian (2.23). The position $x_l = l - (L+1)/2$ along the chain is measured from the center. The polarization is the response of the system this linear electric field and is given by

$$\langle P \rangle = \frac{1}{L} \sum_l x_l \hat{n}_l \ , \tag{10.16}$$

The electric susceptibility can then be defined via

$$\chi_{\text{el}} = \left. \frac{\partial \langle P \rangle}{\partial F} \right|_{F=0} \ . \tag{10.17}$$

Numerically, we determine this derivative with the finite difference

$$\chi_{\text{el}} = \frac{\langle P(F) \rangle - \langle P(F=0) \rangle}{F} \tag{10.18}$$

for sufficiently small F. We will find later that close to the critical point the linear response regime becomes very small. This is due to the fact that even small values of the electric field can become comparable with the vanishing energy scale of the critical system. The fields we apply do not exceed $F = 10^{-5}t$. In order to extract critical exponents from the electric susceptibility we perform a hyperscaling analysis of the data using the hyperscaling Ansatz [109]

$$\chi(\delta, L) \sim L^{2-\eta} \chi(L/\xi) \tag{10.19}$$

with $\xi = |\delta - \delta_c|^{-\nu}$ and critical exponents ν and η. This hyperscaling analysis is shown in figure 10.6.

From the collapse of the data for the position of the peaks we find an exponent $\nu \approx 1$ in figure 10.6. This is fully consistent with the value found in the previous section through scaling relations (10.7) and (10.12). Since all critical exponents are related through scaling relations only two of them are independent and determine all the other critical exponents. Again, we conclude that the quantum phase transition belongs to the same universality class as the two-dimensional classical Ising model.

We can determine the exponent η directly through the hyperscaling Ansatz (10.19). It turns out, however, that the electric fields we applied ($F \leq 10^{-5}t$) are not small enough to ensure that we are in the linear response regime. A closer analysis shows that only fields which are smaller by two orders of magnitude ($F < 10^{-7}t$) are in this regime.

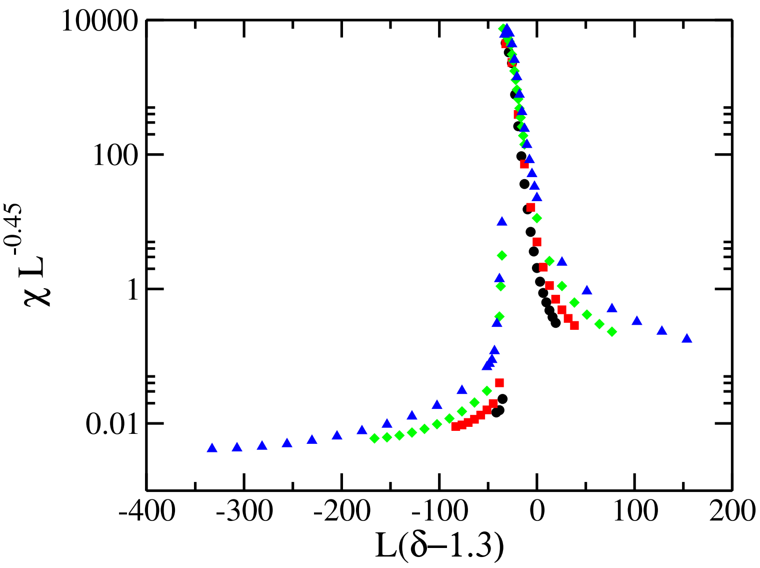

Figure 10.6: Hyperscaling Ansatz for the polarizability of the extended Hubbard model. The exponent derived from collapsing the peak positions onto each other yields $\nu \approx 1$ consistent with previous results. The collapse of the peak heights does not yield a consistent exponent, see text.

Since there is a finite truncation error in the DMRG energies, we cannot access such small fields with reasonable computational effort. In the range of electric fields $F \geq 10^{-7}t$, the response of the system saturates and we therefore strongly underestimate the value of $\chi(\delta)$. Therefore, the exponent $\eta \approx 1.55 = 2 - 0.45$ which one can infer from (10.19) and figure 10.6 is much larger than the true value. We conclude that we can safely disregarded this value as an artefact of the non-linear response of the system.

The divergence of the electric susceptibility is interesting since we found earlier that the one-particle gap of the system remains finite for all values of δ. Of course, the one-particle gap is the lowest energy that is necessary to form charge carrying particle-hole excitations. Therefore, we should not expect the system to be metallic at δ_c, despite a diverging susceptibility χ.

10.4 Conclusion

In this chapter we have shown that there is a quantum phase transition from a mixed CDW-BOW to a BOW phase in the extended Peierls-Hubbard model. For parameters $U/t = 4$, $V/t = 3$ this transition occurs at a critical value $\delta_\mathrm{c} = 1.3$ and is signaled by the vanishing CDW order parameter $m_\mathrm{CDW}(\delta)$. The onset of $m_\mathrm{CDW}(\delta \to \delta_\mathrm{c})$ at the quantum critical point is compatible with an Ising-type phase transition. We verified this in section 10.1 by different means. First, by calculating the critical exponent the CDW order parameter. Second, we determined the δ-dependent gap of the mode that becomes critical at δ_c. And, third, we calculated ν independently through a hyperscaling Ansatz for the electric susceptibility. Both the existence of the transition at intermediate values of the interaction as well as the nature of the quantum phase transition can not be derived from the field theory approach alone.

Further investigations of the model would be highly desirable since the phase diagram is not known except in the limit $\delta \to 0$ [9]. Even there details of the phase diagram are still disputed. A more detailed analysis of the phase diagram of the extended Peierls-Hubbard model is currently in progress.

Chapter 11

Summary and Outlook

11.1 Achievements

In this thesis, we have presented a dynamical density-matrix renormalization group method for calculating momentum and frequency dependent dynamical correlation functions for one-dimensional model Hamiltonians of correlated electrons. In chapter 5 we have described in detail how this is possible for both periodic and open chain geometries. We have thoroughly tested the method in a variety of non-trivial cases. The agreement between the DDMRG results and independent numerical and analytical results is excellent as we have documented in detail in chapter 6.

In chapter 7 we have presented DDMRG results for the one-particle spectral function of Hubbard chains away from half band-filling. The precision of the data is unprecedented, as seen from the comparison with exact Bethe-Ansatz dispersions. This has enabled us to identify the nature of the dispersive structures of the one-particle spectral function in terms of features such as holon and spinon branches or $4k_{\mathrm{F}}$-singlet excitations. The high precision of the data permits an interpretation of a recent ARPES experiment in terms of holon-spinon excitations of the Hubbard model at fillings $n = 0.6$ and $n = 1.4$. The agreement of the spectral features provides strong evidence for spin-charge separation in TTF-TCNQ over an energy scale of 1 eV. We believe this is the best direct spectroscopic observation of spin-charge separation at finite energies in a real material.

Furthermore, we have determined the local density of states of the Hubbard model. Consistent with Luttinger-liquid theory, the electron-addition and electron-removal density of states are separated by a pseudo-gap at zero energy. The upper Hubbard band can, in part, be explained by a Bethe-Ansatz excitation called the k-Λ-string excitation which corresponds to a bound state in the charge sector.

The optical properties of quarter-filled chains have been analyzed in chapter 8. We have studied the optical conductivity of the extended Peierls-Hubbard model in three limits of the parameter space. The large-dimerization limit ($\delta \to 2$, $U > 0$, $V = 0$) can be understood in terms of intra-dimer and inter-dimer excitations at high energies. At low energies, the large-dimerization limit is well-described by an effective half-filled Hubbard model. Thus, optics in this system is described by two different (effective) models at different energy scales. The strong-coupling limit ($0 < \delta < 2$, $U \gg t$, $V = 0$) can be understood from the free-electron Peierls physics where only inter-band transitions between an effective lower and upper Peierls band contribute. In the weak-coupling limit ($0 < \delta < 2$, $U \ll t$, $V = 0$), an effective Hubbard model is consistent with the numerical data. Between these limits, the spectrum changes continously and is strongly affected by the dimerization but less so by the on-site interaction. When a nearest-neighbor interaction is included ($0 < \delta < 2$, $U > 0$, $V > 0$), the spectrum is strongly altered as soon as V is large enough to form excitons below the single-particle gap. A finite-size analysis of optical and single-particle gaps has led us to conclude that excitons are relevant in the family of TMTTF salts.

In chapter 9 we have presented a complete theoretical picture of the dynamical properties of the one-dimensional Mott-insulator $SrCuO_2$. By fitting to highly accurate experimental data for the optical conductivity, we have determined a set of parameters ($U/t = 7.8$, $V/t = 1.3$, $t = 0.435\,\mathrm{eV}$) for the extended Hubbard model which is also consistent with the spin exchange coupling J. Using this parameter set, we have calculated the dynamic spin structure factor and have found that it agrees well with high-precision neutron scattering data. Using the same set of parameters, we have quantitatively explained the dispersion of RIXS spectral features in terms of the dynamic charge structure factor. We have found a holon-antiholon resonance at the zone boundary which acquires a finite life time through scattering of magnetic excitations, in contrast to the strong-coupling picture where a long-lived exciton is present. A single extended Hubbard model has been used to describe three different dynamical correlation functions from three different scattering experiments. This demonstrates the predictive power of our approach and the high accuracy of our numerical method.

In the final chapter, chapter 10, we have further studied the extended Peierls-Hubbard model and have shown that a quantum phase transition from a CDW-insulating ground state with coexisting BOW order to a ground state where only BOW order is present occurs. By performing finite-size scaling on systems with up to 1024 lattice sites, we have extracted the critical exponent of the CDW order parameter. In addition, we have identified the excitation which becomes critical at the transition and have extracted the critical exponent that governs the vanishing of the critical energy scale. The transition belongs to the same universality class as the classical two-dimensional Ising model. A hyperscaling analysis of the electric polarizability has corroborated this conclusion.

11.2 Outlook

We conclude by giving a short outlook on future developments. The list is not exhaustive and only reflects the authors interests at the time of writing.

11.2.1 Algorithmical Improvements

The DMRG algorithm could be developed further along the following lines.

1. In this work, we have used a position-space DMRG code to calculate momentum- and frequency-dependent dynamical correlation functions by expanding the perturbing operators in plane waves or particle-in-a-box eigenstates. A momentum-space (k-DMRG) algorithm would enable us to calculate the dynamics in models with long-range interactions and periodic boundaries.

2. Recently, S. White introduced an efficient method to directly calculate the time evolution of the ground state of one-dimensional lattice Hamiltonians [110, 111]. When a perturbation is applied at time $t = 0$, the propagation of the perturbation can be calculated explicitly in real-space. A Fourier transformation yields the momentum and frequency dynamics of the associated response function directly. The numerical effort is significantly reduced because only the time evolution over a time interval $\Delta\tau$ has to be calculated rather than the spectrum for all k and ω.

3. Analytically and numerically, two-dimensional systems are the final frontier. It is known that DMRG performs poorly in two-dimensional systems. An efficient parallel implementation of the code may push the limit far enough to determine dynamical properties in two dimensions.

11.2.2 Physical Questions

1. In this work, we have presented results for the dynamics of correlated electrons in one dimension. Much less is known for coupled chains or ladders. These systems are the stepping stone from one to two dimensions. DDMRG studies can elucidate the fate of spin-charge separation and Luttinger-liquid physics when single chains are coupled.

2. In TTF-TCNQ, the low-energy properties of the local density of states cannot be convincingly described by a simple Hubbard Hamiltonian. Can the presence of phonons reconcile the apparent discrepancies? DMRG can handle a finite number of phonons per lattice site [112, 113] which is a good approximation at low excitation energies. Therefore, the influence of phononic degrees of freedom on the finite-energy dynamics can be studied.

3. We have only considered effective one-band models in this thesis. What happens to the dynamics of the model when we include more bands? The answer to this question is highly relevant for real materials such as the quasi one-dimensional chain cuprates.

4. Cold atoms in optical traps have attracted a flurry of research on both the experimental and the theoretical side. In particular, the physics of mixed Fermi-Bose gases is a hot topic in this field. DDMRG could be an excellent tool for calculating both static and dynamical properties of these macroscopic quantum states.

Bibliography

[1] J. Hubbard, Proc. R. Soc. London, Ser. A **276**, 238 (1963).

[2] E.W. Carlson, V.J. Emery, S.A. Kivelson, and D. Orgad, in *The Physics of Conventional and Unconventional Superconductors*, ed. by K.H. Bennemann and J.B. Ketterson (Springer, Berlin, 2004), and references therein.

[3] J.G. Bednorz and K.A. Müller, Z. Phys. B **64**, 189 (1986).

[4] F. Gebhard, *The Mott Metal–Insulator Transition* (Springer, Berlin, 1997).

[5] F.H.L. Essler, H. Frahm, F. Göhmann, A. Klümper, V.E. Korepin, *The One–Dimensional Hubbard Model* (Cambridge University Press, Cambridge, 2005).

[6] N.F. Mott, *Metal-Insulator Transitions* (Taylor and Francis, London, 2nd ed., 1990).

[7] R.E. Peierls, *Quantum Theory of Solids* (Clarendon, Oxford, 1995).

[8] F. Gebhard, K. Bott, M. Scheidler, P. Thomas, and S.W. Koch, Phil. Mag. B **75**, 1 (1997).

[9] E. Jeckelmann, Phys. Rev. Lett. **89**, 236401 (2002).

[10] E. Jeckelmann, Phys. Rev. B **67**, 075106 (2003).

[11] D. Baeriswyl, D.K. Campbell, and S. Mazumdar, in *Conjugated Conducting Polymers*, ed. by H. Kiess (Springer, Berlin, 1992).

[12] J.-P. Farges (Ed.), *Organic Conductors* (Marcel Dekker, New York, 1994).

[13] T. Ishiguro, K. Yamaji, and G. Saito, *Organic Superconductors*, (Springer, Berlin, 1998).

[14] C. Bourbonnais and D. Jérome, in *Advances in Synthetic Metals, Twenty Years of Progress in Science and Technology*, ed. by P. Bernier, S. Lefrant, and G. Bidan (Elsevier, New York, 1999).

[15] K. Schönhammer, in *Strong Interactions in Low Dimensions*, ed. by D. Baeriswyl and L. Degiorgi (Springer, Berlin, 2005).

[16] J. Voit, Rep. Prog. Phys. **57**, 977 (1994).

[17] J. Voit, Phys. Rev. B **47**, 6740 (1993).

[18] V. Meden and K. Schönhammer, Phys. Rev. B **46**, 15753 (1992).

[19] H.J. Schulz, in *Correlated Electron Systems*, ed. by V.J. Emery (World Scientific, Singapore, 1993).

[20] E.H. Lieb and F.Y. Wu, Phys. Rev. Lett. **20**, 1445 (1968).

[21] T. Deguchi, F.H.L. Essler, F. Göhmann, A. Klümper, V.E. Korepin, K. Kusabe, Phys. Rep. **331**, 197 (2000).

[22] N. Andrei, in *Low-dimensional Quantum Field Theories for Condensed Matter Physicists*, ed. by S. Lundquist, G. Morandi, and Y. Lu (World Scientific, Singapore, 1995).

[23] M.W. Long and R. Fehrenbacher, J. Phys. Cond. Matt. **2**, 10343 (1990).

[24] C.N. Yang, Phys. Rev. Lett. **19**, 1312 (1967).

[25] W.H. Press, S.A. Teukolsky, W.T. Vetterling, and B.P. Flannery, *Numerical Recipes in C++* (Cambridge University Press, Cambridge, 2002).

[26] M. Takahashi, Prog. Theor. Phys. **47**, 69 (1972).

[27] F. Woynarovich, J. Phys. C **15**, 85 (1982).

[28] F. Woynarovich, J. Phys. C **15**, 97 (1982).

[29] F. Woynarovich, J. Phys. C **16**, 5293 (1983).

[30] S.R. White, Phys. Rev. Lett. **69**, 2863 (1992); Phys. Rev. B **48**, 10345 (1993).

[31] I. Peschel, X. Wang, M. Kaulke, and K. Hallberg (Eds.), *Density-Matrix Renormalization* (Springer, Berlin, 1999).

[32] U. Schollwöck, Rev. Mod. Phys. **77**, (2005).

[33] I. Peschel, M. Kaulke, and Ö. Legeza, Ann. Phys. **8**, 153 (1999).

[34] I.P. McCulloch and M. Gulacsi, Eur. Phys. Lett. **57**, 852 (2002).

[35] S. Östlund and S. Rommer, Phys. Rev. Lett. 75, 3537 (1995).

[36] F. Verstraete, D. Porras, and J.I. Cirac, Phys. Rev. Lett. **93**, 227205 (2004).

[37] F. Verstraete and J.I. Cirac, preprint `cond-mat/0407066`.

[38] Ö. Legeza and J. Solyom, Phys. Rev. B **68**, 195116 (2003); Phys. Rev. B **70**, 205118 (2004).

[39] E. Jeckelmann, Phys. Rev. B **66**, 045114 (2002); E. Jeckelmann, F. Gebhard, and F.H.L. Essler, Phys. Rev. Lett. **85**, 3910 (2000).

[40] E. Jeckelmann, *Dynamical Density-Matrix Renormalization Group*, Habilitationsschrift (Marburg, 2002).

[41] S.K. Pati, S. Ramasesha, Z. Shuai, and J.L. Brédas, Phys. Rev. B **59**, 14827 (1999).

[42] S. Ramasesha, S.K. Pati, H.R. Krishnamurthy, Z. Shuai, and J.L. Brédas, Synth. Met. **85**, 1019 (1997).

[43] C. Raas and G.S. Uhrig, preprint `cond-mat/0412224` (2004).

[44] F. Gebhard, E. Jeckelmann, S. Mahlert, S. Nishimoto, and R.M. Noack, Eur. Phys. J. B **36**, 491 (2003).

[45] E. Jeckelmann and S. Nishimoto, private communication (2004).

[46] Ö. Legeza, J. Röder, and B.A. Hess, Phys. Rev. B **67**, 125114 (2003).

[47] S. Nishimoto, E. Jeckelmann, F. Gebhard, and R.M. Noack, Phys. Rev. B **65**, 165-114 (2002).

[48] T.D. Kühner and S.R. White, Phys. Rev. B **60**, 335 (1999).

[49] Ö. Legeza, private communication (2003).

[50] W. Stephan and K. Penc, Phys. Rev. B **54**, R17269 (1996).

[51] M. Ogata and H. Shiba, Phys. Rev. B **41**, 2326 (1990).

[52] Y.-J. Kim, J.P. Hill, H. Benthien, F.H.L. Essler, E. Jeckelmann, H.S. Choi, T.W. Noh, N. Motoyama, K.M. Kojima, S. Uchida, D. Casa, and T. Gog, Phys. Rev. Lett. **92**, 137402 (2004).

[53] R. Neudert, M. Knupfer, M.S. Golden, J. Fink, W. Stephan, K. Penc, N. Motoyama, H. Eisaki, and S. Uchida, Phys. Rev. Lett. **81**, 657 (1998).

[54] M.J. Bhaseen, F.H.L. Essler, and A. Grage, preprint `cond-mat/0312055`.

[55] S. Kagoshima, H. Nagasawa, and T. Sambongi, *One-dimensional Conductors* (Springer, Berlin, 1998).

[56] K. Penc, F. Mila, and H. Shiba, Phys. Rev. Lett. **75**, 894 (1995).

[57] K. Penc, K. Hallberg, F. Mila, and H. Shiba, Phys. Rev. Lett. **77**, 1390 (1996); Phys. Rev. B **55**, 15475 (1997).

[58] J. Favand, S. Haas, K. Penc, F. Mila, and E. Dagotto, Phys. Rev. B **55**, 4859 (1997).

[59] R.N. Bannister and N. d'Ambrumeneil, Phys. Rev. B **61**, 4651 (2000).

[60] R. Preuss, A. Muramatsu, W. von der Linden, P. Dieterich, F.F Assaad, and W. Hanke, Phys. Rev. Lett. **73**, 732 (1994); M.G. Zacher, E. Arrigoni, W. Hanke, and J.R. Schrieffer, Phys. Rev. B **57**, 6370 (1998).

[61] D. Sénéchal, D. Perez, and M. Pioro-Ladrière, Phys. Rev. Lett. **84**, 522 (2000).

[62] R. Claessen, M. Sing, U. Schwingenschlögl, P. Blaha, M. Dressel, and C.S. Jacobsen, Phys. Rev. Lett. **88**, 096402 (2002).

[63] H. Benthien, F. Gebhard, and E. Jeckelmann, Phys. Rev. Lett. **92**, 256401 (2004).

[64] T.J. Kistenmacher, T.E. Phillips, and D.O. Cowan, Acta Crystalogr., Struct. Crystallogr. Crystal Chem. **30**, 763 (1974).

[65] M. Sing, U. Schwingenschlögl, R. Claessen, P. Blaha, J.M.P. Carmelo, L.M. Martelo, P.D. Sacramento, M. Dressel, and C.S. Jacobsen, Phys. Rev. B **68**, 125111 (2003).

[66] H.J. Schulz, Phys. Rev. Lett. **64**, 2831 (1990).

[67] V. Meden, Phys. Rev. B **60**, 4571 (1999).

[68] J.M.P. Carmelo, K. Penc, P.D. Sacramento, and R. Claessen, J. Phys. IV France **114**, 45, 51 (2004).

[69] A.K. Zhuravlev and M.I. Katsnelson, Phys. Rev. B **61**, 033102 (2001).

[70] S. Ejima, F. Gebhard, S. Nishimoto, and Y. Ohta, preprint `cond-mat/0411151` (2004).

[71] J. Voit, Y. Wang, and M. Grioni, Phys. Rev. B **61**, 7930 (2001).

[72] J.E. Eldrigde, Y. Lin, T.C. Mayadunne, L.K. Montgomery, S. Kaganov, and T. Miebach, Solid State Commun. **105**, 427 (1998).

[73] K. Penc and F. Mila, Phys. Rev. B **50**, 11429 (1994).

[74] F. Mila, Phys. Rev. B **52**, 4788 (1995).

[75] J. Favand and F. Mila, Phys. Rev. B **54**, 10425 (1996).

[76] S. Nishimoto, M. Takahashi, and Y. Ohta, J. Phys. Soc. Jpn. **69**, 1594 (2000).

[77] Y. Shibata, S. Nishimoto, and Y. Ohta, Phys. Rev. B **64**, 235107 (2001).

[78] M. Tsuchiizu, H. Yoshioka, and Y. Suzumura, J. Phys. Soc. Jpn. **70**, 1460 (2001).

[79] D. Pedron, R. Bozio, M. Meneghetti, and C. Pecile, Phys. Rev. B **49**, 10893 (1994).

[80] M. Dressel, A. Schwartz, G. Grüner, and L. Degiorgi, Phys. Rev. Lett. **77**, 398 (1996).

[81] V. Vescoli, L. Degiorgi, W. Henderson, G. Grüner, K.P. Starkey, and L.K. Montgomery, Science **281**, 181 (1998).

[82] A. Schwartz, M. Dressel, G. Grüner, V. Vescoli, L. Degiorgi, and T. Giamarchi, Phys. Rev. B **58**, 1261 (1998).

[83] V. Vescoli, F. Zwick, W. Henderson, L. Degiorgi, M. Grioni, G. Grüner, and L.K. Montgomery, Eur. Phys. J. B **13**, 503 (2000).

[84] D. Controzzi, F.H.L. Essler, and A.M. Tsvelik, Phys. Rev. Lett. **86**, 680 (2001).

[85] T. Giamarchi, Phys. Rev. B **46**, 342 (1992); Physica B **230-232**, 975 (1997).

[86] J.E. Hirsch and D.J. Scalapino, Phys. Rev. B **29**, 5554 (1984).

[87] F. Mila and X. Zotos, Europhys. Lett. **24**, 133 (1993).

[88] F.H.L. Essler, F. Gebhard, and E. Jeckelmann, Phys. Rev. B **64**, 125119 (2001).

[89] F. Gebhard, K. Bott, M. Scheidler, P. Thomas, and S.W. Koch, Phil. Mag. B **75**, 47 (1997).

[90] G. Weiser, Phys. Rev. B **45**, 14076 (1992).

[91] N. Motoyama, H. Eisaki, and S. Uchida, Phys. Rev. Lett. **76**, 3212 (1996).

[92] F.C. Zhang and T.M. Rice, Phys. Rev. B **37**, 3759 (1988).

[93] S. Maekawa and T. Tohyama, Rep. Prog. Phys. **66**, 383 (2001).

[94] I.A. Zaliznyak, H. Woo, T.G. Perring, C.L. Broholm, C.D. Frost, and H. Takagi, Phys. Rev. Lett. **93**, 087202 (2004).

[95] P.G.J. van Dongen, Phys. Rev. B **49**, 7904 (1994).

[96] G. Müller, H. Thomas, H. Beck, and J.C. Bonner, Phys. Rev. B **24**, 1429 (1981).

[97] M. Karbach, G. Müller, A.H. Bougourzi, A. Fledderjohann, and K. Mütter, Phys. Rev. B **55**, 12510 (1997).

[98] P. Abbamonte, C.A. Burns, E.D. Isaacs, P.M. Platzman, L.L. Miller, S.W. Cheong, and M.V. Klein, Phys. Rev. Lett. **83**, 860 (1999).

[99] K. Tsutsui, T. Tohyama, and S. Maekawa, Phys. Rev. B **61**, 7180 (2000).

[100] P.M. Platzman and E.D. Isaacs, Phys. Rev. **57**, 11107 (1998).

[101] J. van den Brink and M. Veenendaal, preprint `cond-mat/0311446` (2003).

[102] M.Z. Hasan, P.A. Montano, E.D. Isaacs, Z.-X. Shen, H. Eisaki, S.K. Sinha, Z. Islam, N. Motoyama, and S. Uchida, Phys. Rev. Lett. **88**, 177403 (2002).

[103] D. Controzzi and F.H.L. Essler, Phys. Rev. B **66**, 165112 (2002).

[104] U. Fano, Phys. Rev. **124**, 1866 (1961).

[105] A. Grage, *Optische Anregungen in eindimensionalen Peierls-Hubbard-Modellen*, PhD. Dissertation (Marburg, 2004).

[106] H. Benthien, A. Grage, and F. Essler, *publication in preparation.*

[107] G. Beduerftig, B. Brendel, H. Frahm, and R.M. Noack, Phys. Rev. B **58**, 10225 (1998).

[108] S. Sachdev, *Quantum Phase Transitions* (Cambridge University Press, Cambridge, 1999).

[109] S.R. Manmana, V. Meden, R.M. Noack, and K. Schönhammer, Phys. Rev. B **70**, 155115 (2004).

[110] S.R. White and A.E. Feiguin, Phys. Rev. Lett. **93**, 076401 (2004).

[111] A.J. Daley, C. Kollath, U. Schollwoeck, and G. Vidal, J. Stat. Mech.: Theor. Exp. P04005 (2004).

[112] E. Jeckelmann and S.R. White, Phys. Rev. B **57**, 6376 (1998).

[113] C. Zhang, E. Jeckelmann, and S.R. White, Phys. Rev. Lett. **80**, 2661 (1998).

Danksagung

Viele Leute haben auf ihre ganz eigene Art und Weise zum Gelingen dieser Arbeit beigetragen. Ihnen allen möchte ich an dieser Stelle danken.

An erster Stelle danke ich sehr herzlich meinem Doktorvater und Mentor Herrn Prof. Dr. Florian Gebhard. Er hat mich während meiner Promotion in jeder Hinsicht gefördert und stand mir stets mit Rat und Tat zur Seite. Ohne seine warmherzige Unterstützung wäre diese Arbeit nicht möglich gewesen.

Besonderer Dank gebührt auch Herrn Priv.-Doz. Dr. Eric Jeckelmann, mit dem ich seit Beginn meiner Doktorarbeit zusammengearbeitet habe. Seine Geduld und freundliche Art haben mir stets sehr geholfen.

Im Rahmen meines Promotionsstipendiums im internationalen Graduiertenkolleg "Electron-Electron Interactions in Solids" hatte ich die Gelegenheit, längere Zeit an Forschungsinstituten im Ausland zu verbringen. Ein halbes Jahr habe ich am KFKI in Budapest (Ungarn) gearbeitet; an dieser Stelle möchte ich Herrn Prof. Dr. Jenő Sólyom und Herrn Dr. Örs Legeza meinen Dank für die liebenswürdige Aufnahme im Gastland Ungarn aussprechen. Herrn Prof. Dr. Peter Thomas sei hiermit für seine Hilfe bei der Organisation des Aufenthaltes und für seine ansteckende Begeisterung für Land und Leute gedankt. Herrn Dr. Fabian Eßler danke ich herzlich für die Einladung an das Brookhaven National Laboratory, Upton, New York (USA), wo ich drei Monate verbracht habe. Sein Interesse und sein freundlicher Zuspruch haben mich sehr vorangebracht und die Ausrichtung meiner Arbeit entscheidend geprägt. Die Seminare des Graduiertenkollegs in Ráckeve und Riezlern halte ich in schöner Errinnerung. Frau Marina Koch und Herrn Peter Bozsoki danke ich für die unermüdliche Hilfe bei der Organisation des Seminars 2004 in Ráckeve.

Mein spezieller Dank gilt Herrn Prof. Dr. Reinhard Noack für die herzliche Aufnahme in seine Arbeitsgruppe und seine freundliche Unterstützung.

Für das angenehme Arbeitsklima und die gute Zusammenarbeit in den Arbeitsgruppen Vielteilchentheorie und Vielteilchennumerik danke ich allen Mitgliedern und insbesondere unserer Arbeitsgruppensekretärin Frau Waltraud von den Bergen.

Desweiteren danke ich meinen Freunden, die mir immer zur Seite gestanden haben. Insbesondere danke ich Anke Raufuß für die gewissenhafte Durchsicht des Manuskripts. Meiner Familie möchte ich für ihre liebe Unterstützung danken, ohne die diese Arbeit nie entstanden wäre. Und schließlich danke ich ganz besonders meiner langjährigen Weggefährtin Anja Grage; sie weiß schon warum.